EFFICIENT RF ENERGY HARVESTING SCHEMES FOR SECURE COMMUNICATION IN WIRELESS NETWORKS

Thesis submitted by

CHANDRIMA THAKUR

Doctor of Philosophy (Engineering)

Department of Electronics & Telecommunication Engineering

Faculty Council of Engineering & Technology

Jadavpur University

Kolkata, India

2025

JADAVPUR UNIVERSITY
KOLKATA-700 032, INDIA

INDEX NO.: **30/18/E**

1. Title of the Thesis: **Efficient RF Energy Harvesting Schemes for Secure Communication in Wireless Networks**

2. Name, Designation & Institution of the Supervisor:

Name: **Prof. Sudipta Chattopadhyay**

Designation: **Professor, Department of Electronics & Telecommunication Engineering**

Institution: **Jadavpur University, Kolkata, India**

3. List of Publications

• Book Chapters

1. **Thakur, C.,** & Chattopadhyay, S. (2024). Development and Analysis of an RF-Powered Rechargeable Wireless Sensor Network for LR-WPAN. In *5G and Beyond Wireless Communications* (pp. 125-153). CRC Press.

2. **Thakur, C.**, & Chattopadhyay, S. (2025). Experiment, Modelling, and Analysis of an RF WPT-Enabled Wireless Sensor Network for Industry 5.0. In *The Intersection of 6G, AI/Machine Learning, and Embedded Systems* (pp. 107-124). CRC Press.

• International Journals

1. **Thakur, C.**, & Chattopadhyay, S. (2021). Secrecy performance of a novel energy efficient hybrid CIoT network with beacon-aided RF energy harvesting under dissimilar fading environments. *Journal of Ambient Intelligence and Humanized Computing*, 13, 4057–4075, Springer (**Impact Factor: 7.104, SCI Indexed in 2021**)

2. Majumdar, S., **Thakur, C.**, & Chattopadhyay, S. (2022). A novel relay-aided centralized cooperative spectrum sensing scheme using radio frequency energy harvesting. *International Journal of Communication Systems*, 36(1), e5356, Wiley **(Impact Factor: 2.1, SCI Indexed**)

3. Chowdhury, R. S., Sadhu, J. K., **Thakur, C.**, & Chattopadhyay, S. (2022). Performance analysis and optimization of a hybrid TSR–PSR protocol for AF, DF and hybrid AF–DF relaying under Weibull fading. *Telecommunication Systems*, 82(1), 61-90, Springer (**(Impact Factor: 2.5, SCI Indexed)**

4. **Thakur, C.**, & Chattopadhyay, S. (2024). Performance Analysis of RF-Powered Multi-device Diamond Relay IoT Network Using Adaptive NOMA. *Arabian Journal for Science and Engineering*, 1-15, Springer **(Impact Factor: 2.6, SCI Indexed)**

5. **Thakur, C.,** & Chattopadhyay, S. (2025). An RF-powered multi-device diamond relay IoT network using A-NOMA for WBAN. *International Journal of Electronics*, 1–20, Taylor & Francis (**I.F.: 1.2, SCI Indexed**)

• International Conferences

1. **C. Thakur** and S. Chattopadhyay, "A novel Interference-aided Energy Harvesting Scheme for Cooperative Network," *2019 IEEE Region 10 Symposium (TENSYMP)*, Kolkata, India, 2019, pp. 84-89, doi: 10.1109/TENSYMP46218.2019.8971278.

2. **C. Thakur** and S. Chattopadhyay, "Enhancement of Secrecy Throughput Performance in a Cooperative Network with Interference-assisted Energy Harvesting," *2019 International Symposium on Advanced Electrical and Communication Technologies (ISAECT)*, Rome, Italy, 2019, pp. 1-6, doi: 10.1109/ISAECT47714.2019.9069728.

3. S. Roy, P. Kabiraj, S. Dey, **C. Thakur** and S. Chattopadhyay, "Throughput Analysis of Multi-Source Multi-Antenna Cooperative Relay Network with RF Energy Harvesting using Improved Relay Selection schemes," *2020 4th International Conference on Electronics, Materials Engineering & Nano-Technology (IEMENTech)*, Kolkata, India, 2020, pp. 1-6, doi: 10.1109/IEMENTech51367.2020.9270109.

4. **C. Thakur** and S. Chattopadhyay, "Secrecy Performance of an improved Interference-aided RF Energy Harvesting scheme in Two-Way Multi-Antenna Relay Network," *2020 IEEE Applied Signal Processing Conference (ASPCON)*, Kolkata, India, 2020, pp. 123-127, doi: 10.1109/ASPCON49795.2020.9276720.

5. N. Das, S. Debnath, **C. Thakur** and S. Chattopadhyay, "Adaptive RF Energy Harvesting Relaying Protocol for Bidirectional Multi-Relay Multi-antenna Cooperative Network over Nakagami Fading," *2021 International Conference on Advances in Electrical, Computing, Communication and Sustainable Technologies (ICAECT)*, Bhilai, India, 2021, pp. 1-6, doi: 10.1109/ICAECT49130.2021.9392510.

6. **C. Thakur** and S. Chattopadhyay, "A Novel Interference-aided RF Energy Harvesting scheme for Cooperative NOMA Network," *2021 IEEE 18th India Council International Conference (INDICON)*, Guwahati, India, 2021, pp. 1-6, doi: 10.1109/INDICON52576.2021.9691663.

7. **C. Thakur**, S. Majumdar and S. Chatterjee, "Performance of Combined RF and non-RF based Energy Harvesting scheme for Multi-Relay Cooperative Cognitive Radio Network," *2022 First International Conference on Electrical, Electronics, Information and Communication Technologies (ICEEICT)*, Trichy, India, 2022, pp. 1-5, doi: 10.1109/ICEEICT53079.2022.9768567.

8. S. Majumdar, **C. Thakur** and S. Chatterjee, "Cooperative Spectrum Sensing based Hybrid Smart Home Energy Management System with Energy Harvesting," *2023 Third International Conference on Advances in Electrical, Computing, Communication and*

Sustainable Technologies (ICAECT), Bhilai, India, 2023, pp. 1-5, doi: 10.1109/ICAECT57570.2023.10117746.

9. M. Saha, **C. Thakur** and S. Chattopadhyay, "A Novel Relay Selection Strategy for RF Energy Harvested Communication Network," *2023 IEEE Silchar Subsection Conference (SILCON)*, Silchar, India, 2023, pp. 1-6, doi: 10.1109/SILCON59133.2023.10404807

- **National Conferences**

1. P. Biswas, **C. Thakur**, A. Haldar, and S. Chattopadhyay, "Secrecy Performance of Novel Destination Assisted Jamming in Wireless Cooperative Networks under the Influence of Trusted and Untrusted Relays," *A Collection of Contemporary Research Articles in Electronics, Communication and Computation*, p. 13-16, 2021.

2. D. K. Lal, **C. Thakur**, S. Chattopadhyay, and S. Nag, "Throughput Analysis Using Three-Step Two-Way Decode and Forward Multi Relay Network For Wireless Energy Harvesting," *A Collection of Contemporary Research Articles in Electronics, Communication and Computation*, p. 62-68, 2021.

4. List of Patents: **Nil**

5. List of Presentations in National/International Conferences

1. **C. Thakur** and S. Chattopadhyay, "A novel Interference-aided Energy Harvesting Scheme for Cooperative Network," 2019 IEEE Region 10 Symposium (TENSYMP), Kolkata, India, 2019, pp. 84-89, doi: 10.1109/TENSYMP46218.2019.8971278.

2. **C. Thakur** and S. Chattopadhyay, "Secrecy Performance of an improved Interference-aided RF Energy Harvesting scheme in Two-Way Multi-Antenna Relay Network," 2020 IEEE Applied Signal Processing Conference (ASPCON), 2020, pp. 123-127, doi: 10.1109/ASPCON49795.2020.9276720.

3. **C. Thakur** and S. Chattopadhyay, "A Novel Interference-aided RF Energy Harvesting scheme for Cooperative NOMA Network," 2021 IEEE 18th India Council International Conference (INDICON), 2021, pp. 1-6, doi: 10.1109/INDICON52576.2021.9691663.

4. **C. Thakur**, S. Majumdar and S. Chatterjee, "Performance of Combined RF and non-RF based Energy Harvesting scheme for Multi-Relay Cooperative Cognitive Radio Network," *2022 First International Conference on Electrical, Electronics, Information and Communication Technologies (ICEEICT)*, Trichy, India, 2022, pp. 1-5, doi: 10.1109/ICEEICT53079.2022.9768567.

6. List of Achievements

1. The paper entitled "Throughput Analysis Using Three-Step Two-Way Decode and Forward Multi-Relay Network for Wireless Energy Harvesting," authored by Dipak Kumar Lal, **Chandrima Thakur**, Sudipta Chattopadhyay and Srinjana Nag has received the Best Paper Award in National Conference on Electronics, Communication and Computation (NCECC 2020) at Nit Jamshedpur, India, September 5-6, 2020.

2. The paper entitled " Throughput Analysis of Multi-Source Multi-Antenna Cooperative Relay Network with RF Energy Harvesting using Improved Relay Selection schemes," authored by S. Roy, P. Kabiraj, S. Dey, **C. Thakur** and S. Chattopadhyay has received the Best Paper Award in 4th International Conference on Electronics, Materials Engineering and Nano-Technology (IEMENTech 2020) IEM, Kolkata, India, October 2-4, 2020.

STATEMENT OF ORIGINALITY

I, **Chandrima Thakur**, registered on 12/06/2018 do hereby declare that this thesis entitled "**Efficient RF Energy Harvesting Schemes for Secure Communication in Wireless Networks"** contains literature survey and original research work done by the undersigned candidate as part of Doctoral studies.

All information in this thesis have been obtained and presented in accordance with existing academic rules and ethical conduct. I declare that, as required by these rules and conduct, I have fully cited and referred all materials and results that are not original to this work.

I also declare that I have checked this thesis as per the "Policy on Anti-Plagiarism, Jadavpur University, 2019", and the level of similarity as checked by iThenticate software is **8%**

Chandrima Thakur

Signature of Candidate (Chandrima Thakur):

Date: 29/07/2024

Sudipta Chattopadhyay 29/07/2024

Certified by Supervisor (Prof. Sudipta Chattopadhyay):

(Signature with date, seal)

Dr. Sudipta Chattopadhyay
Professor
Department of Electronics and Telecommunication Engineering
Jadavpur University
Kolkata- 700 032
India

CERTIFICATE FROM THE SUPERVISOR

This is to certify that the thesis entitled **Efficient RF Energy Harvesting Schemes for Secure Communication in Wireless Networks** submitted by **Chandrima Thakur**, who got her name registered on **12/06/2018** for the award of **Ph.D. (Engineering)** degree of Jadavpur University is absolutely based upon her own work under the supervision of **Prof. Sudipta Chattopadhyay** and that neither her thesis nor any part of the thesis has been submitted for any degree/diploma or any other academic award anywhere before.

Sudipta Chattopadhyay 29/07/2024

Signature of the Supervisor with date and office Seal

Dr. Sudipta Chattopadhyay
Professor
Department of Electronics and Telecommunication Engineering
Jadavpur University
Kolkata- 700 032
India

ACKNOWLEDGEMENT

First and foremost, I humbly offer my deepest gratitude and praise to Almighty God, whose divine blessings, infinite wisdom, and unwavering guidance have been the foundation of this research, enabling its successful completion.

I express profound and sincere gratitude to my supervisor Prof. Sudipta Chattopadhyay, Department of Electronics and Communication Engineering, Jadavpur University, for her full support, constant encouragement, and advice, both in technical and non-technical matters during the entire period of the investigation.

I would like to thank our present Head of the Department, Prof. Sudhabindu Ray, for his encouragement and guidance for this research. Besides my advisor, I am thankful to the RAC committee expert Prof. Sayan Chatterjee, who asked me challenging questions and gave insightful comments on my work. I gratefully acknowledge the valuable advice and necessary support received from Prof. Monotosh Biswas, Prof. P. Venkateshwaran, Prof. Sheli Sinha Chowdhuri and Prof. Ananda Shankar Chowdhury, Ex Heads of the Department of ETCE.

I dedicate this thesis to my parents and brother for their unwavering support, invaluable guidance, and constant encouragement throughout the entire course of this thesis.

I wish to thank my colleague, Suvaditya Majumdar for taking the time to discuss my research problems and helping me prepare presentations. More importantly, thank you for creating an intellectual and enjoyable atmosphere in the lab.

Finally, I wish to acknowledge the financial support of State Government Fellowship Scheme of Jadavpur University as Senior Research Fellow which greatly facilitated the successful execution of my research. A part of the research work was also supported by the Department of Science & Technology and Biotechnology, Government of West Bengal (Sanction Order no. 508 (Sanc.)/STBT-11012(16)/29/2021-ST SEC).

Chandrima Thakur

Index No: 30/18/E

Dedicated to my grandfather

Late Shri Saroj Kumar Mukherjee

my parents

and

my brother

Abstract

Wireless communication has grown explosively and significant efforts have been made for increasing the data transmission rate over a bandwidth-limited wireless channel with high reliability simultaneously causing low power consumption. One of the most prominent solutions can be regarded as the ambient Radio Frequency (RF) Energy Harvesting (EH) which is a potential green communication technology and an energy efficient approach to energize the relay devices while preventing battery drainage issue and simultaneously enabling data transmission as well.

The integration of RF Wireless Power Transfer (WPT) technology in relay-aided communication systems have led to the implementation of green communication systems. The performance of communication networks can be improved using the best relay from multiple relay communication. Two-way relaying techniques have emerged as a spectral-efficient scheme for bidirectional message exchange between two users and have shown to increase diversity capacity and thus improve the range of wireless communication.

For improved Spectral Efficiency (SE) and capacity enhancement, Non-Orthogonal Multiple Access (NOMA)-assisted cooperative network has emerged as an effective and efficient scheme to support the rigorous demands of Fifth Generation and Beyond (5G+) wireless networks. However, maintaining Energy Efficiency (EE) and sustainability in the design and operation of wireless communication systems is a major concern. Thus, the concept of energy-efficient NOMA or 'green' NOMA has been introduced in the upcoming 5G mobile network design to cater for the goal of achieving a low cost, self-sustaining, environment-friendly wireless network. Although NOMA technique is far superior to traditional multiple access ones, there is still a paucity of research contributions on investigating the security issues of NOMA with EH. Therefore, Physical Layer Security (PLS)-aware RF-powered NOMA systems have gained much interest from researchers.

An important application of WPT that plays a crucial role in time-critical applications is the time requirement for charging a battery/supercapacitor. Battery usage and recharging is challenging especially for autonomous operation of ultra-low battery-powered smart sensors in applications of Internet of Things (IoT) and Wireless Sensor Network (WSN). RF-WPT provides reliable and stable energy supply to the in-built batteries by transmission of RF energy.

Motivated by the above research trends and challenges, different relay selection strategies have been implemented with Interference-Aided (IA) EH. Moreover, new two-way relaying schemes have been developed under realistic assumptions to achieve improved

performance related to energy efficiency, secrecy capacity and harvested power. Simulations are performed in MATLAB 2022b. Additionally, Netsim v13.1 modeller tool has been used to create a virtual Industrial IoT (IIoT) scenario. To validate the proposed model, Bluetooth-enabled PowerSpot RF Wireless Power Development Module (P1110-EVAL-PS) has been utilized to charge various sensors and multiple consumer devices using the harvested RF power.

In the first instance, performance of RF-powered one-way single relay networks has been investigated. The throughput performance of a DF relay system has been studied using Hybrid TSR-PSR protocol architecture with IA-EH scheme. Next, Destination-based Jamming (DBJ) technique has been incorporated in an ideal interference-free environment to investigate the system security in the presence of an Eavesdropper (EAV). Moreover, a secure one-way communication model has been presented in an interference-limited untrusted environment.

In the second scenario, various relay selection strategies have been applied to analyse the throughput and secrecy performance of multi-relay cooperative network. The throughput analysis of a Multi-Source Multi-Antenna Cooperative Relay Network (CRN) with RF-EH has been carried out using maximum energy accumulated selection and optimal relay selection schemes in an ideal interference-free environment. Next, a generalized RF energy harvesting framework has been designed with Hybrid TSR-PSR protocol for AF, DF and hybrid AF-DF relaying schemes under the Weibull fading channel. Additionally, the security performance in multi-relay network with a friendly jammer has been evaluated.

In the third part of our research, the performance of two-way cooperative networks has been analysed. Here an energy-efficient and secure transmission scheme has been devised for bidirectional IoT relay network with energy accumulation using RF-EH in interference-limited environment. The untrusted relays accumulate the harvested energy from the surrounding RF sources and Co-Channel Interferers (CCIs) and utilize that energy to forward the confidential information to the respective destinations.

In the fourth instance, the impact of RF-EH in NOMA-assisted CRN has been shown. The performance of an autonomous and energy-efficient RF-powered Multi-Device (MD) Diamond Relay Network (DRN) in an IoT environment has been studied using an improved Adaptive NOMA (A-NOMA) protocol. Alongwith this, the secrecy performance of a two-user Cooperative NOMA network has been examined under the influence of a cluster of interferers using jamming cancellation scheme.

Finally, the impact of RF-WPT on Rechargeable Wireless Sensor Network (R-WSN) has been observed in IIoT application.

Contents

List of Figures

List of Tables

List of Abbreviations

4G: Fourth Generation

5G+: Fifth Generation and Beyond

AF: Amplify-and-Forward

AN: Artificial Noise

A-NOMA: Adaptive NOMA

ARP: Adaptive Relaying Protocol

AS: Antenna Selection

ASR: Achievable Sum Rate

AWGN: Additive White Gaussian Noise

BS: Base Station

BER: Bit Error Rate

BLE: Bluetooth Low Energy

CCI: Co-Channel Interferer

CCRN: Cooperative Cognitive Radio Network

CIoT: Cooperative Internet of Things

CJ: Cooperative Jamming

CRN: Cooperative Relay Network

CSI: Channel State Information

DBJ: Destination-based Jamming

DF: Decode-and-Forward

DL: Downlink

DoD: Depth of Discharge

DRN: Diamond Relay Network

DT: Delay Tolerant

EAV: Eavesdropper

EE: Energy Efficiency

EH: Energy Harvesting

EH-CN: Energy Harvesting Cooperative Network

EIRP: Equivalent Isotopically Radiated Power

ESR: Ergodic Sum Rate

EVB: Evaluation Board

FD: Full-Duplex

HD: Half-Duplex

HDAF: Hybrid AF-DF

IA: Interference-Aided

IoT: Internet of Things

IIoT: Industrial Internet of Things

IUI: Inter-User Interference

MA: Multiple Access

NL: Network Lifetime

NOMA: Non-Orthogonal Multiple Access

NR-WSN: Non-Rechargeable Wireless Sensor Network

OFDMA: Orthogonal Frequency Division Multiple Access

OMA: Orthogonal Multiple Access

OP: Outage Probability

ORS: Opportunistic Relay Selection

OWR: One Way Relay

PA: Power Allocation

PLS: Physical Layer Security

PRS: Partial Relay Selection

PS: Power-Splitting

PSR: Power Splitting Relaying

QoS: Quality of Service

RF: Radio Frequency

RS: Relay Selection

RSSI: Received Signal Strength Indication

R-WSN: Rechargeable Wireless Sensor Network

SC: Secrecy Capacity

SE: Spectral Efficiency

SIC: Successive Interference Cancellation

SINR: Signal-to-Interference and Noise Ratio

SNR: Signal-to-Noise Ratio

SOP: Secrecy Outage Probability

SR: Secrecy Rate

SWIPT: Simultaneous Wireless Information and Power Transfer

TS: Time-Switching

TSR: Time Switching Relaying

TWC: Two Way Communication

TWR: Two Way Relay

UR: Untrusted Relay

UL: Uplink

Wi-Fi: Wireless Fidelity

WPCN: Wireless Powered Cooperative Network

WPT: Wireless Power Transfer

WSN: Wireless Sensor Network

List of Symbols

S : Source

S_1 and S_2: Sources

$\{s_1, s_2, ...s_n\}$: Sensor motes

R , *DFR1, DFR2*: Relay

D : Destination

I : CCI

B: Power Beacon

EAV: Eavesdropper

HDAF: Hybrid Decode-Amplify Forward Relay

T_x : Transmitter

R_x : Receiver

J: Jammer

NU: Near User

FU: Far User

α : EH coefficient

ρ : Power-splitting factor

α_1, α_2 : Power allocation coefficients for NU and FU respectively

η : RF-DC Energy Conversion Efficiency

T : Total time period

τ : Throughput

P_{out} : OP

P_I : Transmit power of CCI

P_S : Transmit power of S

P_D : Transmit power of D

P_R : Transmit power of R

P_B : Transmit power of B

P_J : Transmit power of J

d_{SR} : S-R distance

d_{RD} : R-D distance

d_{IR} : I-R distance

d_{ID} : I-D distance

W : Bandwidth

$|h_{SR}|^2$: Channel mean coefficient from S to R

$|h_{RD}|^2$: Channel mean coefficient from R to D

$|f_{IR}|^2$: Channel mean coefficient from I to R

R_{th} : Threshold Secrecy Rate

$|f_{RD}|^2$: Channel mean coefficient from I to D

m : Path loss coefficient

γ_{th} : SINR threshold

R_S : Fixed source transmission rate

μ : Amplification factor in AF mode

C_S^{DF} : Secrecy Rate in DF mode

C_S^{AF} : Secrecy Rate in AF mode

γ_M : SNR of legitimate link

γ_E : SNR of EAV/wiretap link

C_{SEC} : Secrecy Capacity

C_{SD} : Capacity of main link

C_E : Capacity of EAV link

v_m : Weibull shape parameter for main link

v_e : Weibull shape parameter for EAV link

q_m : Weibull shape parameter for main link

q_e : Weibull shape parameter for EAV link

η_{EE} : System Energy Efficiency

η_b : Conversion Efficiency of Power Beacon

G_T : Gain of Transmitter

G_R : Gain of Receiver

P_T : Power transmitted by the RF transmitter

L_P : Polarization loss

θ: Charging orientation angle between transmitter and sensor

T_{Bat} : Time to recharge battery

V_B : Charging Voltage

C_B : Battery Capacity

D_B : DoD of the battery

l_{beacon} : length of beacon packet

τ^{ON} : Duration when a sensor mote in 'ON'

T_{Net} : Network Lifetime

χ : Packet arrival rate

$E_{initial}$: Initial Network Energy

E_C : Energy consumption

E_W : Expected wasted (unused) energy in the network when it dies

E_S is the expected energy consumption

t_C : Recharging time

E_{T_X} : Energy consumption during data transmission

E_{T_X} : Energy consumption during data reception

E_{idle} : Energy consumption during idle mode

E_{sleep} : Energy consumption during sleep mode

λ : wavelength of transmitted signal

$\Gamma(.)$: Gamma function

P_{out}^{sec} : Secrecy Outage Probability

Chapter 1
INTRODUCTION

1.1 BACKGROUND

Spectrum scarcity, security threats, limited battery power of wireless nodes, greater energy consumption, large volume of data transmission with greater reliability, long distance coverage and so on are some of the issues in upcoming Fifth Generation and Beyond (5G+) wireless networks. Cooperative relaying techniques can be used in cooperative communication networks to alleviate fading and attenuation issues by placing relay nodes between a transmitter and a receiver. As a result, network performance characteristics such as efficiency, throughput, and reliability can be enhanced. An energy-constrained relay node, on the other hand, cannot ensure acceptable Quality of Service (QoS). In extreme situations, replacing or recharging the traditional power supply is impossible. For instance, devices implanted in patients to monitor health data are increasing in number; however, these devices are expensive, and their batteries can be difficult to replace. This issue has increased the demand for wireless battery charging using external sources or battery-free wireless charging, which has fuelled the emergence of wireless Energy Harvesting (EH) [1]. Conventional EH technologies depend on external energy sources like wind, vibration and solar which is intermittent in nature and suffers from the time-varying issue as well as material inefficiency. Since Radio Frequency (RF) signals carry energy as well as information without frequent monitoring and maintenance, Radio Frequency Energy Harvesting (RF-EH) has emerged as a potential green communication technology facilitating the low power devices to collect energy from the surrounding environment.

One Way Relaying (OWR) or unidirectional networks have been widely applied in practical data communication for long-distance information transmission in wireless networks. Owing to its superior spectrum efficiency, Two Way Relaying (TWR) [2] has gained significant attention as an efficient scheme for bidirectional data transfer that improves the coverage and capacity of wireless networks. Relay Selection (RS) is a practical solution to exploit the cooperative diversity in a wireless network where multiple relays are available. In EH-assisted

relay networks, the transmit power of relays is not restricted by the volume of their batteries. Instead, the energy used for relaying is harvested from the received signals.

The broadcasting nature of wireless communication medium enables any node within its range to pry on the confidential information. As a complementary and alternative technology to traditional cryptographic approach, Physical layer security (PLS) has drawn attention as a security provisioning scheme for 5G+ networks and beyond as it explores the random characteristics (i.e., fading and interference) of the transmission medium. In the context of two-way cooperative relaying, a practical and attractive area is the untrusted scenario, where a relay assists communication between two nodes as a legitimate entity but acts as a silent Eavesdropper (EAV). Generally, in practical Internet of Things (IoT) environment, interference is an obnoxious phenomenon in wireless communication system since it becomes a menace to the wireless channel capacity if not being totally decoded and removed. Contrary to this view, recent interests have emanated on innovative approaches that consider interference as a useful resource for developing energy efficient and secure communication systems [3]. However, it is still an open research problem to design new methods to exploit Co-Channel Interference (CCI) signals efficiently in a two-way IoT network with EH capability that can simultaneously improve the performance of the network and promote continuous energy transfer.

Due to its low cost, low complexity receivers, and lack of Inter-User Interference (IUI), Orthogonal Multiple Access (OMA) was thought to be a practical technique for Fourth Generation (4G) wireless networks. In order to support the high demand of multimedia traffic in IoT network, an efficient Multiple Access (MA) technology referred as Non-Orthogonal Multiple Access (NOMA) [4] has been designed to provide high Spectral Efficiency (SE) as required for 5G+ wireless networks. NOMA offers massive connectivity, broader coverage, enhanced data rate, high SE and reliability by sending superimposed RF signals over the same radio resources from multiple users by allocating different power factors followed by Successive Interference Cancellation (SIC) scheme. However, one prominent disadvantage is that it imposes extra receiver complexity in order to reduce the IUI using SIC. When the interference is severe, the throughput of NOMA declines dramatically and can eventually fall below that of OMA. Another distinctive feature between OMA and NOMA is that OMA may be a preferred option for a small network where the near-far effect is negligible; whereas NOMA would be the better solution for a larger network. The above discussion points towards the need of an adaptive MA scheme to dynamically select the proper access mode between OMA and NOMA to enhance the sum rate of the network. Although Cooperative NOMA (CR-

NOMA) improves transmission reliability due to openness of wireless channel, security in the physical layer is still a major issue.

For devices powered by EH from the ambient environment, the energy arrival process is inherently time-varying in nature. Such fluctuations in the energy arrival process may affect the transmission delay of an EH device, i.e., there may not be sufficient energy available at the device when it has to transmit information, thus, it has to wait until there is sufficient harvested energy. Therefore, how to accurately measure and control the delay in EH wireless communication network is a very important problem, especially for time-relevant wireless applications, such as a status-monitoring Wireless Sensor Network (WSN). Energy provisioning has led to the development of Rechargeable Wireless Sensor Networks (R-WSNs) [5,6] where sensors are equipped with a rechargeable lithium-ion battery and an energy harvesting module. In R-WSNs, the sensors recharge their batteries by harvesting renewable energy from ambient sources (wind, solar, etc.) or electrical power from wireless chargers. However, the success of Renewable EH (REH) for R-WSNs remains very limited in practice. This is because the amount of energy harvested from REH is a function of the deployment environment. In contrast, RF Wireless Power Transfer (RF-WPT) technology [7] has gained significant interest as a prospective technology for enabling stable and reliable energy supplies to the rechargeable sensors through transmitting RF energy and has a powerful advantage in Industrial IoT (IIoT) as it exploits low level, ambient RF power to sustain autonomous operation of sensor motes.

1.2 MOTIVATION

In the recent past, RF-EH has gained interest in enabling sustainable power supply for stable operation of wireless networks. Due to limited battery capacity of a relay node, a wireless network does not remain operational in perpetuity. To prolong the network operational lifetime, many strategies and techniques have emerged; the most recent being the EH technique. There are two main categories of RF-EH. The first category uses ambient RF power. For example, the ambient TV signals or cellular signals can be harvested for energy. Unlike the conventional batteries or mains connections that have fixed power supply, the power supply from harvested energy is not fixed any more. Hence, many works in the literature have investigated the exploitation of EH for wireless communications. The second category uses intentional (dedicated) RF power. For example, in hybrid access point systems, the Base Station (BS) broadcasts wireless energy to the remote devices in the Downlink (DL), and then the remote

devices transmit their data in the Uplink (UL) using the received power. In power beacon systems, power beacons are used to provide power coverage for mobile devices in the network, in addition to the BSs that provide information coverage. To satisfy the requirements of security, Energy Efficiency (EE) and SE simultaneously, some recent works have explored the combined effect of PLS and RF-EH for relay networks.

Generally, in practical IoT environment, CCI signals result in degradation of the system performance by corrupting the message signals. However, these interferer signals can purposely be used as a new energy source to empower the relay nodes [8,9] where the extra energy acquired from the interferer is utilised to improve the system performance. When power is extracted from a noisy environment, the Signal-to-Noise Ratio (SNR) decreases because energy is harvested from the same noise that contributes to the interference. This reduction in SNR leads to a lower channel capacity and, hence, reduced throughput. EH can compensate for the reduction in channel capacity caused by noise by allowing increased transmission power which can offset the negative impact of a lower SNR. By harvesting energy from co-channel interferers, the additional power from the harvested energy can be used to boost the transmission power of the receiver or to enhance the processing capabilities of the receiver's circuitry. This effectively reduces the impact of noise relative to the signal, thus improving SNR. Hence, it is still an open research problem to design new methods to exploit CCI signals efficiently in a two-way IoT network with EH capability that can simultaneously improve the secrecy of the network and promote continuous energy transfer.

A significant amount of research was carried out to investigate the impact of integrating IoT with EH, NOMA and cooperative communication. Along with significant increase in SE, the energy consumption in NOMA-enabled system increases with the average cluster size growth. Thus, integration of RF-EH technology into CR-NOMA has gradually become an innovative research direction.

Redesigning existing wireless networks to support both information transmission and RF-EH is becoming increasingly important as the demand for WPT grows, particularly in applications like IoT devices, wireless sensor networks, healthcare monitoring, and smart cities. Traditional wireless networks are optimized primarily for data communication—ensuring high throughput, low latency, and reliable connectivity. However, when RF-EH is introduced, the network must now balance the energy transfer efficiency with the data transmission performance. This creates a new set of requirements that existing systems aren't optimized for resource allocation where wireless networks need to allocate resources (like spectrum, time slots, power) between information signals and energy signals, which can be

challenging without a redesign. RF-EH often operates in the same frequency bands as data communication. This can cause interference between energy signals and data signals, degrading network performance. To mitigate this, networks may require advanced frequency allocation schemes (like dynamic spectrum access) and interference management techniques (like beamforming, adaptive coding). In general, the amount of harvested energy is small. Hence, one of the main application scenarios of EH communications is low-power WSNs. Interestingly, the latest breakthrough in WPT technology has shown its strong and high potentials to address these fundamental bottlenecks surrounding the finite node lifetime and operational performance of IIoT applications.

Being motivated by the above research trends and the progress in the field of RF-EH in different areas of wireless communication networks, some efficient and improved relaying schemes and protocols have been proposed to achieve better network performance. The effectiveness of the proposed works has also been established by comparing the performance with some existing relevant network models in terms of several performance parameters.

1.3 OBJECTIVES

Specifically, our research objectives are:

- Developing sophisticated RS strategies for better reception reliability in OWR and TWR networks with Interference-Aided EH (IA-EH)
- Improving the secrecy performance in untrusted scenarios by developing different network schemes and protocols
- Improving the EE, SE and secrecy performance by integration of RF-EH technology into CR-NOMA network
- Addressing the problem of long-term autonomous operation of a network in IIoT environment by applying RF-WPT technology

1.4 METHODOLOGY

The global energy crisis has urged the development of green technologies which aim to improve energy utilization. In this dissertation, an attempt has been made to design efficient RF-EH schemes for secure communication in wireless networks. Based on the idea of energy reuse, RF-EH has been recently applied to cooperative communications, where the information

delivery from a source node to a destination node can be assisted via single or several intermediate energy-constrained relay nodes. Inception of cooperative relaying in EH technology has been shown to enhance the EE, improve the network connectivity and increase the reliability [10]. Considerable research effort has been devoted to develop different relay selection strategies in multi-relay networks with IA-EH in presence of EAVs. However, conventional OWR involves additional time phases to complete bi-directional signal transmission, which reduces SE. To address the issue, new TWR schemes have been developed under realistic assumptions to achieve improved performance related to EE, Secrecy Capacity (SC) and harvested power.

Further enhancement of secrecy in NOMA has been accomplished. Furthermore, RF-powered Multi-Device Diamond Relay Network (MD-DRN) has been designed to boost the Achievable Sum Rate (ASR) and EE of the network using A-NOMA. The performance analysis of the proposed models has been carried out and compared with the existing benchmarks with respect to various network parameters by considering mathematical operations involved in the models. The above investigations are based on analytical modelling and its validation by simulation frameworks developed by us. Simulations are performed using MATLAB 2022b in Windows operating system. Simulation results are supported by analytical results wherever possible.

Recent advances in wireless energy transfer have made it possible for self-sustainable relays that power themselves by capturing ambient energy wirelessly. For our real-world usage tests, commercially available of-the-shelf measurement tools have been utilized to calculate the battery recharging time of on-board rechargeable batteries. Bluetooth-enabled PowerSpot RF Wireless Power Development Module (P1110-EVAL-PS) [11] has been used to charge various sensors and multiple consumer devices using the harvested RF power. Measurements are taken at different distance using vertically polarized PCB dipole and patch antennas. Apart from that, Netsim v13.1 [12] has been used re-create the IIoT environment. Here the residual energy as well as energy consumption in each battery node has been estimated by battery model metrics table. Rechargeable or EH mode represents the harvesting sub-module to increase battery residual energy periodically. In NR or no-harvesting mode, each node in the network is powered solely by its own battery.

1.5 CONTRIBUTIONS

The pertinent contributions of this research are summarized below:

- A Hybrid TSR-PSR scheme has been proposed in a cooperative relay network considering interference as an energy source. Here, comparison of throughput with respect to several parameters such as EE, relay position and location of interferer for each of Time Switching Relaying (TSR), Power Splitting Relaying (PSR) and Hybrid protocols, with and without the influence of CCI has been studied.
- Destination-based Jamming (DBJ) technique has been introduced in Cooperative IoT (CIoT) network with beacon aided RF-EH to analyse the secrecy performance in terms of Secrecy Rate (SR) analysis and System Energy Efficiency (SEE) over dissimilar faded channels (Rayleigh/Weibull, Weibull/Rayleigh, Hoyt/Rayleigh, Rayleigh/Hoyt). Furthermore, joint effect of IA-EH and DBJ has been studied for improving the SR.
- A novel architecture of a cooperative relay network containing multiple sources with multiple antennas and RS over Rayleigh fading channel has been developed incorporating two improved RS schemes namely Optimal Relay Selection (OPT-RS) and Maximum Energy Accumulated Relay Selection (MEA-RS).
- A generalized RF-EH system model has been proposed by optimizing the throughput expression with hybrid TSR-PSR protocol and performance of the model has been investigated for Amplify and Forward (AF), Decode and Forward (DF) and Hybrid AF-DF (HDAF) relaying schemes under the Weibull fading channel.
- An RF-powered multi-relay network has been proposed to analyse the secrecy performance in terms of SOP and SC. Subsequently, the best node scheduling scheme has been applied to enhance the secrecy of the proposed network.
- A bidirectional HD multi-relay multi-antenna adaptive relaying network over the Nakagami fading environment has been proposed in Delay-Limited (DL) as well as Delay-Tolerant (DT) transmission modes and detailed analyses have been presented.
- A novel method of RF-EH in Two Way Communication (TWC) with Maximum Harvested Energy Antenna Selection (MHE-AS) protocol has been presented to enhance the security of the system in terms of SC in the presence of an interferer.
- A secure and energy-efficient scheme for RF-powered two-way untrusted IoT relay network has been proposed in an interference-limited environment and the closed form expressions for Secrecy Outage Probability (SOP) and accumulated harvested energy have

been derived. Also, Average Secrecy Capacity (ASC) has been analyzed using monte-carlo simulations. An in-depth analysis on the accumulated harvested energy and SC of the network in terms of saturation power threshold for non-linear mode has also been performed.

- CR-NOMA network with IA-EH has been designed in an untrusted scenario where the effectiveness of the proposed model has been investigated in terms of SOP considering various key parameters such as source transmission power, transmit power of jammer, number of interferers and interferer transmit power. Also, the Ergodic Secrecy Rate (ESR) of individual users has been evaluated highlighting the impact of allocated power factors on ESR for both near and far users.
- An improved Adaptive NOMA (A-NOMA) protocol has been applied in an RF-powered Multi-Device Diamond Relay Network (MD-DRN) to enhance the Achievable Sum Rate (ASR) in an IoT scenario. Also, the Bit Error Rate (BER) performance and Energy Efficiency (EE) of the proposed model has been studied.
- A realistic virtual IIoT environment has been developed using NETSIM and tested with the commercially available of-the-shelf PowerSpot® RF Wireless Power Development module to analyse different system parameters namely battery recharging time, network energy consumption, Network Lifetime (NL) and throughput. Also, the effect of antenna gain on the battery recharging time has been observed with respect to variation in distance and Depth of Discharge (DoD).

1.6 DISSERTATION OVERVIEW

This main body of this dissertation is organized into eight chapters with five contributory chapters. The thesis is outlined as follows:

Chapter 1 discusses the background, motivation, objectives, methodology and contribution of the present work and outlines the organization of the thesis.

In **Chapter 2**, an extensive survey of existing literatures on the current state-of-the-art techniques related to RF-EH has been carried out. A comprehensive summary of various EH schemes, RS strategies, fading models, security issues as well as application of RF-WPT in IIoT has been discussed in this thesis.

In **Chapter 3**, the performance analysis of one-way single relay network has been carried out. A Hybrid TSR-PSR protocol for IA-EH in a Cooperative Relay Network CRN has been

presented to improve the network throughput. Moreover, an energy-efficient RF-EH scheme has been presented in the next system model to evaluate the secrecy performance in an IoT network using cooperative communication approach in an interference-free environment. Here, new analytical expressions for both SC and EE in Rayleigh, Hoyt and Weibull fading channels have been obtained. Apart from that, our next framework incorporates DBJ approach to increase the system security in the presence of an interferer.

In **Chapter 4**, various RS strategies have been implemented for better reception reliability in multi-relay network with RF-EH. The performance of the network has been investigated in both interference-limited and interference-free environment. Also, the secrecy performance has been analysed in multi-relay network using best node scheduling scheme.

In line with Chapter 3 and 4, a Two-Way Multi-antenna Relay network has been designed in **Chapter 5** where the throughput performance of a two-way multi antenna multi-relay network over Nakagami fading has been carried out for both DL and DT transmission modes. In addition, the secrecy performance has been evaluated with IA-EH using MHE-AS scheme. This model has been further extended to analyse the secrecy in an RF-powered TWR comprising of two untrusted relays where the joint effect of PLS and IA-EH under accumulation of the harvested RF energy for both linear and non-linear scenarios has been highlighted.

In **Chapter 6**, a secure transmission scheme in CR-NOMA network employing IA-EH has been depicted to enhance the system security performance by introducing jamming cancellation technique. Apart from that, design and analysis of an RF-powered network has been carried out using an upgraded A-NOMA protocol where the IoT relay devices are deployed in a diamond relay topology and are empowered by ambient RF energy for sustainable operation of the network.

In **Chapter 7**, a practical approach and real-time implementation of an RF-enabled EH-WPT technique has been presented to demonstrate the application of RF-WPT in IIoT using Powercast energy harvesters and Netsim Modeller tool.

Chapter 8 provides the main findings of the thesis and discusses some possible future research directions.

Chapter 2
LITERATURE SURVEY

2.1 OVERVIEW

Advancement in communication technology demands for promising solutions to power a large number of devices for a longer time. In this regard, RF Energy Harvesting (RF-EH) has come up as a potential solution for energy constrained networks such as the Internet of Things (IoT) by converting RF signals into electrical energy which can be used to satisfy the energy needs of the smart devices in order to prolong their lifetime. RF energy refers to the amount of energy harvested from the RF signals both ambient and dedicated, emitted by a transmitter and received by the harvesting circuit to generate an electrical energy [13,14]. This chapter presents a detailed survey of the existing approaches for various Relay Selection (RS) strategies and security issues in EH-enabled wireless relay networks. The relaying protocols and schemes of EH along with some potential applications of EH technology have been outlined and discussed. Various metrics for network performance such as Outage Probability (OP), throughput, Secrecy Capacity (SC), Bit Error Rate (BER), Energy Efficiency (EE), Network Lifetime (NL) etc. have been studied. The performance analysis of NOMA using RF-EH has also been studied. Finally, the concept of Wireless Power Transfer (WPT) using RF-EH has been presented. For better understanding, the reviews of the relevant research articles have been summarized in distinct sections.

2.2 RADIO FREQUENCY ENERGY HARVESTING

With the enormous use of RF signals for wireless communication and technology, RF-EH has attracted a lot of attention due to ambient RF energy residue present in the surrounding. Major RF sources are Bluetooth, mobile phone, Wireless Fidelity (Wi-Fi) signal transmitters, television/radio broadcasters, mobile phones, Base Stations (BSs) and any RF transmitter that transmits RF signals of certain frequency present in the environment [15]. Fig. 2.1 represents schematic of a general RF-EH system [16]. The key elements of an RF-EH network include the following components: a receiving antenna, for capturing RF signals radiated by an RF

transmitter; an impedance matching circuit, to optimize the power harvesting by aligning the impedance of the receiving antenna with the rectifier; and an AC to DC rectifier, that converts the collected signals into usable electrical power. Depending on its application, an RF-EH may consist of a voltage booster or regulator at the output end to boost up the output voltage level for specific applications at the cost of size and efficiency of the harvester.

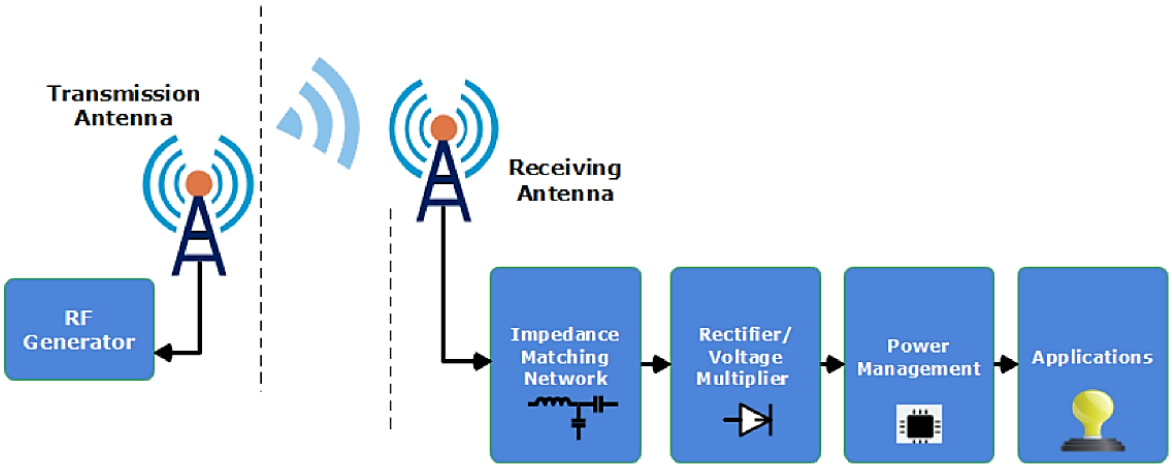

Fig. 2.1 An RF-EH system conceptual block diagram [16]

2.3 RF ENERGY HARVESTING IN COOPERATIVE RELAY NETWORKS

Cooperative relaying is a novel technology which improves the EE and the reliability of wireless networks by employing intermediate relay nodes between various source and destination nodes [17]. Van der Meulen [18] presented the first classical relay channel in his 1971 PhD thesis. As presented in the literature, two distinct receiver architectures namely Time-Switching (TS) and Power-Splitting (PS) [19] were taken into consideration when examining cooperative relay techniques for an RF-EH network. Particularly, for low data transmission rate, the TS protocol can achieve higher OP and throughput performance than that of PS scheme. However, PS protocol is better than TS protocol for high data transmission rates. The TS protocol is considerably easier to achieve than the PS protocol when comparing the two. On the other hand, theoretical research has demonstrated that the PS protocol can provide far superior trade-offs between harvested energy and transmission rate. Furthermore, in the TS protocol, precise time synchronization between the transmitter and receiver is necessary, and the receiver's switching function must be adjusted in accordance with the transmitter's time

information. Therefore, in the practical systems, the PS protocol is more suitable to be utilized than the TS protocol, and most of the research works are based on the PS protocol. Authors in [20] established a Hybrid TS-PS protocol which showed the superiority of the protocol over both Power Splitting Relaying (PSR) and Time Switching Relaying (TSR). However, the above works focused on system performance over Rayleigh fading channel which is valid only for outdoor wireless channel. In contrast, for indoor environment, the OP of the system was studied by adopting PSR and TSR over log-normal fading channel [21]. In [22], a modified TSR protocol had been presented in multi-destination network with Simultaneous Wireless Information and Power Transfer (SWIPT). The disadvantages associated with these protocols were addressed by introducing a new Adaptive Relaying Protocol (ARP) [23]. In this work, the ARP for bidirectional Half Duplex (HD) system was investigated over Rician fading channel including a single relay with single antenna between the source and destination nodes.

In practice, HD relays are preferred over Full-Duplex (FD) as they are easier to implement than the latter. However, half-duplexing comes at the cost of multiplexing gain loss as compared to full-duplexing. In [24], the OP of the FD relay system was investigated. In [25], the FD Cooperative Cognitive Radio Network (CCRN) with multiple FD secondary users had been analysed, and the optimal system throughput had been derived. However, the EH technique was not implemented in the above works. This issue was addressed in [26, 27] where the FD relay system was investigated using EH with TSR protocol to optimize the time allocation aiming at improving its own performance.

Depending on the network configuration and available resources, two well-known relaying strategies i.e. Decode-and-Forward (DF) and Amplify-and-Forward (AF) have been introduced in [28]. In [29], the ergodic capacity and throughput of a DF relaying protocol was examined. In the following year, the OP and throughput for a TSR network operating in AF protocol was investigated in [30]. In AF relaying, relays simply scale the received signal by a predefined gain factor and retransmit it. Thus, AF relays have relatively less complex circuitry and cost. However, as simple repeaters, AF relays are well known for transmitting an amplified version of noise signals over the communication channel since it amplifies the noise parts as well as the signal during the scaling process. In contrast to AF relaying, DF scheme limits the propagation of noise at the expense of circuit complexity. However, if the signal is commuted over multi-hop paths, DF relays propagate the errors over the network. The AF relays have a number of drawbacks, including noise introduced by the information receiver and non-linear distortion. Whereas AF retransmits and amplifies signals without decoding, DF decodes, re-modulates, and re-transmits the received signal. The DF complexity compared to AF relays

significantly high due to its full processing capability. The DF protocol also requires an advanced media access control layer, which is not required for the AF protocol. On the other hand, a Hybrid AF-DF (HDAF) relaying protocol could be used in certain applications [31].

The aforementioned literature focused on One-Way Relay (OWR) system where data transmission occurs in one direction. In comparison with the FD-OWR system, the OP and throughput calculation of the FD Two-Way Relay (TWR) system is more complicated, as both destination nodes are to be considered simultaneously. In [32], a PS-based SWIPT with a DF scheme had been employed at TWR to harvest energy from RF signals. In [33], a new system model of DF-FD relaying network over the Rician fading environment was introduced. SWIPT for the AF-based TWR networks had been adopted in [34]. In [35], the performance of the EH scheme had been investigated in a WSN showing that the HDAF protocol outperformed the conventional DF and AF protocols.

2.4 RF ENERGY HARVESTING IN TWO WAY COMMUNICATION (TWC)

The idea of bidirectional or TWR was first introduced by Shannon in [36]. Subsequently, OWR or unidirectional networks had been widely applied in practical data communication for long-distance information transmission in wireless networks. Fig. 2.2 presents a simple TWR technique. In transmission phase 1, both the source and destination transmit their information simultaneously to the relay, whereas in phase 2, the relay amplifies/decodes the received signal and broadcast the information. To achieve EH and information decoding, TSR and PSR architectures of the receiver were proposed in [37-39]. Joint TS and PS schemes have been presented in [40–43] as an extension of these studies for TWR networks with an energy-constrained relay node. In [44], the authors considered the scenario where the Secondary Users (SUs) or relay nodes share their reporting channel with the Primary User (PU). Their Proposed Voting Rule (PVR) optimized the majority rule by exploiting the difference in outage of the reported information due to the presence or absence of the PU in the channel. Opportunistic Amplify and Forward (OAF) relaying and Partial Relay Selection (PRS) was considered in [45]. Previous research had investigated TWC in SWIPT-enabled CCRN employing PS, TS, and HPTS protocols [46,47]. Moreover, in the performance analysis of SWIPT in [48,49], the non-linear EH mode and piece-wise linear EH model have been taken into consideration. A

dual-hop AF TWR system with a non-linear amplifier was introduced in [50, 51]. Based on TS or PS scheme, the throughput performance had been analyzed and formulated.

Fig 2.2 Two-way relaying in wireless communication

2.5 RELAY SELECTION (RS) STRATEGIES

In wireless cooperative networks, several intermediate relay nodes are available to assist communication between a pair of data source and destination. These nodes have different locations and so each transmitted signal from source to destination must pass through different paths causing different attenuations within the signals received at the destination which results in reducing the overall system performance. To minimize this effect, design of proper relaying strategy is an essential issue where high-quality links can be chosen by using proper RS techniques. The most interesting one had been discussed in [52], where Bletsas proposed the idea of totally distributed RS, i.e. the network did not require centralized Channel State Information (CSI) to select the best relay. In multi-relay cooperative networks, selection of the best relay is highly required. Two different best RS strategies were proposed in [53]. In the first strategy, the best relay was selected based on the harvested energy during the current block of time, whereas the second strategy was based on harvested energy during current block of time as well as stored energy from the previous blocks of time. The relay with the lowest energy consumption was picked as the best relay in [54]. In [55], a multi-relay scenario with a SWIPT-assisted cellular IoT network was examined where the optimal relay was chosen by maximizing the energy gathered from both the source and CCI signals. For networks with multiple relays operating with TS protocol, an RS protocol had been discussed in [56], where the best relay was selected based on maximum harvested energy from the signal of source. The authors in [57] studied two RS methods, Partial Relay Selection (PRS) and Opportunistic Relay Selection

(ORS), in a multi-relay DF wireless EH network. In PRS, the relay that aids S-D transmission was selected based on the CSI of either S-R or R-D hop; whereas, in ORS, the relay that ensures best end-to-end path between S and D was selected as the best relay. The performance of both the schemes had also been evaluated in terms of OP, where ORS scheme clearly outperformed PRS. The authors in [58] had studied the comparison between three RS schemes where the effect of various parameters on throughput and OP had been studied. However, the analysis was limited to a single source with a single antenna. A distributed RS strategy had been proposed in [59] in order to incorporate fairness among the relay nodes in terms of equal energy consumption, where a central unit numerically calculates a weight factor for each relay node such that the power consumption for each relay is almost equal. The model proposed by [60] derived an optimal PSR value in order to maximize the end-to-end SNR of a link. However, neither [59] nor [60] had considered the arbitrary relay positions for selection of the best relay channel.

2.6 PHYSICAL LAYER SECURITY (PLS) in RF ENERGY HARVESTING

Physical Layer Security (PLS) is an information-theoretic procedure that achieves secrecy by using signal processing techniques and channel codes. The main idea of PLS is to utilize wireless channels and interference environments to keep the secret message from eavesdropping [61-63]. Wyner conducted the first research on PLS in [64] comprising of a three-node configuration including a Source (S), a Destination (D), and an Eavesdropper (EAV) as depicted in Fig. 2.3. PLS techniques based on cooperative relay transmission are especially important in situations where devices typically have limited power supplies and coverage ranges for reliable communication. In the past decade, substantial research had been made to deal with the problem of PLS in cooperative relay networks. However, these existing secure schemes are based on the assumption that the nodes in the network are ideal i.e. secure, and they are designed to prevent interception from the EAVs outside. Nonetheless, in certain scenarios, such as heterogeneous networks, relays could be considered unreliable because they could act as potential EAVs, attempting to illegally decode the information signal received from legitimate sources while aiding in S-D transmission. To overcome this problem, He and Yener

[65] proposed a breakthrough in one-way untrusted relay network by employing a friendly jammer without direct transmission to obtain a positive Secrecy Rate (SR).

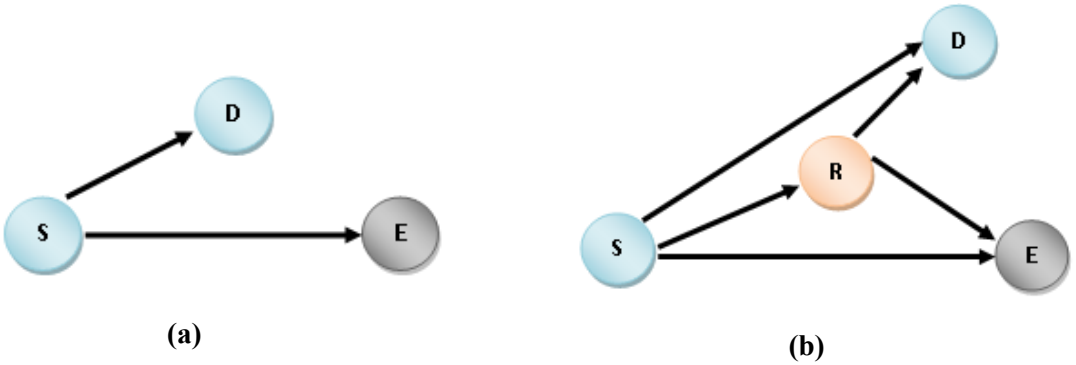

Fig. 2.3 (a) Wyner's wire-tap channel [64] **(b)** Wire-tap channel with cooperative relaying for enhanced security

The secrecy performance of HDAF was observed in [66] and compared with AF and DF schemes. Furthermore, it had been observed that the performance improves with increasing number of cooperative relays. The work presented in [67] applied a Cooperative Jamming (CJ) scheme for harvesting energy using a multi-antenna. PSR and beamforming methods had been used by [68] to increase the SR by applying Destination-based-Jamming (DBJ) that deteriorates the Signal-to-Noise Ratio (SNR) at the EAV. The study in [69] used different RS strategies to improve the network performance in terms of Secrecy Outage Probability (SOP). In [70], the secrecy rate performance of an untrusted unidirectional relay network with EH was evaluated under the impact of hardware impairments in interference-free environment. [71] had investigated secrecy performance of DF relay system over κ-μ shadowed fading channels. The exact closed-form expressions of SR and SOP had also been derived. The secrecy performance of DF relay network had been analyzed in [72] under composite Weibull/Lognormal fading. More interestingly, the confidentiality of a single-hop EH relay network was studied in [73]. Comparing AF relay with DF relay, it was concluded that the confidentiality rate of AF relay is higher than those of DF relay in both EH and conventional systems. Despite considerable contribution of the aforementioned study, very few investigations have been conducted to investigate secrecy and EE performance under Nakagami-q (Hoyt) or Weibull fading. Furthermore, the results for SR analysis across Hoyt and Weibull fading in a hybrid Cooperative IoT (CIoT) network have not yet been reported in literature. A detailed study on EE performance with beacon-assisted EH was carried out in [74] under a Rayleigh fading

environment. But, the concept of cooperative relaying and jamming was not addressed. Although the work by [75] provided secure communication via EH untrusted relay, the authors did not demonstrate how EH affected the system performance. By incorporating the advantages of conventional relaying schemes, a new adaptive scheme i.e. HDAF protocol was applied in [76] and [77] where the secrecy performance had not been analysed. Energy can be harvested by using multiple antennas at the relays as in [78], but in the case of a single antenna at the relay, the relay may not be able to harvest the sufficient energy in a single transmission frame. The accumulation of harvested energy was explored in [79], where the destination transmitted a jamming signal after its battery was fully charged. On the other hand, a backup energy source, such as a grid or a battery power supply, may be used during the frames when the captured energy is insufficient and is being stored. In [80], the performance of a linear TWR network has been assessed for a case that is limited to equal power transmission by the two transmitters considering a single interferer node. Here a separate external jammer has been deployed for maintaining security of the network. Meanwhile, the work in [81] has incorporated a Parallel Interference Cancellation (PIC) technique to achieve enhanced secrecy rate in a linear RF-powered TWR network.

2.7 ROLE OF INTERFERENCE IN RF-EH

The interference network is a fundamental type of topology for multi-user networks, where each transmitter provides independent information to its associated receiver, and the signals received at the undesired receiver are considered interference. Interference is traditionally considered to be one of the major challenges in wireless communications due to its detrimental effects on throughput and secrecy. Considering the practical implications, interference modeling in wireless networks is a very interesting problem. Interference induced in wireless networks, commonly referred to as Co-Channel Interference (CCI), depends mainly on physical factors, such as the spatial distribution of interferers, interfering channel fading and the power of the interferers. The presence of CCI in EH-enabled wireless communication is expected to have an intriguing impact on the system performance. On one hand, it can be considered as a useful source to scavenge additional energy through the RF-EH technique. A OWR strategy was investigated in [82] under three schemes where the EE was optimized. In literature, various cooperative EH protocols were examined under two different relaying scenarios: single-relay [83–85] and multi-relay [86, 87], where the transmitted power of source

was considered as the main source of harvesting energy. In [86], a model has been studied where source node selects the best relay to transmit signal to the base station. An algorithm has been established to calculate the highest throughput of the best relay. Most of the research works on Interference-Aided (IA) wireless EH has been conducted in cooperative networks, where the interferences among users might be used as a source of extra energy for wireless EH. The authors in [88,89] developed a single relay-aided EH protocol where both CCI signals and source signal were considered as potential energy sources for powering the relay node during the EH phase while CCI signals were treated as noise during the information decoding phase. A three-node cooperative RF-EH protocol had been proposed in [90], where the relay node operated in EH mode when the CCI signals were very strong and harvested energy from both CCI signals and source signal. On the contrary, when the CCI signals were weak, the relay node processed information by operating in information decoding mode. Hence, it remains an ongoing research challenge to propose new strategies to exploit CCI signals efficiently as a source of power to recharge energy constrained nodes with minimal decrease in system performance. A significant contribution on harvesting energy from the interference was illustrated in [91], where the EE of data transmission was maximized for an Orthogonal Frequency Division Multiple Access (OFDMA)–based non–cooperative communication system. A CRN had been considered in [92], where the energy–limited relay harvested energy from the received signal and interference, and then exploited the energy for relaying operation. Although the authors of [93] developed a closed-form equation for throughput for cooperative communication networks with EH capability, they did not give any security framework for such systems. A hybrid protocol for IA-EH was developed in [94], in which the power-constrained relay collected energy from both the source and the interferer's signals. In order to choose which EH source is better, two different cases were considered in [95]. While the relay in the first scenario harvested energy only from the source signal under the assumption of negligible interference signal, in the second situation the relay harvested from both the source as well as the interfering transmitter. It has to be noted that [93], [94] and [95] had considered single relay operating in the cooperative networks.

Similar to OWR, TWR systems are also affected by CCIs due to heavy spectral reuse, which can be regarded as a constant energy source and has a major role to maximize the SC under an EAV attack. The authors in [96] had proposed an opportunistic IA-EH scheme for two-way multi-antenna relaying networks in presence of CCI. Because of security vulnerability along with energy insufficiency in TWR networks, both EH framework along with PLS had been

included together in CRNs [97]. In [98], the system performance of a bidirectional multi-antenna relay network had been investigated in interference free scenario. The authors in [99] had studied the impact of CCI on the outage performance of an EH-assisted two-way DF relaying system. whereas in [100], a relay selection policy that maximizes the achievable secrecy rate was developed. Some recent works [101-106] had explored the combined effect of PLS and RF-EH for TWR networks. The authors in [107] had analysed the security performance in interference-limited environment where the impact of EH on the existing model was ignored. In contrast to this work, [108] had introduced an approach to demonstrate the positive effect of CCI for a linear TW cognitive network. Authors in [109-111] had assumed linear EH model where the problem of maximizing the sum throughput of TWR networks with wireless powered nodes was studied. The problem related to this work is that linear EH model is too idealistic and impractical as this model is unable to demonstrate the nonlinear behaviour of any practical EH circuit. The work in [112] had modified the logistic EH model to address the sensitivity issue. Meanwhile, the authors in [113-116] had proposed a nonlinear EH model where a resource allocation algorithmic model was designed to improve the harvested energy. Here, the results for non-linear model were shown to outperform linear model in terms of throughput. Despite the above achievements, joint effect of PLS and IA-EH in TWR under accumulation of harvested energy for non-linear scenario was not applied in the above existing works.

2.8 RF ENERGY HARVESTING IN NON-ORTHOGONAL MULTIPLE ACCESS (NOMA)

A significant amount of research was carried out to investigate the impact of integrating IoT with EH, NOMA and cooperative communication [117], [118] and [119]. For the past few decades, OMA was considered a viable approach for 4G wireless networks due to its cost-effectiveness, low complexity receivers and lack of inter-user interference. In this context, a unique approach to increase the resource block efficiency in small cell networks by lowering cell interference was proposed in [120]. Here, based on Quality of Service (QoS) criteria, the resources were distributed dynamically. The outcomes revealed a decrease in interference and an improvement in Spectral Efficiency (SE). Different from [120], the authors in [121] had applied the OMA technique to a macro-base station-only network to increase the network throughput by allocating optimal energy and time. However, restricted bandwidth and the use of multiple OMA approaches in 4G technology made it insufficient to meet the increasing

capacity requirement for smart gadgets and mobile internet usage in 5G+ [122]. This is because the user was assigned an orthogonal subcarrier, which resulted in lower network throughput. NOMA was initially proposed in [123], where the authors demonstrated how NOMA-enabled systems outperformed OMA systems with respect to fairness and SE. In [124], the authors studied a cellular Downlink (DL) network with randomly scattered users and compared NOMA and OMA systems with respect to fairness and sum rate. In contrast, the average sum capacity of both the systems was investigated and compared in a cooperative relaying power line communication system [125]. A Cooperative NOMA (CR-NOMA) network had been presented in [126], where Power Allocation (PA) was used to improve global EE. In line with this, the performance of DL CR-NOMA using fixed or adaptive gain had been evaluated in [127]. The authors in [128] calculated the OP and Achievable Sum Rate (ASR) in a NOMA-functioned DL scenario. While all of the studies described above focused on DL networks, several researchers also made an effort to explore UL scenarios. It was discovered in [129] that employing NOMA in 5G wireless networks can increase SE and fairness. In comparison to [126], similar investigations were conducted for the UL NOMA-based network in [130]. Although NOMA offers many benefits, including enhanced resource allocation, improved SE and lower latency, one major drawback of NOMA is the additional receiver complexity that is necessary to eliminate the IUI. Although NOMA reduces both signaling overhead and transmission latency, it may still introduce additional latency as a result of the SIC process, which can be reduced by limiting the number of users that rely on SIC. Since multiple users are accommodated within the same spectrum in the network, NOMA suffers from high decoding delay and complexity problems. All of these issues were addressed with the hybrid NOMA (H-NOMA) protocol [131, 132]. In [131], a resource allocation scheme developed for a “hybrid time division multiple access (TDMA) – NOMA” network with opportunistic time allotment. For 5G DL, an accurate PA strategy was implemented in a “hybrid code division multiple access (CDMA)–NOMA” network with the user clustering technique called “Best with Poor Model” [132]. Both of the above works improved the system's overall capacity and performance while preserving the SE.

Along with the significant increase in SE, the energy consumption in NOMA-enabled systems increases with the average cluster size growth. Integration of RF-EH technology into CR-NOMA to develop the brand-new RF-powered CR-NOMA network has gradually become an innovative research direction. In this contest, the joint effect of NOMA-assisted relaying systems with RF-EH was studied in [133, 134]. The authors in [133] designed a cellular-based IoT network combining EH with NOMA, where the throughput was maximized under different

density of Base Stations (BSs). In [134], the end-to-end BER had been examined in an RF-powered CR-NOMA system with two users. It had been demonstrated in [135] that integrating self-sustaining EH relay devices into CR-NOMA networks with FD relaying significantly increased SE and EE. In [136], the authors presented an IA-SWIPT based IoT CR system by employing PSR, TSR and NOMA. The authors showed that the improved performance of the proposed system could successfully be used in various IoT applications, e.g., coal mines, underwater applications and hazardous environments. An RF-powered system adopting NOMA protocol was designed in [137] for a multi-relay scenario, where the network performance was assessed in terms of ergodic sum capacity. In [138], a SWIPT-based model was proposed where the BER was explored for DL NOMA networks. The authors in [139] examined the OP in a NOMA-enabled AF CR network. In a very recent study [140], the outage performance of an RF-powered CR-NOMA-assisted IoT system had been successfully analysed. The main disadvantage of this work is that it did not consider EE which is one of the most essential and practical concerns in wireless systems. The authors in [141] introduced the Adaptive NOMA (A-NOMA) protocol in the CR network, where the EE of the network was found to be better compared to that of OMA and NOMA. However, EE and BER analysis in RF-powered MD-DRN still remains an unexplored area of research.

2.8.1 RF ENERGY HARVESTING IN DIAMOND RELAY NETWORK (DRN)

The Diamond Relay Network (DRN) model has recently attracted considerable attention as an efficient cooperative networking configuration in wireless Ad Hoc networks that offers a higher achievable data rate. This network can take advantage of NOMA for both UL and DL transmissions. Based on the max-min criterion and Maximal Ratio Combining (MRC), the work in [142] demonstrated that the network outperformed the other existing cooperative networks in terms of sum rate. Subsequently, they improved their work in [143], in which an analytical expression of the ergodic sum rate (ESR) was derived. A PA scheme for DRN was investigated in [144]. Meanwhile, in [145], a joint PA approach for increasing the achievable rate of NOMA-based DRN was reported where the proposed method offered a higher achievable rate. In continuation, the authors in [146] introduced an efficient algorithm that provided a much higher achievable rate than the other existing approaches. In contrast to the above works, the authors in [147] examined the security performance of an untrusted DRN with a CJ scheme. The

drawback of the above works is that they did not assess the BER and EE of the network. This was taken care of in [148], where the BER performance in DL NOMA networks using BPSK modulation was shown through simulations and real-time tests. Meanwhile, the authors in [150] attempted to improve the BER performance of the single DRN earlier designed in [149] using a joint maximum likelihood detector. Although the performance in [150] was improved considerably, an error floor was still observed. All the above works on NOMA-based DRNs were limited to a single-relay scenario where the advantage of EH was not explored. To meet this requirement, a NOMA-enabled DRN model was deployed in a multi-relay scenario in [151] where an RS scheme was applied to obtain higher transmission reliability. Since DRN is an efficient cooperative strategy to improve the achievable rate of the network, DRN powered with RF-EH can be an efficient approach to enhance the ASR and EE of the network.

2.8.2 PHYSICAL LAYER SECURITY IN NOMA-ENABLED NETWORKS

Although CR-NOMA improves transmission reliability due to openness of wireless channel, security in physical layer is still a major issue. From a security view-point, when multiple users are utilizing the same time-frequency resource, there may be concerns regarding keeping information confidential Thus the notion of PLS that is currently among the hot spots in wireless communications and information security was initially proposed in [152]. Afterwards, PLS had been incorporated in NOMA system [153], where the SOP played a significant role. The effect of PLS on the performance of NOMA framework had been studied for both external and internal eavesdropping environment [154] in interference-limited system. In [155], the security performance analysis of NOMA in PLS had been carried out under jamming cancellation technique in interference-free environment. But the influence of EH on the performance of the system had not been addressed here. Authors in [156] developed UL and DL NOMA scheme in untrusted environment where the influence of EH had not been explored. From literature, we find that the impact of CCI on the secure performance of CR-NOMA network with incorporation of RF-EH has not been addressed yet.

2.9 RF ENERGY HARVESTING IN WIRELESS SENSOR NETWORK (WSN)

Wireless Sensor Network (WSN) is an essential part of IoT and that has been widely used for information collection including patient health monitoring, smart buildings, object tracking, habitat monitoring, emergency circumstances, and monitoring of air quality. Also, WSNs play a crucial role for an actuating environment by alerting the accidental events like changes in pressure, temperature, or humidity, leakage of toxic chemicals or gas emissions, humidity, vibration, fire, and many other safety signals. However, the most well-known issue with WSN is energy consumption, as battery power is now the main energy source in sensor nodes. A sensor node loses its ability to function in the network when its energy is exhausted. So, it requires an uninterrupted power supply continuously, whether the sensor node is in active mode (communicating and processing data), sleep mode, or inactive mode. These entire aspects encourage the usage of EH in WSNs.

2.9.1 WIRELESS POWER TRANSFER (WPT)

Due to their energy limitations and short operational lifetime, conventional WSNs require an optimization of the Network Lifetime (NL). On the other hand, the EH-WPT WSNs are designed to sufficiently consider the network's operational lifetime in order to achieve energy neutrality and an infinite lifetime of operation when installed in an environment with a consistent energy supply. The technology behind WPT dated back to the early 20th century had been credited to Nikola Tesla [158]. WPT could increase the portability and can meet the high demand of new smart devices that currently utilize wireless technology for various operations and communications, such as Wi-Fi, which is nowadays used in laptops and smartphones for internet access. The study in [159] provided some insights into the recent applications of WPT technology in the following domains: mobile phones, medical implants, Electric Vehicles (EVs), Unmanned Aerial Vehicles (UAVs), WSNs and audio players. Meanwhile, [160] investigated the performance of distributed WPT system and found that distributed wireless charging has numerous advantages in terms of coverage probability as long as the optimal beamforming is available in the distributed WPT system. Low-power transfer efficiency was a problem for RF-WPT systems, which are used to power IoT devices, because of the significant

power attenuation of electromagnetic waves. In [160] and [161], the distribution of antenna systems was taken into consideration as a feasible solution to the EM wave attenuation problem. A sensor node's power supply subsystem can be categorized into two types based on the battery type: rechargeable and non-rechargeable.

2.9.2 RF-ENABLED EH-WPT IN IOT

"Smart-X" applications, like smart city, homes and transportation have become increasingly important in our daily lives as a result of growing interest in IoT, of which WSN is one of the enabling technologies [162]. Since the sensor network's limited energy resources prevent their deployment in applications requiring unattended and long-term operation, such as control of air quality in cities, detection of combustible gases, etc, the integration of EH technology in IoT has proven to be a popular trend over the last 20 years [163,164]. The widespread development and use of digital TV, cellular and wireless communications operating at 900/1800/1900 MHz and 2.4 GHz, has created plenty of opportunities for far-field RF-EH and its application in powering small, autonomous WSNs [165]. The WPT approach relies on the intentional EH in which an active component (e.g. RF transmitter) is utilized to provide the desired energy needed in the environment for the devices. This type of approach is implemented by Powercast with RF transmitter (3W,915MHz) and receivers (P2110 and P1110) [166]. Powercast's ongoing objective is to provide long-range wireless power capable of remotely charging equipped devices, as well as better efficiency in harvesting RF energy to power embedded devices. Powercast had helped in finding solutions to wireless charging issues, such as RFID tags, waterproof designs and reusable wristbands. Powercast used its contactless charging technology to supply wireless power to numerous enabled devices that came within the charging range without the need for any direct line of sight. In [167], a comparison of two RF-based power harvesters and WPT technologies for IoT-WSN scenarios was discussed. According to the experimental results, P2110 power harvesters are more effective for long-range applications, and P1110 power harvesters are more effective for short-range applications. The experimental findings also revealed that the P1110 power harvester provided a higher RF-to-DC conversion efficiency than P2110 power harvester for the same transmission range. However, it required a longer recharge time than P2110 power harvester for the same transmission distance. These results essentially provided useful insights into the uniqueness of

the two RF-based power harvesters for their different requirements and application scenarios in WSNs.

2.9.3 RF WIRELESS POWER TRANSFER (RF-WPT) IN RECHARGEABLE WSN (R-WSN)

In the present-day wireless communication network, due to the advancement of the silicon technology that reduces the power requirement for electronic devices, there is a rising number of low-powered devices used, that can be wirelessly charged by the RF-EH technique. Energy provisioning methods include Renewable EH (REH) [168] where the sensors recharge their batteries by harvesting renewable energy from ambient sources (solar, wind etc.) and WPT [169] where battery recharging takes place using electrical power from wireless chargers. The authors in [170] proposed a cooperative integration of ambient RF-EH with dedicated WPT that could prove to be an effective approach for different power-constrained sensor networks. The key benefit of RF-EH over WPT is that the power does not have to be intentionally provided by the operator of the harvester, making it a "free" energy source. However, the success of ambient RF for Rechargeable WSN (R-WSN) is very limited in practice as the amount of harvested energy can be very low [171]. Also, RF-EH is considered to be one of the most challenging energy sources since the amount of energy harvested using REH is a function of the deployment environment i.e. the available harvestable power varies with time, frequency, distance from the energy source, location and various environmental conditions. Moreover, the biggest hurdle of ambient RF energy is the low energy density due to spreading loss. Furthermore, the power density from RF-EH is limited compared to other renewable energy sources. Moreover, appropriate circuit design is required to improve the RF-to-DC efficiency keeping the harvester small in size. In contrast, RF-WPT technology [172,173] had gained significant interest as a prospective technology that provided stable energy supply to the sensors through transmitting RF energy and had a powerful advantage in Industrial IoT (IIoT) as it exploited low level, ambient RF power to sustain autonomous operation of sensor motes. However, there is currently no published work which analyses the potential of powering IIoT applications through RF-WPT using P1110-EVAL-PS.

Low-Rate Wireless Personal Area Network (LR-WPAN) [174] has emerged as an appealing communication system in IIoT. ZigBee/ IEEE 802.15.4 [175, 181] is a low cost WSN for industrial application that operates in the unlicensed RF worldwide (915 MHz Americas, 2.4

GHz global or 868 MHz Europe). EH using dedicated RF source has gained popularity due to its ability to provide stable energy supply to the sensor motes. Four battery chemistries had been investigated in [176] to determine the best battery type for IoT applications. In [177], the total harvested energy was typically modelled linearly. However, in practice, EH circuits result in a non-linear end-to-end WPT. A realistic parametric non-linear EH model based on a logistic function was designed in [178] based on logistic function to represent the dynamics of the RF energy conversion efficiency at various input power levels. In contrast to [178], the authors in [179] proposed a quadratic RF-EH efficiency model that obtained better results. Meanwhile, the authors in [180] had designed a piecewise linear approximation model and obtained better performance but they did not analyse the battery recharging time. In contrast to existing simulators like Castalia, EKHO, and COOJA that do not have energy modelling metrics table, Netsim v13.1 [12] provided EH model where the residual energy as well as energy consumption in each battery node was estimated by battery model metrics table. In [181], an agricultural simulation environment of WSN was modelled with solar EH model in Netsim where recharging state and recharge current duration were used to determine the longevity of the sensor network with and without EH feature. Authors in [182] found out the Network Lifetime (NL) curves of the sensor nodes deployed in an IoT environment using NetSim and evaluated the throughput and battery life. In recent years, flourishing achievements have been made for improving the system performance of RWSNs in terms of path planning, charging scheduling, charging direction, and so on. However, little attention has been paid on the network lifetime issue using RF-WPT for battery-driven sensor motes. It has been shown that environmental EH from external sources (e.g., thermal energy, solar power, wind energy, vibration energy etc) can potentially prolong the network lifetime of WSNs. However, climate has a significant influence on energy harvesting from these sources, and their erratic availability can pose a threat to their continuous operation.

There is an inverse relationship between charging time and harvested RF energy. In other words, the charging time decreases as the harvested RF energy increases. In [183], the battery recharging time was analyzed when multiple RF sources were available. In [184], a statistical distribution model had been proposed for RF-EH systems. Here, an RF-EH system including multiple RF sources had been analyzed. Depending on system variables, the distributions of charging times had been shown. The impacts of the number of RF sources and wireless channel conditions on the charging time were demonstrated by simulations. Although the study provided an insight about the charging time theoretically, the experimental studies on the charging time is still missing in the literature.

2.10 DISCUSSION

Comprehensive analysis in the relevant research on RF-EH networks has been presented in this chapter. Firstly, an overview on the architecture of RF-EH has been provided along with various relaying schemes and protocols. Next, a brief survey on various wireless relaying strategies in unidirectional and bidirectional networks has been presented. Moreover, the security issues in RF-EH have been highlighted. In addition, the coexistence of RF-EH with PLS and NOMA has been briefly explained to understand the potential benefits of this incorporation. Lastly, a thorough analysis and discussion on the application of RF-WPT in WSN has been provided. This review enlightens the progress of various EH techniques with their benefits and shortcomings. The review presented in this chapter also indicates that there is enormous possibility of enhancement of work in this arena.

Chapter 3

RF ENERGY HARVESTING IN ONE-WAY RELAY NETWORKS

3.1 OVERVIEW

This chapter presents the performance analysis of an RF-powered one-way single relay network. Firstly, a novel Interference Aided (IA)-EH scheme is proposed by incorporating DF relaying over Rayleigh fading channel using hybrid TSR-PSR protocol. Here, a single interference node is exploited to replenish energy for the relay. The impact of various associated parameters such as, location of relay, position of interferer and conversion efficiency is studied on the throughput performance of the system. In the next section, Destination based Jamming (DBJ) technique is incorporated in an ideal interference-free environment to enhance the system security in the presence of an Eavesdropper (EAV). Three fading scenarios namely, Rayleigh, Weibull, and Nakagami-q (Hoyt) are considered to examine the effect of fading on the secrecy performance of the system. Finally, in the last section, a secure one-way communication model with IA-EH is provided in presence of a single EAV to observe the effect of interference power and jamming on the secrecy performance of the cooperative system.

3.2 BACKGROUND

In conventional relaying, Co-Channel Interference (CCI) deteriorates the system performance [93] and thus needs to be eliminated either by applying interference alignment approach or by decoding the interfering signals when they are strong. As opposed to this, the CCI signals are depicted as a new source of power for relay recharging. Motivated by this, an IA-EH cooperative relaying scheme adopting hybrid TSR-PSR protocol has been proposed to improve the network throughput. [66] showed that source and destination nodes try to maintain a secure link while wiretapper tries to capture the secret data. [67] have applied a Cooperative Jamming (CJ) scheme for harvesting energy using a multi-antenna. Beamforming and power-splitting

schemes have been used by [68] to increase the Secrecy Rate (SR) by applying DBJ that deteriorates the SNR at the EAV. The authors in [69] have used various relay selection strategies to enhance the network performance in terms of Secrecy Outage Probability (SOP) and SR. The secrecy performance of DF relay network over composite weibull/lognormal fading has been analyzed by [72]. More interestingly, Physical Layer Security (PLS) in cooperative wireless network with multiple relays where both AF and DF schemes are considered in the presence of an EAV over Rayleigh fading channels have been evaluated by [73]. Despite considerable contribution of the above-mentioned research, very few studies have been carried out to investigate the secrecy performance under Weibull or Hoyt fading. Moreover, most works on secrecy in Cooperative Relay (CR) networks do not consider the potentially beneficial role of network interference for communication secrecy. This leads to the development of interference management strategies that exploit network interference to enhance the level of secrecy. Following these advances, this chapter investigates the performance of one-way single relay network using RF-EH in three different scenarios: (i) interference-limited environment in absence of EAV (ii) interference-free environment in presence of an EAV (iii) interference-limited environment in presence of an EAV.

3.3 COOPERATIVE RELAY NETWORK WITH IA-EH USING HYBRID TSR-PSR PROTOCOL

This section describes the proposed single relay cooperative network involving an interferer.

3.3.1 System Model

Fig. 3.1 presents a simple one-way EH CR network in a smart city environment comprising of a Source *S*, Relay *R*, Interferer *I* and Destination *D* located at (0,0), (20,10), (40,30) and (100,0) respectively. Source *S* (smart traffic camera) at a streetlight sends video data to the Destination *D* (central control unit) via a Relay *R* (smart sensor node installed on a traffic pole). An Interferer *I* (a nearby 5G small cell tower or public hotspot that operates on a similar frequency band) unintentionally interferes with the relay but also becomes a source of harvestable RF energy. *S* transfers information to *D* with the help of *R* under the effect of *I*. Here, *R* harvests energy from *S* and *I* using Hybrid TSR-PSR protocol [20]. The DF scheme is applied at *R* to

decode the data of *S* and forwards the re-encoded data to *D* using the overall energy harvested. In this context, following assumptions are made:

- The nodes operate in the Half Duplex (HD) mode and are configured with a single antenna.
- No direct link is presumed to exist between *S* and *D* due to deep fade and shadowing.
- The source *S* is assumed to have a constant energy supply.
- The effect of noise is neglected as the interferer power P_I is presumed to be greater than the noise.

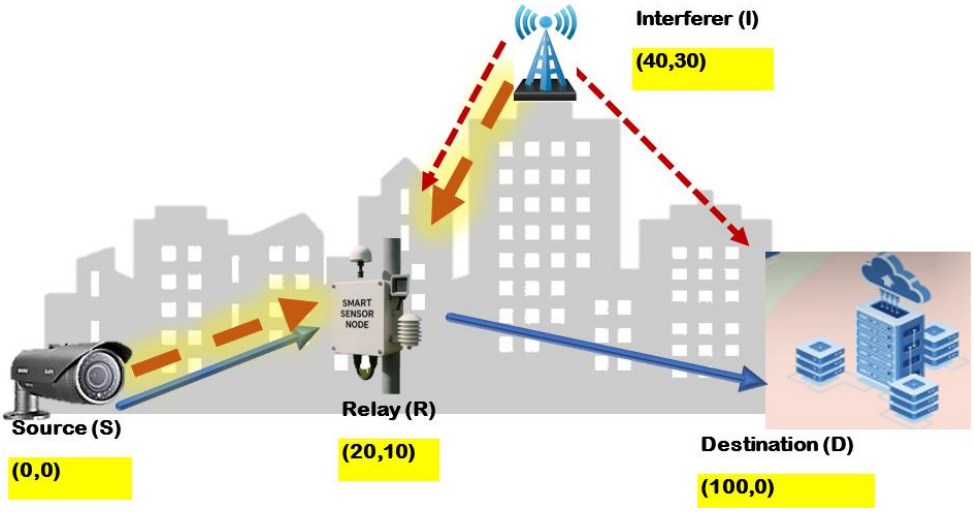

Fig. 3.1 System Model

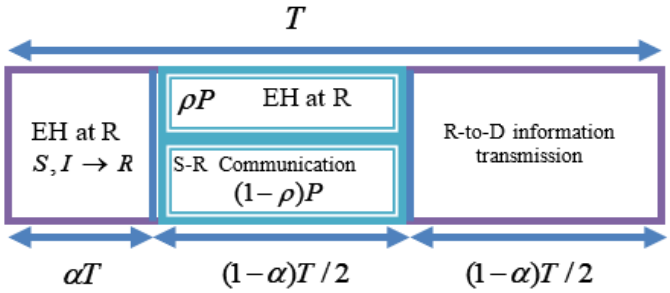

Fig. 3.2 Time frame structure for hybrid TSR-PSR protocol

Fig. 3.2 depicts the time slot structure of hybrid protocol for both harvesting energy and information forwarding. Here, the total time period T is divided into three time slots: (1) EH time slot, αT ; (2) 1st time slot, $(1-\alpha)T/2$;(3) 2nd time slot, $(1-\alpha)T/2$. Here, *R* harvests energy from *S* and *I* within the duration of αT , where α is the EH coefficient, which lies in the range $0 \le \alpha \le 1$. The 1st time slot is used to decode the source information. A fraction, ρ (

$0 \le \rho \le 1$) of the received signal is also available for EH at *R* and the remaining $(1-\rho)$ of the received signals is used for S−R communication. The 2nd time slot is reserved to forward the re-coded source signal to *D*. The channel gain coefficients from *S* to *R* and from *R* to *D* are h_{SR} and h_{RD} respectively. *I* is positioned at distances d_{IR} and d_{ID} from *R* and *D* respectively; f_{IR} and f_{ID} are the corresponding channel gains; d_{SR} and d_{RD} represent *S*-*R* and *R*-*D* distances respectively. Here, $|h_{SR}|^2$, $|h_{RD}|^2$, $|f_{IR}|^2$ and $|f_{RD}|^2$ are exponential random variables with mean λ_1, λ_2, v_1 and v_2 respectively. For simplicity, $|h_{SR}|^2$, $|h_{RD}|^2$, $|f_{IR}|^2$ and $|f_{RD}|^2$ are represented by X_1, X_2, Z_1 and Z_2 respectively.

3.3.2 Mathematical Modelling

For Delay Limited (DL) mode, the achievable throughput τ is governed by the Outage Probability (OP), P_{out} of the system.

➢ Signal-to-Interference and Noise Ratio (SINR) Calculation:

The interference power received at *R* and *D* are given as [93]:

$$P_{IR} = \frac{P_I |f_{IR}|^2}{d_{SR}^m} \tag{3.1}$$

$$P_{ID} = \frac{P_I |f_{ID}|^2}{d_{RD}^m} \tag{3.2}$$

where, P_I is the transmit power of the interferer and m is the path loss exponent. All the wireless links are assumed to exhibit frequency non-selective Rayleigh fading, i.e., channel coefficients are constant during one block time *T* as well as independent and identically distributed. *R* harvests energy from the received signals of *S* and *I* for a duration of αT. Therefore, energy harvested by *R* is given by:

$$E_{HR} = \frac{\eta P_S X_1}{d_{SR}^m} \rho T + \frac{\eta P_I Z_1}{d_{IR}^m} \alpha T \tag{3.3}$$

R forwards the decoded signal using the energy harvested during EH period, $(1-\alpha)T/2$.

So, the transmit power of *R* is given by:

$$P_R = \frac{E_{HR}}{(1-\alpha)T/2} \tag{3.4}$$

where, $0<\eta<1$ denotes energy conversion efficiency and P_s represents the Source transmission power.

The SINR at *R* and *D* are given as:

$$\gamma_{SR}=\frac{P_S X_1 d_{IR}^m}{P_I Z_1 d_{SR}^m}=\rho_R \frac{X_1}{Z_1} \tag{3.5}$$

$$\gamma_{RD}=\frac{P_R X_2 d_{ID}^m}{P_I Z_2 d_{RD}^m}=(a_3 X_1+b_3 Z_1)\frac{X_2}{Z_2}=W\frac{X_2}{Z_2} \tag{3.6}$$

where, $a_3=\frac{\alpha\eta\rho P_s \beta_{2,4}}{P_I(1-\alpha)d_3^m}, b_3=\frac{\alpha\eta\rho\beta_{2,4}}{(1-\alpha)d_1^m}$ and $W=a_3X_1+b_3Z_1$

Accordingly, the OP is given as:

$$P_{out}=\Pr\{\gamma_{SR}<\gamma_{th},\gamma_{RD}<\gamma_{th}\} \tag{3.7}$$

where γ_{th} represents the SINR threshold

➢ Throughput

Throughput is the measure of how much data successfully reaches its destination within a specific timeframe. Let R_S be a fixed transmission rate that *S* needs to satisfy such that $R_S=\log_2(1+\gamma_{th})$. Then, the SINR threshold is represented as $\gamma_{th}=2^{R_S}-1$. Thus, the throughput for hybrid protocol in DL transmission is calculated as:

$$\tau=(1-\alpha)R_S(1-P_{out}) \tag{3.8}$$

3.3.3 Results and Discussions

The results of simulation are presented in this section. Monte Carlo simulations are executed using Matlab 2018b to study the throughput performance of the proposed scheme with respect to α, ρ, η, x_1, y_2. The throughput performance is also compared with one of the existing works [93], where the relay node harvests energy from the source alone. In the 2-D plane, the coordinates of different nodes are taken as: *S*: (0, 0); *D*: (100, 0); *R* (20, 10); *I* (40, 30)

Numerical values of some important parameters are indicated in Table 3.1:

Table 3.1 Parameter assumptions

Parameters	Meaning	Default Values
γ_{th}	SINR Threshold	0 dB [93]
η	Energy Conversion Efficiency	1 [93]
P_s	Source Transmit Power	10 dB
P_I	Peak permissible Interference Transmit Power	20 dB
m	Path loss exponent	3 [93]

In Fig. 3.3, the throughput of the proposed network is plotted against α and ρ for TSR, PSR and our proposed hybrid protocols. Solid lines depict the throughput plot for our proposed scheme whereas dotted lines indicate the throughput plot of the existing work [93]. For a fair comparison with [93], we have re-simulated our proposed model in accordance with [93] (i.e. for source only network) and compared all the three protocols in terms of throughput performance.

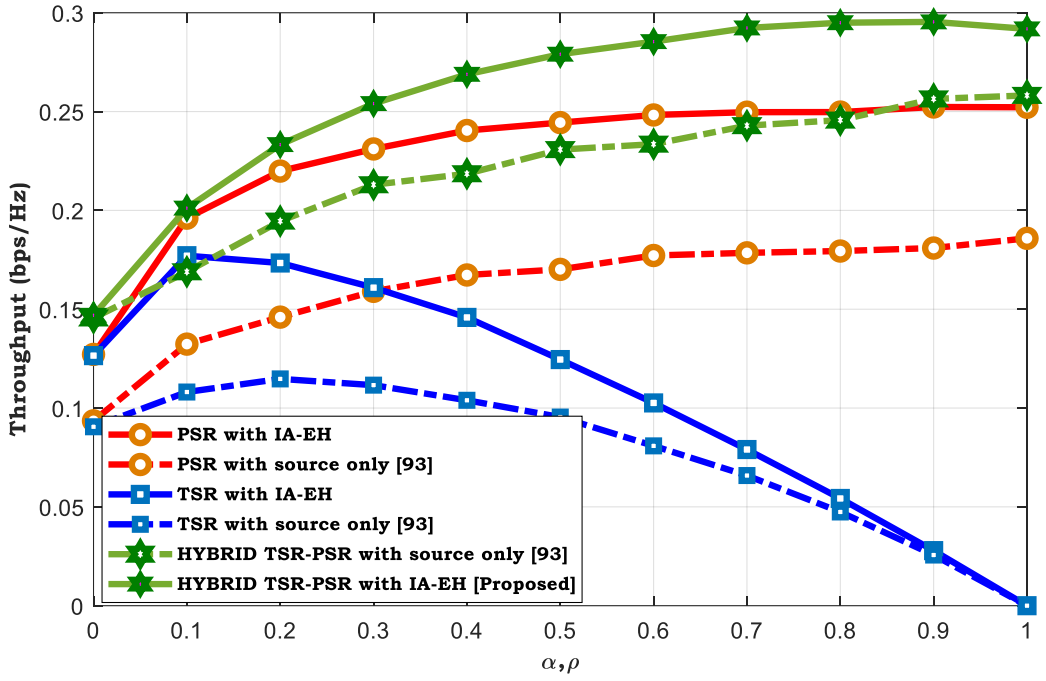

Fig. 3.3 Throughput of TSR, PSR and Hybrid protocols versus α, ρ

On comparing, it has been found that our proposed architecture outperforms the network model in [93]. This betterment comes from extracting the added energy from *I*, which helps to improve the transmission power of *R* on *R*-*D* link which in turn improves the SINR at *D*. In case of TSR, the throughput increases as α increases upto a certain point, and after that point, throughput

begins to decrease as observed from Fig. 3.3. This is because trade-off exists between the EH time and data transmission time. To be more precise, if R spends more time on the energy harvesting procedure, the time for the data transmission will be lessened. In contrast, if lesser amount of power is harvested at the R with less time for energy harvesting, more time will be available to transmit data. On the other hand, for PSR and Hybrid protocols, throughput increases as ρ increases from 0 to some optimal ρ (ρ_{opt}) but later, it gets saturated as ρ goes beyond its optimal value. This is because less power is available for EH for values of ρ smaller than ρ_{opt}, and hence less transmit power P_R is available from R and we observe smaller values of throughput at D due to larger outage probability. Similarly, more power is wasted on EH and less power is left for S-R information transmission for values of ρ greater than ρ_{opt}. As a result, poor signal strength is obtained at R which results in less achievable throughput at D.

The position of Relay with respect to the source has an impact on the throughput performance of the system. This study is depicted in Fig 3.4 where different curves are plotted for various values of α and ρ.

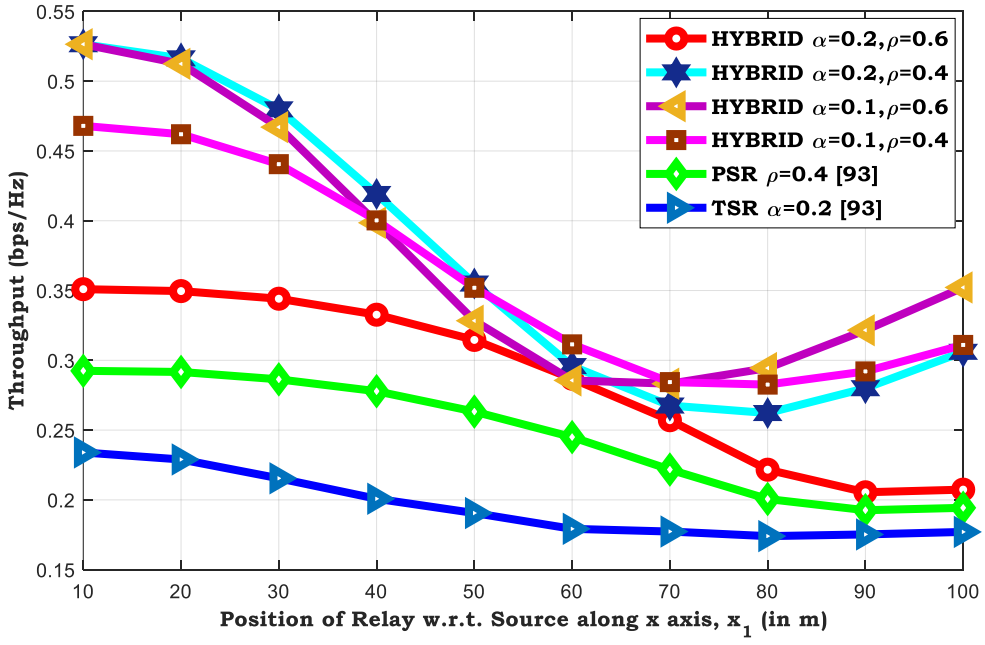

Fig. 3.4 Throughput of TS, PS and hybrid protocols versus location of R along x-axis (x_1)

Above figure shows that for the proposed scheme $(\alpha = 0.2, \rho = 0.4)$, as the position of relay shifts from 10m to 90m along x-axis, the throughput of the system decreases because of the fact that *R* moves far away from *S* towards *D*. This can be justified as follows: As *R* moves away from *S*, the decoding capacity and the energy harvesting at *R* decreases. Also, as the distance between *S* and *R* increases, both the energy harvested by *R* and the received signal strength at *R* decreases due to larger path loss, thus less energy can be harvested. Since the transmit power of *R* in the second phase depends only on the harvested energy during the first phase, the received signal strength at *D* becomes weak and the throughput thus decreases. However, an interesting observation regarding the proposed scheme is that by increasing x_1 beyond 80 m, a slight increase in throughput occurs. This reason may be that when *R* gets closer to *D*, reliable communication between *R* and *D* becomes possible for low values of harvested energy due to very small *R*-*D* path loss. It can be said that the proposed scheme with $(\alpha = 0.2, \rho = 0.4)$ is found to outperform the existing work.

Fig. 3.5 presents the plot of throughput versus position of interferer y_2 when the interferer shifts from 40 to 100 keeping x_2 is fixed at 30m.

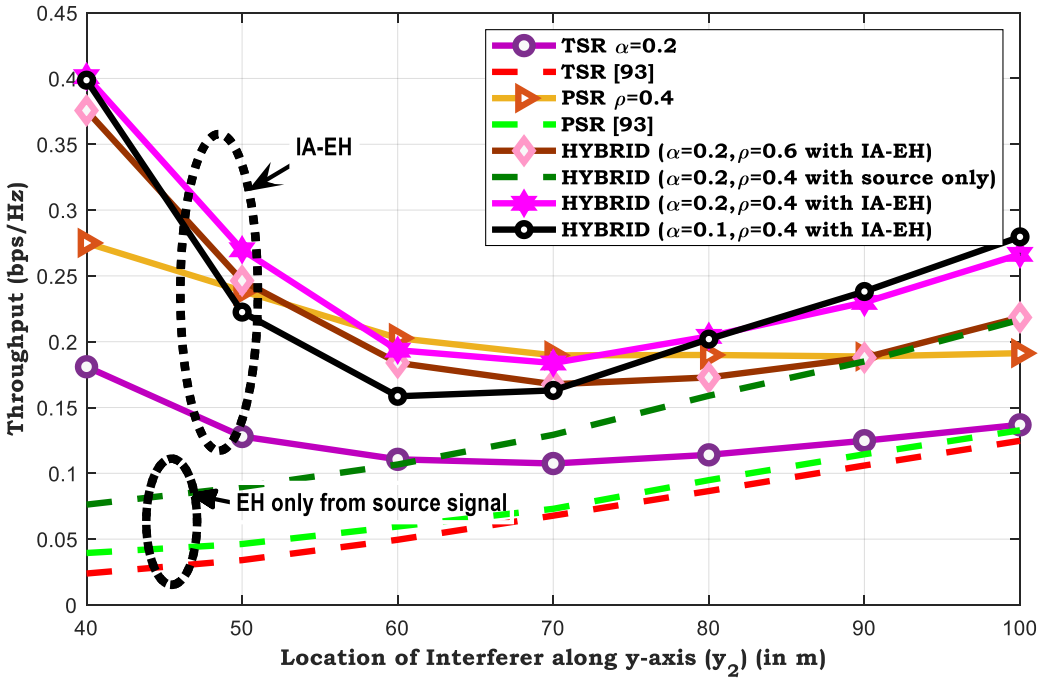

Fig. 3.5 Throughput of TS, PS and hybrid protocols versus position of *I* along y-axis (y_2)

As shown in the above figure, while harvesting energy from *S* alone, the throughput increases with y_2 because the effect of *I* on the decoding capacity of *R* and *D* decreases when *I* moves away from *R* and *D*. But for IA-EH, throughput first decreases, becomes constant and then increases slightly. The proposed scheme $(\alpha = 0.2, \rho = 0.4)$ is found to give much better throughput. At $y_2 = 40m$, when *I* is very close to *R*, the percentage increase in throughput for hybrid protocol $(\alpha = 0.2, \rho = 0.4)$ is found to be 80% initially. As the distance of *I* slowly increases, the amount of energy harvested from *I* decreases and the throughput performance deteriorates. This is because the interference power imposed on *R* and *D* offsets the energy harvested at *S* and *R* i.e. the negative effects brought by the interference from *I* on *R* offsets the positive effects brought by harvesting energy from *I* on *R*. It is also found out that there is no significant improvement in throughput as y_2 exceeds 80 m. This occurs because the interference may restrict the actual transmit power. It can be seen that there is a slight increase in the throughput performance when considering RF energy harvesting from the interference. Fig. 3.6 depicts a plot of throughput versus energy conversion efficiency η between our proposed network with hybrid protocol and the existing TSR and PSR protocols [93]. The throughput perks up as η increases or the transmit relay power increases. Larger values of η lead to more harvested energy. It is also seen that the proposed scheme $(\alpha = 0.2, \rho = 0.4)$ is found to give much better throughput value as compared to the other schemes.

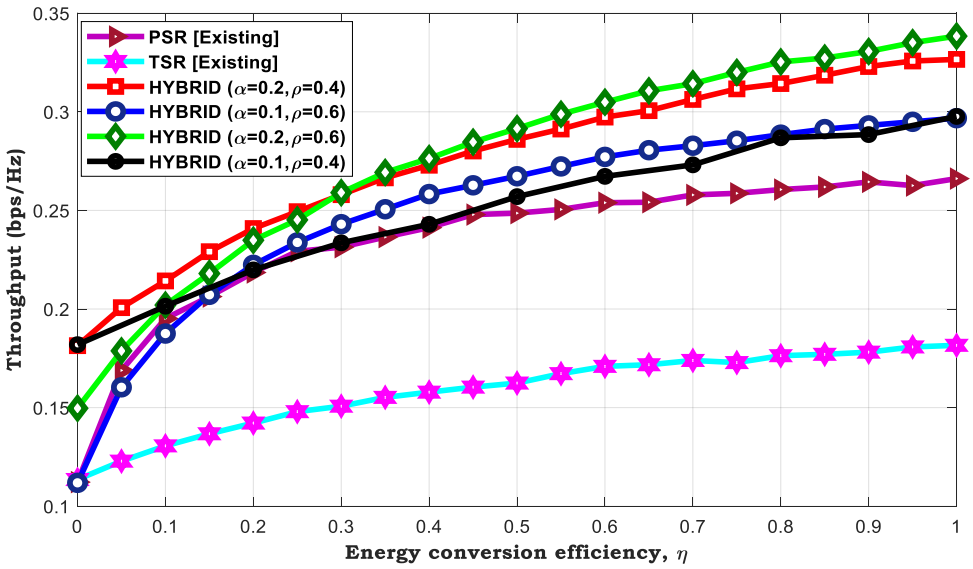

Fig. 3.6 Throughput as a function of η

3.4 BEACON-AIDED RF-EH IN INTERFERENCE-FREE UNTRUSTED SCENARIO

This section presents a Hybrid Decode Amplify Forward (HDAF)-based Cooperative IoT (CIoT) system in an interference free environment which incorporates DBJ technique.

3.4.1 System Model for beacon-aided EH

In the considered CIoT network illustrated in Fig. 3.7, the system comprises a Power Beacon *B*, Source *S*, Hybrid Decode Amplify Forward (HDAF) Relay, Destination *D* and an Eavesdropper EAV.

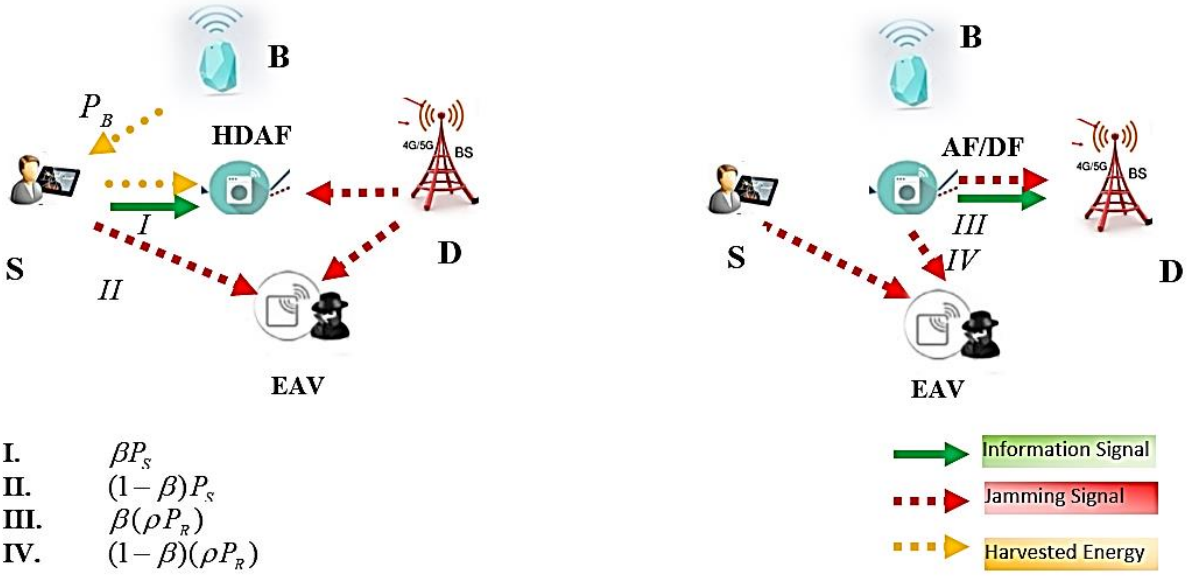

Fig. 3.7 HDAF-based CIoT Network

This setup is directly applicable to secure and sustainable IoT deployments such as industrial automation, remote sensing, or smart grid monitoring, where deploying conventional power infrastructure is infeasible, and secure communication is critical. A beacon is a wireless energy source that transmits high-frequency RF signals to charge or power nearby RF-EH devices. Here, *B* acts as a dedicated energy source, providing power to the IoT network that has limited energy constraints, enabling the network to communicate and operate. Here, *S* tries to transmit information to the destination *D* through a new relaying scheme in order to explore the advantages of both DF and AF relaying schemes. The EAV is an unauthorized passive node trying to intercept the confidential communication between the source and destination. In DBJ

scenario, the EAV plays a role by both passively listening to the communication between the source and destination while simultaneously jamming the destination's signal, thus making it harder for the receiver to decipher the legitimate transmission. To keep the source information secure, *D* sends a jamming signal to HDAF as soon as *S* transmits the information to HDAF.

➢ Channel Model

In this model, it is assumed that each node is provided with a single antenna that operates in Half Duplex (HD) mode. The direct path between *S* and *D* has been assumed to be broken, due to deep fade and shadowing. It is assumed that the channels are reciprocal. Furthermore, it is assumed that all the nodes except EAV have perfect knowledge of the jamming signals transmitted as well as CSI of the links. Each channel gain (g_{mn}) is the square of channel coefficient as $g_{mn} = |h_{mn}|^2, (\mathrm{m,n} \in \{\mathrm{bs},\ sr,\ rd, se, re, de\})$ where '*m*' is the transmitting node, '*n*' is the receiving node, and Ω_{MN} represents the mean channel gain between nodes m and n. The corresponding distances are given as $d_1, d_2, d_3, d_4, d_5, d_6$.

➢ Destination-Assisted Jamming

The time frame of the system model is provided in Fig 3.8.

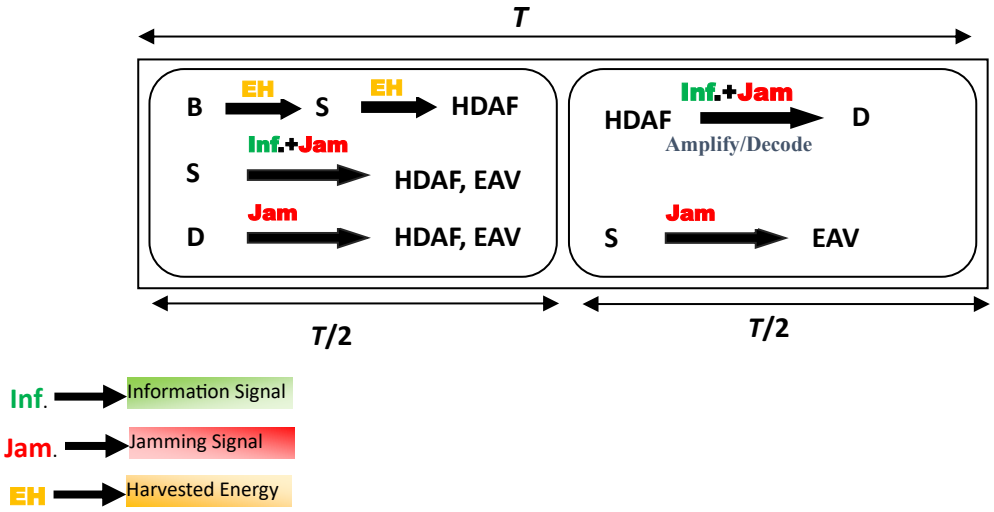

Fig. 3.8 Time Frame of the System Model

Here, *S-D* data transfer takes place in a slot of duration *T*. HDAF Relay uses a part ρ of the received power for EH and the remaining part $(1-\rho)$for information processing, where $0 \leq \rho \leq 1$. In the 1st time slot, *S* broadcasts a combination of information and jamming signal to both HDAF and EAV. The total power transmitted by the source is P_S which is divided into two parts i.e. β amount of power is allocated to information signal and remaining $(1-\beta)$ amount of power is allocated to jamming signal. At the same time, *D* cooperates with *S* to transmit the jamming signal to both HDAF and EAV with some of power that is known to the relay and received by it. In the 2nd time slot, using this harvested energy, HDAF forwards the amplified/decoded information signal-plus-jamming signal received in the first time slot to *D* and EAV. *D* detects and subtracts the jamming signal, which had been sent in the first time slot on the basis of perfect knowledge of CSI and hence separates it. During the same time, *S* cooperates with the relay to transmit the jamming signal to reduce SNR at EAV.

4.4.2 Mathematical modelling

In the proposed system, *S* harvests energy from *B*. Next, the HDAF relay harvests energy from *S* and uses it to forward to *D*. The HDAF Relay acts as an intermediary to enhance the overall signal strength and reliability of communication. It is positioned strategically between the source and the destination. This helps the source to transmit data to the relay. The relay then forwards the data to the destination, either by amplifying or decoding the signal and retransmitting it. This cooperative action ensures that the data reaches the destination reliably.

❒ *Energy Harvesting and Information Processing*

- **Energy harvesting by *S***

In the 1st time slot, the harvested energy at *S* from *B* is given by

$$E_{HS} = \frac{\eta_b P_B g_{bs}}{d_1^m}\left(\frac{T}{2}\right) \tag{3.9}$$

where η_b is the conversion efficiency and $0 < \eta_b < 1$. P_B is the transmission power of Beacon *B*. The maximum power that *S* can use for information transmission is expressed as:

$$P_S = \frac{E_{HS}}{T/2} = \frac{\eta_b P_B g_{bs}}{d_1^m} \tag{3.10}$$

The total power transmitted by *S* is P_S which is split into two parts i.e. βP_S for information signal and $(1-\beta)P_S$ for jamming signal.

- **Energy harvesting by HDAF**

In the 1st time slot, *S* broadcasts information signal and *D* broadcasts jamming signal, which is received by HDAF as:

$$y_R = \sqrt{\frac{(\rho)(\beta P_S)}{d_2^m}} g_{sr} x_s + \sqrt{\frac{(\rho)(\beta P_D)}{d_3^m}} g_{rd} x_{jd} + N_o \tag{3.11}$$

where P_D is the Power transmitted by *D*

Thus, energy harvested by the EH receiver in HDAF is given by:

$$E_{HR} = \eta_s \rho \left(\frac{\beta P_S g_{sr}}{d_2^m} + \frac{P_D g_{rd}}{d_3^m} \right) \frac{T}{2} \tag{3.12}$$

where η_s is the energy conversion efficiency at *S* and lies in the range $0 < \eta_s < 1$

The maximum transmit power by HDAF is given as:

$$\begin{aligned} P_R &= \frac{E_{HR}}{T/2} \\ &= \frac{\eta_s \beta P_S g_{sr}}{d_2^m} + \frac{\eta_s \beta P_D g_{rd}}{d_3^m} \\ &= \frac{\eta_b \eta_s \beta P_B g_{sr} g_{bs}}{d_1^m d_2^m} + \frac{\eta_s \beta P_D g_{rd}}{d_3^m} = \eta_s \beta \left(\frac{\eta_b P_B g_{bs} g_{sr}}{d_1^m d_2^m} + \frac{P_D g_{rd}}{d_3^m} \right) \end{aligned} \tag{3.13}$$

HDAF uses a fraction β of the harvested power i.e $\beta(\rho P_R)$ to transmit the information and a fraction $(1-\beta)(\rho P_R)$ of the harvested power to transmit the jamming signal

❒ *Information Processing at* HDAF

- **AF mode:**

Here, HDAF combines the two received signals and broadcasts the resulting signal by applying AF operation.

PHASE I:

In the 1st time slot, the remaining part of the received signal after using for harvesting is used for information processing, which can be expressed as:

$$y_{SR} = \sqrt{(1-\rho)(\beta P_S)}g_{sr}x_s + \sqrt{(1-\rho)P_D}g_{rd}x_{jd} + N_O \tag{3.14}$$

where x_S is the source message, x_{jd} is the jamming signal sent by D, and N_O represents the AWGN at HDAF. Thus, SNR at HDAF is given as:

$$\gamma_{SR} = \frac{(1-\rho)(\beta P_S)g_{sr}}{(1-\rho)P_D g_{rd} + N_o} \tag{3.15}$$

The received signal and SNR at EAV node in 1st time slot is given by:

$$y_{SE} = \sqrt{\frac{(1-\rho)(1-\beta)P_S}{d_4^m}}g_{se}x_{js} + \sqrt{\frac{(1-\rho)P_D}{d_6^m}}g_{de}x_{jd} + N_o \tag{3.16}$$

$$\gamma_{SE} = \frac{(1-\rho)(\beta P_S)g_{se}}{(1-\rho)\{(1-\beta)P_S g_{se} + P_D g_{de}\} + N_o} \tag{3.17}$$

PHASE II:

HDAF amplifies the signal by an amplification factor μ given as:

$$\mu = \sqrt{\beta P_R \psi_P}$$

where μ is the amplification factor

and $\psi_P = \dfrac{1}{\dfrac{(1-\rho)P_S}{d_1^m}g_{sr} + \dfrac{(1-\rho)P_D}{d_2^m}g_{rd} + N_o}$ (3.18)

Thus, $\mu = \sqrt{\dfrac{\rho(\beta P_R)}{\dfrac{(1-\beta)(\rho P_S)g_{sr}}{d_1^m} + \dfrac{(1-\beta)P_D g_{rd}}{d_2^m} + N_o}}$ (3.19)

In the 2nd time slot, the relay forwards the amplified x_R signal to D as:

$$x_R = \mu y_R = \mu\sqrt{(1-\rho)P_S g_{SR}}\,x_S + \mu\sqrt{(1-\rho)P_D g_{RD}}\,x_{jd} + \mu N_O \tag{3.20}$$

The received signal at *D* from HDAF after amplification is expressed as:

$$\begin{aligned} y_d &= \sqrt{g_{rd}}\,x_R + N_O \\ x_R &= \mu(\sqrt{(1-\rho)(\beta P_S)}\,g_{sr}x_s + \sqrt{(1-\rho)P_D}\,g_{rd}x_{jd} + \sqrt{g_{RD}}\,n_R + N_O) \\ \therefore \mathrm{y}_d &= \sqrt{g_{rd}}\,(\mu(\sqrt{(1-\rho)(\beta P_S)}\,g_{sr}x_s + \sqrt{(1-\rho)P_D}\,g_{rd}x_{jd} + \sqrt{g_{RD}}\,n_R)) + N_O \end{aligned} \tag{3.21}$$

where n_R is the noise at the relay and N_O is the AWGN. *D* removes the jamming part of the information signal from the received signal and uses the remaining part for detection, which is expressed as:

$$\mathrm{y}_d = \sqrt{g_{rd}}\,(\mu\sqrt{(1-\rho)(\beta P_S)}\,g_{sr}x_s + \mu\sqrt{g_{RD}}\,N_O)) + N_O \tag{3.22}$$

Thus, the SNR at *D* can now be represented as:

$$\gamma_{RD_{AF}} = \frac{\mu^2(1-\rho)(\beta P_S)g_{sr}g_{rd}}{N_O\{(1-\rho)(P_S g_{SR} + P_D g_{RD}) + N_O\}} \tag{3.23}$$

The received signal at EAV node in the 2nd time slot after amplification is given by:

$$y_{RE} = \sqrt{\frac{(1-\beta)P_S(1-\rho)(\beta P_R)\psi}{d_1^m d_5^m}}\,g_{re}x_{jr} + \sqrt{\frac{(1-\rho)P_D(\beta P_R)\psi}{d_2^m d_5^m}}\,g_{se}x_{js} + \sqrt{\frac{\beta P_R\psi}{d_5^m}} + N_o \tag{3.24}$$

where x_{jr} is the jamming signal sent by *HDAF.*

Now, the received signal at *D* can be written as:

$$y_d = \sqrt{\frac{(\beta)(\rho P_R)\psi}{d_3^m}}\,g_{rd}x_r + \sqrt{\frac{(1-\beta)(\rho P_R)\psi}{d_3^m}}\,g_{dr}x_{jd} + N_o \tag{3.25}$$

Here, *D* detects the known jamming signal on the basis of perfect knowledge of jamming signal and CSI. Now, *D* subtracts the jamming part from the received signal and the remaining fraction of signal used by *D* to decode the message can be expressed as:

$$y_D = \sqrt{\frac{(\beta)(\rho P_R)\psi}{d_3^m}}\,g_{rd}x_r + N_o \tag{3.26}$$

and SINR at *D* is given by

$$\gamma_{RD_{AF}} = \frac{\mu^2(1-\rho)(\beta P_S)g_{sr}g_{rd}}{(\mu^2 g_{rd}+1)N_o} \tag{3.27}$$

But, the EAV has no knowledge about the CSI of HDAF-EAV link, and hence no information regarding the jamming signal. Thus, it cannot separate the jamming signal from the received signal. The received signal and SNR at the EAV are expressed as:

$$y_{RE} = \sqrt{\frac{(1-\beta)(\rho P_R)\beta_P}{d_3^m}}g_{re}x_r + \sqrt{\frac{(1-\beta)(1-\rho)P_S\psi}{d_3^m}}g_{se}x_{jd} + N_o \tag{3.28}$$

$$\gamma_{RE_{AF}} = \frac{\mu^2(1-\rho)(\beta P_S)g_{sr}g_{re}}{\mu^2\{(1-\rho)(1-\beta)P_S g_{sr}g_{re} + P_D g_{re}\} + N_o} \tag{3.29}$$

- **DF mode:**

PHASE I:

The received signal at HDAF and EAV node in the 1st time slot is given by:

$$y_{SR} = \sqrt{(1-\rho)(\beta P_S)}g_{sr}x_s + \sqrt{(1-\rho)P_D}g_{rd}x_{jd} + N_o \tag{3.30}$$

$$y_{SE} = \sqrt{(1-\rho)(1-\beta)P_S}g_{se}x_{js} + \sqrt{(1-\rho)P_D}g_{de}x_{jd} + N_o \tag{3.31}$$

While processing the data, HDAF removes the known jamming term $(1-\rho)\,\mathrm{P}_D\, g_{rd}x_{jd}$.

So the resultant signal is expressed as:

$$y_{SR} = \sqrt{(1-\rho)(\beta P_S)}g_{sr}x_s + N_o \tag{3.32}$$

Thus, SNR at HDAF is given as:

$$\gamma_{SR} = \frac{(1-\rho)(\beta P_S)g_{sr}}{(1-\rho)P_D g_{rd} + N_o} \tag{3.33}$$

and SNR at EAV is given as:

$$\gamma_{SE} = \frac{(1-\rho)(\beta P_S)g_{se}}{(1-\rho)\{(1-\beta)P_S g_{se} + P_D g_{de}\} + N_o} \tag{3.34}$$

PHASE II:

The relay decodes the information from the received signal indicated as:

$$\gamma_{RD_{DF}} = \frac{(1-\rho)(\beta P_S) g_{sr} g_{rd}}{N_O\{(1-\rho)(P_S g_{SR} + P_D g_{RD}) + N_O\}} \tag{3.35}$$

The received signal at EAV node in the 2nd time slot after decoding is given by:

$$y_{RE} = \sqrt{(1-\beta)P_R}\, g_{re} x_{jr} + \sqrt{(1-\beta)P_S}\, g_{se} x_{js} + N_o \tag{3.36}$$

Thus, SNR at EAV is given by:

$$\gamma_{RE_{DF}} = \frac{(1-\rho)(\beta P_S) g_{sr} g_{re}}{(1-\rho)(1-\beta) P_D g_{re}\, g_{rd} + N_o} \tag{3.37}$$

➢ *Secrecy Rate (SR) and System Energy Efficiency (SEE) for CIoT network*

The closed form expression for SR of HDAF-based CIoT system over dissimilar faded environment is presented and then the SEE of the considered system is investigated.

❒ Secrecy Rate (SR) Analysis

In cooperative communications, SR refers to the amount of information that can be transmitted securely over a communication channel, taking into account both the legitimate user's ability to decode the signal and an EAV's (or "wiretapper's") ability to intercept and decode that same signal. SR in PLS is defined as the difference between the capacity of the legitimate communication channel (the channel between the transmitter and receiver) and the capacity of the EAV channel (the channel between the transmitter and the EAV). SR of HDAF is expressed as:

$$C_S^{HDAF} = \Pr(\gamma_{SR} \geq \gamma_{th})\, C_S^{DF} + \Pr(\gamma_{SR} < \gamma_{th}) C_S^{AF} \tag{3.38}$$

where C_S^{DF} is the SC of DF relaying scheme and C_S^{AF} is the SC of AF relaying scheme defined below:

$$C_S^{\Delta} = [C_{RD_{\Delta}} - C_{RE_{\Delta}}]^+ \tag{3.39}$$

where $\Delta \in (AF, DF)$; C_{RD} is the capacity of legitimate link and C_{RE} is the capacity of EAV link

Lemma 1: The SR of quasi-static complex fading wiretap-channel is given by [76]

$$C_S(\gamma_M,\gamma_E)=\begin{cases}\log(1+\gamma_M)-\log(1+\gamma_E) & ; \quad if \quad \gamma_M \geq \gamma_E \\ 0 & ; \quad if \quad \gamma_M < \gamma_E\end{cases} \tag{3.40}$$

Here we assume, $\gamma_M = \gamma_{RD}$ and $\gamma_E = \gamma_{RE}$

Case I: Legitimate and Wiretap links undergo Rayleigh fading

Lemma 2: Let C be a strictly positive constant, and let X and Y be two exponential random variables with mean λ_x and λ_y, respectively. Therefore, we have the following results:

$$\begin{aligned}&\mathrm{E}\{\ln(X)\}=\ln(\lambda_x)-\Phi \\ &\mathrm{E}\{\ln(X+C)\}=\ln(C)-e^{\frac{C}{\lambda_x}}Ei(-\frac{C}{\lambda_x})\end{aligned} \tag{3.41}$$

Lemma 3: For any network operating under Rayleigh fading with average SNR at the receiver given by $\overline{\gamma}$, a closed-form expression for SR is obtained in [185, Equation (34)] as:

$$C_{S_{RAY}}=\log_2(e)\exp(\overline{\gamma}^{-1})E_1(\overline{\gamma}^{-1}) \tag{3.42}$$

Proposition 1: In a framework where the wireless links experience Rayleigh Fading, closed-form expression for SR is given as:

$$C_{S_{RAY}}^{HDAF}=\Pr(\gamma_{SR}\geq\gamma_{th})\mathrm{C}_S^{DF}+\Pr(\gamma_{SR}<\gamma_{th})C_S^{AF}$$

$$\begin{aligned}=\frac{1}{2\ln 2}\Bigg\{&\Bigg[\left(\frac{1}{\psi\ (\gamma_{th}+\psi^{-1})}\exp\left(-\frac{\gamma_{th}\lambda_{X_{DF}}}{p_S}\right)\right)\times\Bigg\{\ln\left(1+\exp\left(-2\phi-\ln\left(\frac{1}{\lambda_{X_{DF}}\lambda_{Y_{DF}}}\right)\right)+\exp(\lambda_{Y_{DF}}^{-1})Ei\left(-\frac{1}{\lambda_{Y_{DF}}}\right)\right) \\ &-\left(1-\frac{\lambda_{RD_{DF}}R_{th}}{a_1\lambda_{RE_{DF}}\lambda_{SR}}\exp\left(\frac{\lambda_{RD_{DF}}R_{th}}{a_1\lambda_{RE_{DF}}\lambda_{SR}}\right)Ei\left(-\frac{\lambda_{RD_{DF}}R_{th}}{a_1\lambda_{RE_{DF}}\lambda_{SR}}\right)-\frac{\lambda_{RE_{DF}}}{\lambda_{RD_{DF}}}\right)\Bigg\}\Bigg] \\ &+\Bigg[\left(1-\frac{1}{\psi\ (\gamma_{th}+\psi^{-1})}\exp\left(-\frac{\gamma_{th}\lambda_{X_{AF}}}{p_S}\right)\right)\times\Bigg\{\ln\left(1+\exp\left(-2\phi-\ln\left(\frac{1}{\lambda_{X_{AF}}\lambda_{Y_{AF}}}\right)\right)+\exp(\lambda_{Y_{AF}}^{-1})Ei\left(-\frac{1}{\lambda_{Y_{AF}}}\right)\right) \\ &-\left(1-\frac{\lambda_{RD_{AF}}R_{th}}{a_1\lambda_{RE_{AF}}\lambda_{SR}}\exp\left(\frac{\lambda_{RD_{AF}}R_{th}}{a_1\lambda_{RE_{AF}}\lambda_{SR}}\right)Ei\left(-\frac{\lambda_{RD_{AF}}R_{th}}{a_1\lambda_{RE_{AF}}\lambda_{SR}}\right)-\frac{\lambda_{RE_{AF}}}{\lambda_{RD_{AF}}}\right)\Bigg\}\Bigg]\Bigg\}\end{aligned} \tag{3.43}$$

A formal proof of (3.43) is provided in Section A.1 of Appendix A.

Case II: The links are Hoyt faded

Proposition 2: In a scenario where the wireless links experience more severe fading than Rayleigh, i.e. Hoyt, where q_m and q_e represent the Hoyt shape parameters for the desired and EAV links, respectively, closed-form expression for SR are given by:

$$C_{S_{HOYT}}^{HDAF} = \frac{1}{2\ln 2}\left\{\left(Q\left(\alpha(q_{RD})\sqrt{\frac{\gamma_{RD_{DF}}}{\overline{\gamma}_{RD_{DF}}}},\beta(q_m)\sqrt{\frac{\gamma_{RD_{DF}}}{\overline{\gamma}_{RD_{DF}}}}\right)-Q\left(\beta(q_m)\sqrt{\frac{\gamma_{RD_{DF}}}{\overline{\gamma}_{RD_{DF}}}},\alpha(q_m)\sqrt{\frac{\gamma_{RD_{DF}}}{\overline{\gamma}_{RD_{DF}}}}\right)\left(\frac{\overline{\gamma}_{RD_{DF}}}{\overline{\gamma}_{RD_{DF}}+\overline{\gamma}_{RE}}\frac{1}{\sqrt{1-\left(\frac{q_e\overline{\gamma}_{\mathrm{RE}}}{\overline{\gamma}_{RD_{DF}}+\overline{\gamma}_{\mathrm{RE}}}\right)^2}}\right)\right)\right.$$
$$\left.+\left(1-Q\left(\alpha(q_{RD})\sqrt{\frac{\gamma_{RE_{AF}}}{\overline{\gamma}_{RE_{AF}}}},\beta(q_m)\sqrt{\frac{\gamma_{RE_{AF}}}{\overline{\gamma}_{RE_{AF}}}}\right)-Q\left(\beta(q_m)\sqrt{\frac{\gamma_{RE_{AF}}}{\overline{\gamma}_{RE_{AF}}}},\alpha(q_m)\sqrt{\frac{\gamma_{RE_{AF}}}{\overline{\gamma}_{RE_{AF}}}}\right)\left(\frac{\overline{\gamma}_{RD_{AF}}}{\overline{\gamma}_{RD_{AF}}+\overline{\gamma}_{RE_{AF}}}\frac{1}{\sqrt{1-\left(\frac{q_e\overline{\gamma}_{RE_{AF}}}{\overline{\gamma}_{\mathrm{RD}_{AF}}+\overline{\gamma}_{RE_{AF}}}\right)^2}}\right)\right)\right\} \tag{3.44}$$

A formal proof of (3.44) is provided in Section A.3 of Appendix A

Case III: The links are Weibull Faded

Proposition 3: SR of Weibull faded channel where v_m and v_e represent the Weibull shape parameters for the desired and *EAV* links, respectively, is given as follows:

$$C_{S_{WEIBULL}}^{HDAF} = \frac{1}{2\ln 2}\{(1-\exp\left(-\left[\frac{\gamma_{RD}}{\overline{\gamma}_{RD}}\Gamma\left(1+\frac{2}{v_m}\right)\right]^{v_m/2}\right)(\frac{2}{v_m}\log_2(1+r^{v_m/2})))$$
$$+(\exp\left(-\left[\frac{\gamma_{RE}}{\overline{\gamma}_{RE}}\Gamma\left(1+\frac{2}{v_e}\right)\right]^{v_e/2}\right)(\frac{2}{v_m}\log_2(1+r^{v_m/2})))\} \tag{3.45}$$

A formal proof of (3.45) is provided in Section A.2 of Appendix A

❒ SEE Analysis

The study the SEE performance of the proposed HDAF-based CIoT system is presented here. Fundamentally, SEE as the ratio of the SR to the total energy consumed in a single transmission time *T*.

$$\eta_{EE} = \frac{C_S}{E_C} \tag{3.46}$$

where C_S is the total information rate and E_C is the total energy consumption given as:

$$E_C = P_C + \kappa(P_B + P_S) - \eta_b(P_B + P_S)\rho \tag{3.47}$$

κ is the inverse power amplifier efficiency, P_C is the circuit power consumption,

The expression of SEE can be given as:

$$\eta_{EE} = \frac{C_S^{HDAF}}{E_C} = \frac{\Pr(\gamma_{SR} \geq \gamma_{th})C_S^{DF} + \Pr(\gamma_{SR} < \gamma_{th})C_S^{AF}}{P_C + \kappa(P_B + P_S) - \eta_b(P_B + P_S)\rho} \tag{3.48}$$

3.4.3 Results and Discussions

A simulation test bed is developed to evaluate the performance of Hybrid CIoT Network. Simulation has been carried out using Matlab R2019b. Different parameters required for simulation are summarized in Table 3.2.

Table 3.2 Parameter assumptions

Parameters	**Meaning**	**Default Values**
γ_{th}	Target Bit Rate	0 dB [93]
η_b	Energy Conversion Efficiency for Power Beacon	0.9
η_S	Energy Conversion Efficiency for Source	0.9
α	EH coefficient	0.2
ρ	Power splitting coefficient	0.6
β	Power allocation coefficient	0.2
P_B	Beacon Transmit Power	100W
P_S	Source Transmit Power	10 dBW
P_D	Destination Transmit Power	10 dBW
m	Path loss exponent	3

Fig. 3.9 highlights the comparison of SR performance of the proposed scheme with some of the conventional relaying schemes in Rayleigh faded environment. Fig. 3.9 (a) and depicts the plot of SR vs ρ; whereas, (b) presents the plot of SR vs ρ for various values of channel variance. From Fig. 3.9 (a), it is observed that the proposed Hybrid CIoT network outraces the existing schemes in terms of SR. This is because HDAF works in a dual manner, i.e., if the incoming signal is decoded successfully at the relay then DF scheme is followed; else it switches to AF scheme which increases the overall relay selection diversity. Also, there is a

close resemblance between the simulation and analytical results which verifies the correctness of both the theoretical derivations and simulations.

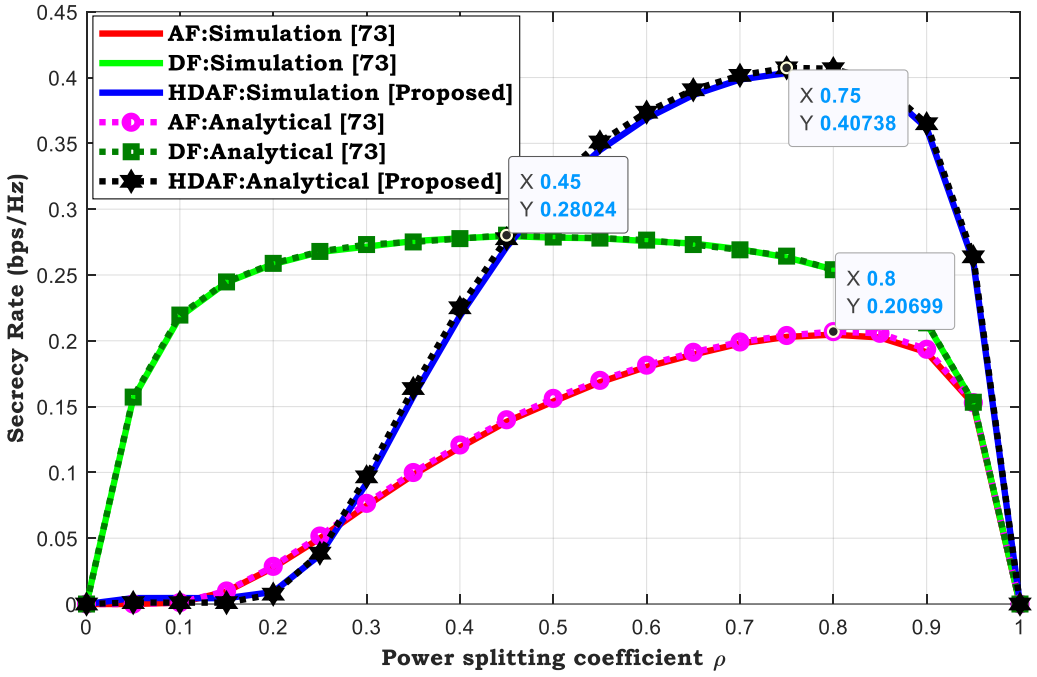

(a)

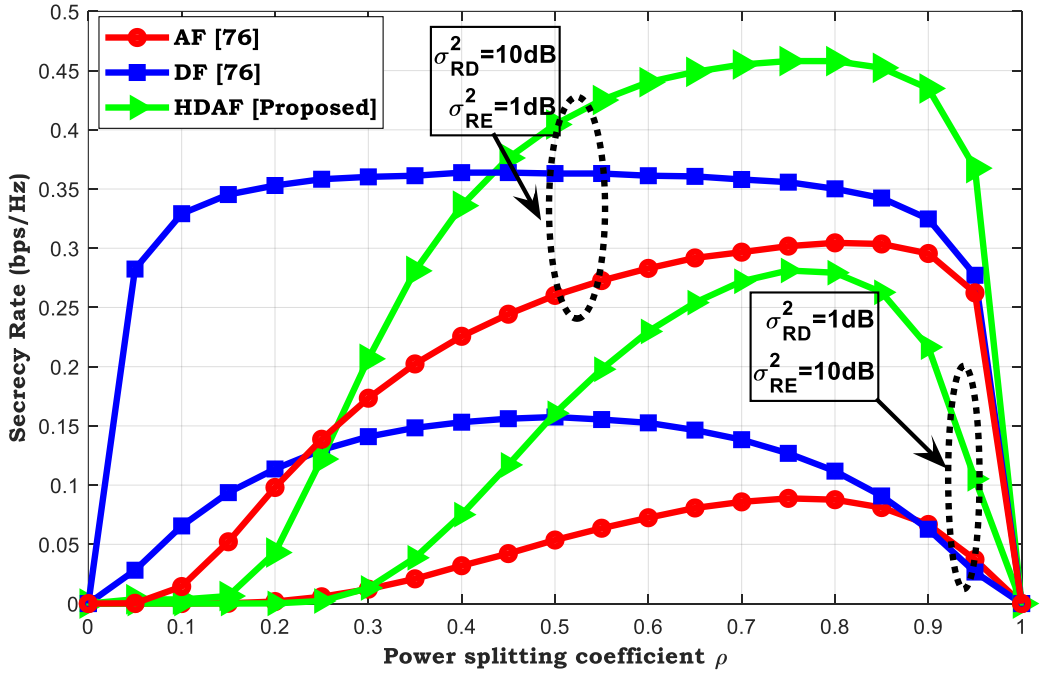

(b)

Fig. 3.9 SR comparison of HDAF relay with conventional relaying schemes for Rayleigh Faded Environment. **(a)** SR vs ρ **(b)** SR vs ρ for various values of channel variance

In Fig. 3.10, the impact of SR of the proposed scheme is evaluated with varying ρ. It is observed that the value of SR improves as the severity of fading increases for superior main channel i.e. $q_m > q_e$; whereas, it deteriorates for superior EAV channel i.e. $q_e > q_m$. When q_m increases from 0.1 to 1, fading decreases for the desired link, thus SR increases. Similarly, for Weibull fading, as v_m increases, SR also increases. Here, $v_m < 2$ indicates more severe fading than Rayleigh; whereas, $v_m > 2$ indicates less severe fading than Rayleigh. So when wiretap link is Rayleigh and the desired is Weibull, main link is less severely faded, hence SR rises. In the proposed system model, Weibull/Rayleigh fading on the main/EAV link is more secure because it limits the eavesdropper's ability to intercept and decode the signal by introducing a higher degree of channel variability in the EAV link. Thus, it can be inferred that severe fading provides more secure communication over the main link.

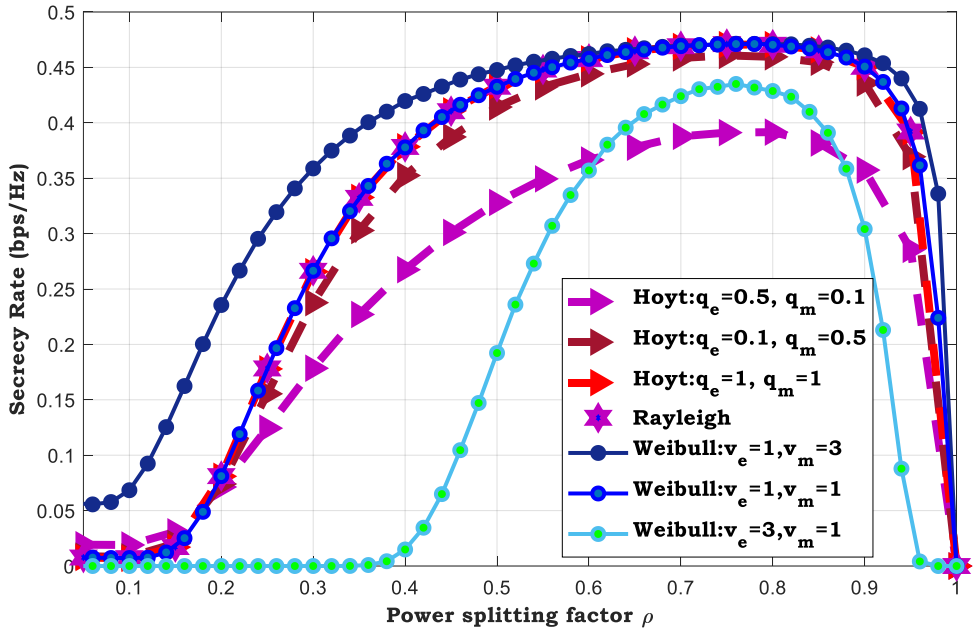

Fig. 3.10 SR of the proposed HDAF scheme with varying ρ for different fading conditions

Fig. 3.11 shows the impact of EAV position on SR at different channel mean power values. In order to investigate the impact of EAV location and jamming power on the SR of the system, it is considered that *S* and *D* are located at (0, 0) m and (2, 0) m, respectively. Firstly, the *EAV* is placed at (0.5, -0.5) m with respect to the source (0, 0) m. At (0.5, -0.5), SR increases with increase in γ_M and saturates at 17dB. As the EAV moves closer to *D* i.e. at (1, -1), the graph shifts to the right; a similar curve nature is observed at higher SNR and floor is observed at 26dB. Thus, the plots converge much faster at (0.5, -0.5) m. Thus, it can be said that, SR is at

its maximum when the EAV is closer to the source node and decreases as the *EAV* moves towards the destination. The channel mean power is inversely proportional to distance between *S*-HDAF and HDAF-*D*. It is further observed that as γ_M increases, SR also decreases with the decreasing value of Ω_{SR} or Ω_{RD} since the received SNR at *D* is upper bounded by SNR of the weakest link. In addition, from the three curves, it is seen that the SR for the case $\Omega_{SR} = 10dB$ and $\Omega_{RD} = 4dB$ converges to 2bits/Hz much faster than that of the case $\Omega_{SR} = 4dB$ and $\Omega_{RD} = 10dB$, meaning that the *S*–HDAF channel has a greater impact on the SR than its *R*–*D* counterpart.

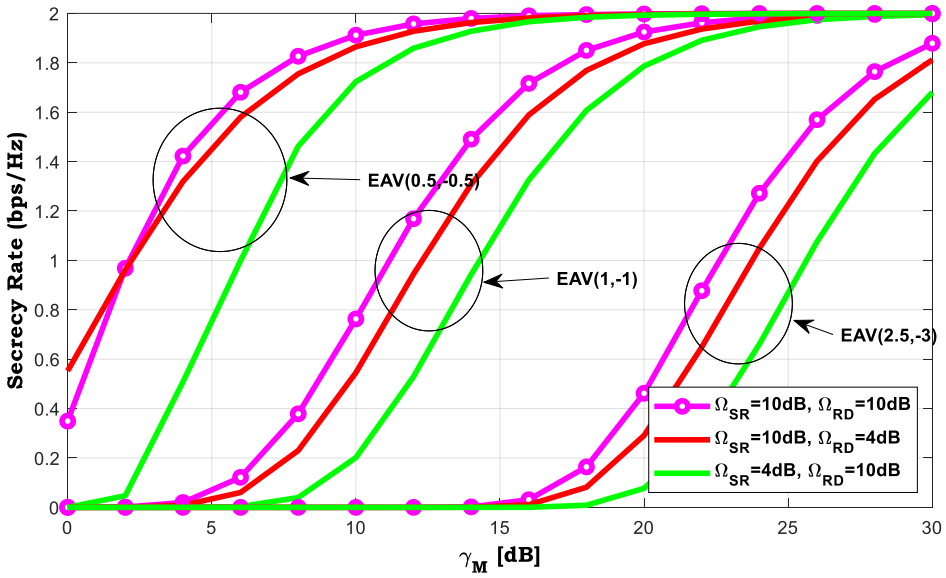

Fig. 3.11 SR versus Source Transmit Power for different values of channel mean power and position of EAV

Fig. 3.12 represents the effect of the power-splitting factor on SEE for HDAF protocol. When the splitting ratio is too small, only a limited amount of energy is harvested, and this directly affects the SEE performance. The SEE decreases as ρ increases from 0.1 to 0.9. For example, $\rho = 0.1$ means that 0.9 portion of the transmitted power from the relay will reach *D*, thus, SEE is maximum; while in case of $\rho = 0.9$, only 0.1 portion of the transmitted power from the relay will reach *D*, which implies that SEE is very less.

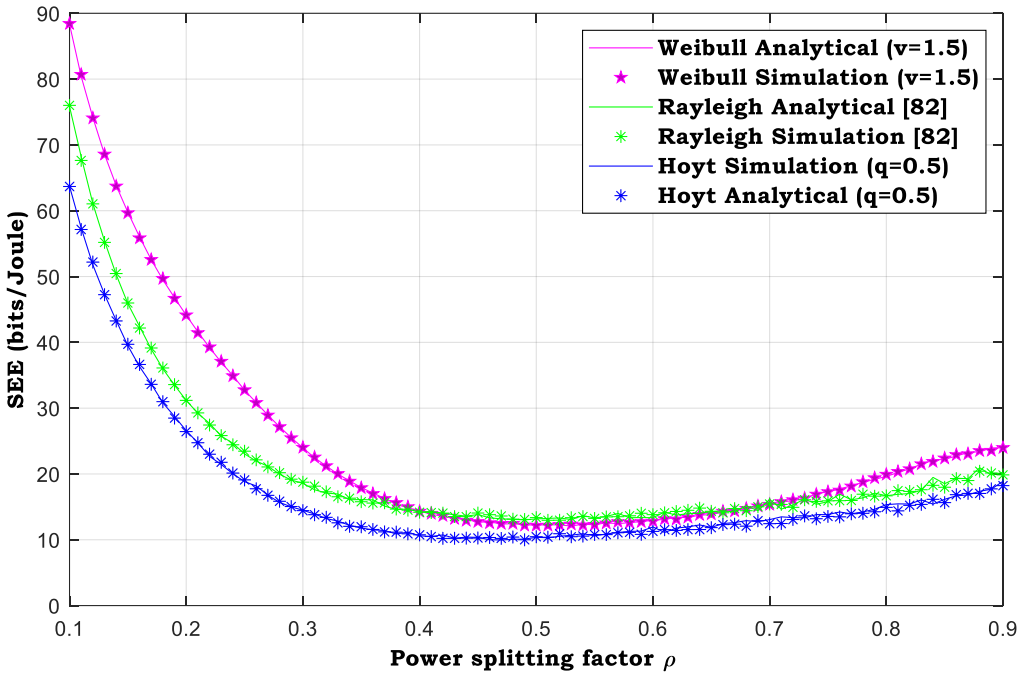

Fig. 3.12 Analytical and simulation results of SEE performance for HDAF Relay under different fading conditions

3.4.4 Critical Analysis

The comparative analysis of the proposed work with some other relevant existing works has been presented here through Table 3.3-3.8. The graphical and critical analyses presented here validate the supremacy of the proposed scheme over other relevant existing works.

Table 3.3 Comparison table of different relaying schemes for varying ρ

Parameter ρ	**SR in Rayleigh Fading Channel**			**% Improvement in SR**
	AF [73]	**DF [73]**	**HDAF [Proposed]**	
0.45	0.14	0.28	0.28	21.43 (DF)
0.55	0.175	0.28	0.35	48.5 (AF)
0.75	0.2	0.27	0.41	32.5 (DF)
0.8	0.21	0.25	0.4	50 (AF)

From Table 3.3, it is observed that AF Relay attains an SR value of 0.2 bps/Hz at $\rho = 0.8$; whereas, DF attains an SR value of 0.28 bps/Hz at $\rho = 0.45$ which is the optimal value for DF Relaying. At this point, SR value for HDAF rises up and at $\rho = 0.75$, HDAF relay attains the peak SR value of 0.4 bps/Hz. Thus, a performance boost is seen with respect to individual AF

and DF schemes. Simulation results show that secrecy rate for HDAF improves by about 32.5% and 50% respectively as compared to DF and AF protocol with the increased value of ρ . Further, it is worth remarking that compared to AF, HDAF relaying scheme enhances the SR by around 21.43% at $\rho = 0.55$ which gradually increases up to 32.5% at $\rho = 0.75$.Similarly, compared to DF, HDAF relaying scheme enhances the SR by around 48.5% at $\rho = 0.55$ which gradually increases up to 50% at $\rho = 0.75$.

Table 3.4 Comparison table of different relaying schemes at various channel variances

Channel Variances (in dB)	**SR (in bps/Hz)**		
$\sigma_{RD}^2 = 1$	**AF [76]**	**DF [76]**	**HDAF [Proposed]**
$\sigma_{RE}^2 = 10$	0.087	0.112	0.28
$\sigma_{RD}^2 = 10$	0.30	0.35	0.46
$\sigma_{RE}^2 = 1$			

Table 3.4, compares the SR for different relaying schemes at different channel variances. When $\sigma_{RE}^2 > \sigma_{RD}^2$, HDAF outperforms both AF and DF by about 68.92% and 60%; whereas, for $\sigma_{RE}^2 < \sigma_{RD}^2$, HDAF outperforms both AF and DF by about 53.33% and 23.9% respectively. Hence for both the cases, HDAF relaying scheme exhibits better performance than the other two schemes. It is further observed that for HDAF relaying, the percentage improvement in SR under the condition $\sigma_{RE}^2 < \sigma_{RD}^2$ is found to be 49.12% over the scenario $\sigma_{RE}^2 > \sigma_{RD}^2$.

Table 3.5 SR Comparison table of Hybrid CIoT network at varying ρ

Parameter	**SR in three types of Fading Channels**						
ρ	**Hoyt**			**Rayleigh**	**Weibull**		
	$q_e < q_m$	$q_e = q_m$	$q_e > q_m$		$v_e < v_m$	$v_e = v_m$	$v_e > v_m$
0.1	0	0	0.02	0	0.07	0	0
0.3	0.24	0.26	0.18	0.26	0.36	0.26	0
0.5	0.42	0.44	0.325	0.44	0.45	0.44	0.19
0.7	0.455	0.462	0.38	0.462	0.462	0.462	0.435
0.9	0.44	0.448	0.354	0.448	0.448	0.448	0.3

Table 3.6 SEE comparison table of Hybrid CIoT network at varying ρ

Parameter ρ	**SEE for HDAF (in bits/Joule)**		
	Hoyt	**Rayleigh [82]**	**Weibull**
0.1	63	77.3	89.6
0.3	14.1	22.8	24.1
0.5	10	12.9	13.2
0.7	12.4	15.4	15.5
0.9	18.6	24.5	24.5

Table 3.7 Comparison table of Hybrid CIoT network at varying P_S

Parameter P_S **(in dB)**	**SR for HDAF (in bits/Hz)**					
	Hoyt		**Rayleigh [66]**		**Weibull**	
	CR	CJ	CR	CJ	CR	CJ
-10	0	0	0.02	0.001	0.04	0.02
0	0.04	0.04	0.1	0.07	0.14	0.16
10	0.13	0.21	0.2	0.27	0.21	0.41
20	0.18	0.38	0.24	0.46	0.22	0.54
30	0.19	0.42	0.24	0.48	0.22	0.57

The statistical analysis of the proposed work along with other relevant existing works corresponding to Fig. 3.9(a) and Fig. 3.12 has also been presented through Table 3.8 and 3.9.

Table 3.8 Comparison of Standard Deviation in SR

(Taking $\rho = 0.5$ as mean for which SR=0.325 bits/Hz)

Parameter ρ	**Standard Deviation for SR (in bps/Hz)**		
	AF [76]	**DF [76]**	**HDAF**
0.2	0.3	0.075	0.315
0.4	0.195	0.05	0.1
0.6	0.145	0.048	0.03
0.8	0.125	0.074	0.075

Table 3.9 Comparison of Standard Deviation in SEE

(Taking $\rho = 0.5$ as mean for which SEE=13 bits/Hz)

Parameter ρ	**Standard Deviation for SEE (in bps/Hz)**		
	Weibull	**Rayleigh [82]**	**Hoyt**
0.2	31	17	15
0.4	1	1	3
0.6	2	0	1
0.8	7	3	1

3.5 INTERFERENCE-AIDED ENERGY HARVESTING IN UNTRUSTED SCENARIO

3.5.1 System Model

A wireless communication scenario in an IoT network has been considered here comprising of Source *S*, Destination *D*, Relay *R*, EAV and an Interferer *I*.

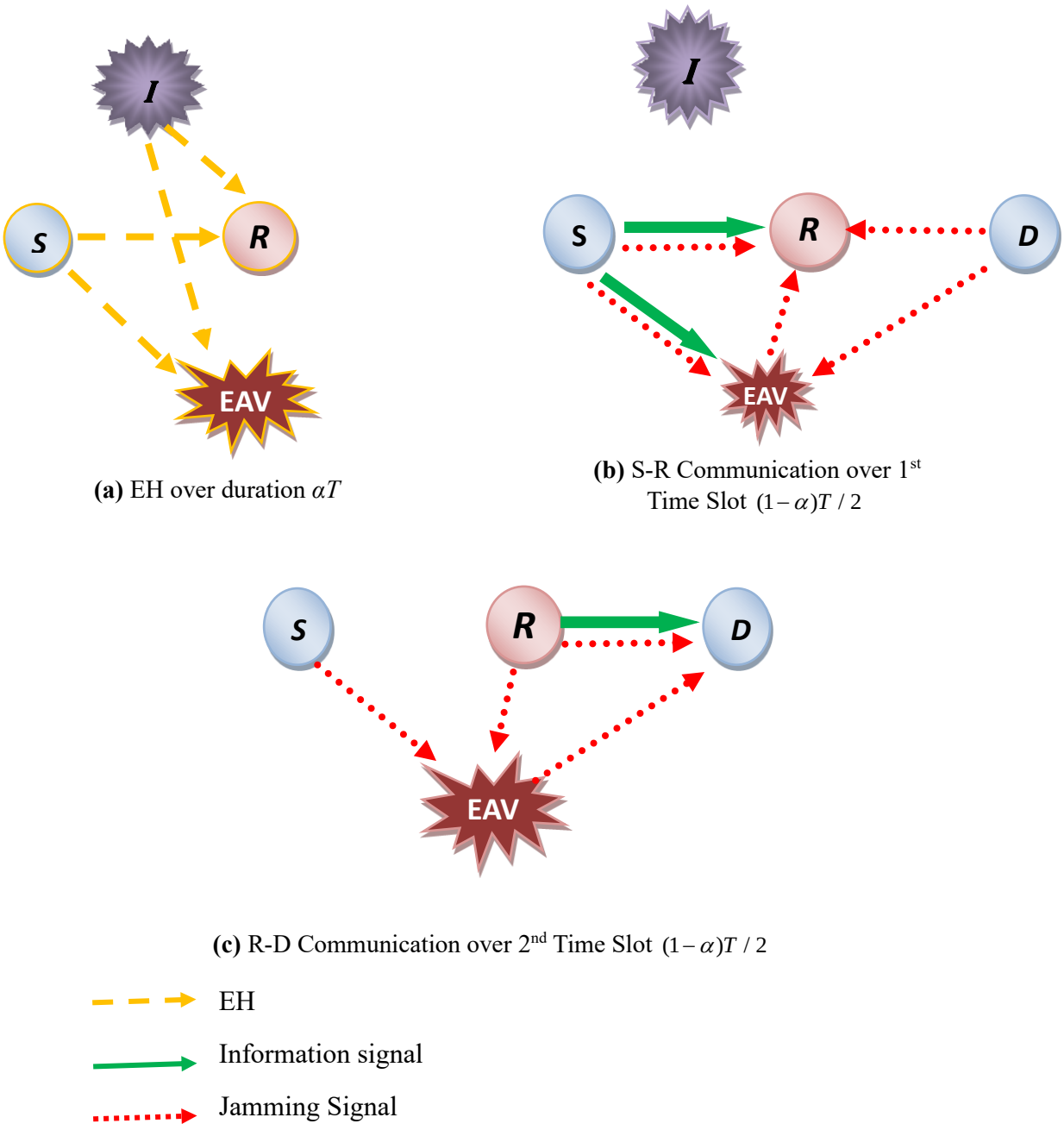

(a) EH over duration αT

(b) S-R Communication over 1st Time Slot $(1-\alpha)T/2$

(c) R-D Communication over 2nd Time Slot $(1-\alpha)T/2$

Fig. 3.13 System model

Such a configuration is highly relevant in smart healthcare systems, IIoT, or smart grid communications, where energy-efficient relaying and secure data transmission are essential. The relay node *R* is assumed to be energy-limited and may rely on RF-EH from the source or ambient interference. Meanwhile, the inclusion of an EAV models the threat of unauthorized access to sensitive data—common in open wireless environments—while the interferer *I* introduces realistic co-channel interference typically found in densely deployed IoT networks. The entire communication between *S* and *D* in presence of EAV is shown in Fig 3.13. The following assumptions are taken into account:

- The undesirable interference effect from *I* have been neglected.
- No direct link is present between the *S* and *D*.
- *R* and EAV harvest energy from signals transmitted by *S* and *I*.
- The battery capacity of *R* and EAV is infinite and they utilize this energy as the transmission power to forward information or send jamming signals to other nodes.
- All channel links are statistically independent and experience Rayleigh fading.

The fading channel coefficients of the links (e.g. $S \rightarrow R$, $R \rightarrow D$ etc.) are denoted by $h_{i,j}$ where i, j indicate channel nodes. The channel gains of these links are represented by $g_{i,j} = \left|h_{i,j}\right|^2$.We consider that there is a peak power constraint on the transmission of the nodes. i.e. the interference at the nodes is maintained below an interference threshold, I_{th} .

Following TSR Protocol [19], the entire communication time duration *T* is divided into three time slots: At EH time slot, *R* and EAV harvests energy from the signals received from *S* and *I* as shown in Fig. 3.17 (a); During 1st time slot, *S* transmits data to *R* which is received by EAV. At the same time *D* sends a jamming signal to the EAV which is known to *R* and received by it. Meanwhile, EAV sends a jamming signal to *R* by using the energy harvested in EH time slot. As the jamming signal is known, *R* separates it and entirely uses it for EH; c) In 2nd time slot, *S* sends a jamming signal to the EAV with full power *Ps* while *R* simultaneously transmits both the information signal and jamming signal to *D* and it separates the known jamming signal.

3.5.2 Mathematical modelling

The received signal power at EH slot (αT) for both *R* and EAV are given as:

$$y_{R_{\alpha T}} = \sqrt{P_S g_{SR} x_S} + \sqrt{P_I g_{SI} x_I} + N_R \tag{3.49}$$

$$y_{E_{\alpha T}} = \sqrt{P_S g_{SE} x_S} + \sqrt{P_I g_{EI} x_I} + N_E \tag{3.50}$$

The harvested energies at *R* and EAV are given as:

$$E_{HR1} = \eta(P_S g_{SR} + P_I g_{SI})\alpha T \tag{3.51}$$

$$E_{HE1} = \eta(P_S g_{SE} + P_I g_{EI})\alpha T \tag{3.52}$$

The transmitted powers at *R* and EAV based on harvested energy are given as :

$$P_{r_1} = \min(P_{R_1}, I_{th} / g_{SI}) \tag{3.53}$$

where $P_{R_1} = \dfrac{E_{HR1}}{(1-\alpha)(T/2)}$

and $P_{e_1} = \dfrac{E_{HE1}}{(1-\alpha)(T/2)}$ (3.54)

A. Energy Harvesting at *R* and EAV in 1st time slot

In 1st time slot, the signals received at *R* and EAV are represented by:

$$y_{SR_1} = \sqrt{\rho P_S g_{SR} x_{SI}} + \sqrt{\rho P_D g_{RD} x_{JD}} + \sqrt{\rho P_{e_1} g_{RE} x_{JE}} + N \tag{3.55}$$

$$y_{SE_1} = \sqrt{\rho P_S g_{SE} x_{SI}} + \sqrt{\rho P_D g_{RD} x_{JD}} + N \tag{3.56}$$

The amount of energies harvested at *R* and EAV in 1st time slot are represented by:

$$E_{HR2} = \eta\{\rho(P_S g_{SR} + P_D g_{RD} + P_{e_1} g_{RE})\}\frac{(1-\alpha)T}{2} \tag{3.57}$$

$$E_{HE2} = \eta\{\rho(P_S g_{SE} + P_D g_{DE})\}\frac{(1-\alpha)T}{2} \tag{3.58}$$

The transmitted powers by *R* and EAV after energy harvested in 1st time slot are:

$$P_{R2} = \frac{E_{HR2}}{(1-\alpha)(T/2)} \tag{3.59}$$

$$P_{e2} = \frac{E_{HE2}}{(1-\alpha)(T/2)} \tag{3.60}$$

B. Information Processing at *R* and EAV in 1st time slot

$$y_{SR}^{ip} = \sqrt{(1-\rho)P_S g_{SR} x_{SI}} + \sqrt{(1-\rho)P_D g_{RD} x_{JD}} + \sqrt{(1-\rho)P_{e_1} g_{RE} x_{JE}} + N \tag{3.61}$$

$$y_{SE}^{ip} = \sqrt{(1-\rho)P_S g_{SE} x_{SI}} + \sqrt{(1-\rho)P_D g_{RD} x_{JD}} + N \tag{3.62}$$

While processing the information, *R* removes the jamming term $(1-\alpha)T/2$

$$y_{SR}^{ip} = \sqrt{(1-\rho)P_S g_{SR} x_{SI}} + \sqrt{(1-\rho)P_{e_1} g_{RE} x_{JE}} + N \tag{3.63}$$

Thus, SINR at *R* in 1st time slot is given as:

$$\gamma_{SR} = \frac{(1-\rho)P_S g_{SR}}{(1-\rho)P_{e_1} g_{RE} + N} \tag{3.64}$$

and SINR at EAV in 1st time slot is given as:

$$\gamma_{SE} = \frac{(1-\rho)\,\mathrm{P}_S\, g_{SE}}{(1-\rho)P_D g_{RD} + N} \tag{3.65}$$

C. Information Processing at *D*, EAV in 2nd time slot

In 2nd time slot, the signal received at *D* is represented by:

$$y_{RD}^{ip} = \sqrt{P_{avg} g_{RD} x_I} + \sqrt{P_{avg} g_{RD} x_{JR}} + \sqrt{P_{e_2} g_{DE} x_{JE}} + N \tag{3.66}$$

$$y_{RD} = \sqrt{P_{avg} g_{RD} x_I} + \sqrt{P_{e_2} g_{DE} x_{JE}} + N \tag{3.67}$$

where $P_{avg} = \frac{P_{r_1} + P_{r_2}}{2}$ (3.68)

The total signal received at EAV in 2nd time slot is:

$$y_{RE} = \sqrt{P_S g_{SE} x_{JS}} + \sqrt{P_{avg} g_{RE} x_{JR}} + N \tag{3.69}$$

Thus, SINR at *D* in 2nd time slot is given as:

$$\gamma_{RD} = \frac{P_{avg} g_{RD}}{P_{e2} g_{DE} + N} \tag{3.70}$$

and SINR at EAV in 2nd time slot is given as:

$$\gamma_{RE} = \frac{P_{avg} g_{RE}}{P_S g_{SE} + P_{avg} g_{RE} + N} \tag{3.71}$$

The overall SNR of the legitimate channel is given by the expression:

$$\gamma_{SD} = \min(\gamma_{SR}, \gamma_{RD}) \tag{3.72}$$

The *EAV* uses Selection Combining technique to obtain the total SNR represented as:

$$\gamma_E = \max(\gamma_{SE}, \gamma_{RE}) \tag{3.73}$$

3.5.3 Calculation of SR

In this subsection, the SR at the main channel link (C_{SD}) and EAV link (C_E) are evaluated using the developed expressions of SINRs. The SR at main channel link is:

$$C_{SD} = \frac{1-\alpha}{2}\log_2(1+\gamma_{SD}) \tag{3.74}$$

and the rate of EAV link is:

$$C_E = \frac{1-\alpha}{2}\log_2(1+\gamma_E) \tag{3.75}$$

Thus the overall SR is given as:

$$C_{SEC} = [C_{SD} - C_E]^+ \tag{3.76}$$

$$= \frac{1-\alpha}{2}[\log_2(1+\gamma_{SD}) - \log_2(1+\gamma_E)]^+$$

$$= \frac{1-\alpha}{2}\left[\log_2\left(\frac{(1+\gamma_{SD})}{(1+\gamma_E)}\right)\right]^+ \tag{3.77}$$

where $[z]^+ = \max(z, 0)$

3.5.3 Results and Discussions

To assess the secrecy performance of the proposed system, a Matlab based simulation has been carried out. The following system parameters have been used for the purpose of simulation:

Table 3.10 Parameter Setting

Parameters	Meaning	Default Values
η	Energy Conversion Efficiency	0.8
α	EH coefficient	0.001
ρ	Power splitting coefficient	0.01
P_S	Source Transmit Power	10dBW
P_D	Destination Transmit Power	10dBW
P_I	Peak permissible Interference Transmit Power	20dB
m	Path loss exponent	3

In Figs. 3.14 and 3.15, simulation results are presented for the traditional DJ secure transmission scheme with the contrast scheme for comparison. The contrast scheme is denoted as non-interference jamming scheme [100] where *S* and *D* jams EAV and relays the confidential messages during the entire transmission period.

Fig 3.14 shows plot of SR versus α for both proposed and contrast scheme [100].

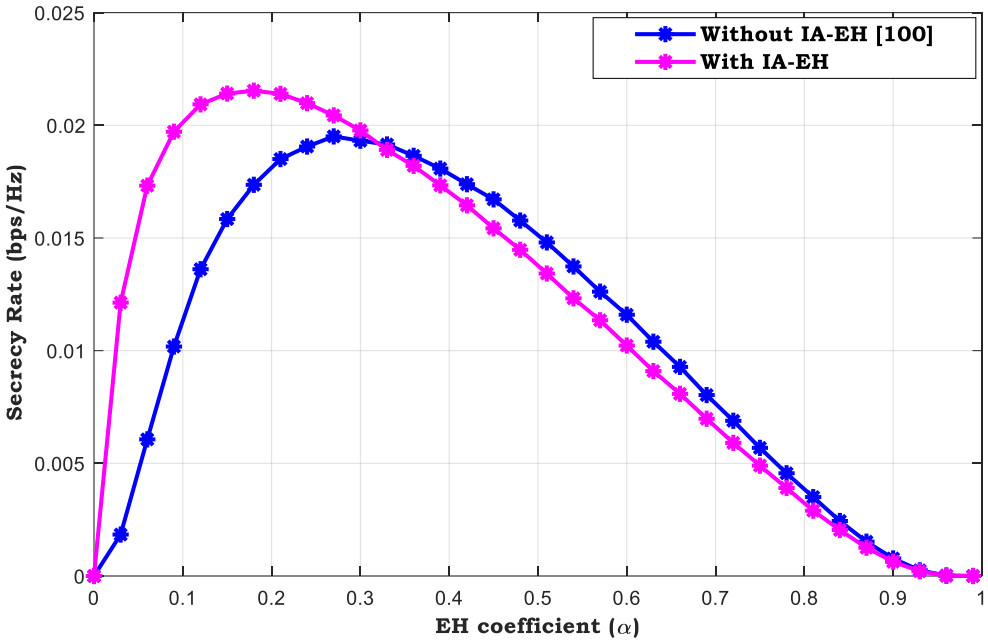

Fig. 3.14 SR versus α for both Proposed and Existing [100] scheme

It is observed that as α increases, SR also increases upto some optimal value of α . This is due to enhanced scope of EH for *R* (during EH slot) and thus, more energy is harvested which increases the information reception at *D*. After the optimal point, SR value decreases with the further increase in α. Because, increase in α reduces the channel capacity at *D* and increases channel capacity of EAV and thus, the SR plot decreases. For $\alpha = 0.15$, we obtain the maximum SR for IA-EH which is 0.022, whereas, the maximal value of secrecy for non-Interference scheme is 0.019 for $\alpha = 0.27$. For a particular value of $\alpha = 0.1$, the percentage improvement in SR of the proposed scheme over the existing scheme is 50%. Upto $\alpha = 0.32$, better secrecy is observed for IA-EH compared to its contrast part. Thus, better secrecy is observed for IA-EH scheme compared to non-interference scheme.

In Fig. 3.15, SR versus R_{th} is plotted for both the proposed and existing cases. It is observed that secrecy is maintained upto $R_{th} = 0.5$ in case of IA-EH; whereas, for contrast model, SR falls after $R_{th} = 0.34$ .Thus the proposed scheme guarantees better secrecy than its contrast part.

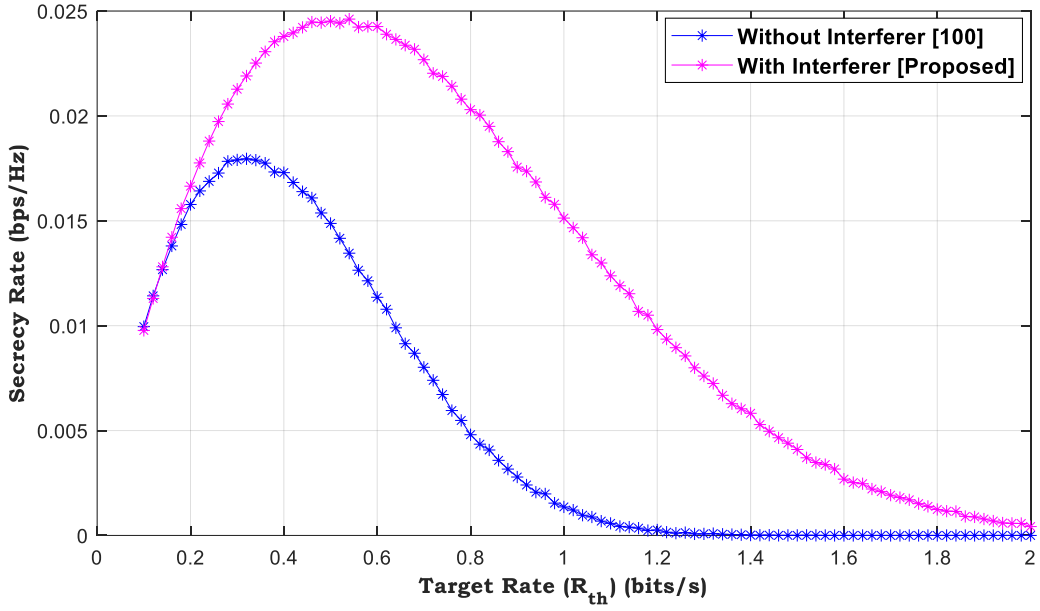

Fig. 3.15 SR versus R_{th} for both Interference and non-Interference Scenario

Fig. 3.16 shows the effect of power splitting factor ρ on SR under the hybrid scheme for several values of interference power. It is seen that with increase in ρ, EH at R increases. But at the same time EAV also scavenges energy. So C_E dominates over C_{SD} which causes SR to decrease. After a particular value, with further increase in ρ, power associated with information processing at R in 1st time slot decreases, which decreases SR further. The impact of one more parameter, i.e. P_I on SR has been depicted in this figure. Higher values of P_I allow the source and EH relay to transmit in a higher power in the network. This increases the main channel capacity which results in increase of SR. As P_I increases from 1 to 10 dB, the secrecy performance of the system improves until peak interference threshold is reached. At higher values of P_I i.e. beyond 5 dB, improvement in secrecy is minimal as the harvested energy from I to R becomes nearly constant.

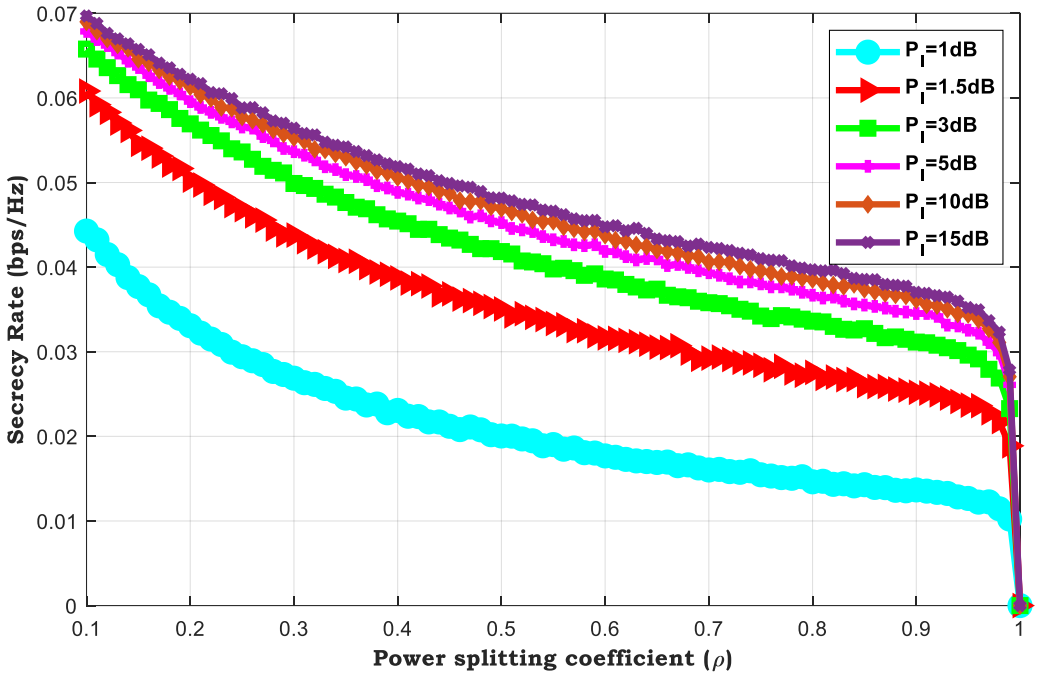

Fig. 3.16 Effect of ρ on SR for various values of P_I

3.6 OVERALL COMPARISON

A critical study and comparison of the above three works namely, Proposed Work 1, Proposed Work 2 and Proposed Work 3 presented in section 3.3, 3.4 and 3.5 respectively with some of the existing relevant state-of-art have been abridged in Table 3.11 and 3.12.

Table 3.11 Comparison table with existing relevant state-of-art

Existing/Proposed Works	Scenario	Protocol used	Scheme used	Fading channel	Performance metric
Existing Works					
[93]	RF harvesting from source only in presence of interferer	Hybrid TSR-PSR	DF	Rayleigh	Throughput
[66]	SNR based HDAF relaying cooperative network in presence of EAV	-	AF, DF & HDAF	Rayleigh	Ergodic Secrecy Capacity
[73]	Single hop relaying system with EH using Power Beacon in presence of EAV	TSR	DF and AF	Rayleigh	SC, EE

[67]	Secrecy performance evaluation of IIoT	-	DF	Weibull/ Rayleigh	SOP, SR
[74]	Cognitive cooperative AF network	-	AF	Rayleigh	EE
[100]	Two-hop untrusted relay network with OPA and EPA schemes	-	AF	Rayleigh	OP, SR
Proposed Works					
Proposed Work 1	*DF Relay Network with Interference-aided EH in absence of EAV*	*TSR*	*DF*	*Rayleigh*	*Throughput*
Proposed Work 2	*CIoT Network in interference-free environment in presence of EAV*	*HYBRID TSR/PSR*	*AF/DF/ HDAF*	*Rayleigh/Weibull/ Hoyt*	*SR, SEE*
Proposed Work 3	*CIoT Network with Interference-aided EH in presence of an EAV*	*HYBRID TSR/PSR*	*DF*	*Rayleigh*	*SR*

Table 3.12 Critical Analysis of the proposed works with existing works

Performance metric used	**Existing/Proposed works**	**Fading Channel**	**Maximum Throughput value (bps/Hz)**	**SR value (bps/Hz)**	**SEE value (bits/Joule)**
Throughput	[93]	Rayleigh	0.25	-	-
	Proposed Work 1		0.4		
Secrecy Rate (SR)	[66]	Rayleigh	-	CR:0.24 CJ:0.48	-
	Proposed Work 2	Hoyt		CR:0.19 CJ:0.42	
		Weibull		CR:0.22 CJ:0.57	
	[73]	Rayleigh	-	AF: 0.21 DF:0.25	-
	Proposed Work 2			HDAF: 0.4	
	[67]	Weibull	-	0.65	-
	Proposed Work 2	Rayleigh		0.62	
		Hoyt		0.48	
	[100]			0.019	
	Proposed Work 3			0.022	
System Energy Efficiency (SEE)	[194]	Rayleigh	0.2	-	77.3
	Proposed Work 2	Weibull	0.32		89.6
		Hoyt	0.18		63

3.7 DISCUSSION

This chapter presents a framework to evaluate the performance of RF-powered one-way single relay networks. Initially, the network throughput is analysed in terms of location of relay, position of interference and energy conversion efficiency of the proposed model 1. Next, in proposed model 2, an SNR-based HDAF scheme has been adopted for analysing the security of CIoT network under dissimilar fading scenarios. Here, the advantages of using a Beacon-aided RF-EH technique are discussed for CIoT network that uses an SNR-based HDAF for maximizing SR and obtaining higher SEE under dissimilar fading environments. Also, it can be observed that severe fading over desired link provides more secure communication over main link. Comparative study of all the fading models shows that weibull fading gives better secrecy and higher energy efficiency than the other fading models. Also, the effect of fading parameters on the SEE performance for HDAF relay has been investigated. Our next model incorporates DBJ technique to increase the system security in the presence of *I* where we have analyzed the beneficial effects of harvesting energy from Interferer in the presence of EAV. By incorporating interferer into the network, the SR of the system is effectively enhanced as compared to non-interferer environment. The study also provides a benchmark on the maximum amount of interferer power that can be harvested so as to maximize the security performance.

Chapter 4

RF ENERGY HARVESTING IN ONE-WAY MULTI-RELAY NETWORKS

4.1 OVERVIEW

The performance analysis of one-way single relay cooperative network was presented in Chapter 3. In continuation with this work, the present chapter focuses on the performance analysis of multi-relay cooperative network where new relay selection schemes are proposed to enhance the throughput and secrecy of the relay networks. In the first instance, two Relay-Selection (RS) schemes namely, Maximum Energy Accumulated (MEA) and Optimal Relay Maximization (OPT) have been presented. In the next section, a generalized IA-EH cooperative network has been designed under Weibull faded environment, where the performance of the system has been studied in terms of throughput and Outage Probability (OP) for various cooperation protocols such as, DF, AF and HDAF. In addition, the throughput of the network has been optimized with respect to the EH fractions of the Hybrid TSR–PSR protocol. Moreover, the OP and throughput performance the proposed network have been studied with respect to a number of system parameters. Lastly, a best-node scheduling technique has been proposed to enhance the system secrecy performance against multiple EAV attack using a friendly jammer.

4.2 BACKGROUND

In wireless cooperative networks, several intermediate relay nodes are available to assist the communication between a pair of data source and destination. Since these nodes have different locations, each transmitted signal from source to destination passes through different paths causing different attenuations within the signals received at the destination. This in turn results in reducing the overall system performance. To minimize this effect, designing of proper relaying strategy is highly necessary so that high-quality links can be chosen. The authors in

[58] have studied a comparison among three RS schemes namely: (i) OPT-RS scheme (ii) MHE-RS scheme and (iii) Minimum Self-Interference (MSI) RS scheme. Here, the effect of various parameters on throughput and OP has been studied. However, analysis is limited to a single source with a single antenna and no analysis has been carried out for a multi-source multi antenna system. With this motivation, RS in multi-source multi-antenna CR Network with RF-EH has been studied, where MEA-RS and OPT-RS schemes have been explored in an ideal interference-free environment. Two RS methods, PRS and ORS have been introduced in [33] where they have used the Rician fading channel to evaluate the OP. [45] have used TSR protocol to facilitate RF-EH in CSS, which shows that OAF relaying outperforms PRS and RRS for two or more number of relays. In [192], the multiple UAV relay-assisted networks using EH have been investigated to avoid large-scale fading from source to destination**.** An analytical expression of ASER is derived in [193] over Fluctuating Two Ray (FTR) fading channel considering multi-hop detect & forward and AF relaying. In [194], a vehicle-to-vehicle communication model has been employed in an FD EH system. The ergodic capacity has been evaluated and compared with the stationary nodes. The effect of residual self-interference on ergodic capacity has been shown. To keep the source information secure from an EH untrusted relay node, the DBJ technique has been used in [196] where they derived analytical expressions for SC and intercept probability to evaluate the secrecy performance of the system. BER for dual-hop AF and DF are analytically derived for both TS and PS relaying protocols in [195]. System optimization is also performed to maximize the BER performance. In this regard, a generalized RF-EH framework with hybrid TSR-PSR protocol for AF, DF and HDAF relaying schemes has been developed under the Weibull fading channel. Here, an optimization process has been applied with respect to the EH fractions. The mathematical expressions for AF, DF and HDAF modes have been derived systematically. Mainly, Rayleigh, Exponential and Gamma distributions have been modelled using Weibull distribution by varying the scale and shape parameters, which shows the flexibility of this fading channel. In the last section of this chapter, the security performance in multi-relay network has been evaluated. One of the novel aspects of the proposed work is the investigation of the secrecy performance of CR network with a friendly jammer and multiple EAVs who attempt to wiretap the communications between the EH relay nodes and BS.

4.3 RELAY SELECTION IN INTERFERENCE-FREE SCENARIO

In this section, a multi-antenna multi-relay network along with its mathematical representation and results have been described in details.

4.3.1 System model for Relay Selection in interference-free environment

The system model shown in Fig 4.1 is a DF relay network consisting of *L* number of Source nodes $S_1, S_2, ..., S_L$ each having *W* number of antennas, one Destination node *D* with a single antenna and *N* number of Relay nodes $R_1, R_2, ..., R_N$, each with two antennas following accumulate-and-forward scheme. This architecture is particularly relevant for cluster-based or multi-source IoT environments, such as smart agriculture, distributed industrial monitoring, or environmental sensing, where multiple sensor nodes need to transmit data reliably to a central destination. The use of multiple antennas at the sources enables spatial diversity, improving the reliability of transmission under fading conditions. Meanwhile, the relay nodes act as energy-aware intermediaries that accumulate incoming data and forward it selectively, based on their energy availability or channel quality—making this approach well-suited for energy-constrained, low-power deployments. The relevant assumptions are as follows:

- A Rayleigh fading channel is employed.
- Power is generated at the relays through EH which takes place through TSR protocol [19].
- Each relay is subjected to AWGN, with mean = 0 and variance = N_0. Each source transmits with the same power p_s, while each relay transmits with a power p_{r_i} (i=1,…,*N*).

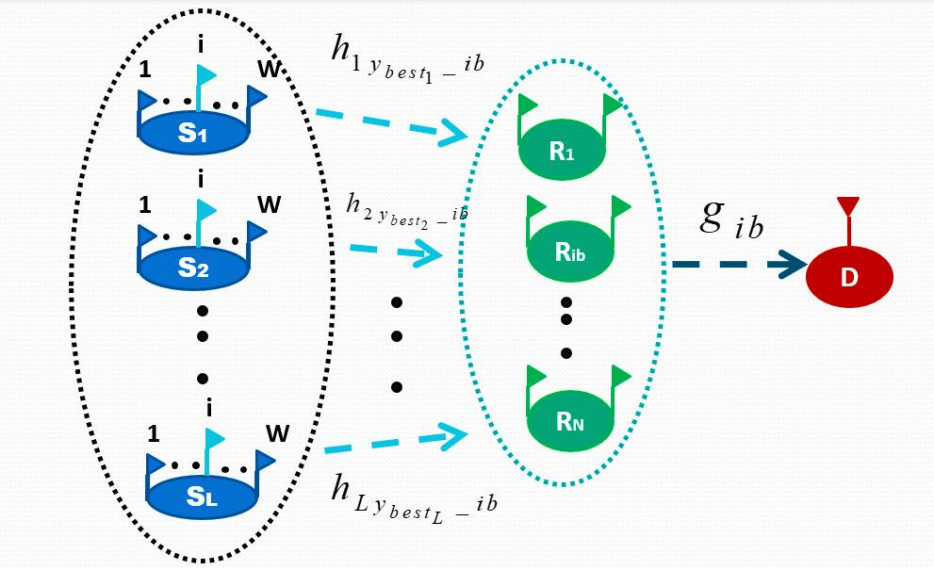

Fig. 4.1 System Model

4.3.2 Mathematical Modelling

Let us assume two sets: $h = \{h_{xyi}, x = 1,\ldots,L; y = 1,\ldots,W \text{ and } i = 1,\ldots,W\}$ and $g = \{g_i, i = 1,\ldots,N\}$. These sets represent the channel coefficients for *S* to *R*, and *R* to *D* transmission. Hence, the power gains for these channels would be $|h|^2$ and $|g|^2$, which are random variables subject to exponential distribution with mean Ω_{hxi} and Ω_{gi} respectively. Here, $\Omega_{hxi} = d_{1xi}^{-m}$ and $\Omega_{gi} = d_{2i}^{-m}$, where d_{1xi} represents distances between the source nodes and the different relay nodes, d_{2i} represents distances between the different relay nodes and *D*, and *m* is the path loss exponent. For simplicity, it has been assumed that $d_{1xi} = d_1$ and $d_{2i} = d_2$, for all *x* and *i*. Therefore, $\Omega_{hxi} = \Omega_h = d_1^{-m}$ and $\Omega_{gi} = \Omega_g = d_2^{-m}$.

➢ Selection Protocols

❒ *Source antenna selection:*

The best source antenna is selected on the basis of *S*-to-*R* SNR link which is expressed as:

$$y_{best_x}: \max_{y=1,\ldots,W} \left(\gamma_{x,r}^{i}\right) \tag{4.1}$$

where $x \in \{1, 2, \ldots, L\}$ and $i \in \{1, 2, \ldots, W\}$

❒ *Relay Selection (RS) schemes:*

The next step is relay selection. Here, it is assumed that the relays have been provided with storage facility (in the form of appropriate battery), to accumulate the energy from the signals

from all the sources that are transmitting, one after the other. After the signals have been received from all the sources, and energy has been accumulated, transmission takes place from *R* to *D*. For RS, following two protocols are used:

- ***Maximum Energy Accumulating Relay Selection (MEA-RS)***

Here, that relay is selected which can accumulate the highest amount of energy through harvesting during the transmission process.

$$i\_b: \max_{i=1,\ldots,N}\left(\sum_{x=1}^{L}\left|h_{xy_{best_x}i}\right|^2\right) \tag{4.2}$$

Here, i_b is calculated for a particular value of x, and subsequently y_{best_x} is also calculated for that particular value of x.

- ***Optimal Relay Selection (OPT-RS)***

In this scheme, the end-to-end SNR (γ_{e2e}) is maximized.

$$i\_b: \max_{i=1,\ldots,N}(\gamma_{e2e}^{i}) \tag{4.3}$$

➢ SNR Calculation

Received signal at the relays is given by:

$$Y_i = \left(\sqrt{p_s}h_{xy_{best_x}i}X_x(t)\right) + n_{r_i}(t) \tag{4.4}$$

where, $X_x(t)$ is the signal transmitted from the source node x and $n_{r_i}(t)$ is the AWGN at relay node *i*. Therefore, energy harvested at the relay for this particular received signal is given by:

$$E_i = \sum_{x=1}^{L}\eta p_S\left|h_{xy_{best_x}i}\right|^2 \alpha T \tag{4.5}$$

where, $0 \leq \alpha$ and $\eta \leq 1$. Here, α is the EH-coefficient and η is the energy conversion efficiency. Moreover, x varies from 1 to L, and for each value of x, there is a single y_{best_x} determined from source antenna selection as given in (4.1). Accordingly, MEA relay selection is adopted on the basis of accumulated energy. This energy is then used for transmitting the signal. So, transmitting power of relay is given by p_{r_i}. Again, DF scheme is employed at the relay nodes. The decoded received signal $X_{r_i}(t)$ is given by:

$$X_{r_i}(t) = \overline{X_s}(t - t_0) \tag{4.6}$$

where, t_0 represents circuit processing delay, which is assumed to be very small, compared to the entire block time.

Next, the received signal at *D* is given by:

$$Y_d(t) = \sqrt{p_{r_i}} g_i X_{r_i}(t) + n_d(t) \quad (4.7)$$

where, $n_d(t)$ is the AWGN at the destination node. Based on the above equations, the SNR received for S-R transmission is given by:

$$\gamma_{x,r}^{i} = \gamma_x \left| h_{xy_{best_x}i} \right|^2 \quad (4.8)$$

Similarly, for received signal at *D*, the SNR is expressed as:

$$\gamma_{r,d}^{i} = 2\mu\gamma_x \left| h_{xy_{best_x}i} \right|^2 |g_i|^2 \quad (4.9)$$

Here, $\gamma_x = p_s/N_0$ and $\mu = \eta\alpha/(1-\alpha)$. Finally, the end-to-end SNR is calculated as:

$$\gamma_{e2e}^{i} = min(\gamma_{x,r}^{i}, \gamma_{r,d}^{i}) \quad (4.10)$$

➢ OP and Throughput Analysis

Suppose R_S is the source transmission rate. To ensure reliable communication, considering B =1 Hz, from Shannon-Hartley theorem, R_S can be expressed as:

$$R_S = \log_2(1+\gamma_{th}) \quad (4.11)$$

Thus, $\gamma_{th} = 2^{R_S} - 1$ (4.12)

Now, the OP is calculated as:

$$P_{out} = P(\gamma_{e2e}^{i\_b} < \gamma_{th}) \quad (4.13)$$

For DL mode of transmission, throughput τ is computed as :

$$\tau = ((1-\alpha)(1-P_{out})R_S)/2 \quad (4.14)$$

4.3.3 Results and Discussions

The proposed model has been simulated using MATLAB Version R2018a and the results of simulations have been presented in this section. The distances d_1 and d_2 are normalized to unit value. For simplicity, the mean values of the exponential random variables $|h|^2$ and $|g|^2$ which are designated as λ_h and λ_g respectively, are set to 0.3 and path loss exponent *m* is taken as 3. The setting of remaining parameters related to simulation has been made according to Table 4.1.

Table 4.1 Simulation Parameters

Symbol	Name	Values
η	Energy conversion efficiency	0.5
γ_{th}	SINR threshold	7 dB [58]
α	EH coefficient	0.25
N	No. of relay nodes	5
L	No. of source nodes	6
W	No. of antennas	7
γ_x	SNR of Source	22 dB
R_S	Source transmission rate	0.3 bps/Hz [58]

The variation of throughput with EH ratio-α has been shown in Fig. 4.2. Here, **MS** corresponds to multi-source and **SS** denotes single source. From above figure, it is observed that the OPT-RS (MS) scheme outperforms the MEA-RS (MS) scheme. This is because in OPT-RS, the best γ_{e2e} is selected which is directly related to decrease in outage much quicker than the case of MEA-RS, where the relay selected is made on the basis of energy accumulated. Also, it is found that the OPT-RS Multi Source (MS) and MEA-RS (MS) schemes outperform the SS schemes in terms of throughput for all values of α. This is because in case of MS schemes, both $\gamma_{x,r}$ and $\gamma_{r,d}$ have a higher value as compared to SS schemes as concluded from the mathematical description of the model.

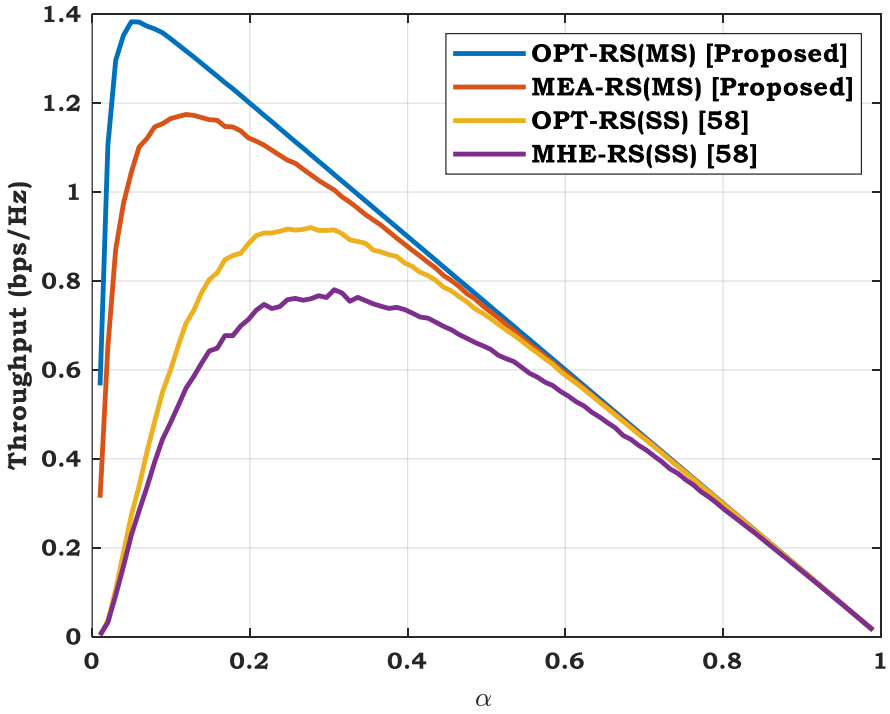

Fig. 4.2 Throughput versus the EH ratio-α with N= 3, γ_x = 22 dB, R_S = 0.3 bps/Hz

The quantitative analysis of Fig. 4.2 has been summarized in Table 4.2 where the proposed work i.e. MS scheme has been compared with the existing models OPT-RS (SS) and MHE-RS (SS) of [58].

Table 4.2 Quantitative Analysis of Throughput

Measured Quantities	**Schemes**	α		
		0.1	0.2	0.3
Throughput (bps/Hz)	**OPT-RS(MS)**	1.345	1.202	1.054
	MEA-RS(MS)	1.165	1.121	1.015
	OPT-RS(SS)	0.598	0.883	0.913
	MHE-RS(SS)	0.480	0.713	0.762
Percentage Improvement In throughput	**OPT-RS(MS) OVER OPT-RS(SS)**	55.5	26.5	13.3
	OPT-RS(MS) OVER MHE-RS(SS)	64.3	40.6	27.7
	OPT-RS(MS) OVER MEA-RS(MS)	13.3	06.7	03.7
	MEA-RS(MS) OVER OPT-RS(SS)	48.6	21.2	10.0
	MEA-RS(MS) OVER MHE-RS(SS)	58.7	36.3	24.9

The variation of throughput with SNR has been shown in Fig. 4.3. It is seen that the curves are increasing for smaller values of γ_x and then saturates or converges at higher values of γ_x. This is because, with the increase in source SNR, $\gamma_{x,r}$ and $\gamma_{r,d}$ also increases. From (4.11), it is seen that the probability that γ_{e2e} falls below γ_{th} is decreased which in turn decreases the possibility of outage and hence increases the throughput. It is also found that the OPT-RS (MS) scheme saturates at a much lower value of γ_x=15dB, followed by MEA-RS (MS) at γ_x=25dB, OPT-RS (SS) at γ_x= 30dB, and MHE-RS (SS) at γ_x=40dB. In addition, the plot shows that the OPT-RS (MS) scheme reaches the saturation much faster than the MEA-RS (MS) scheme. This is because in OPT-RS(MS), the best γ_{e2e} is selected compared to the case of MEA-RS (MS), where the relay selection is made on the basis of maximum energy accumulated. Also, it is observed that the MS schemes reach saturation level quicker than the SS schemes. This is because γ_{e2e} increases at a faster rate in case of MS scheme as a greater number of selections are incorporated. The variation of throughput with the number of relay nodes has been

illustrated in Fig. 4.4. It is found that the OPT-RS (MS) scheme outperforms all other relay selection techniques. The observation implies that on increasing the value of *N*, the probability of $\gamma_{e2e}^{i\_b}$ of the selected relay to be greater than γ_0 increases which increases the throughput.

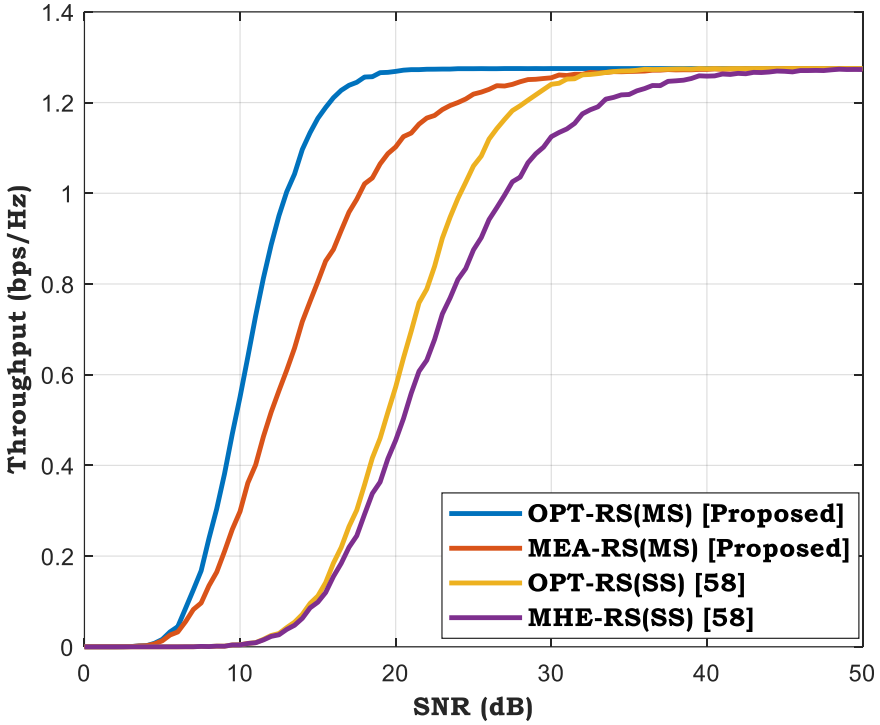

Fig. 4.3 Throughput versus SNR with α=0.25, N=3, R_S = 0.3 bps/Hz

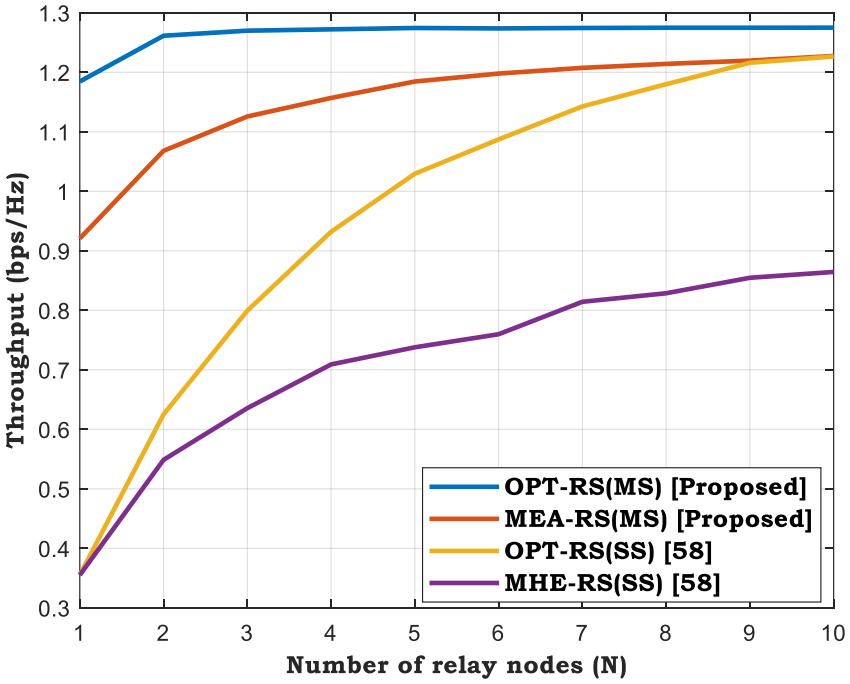

Fig. 4.4 Throughput versus number of relay nodes-N with α=0.25, $\gamma_{x=}$ 22 dB, R_S = 0.3 bits/sec/Hz.

4.4 RELAY SELECTION IN INTERFERENCE-LIMITED SCENARIO

4.4.1 System model

Fig. 4.5 shows a cooperative multi-relay assisted communication network consisting of source node *S*, multiple EH relay nodes $R_j(j = 1, 2, 3, \dots n)$, each affected by a single interferer, and a terminal node *D*. Each relay node is subject to interference from a distinct, single interferer. The relays operate under an RF energy harvesting paradigm, where they extract energy from the received RF signals—both intended and interfering—to power their cooperative forwarding operations. This model is particularly applicable to energy-constrained IoT environments, such as smart cities, remote infrastructure monitoring, and environmental sensing networks, where deploying or recharging batteries is impractical. The presence of distributed interference reflects realistic wireless conditions in dense urban or industrial deployments, where spectrum reuse and coexistence are common.

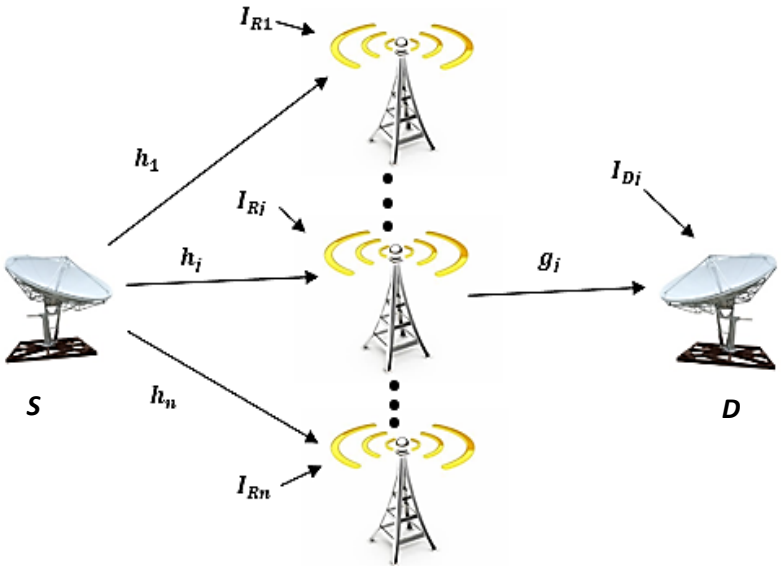

Fig. 4.5 System model

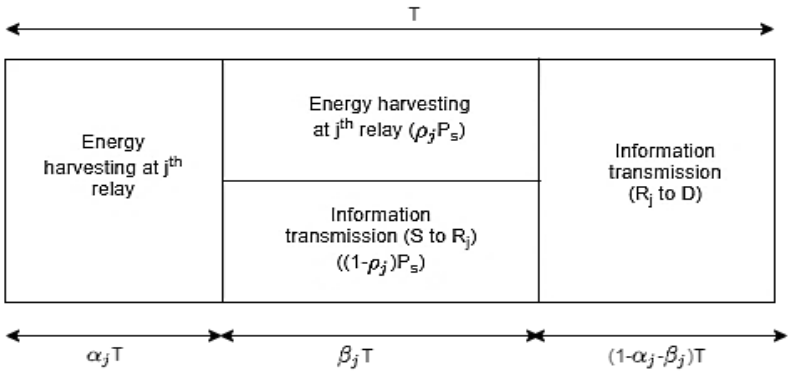

Fig. 4.6 Time frame structure of the system

In the first phase, *S* transmits signal to the selected relay node R_j, which is selected as the best relay based on SINR maximization criterion. Here, ORS strategy has been implemented, where the best relay among *n* relays is chosen on the basis of the SINR value of source to relay and relay to destination links. In the second phase, the energy is harvested in the relay node and in the third phase, the terminal node receives the signal from the selected relay R_j and decodes the received signal. The following assumptions have been considered:

- Here, the communication between source and destination is prone to blockage by physical structures. To reduce this effect, an energy harvesting communication using multi relay is considered.
- The impact of a single interferer on the relays and destination is considered.
- All relay nodes are considered similar in nature.
- The communication mode is taken as HD.

The channel between source and relay has been modelled with Weibull distribution having gain h_j, where the j^{th} relay gets affected by AWGN n_{jRa} and interference signal of power I_{Rj}. An additional noise n_{jRc} is added at the relay which is generated due to conversion or sampling of the signal. In Fig. 4.6, *T* is the total time for EH and information transmission in which the energy is harvested into two separate parts: α_j^{th} fraction of time is used for energy harvesting with efficiency η_{Tj} and for the next β_j^{th} fraction of total time, the total power P_s is divided into two portions: ρ_j of the total transmitted power is used for EH with efficiency η_{Pj} and $1-\rho_j$ of the total transmitted power is used for information transmission. The total harvested energy and power are E_{hj} and P_{jR} respectively. After relay selection, the signal is transmitted from the

selected j^{th} relay to the destination following Weibull distribution with gain g_j. Here, the transmitted signal gets affected by AWGN n_{Dj} and an interference signal of power I_{Dj}.

4.4.2 Mathematical Modelling

This section depicts the mathematical analysis of the proposed scheme. As depicted in figure, the signal $\sqrt{P_s}\, s(t)$ is transmitted from the source with power P_s and normalized signal $s(t)$ with $E(|s(t)|^2) = 1$. A Gaussian noise $n_{jRa} \sim N(0, \sigma_{jRa}^2)$ is introduced in the j^{th}receiver antenna; h_j is the weibull channel gain with $h_j \sim weibull(k_{hj}, \lambda_{hj})$ for j^{th}channel between source and relay; L_{1j} is the loss factor for j^{th} channel. The total interference power at relay *j* is I_{Rj} with normalized signal $s_{jR}(t)$, i.e., $E(|s_{jR}(t)|^2) = 1$. Accordingly, the corrupted signal at j^{th} relay is shown in (4.15).

$$y_{SRj}(t) = \frac{h_j\sqrt{P_s}\, s(t)}{L_{1j}} + \sqrt{I_{Rj}} s_{jR}(t) + n_{jRa} \tag{4.15}$$

This relay uses $(1 - \rho_j)$ portion of power for receiving the transmitted signal. Considering a Gaussian noise $n_{jRc} \sim N(0, \sigma_{jRc}^2)$, the converted signal at j^{th} relay is shown in equation (4.16).

$$y_{SRj} = \sqrt{(1-\rho_j)}[\frac{h_j\sqrt{P_s}\, s}{L_{1j}} + \sqrt{I_{Rj}} s_{jR} + n_{jRa}] + n_{jRc} = \frac{h_j\, s}{L_{1j}}\sqrt{(1-\rho_j)P_s} + \sqrt{(1-\rho_j)I_{Rj}} s_{jR} + n_{jR} \tag{4.16}$$

The 1st part of the above equation corresponds to 'Signal' and the 2nd part represents 'Noise'.

where, $n_{jR} = \sqrt{(1-\rho_j)} n_{jRa} + n_{jRc}$ (4.17)

and $n_{jR} \sim N\left(0, \left(1-\rho_j\right)\sigma_{jRa}^2 + \sigma_{jRc}^2\right)$ is the total Gaussian noise at signal y_{SRj}.

The harvested energy and power at relay '*j*' are shown in equations (4.18) and (4.19) respectively.

$$E_{hj} = \left(\eta_{Tj}\frac{|h_j|^2}{L_{1j}^2} P_s \alpha_j T + \eta_{Pj}\frac{|h_j|^2}{L_{1j}^2} P_s \rho_j \beta_j T\right) + \left(\eta_{Tj} I_{Rj} \alpha_j T + \eta_{Pj}\rho_j I_{Rj}\beta_j T\right)$$

$$= \left(\frac{|h_j|^2}{L_{1j}^2} P_s + I_{Rj}\right)(\eta_{Tj}\alpha_j + \eta_{Pj}\rho_j\beta_j)T \tag{4.18}$$

$$P_{jR} = \frac{E_{hj}}{T(1-\alpha_j-\beta_j)} = \frac{P_s(\eta_{Tj}\alpha_j + \eta_{Pj}\rho_j\beta_j)}{L_{1j}^2(1-\alpha_j-\beta_j)}\left(|h_j|^2 + \frac{L_{1j}^2 I_{Rj}}{P_s}\right) = K_j\left(|h_j|^2 + U_j\right) \tag{4.19}$$

where, $K_j = \frac{P_s(\eta_{Tj}\alpha_j+\eta_{Pj}\rho_j\beta_j)}{L_{1j}^2(1-\alpha_j-\beta_j)}$and $U_j = \frac{L_{1j}^2 I_{Rj}}{P_s}$.

The received SINR at j^{th} relay is formulated as:

$$\gamma_{SRj} = \frac{|h_j|^2(1-\rho_j)P_s}{L_{1j}^2[(1-\rho_j)\sigma_{jRa}^2+\sigma_{jRc}^2+(1-\rho_j)I_{jR}]} = \frac{(1-\rho_j)|h_j|^2 P_s}{L_{1j}^2[\sigma_{jR}^2+(1-\rho_j)I_{jR}]} = P_j|h_j|^2 \quad (4.20)$$

where, $P_j = \frac{(1-\rho_j)P_s}{L_{1j}^2[\sigma_{jR}^2+(1-\rho_j)I_{jR}]}$ and $\sigma_{jR}^2 = (1-\rho_j)\sigma_{jRa}^2 + \sigma_{jRc}^2$

Depending upon different protocol modes, SINR of DF, AF and Hybrid AF-DF protocols are analyzed:

- **DF Protocol**

In DF protocol, the signal $\sqrt{P_{jR}}S_j{}'$ is transmitted from j^{th} relay with power P_{jR} and normalized signal $S_j{}'$, i.e.,$E(|S_j{}'|^2) = 1$. A Gaussian noise $n_{Dj}{\sim}N(0, \sigma_{Dj}^2)$ is introduced at the destination node. Here, g_j is the weibull channel gain with $g_j{\sim}weibull(k_{gj}, \lambda_{gj})$. Total interference power at the destination is I_{Dj} with normalized signal $S_{Dj}{}'$, i.e., $E(|S_D{}'|^2) = 1$. Then, the received signal at the destination from *j-th relay* is given in (4.21) which is divided into signal and noise parts.

$$y_{RDj} = \frac{g_j\sqrt{P_{jR}}S_j{}'(t)}{L_{2j}} + \sqrt{I_{Dj}}S_{Dj}{}' + n_{Dj} \quad (4.21)$$

From the above equation, the expression of destination SINR for the DF protocol is shown below:

$$\gamma_{RDj} = \frac{|g_j|^2 P_{jR}}{L_{2j}^2(\sigma_{Dj}^2+I_{Dj})} = \frac{|g_j|^2}{L_{2j}^2(\sigma_{Dj}^2+I_{Dj})}.K_j(|h_j|^2 + U_j) = Q_j(|h_j|^2 + U_j)|g_j|^2 \quad (4.22)$$

where, $Q_j = \frac{K_j}{L_{2j}^2(\sigma_{Dj}^2+I_{Dj})}$

- **AF Protocol**

In AF mode, the transmitted signal from j^{th} relay is given as:

$$x_{Rj} = \frac{\sqrt{P_{jR}}y_{SRj}}{\sqrt{\frac{(1-\rho_j)P_S|h_j|^2}{L_{1j}^2}+(1-\rho_j)I_{Rj}+\sigma_{Rj}^2}} \tag{4.23}$$

where, $\sqrt{\frac{(1-\rho_j)P_S|h_j|^2}{L_{1j}^2}+(1-\rho_j)I_{Rj}+\sigma_{Rj}^2}$ is the power normalization factor for the j^{th}relay and x_{Rj} is the transmitted signal from j^{th} relay.

The received signal at the destination due to j^{th} communicating relay is given by:

$$y_{RDj} = \frac{g_j x_{Rj}}{L_{2j}^2} + \sqrt{I_{Dj}}S_{Dj}{}' + n_{Dj} = \frac{\frac{g_j\sqrt{P_{jR}}y_{SRj}}{L_{2j}}}{\sqrt{\frac{(1-\rho_j)P_S|h_j|^2}{L_{1j}^2}+(1-\rho_j)I_{Rj}+\sigma_{Rj}^2}} + \sqrt{I_{Dj}}S_{Dj}{}' + n_{Dj} \tag{4.24}$$

The simplified version of the above equation is framed as:

$$\gamma_{RDj} = \frac{a|g_j|^2|h_j|^4+b|g_j|^2|h_j|^2}{c'|h_j|^2+d'|g_j|^2|h_j|^2+e'|g_j|^2+f'} \tag{4.25}$$

where, $a = \frac{P_S.K_j(1-\rho_j)}{L_{1j}{}^2L_{2j}{}^2}$ $\quad b = \frac{P_S.K_j.U_j(1-\rho_j)}{L_{1j}{}^2L_{2j}{}^2}$ $\quad c' = \frac{(1-\rho_j)P_S\left(I_{Dj}+\sigma_{Dj}^2\right)}{L_{1j}{}^2}$

$d' = \frac{\left((1-\rho_j)I_{Rj}+\sigma_{Rj}^2\right).K_j}{L_{2j}{}^2}$ $\quad e' = \frac{\left((1-\rho_j)I_{Rj}+\sigma_{Rj}^2\right).K_j.U_j}{L_{2j}{}^2}$

$f' = \left((1-\rho_j)I_{Rj}+\sigma_{Rj}^2\right)\left(I_{Dj}+\sigma_{Dj}^2\right)$

- **HDAF Protocol**

In the HDAF protocol, the SINR at the destination will be the same as the DF protocol if the value of the destination SINR is greater than or equal to a fixed threshold SINR, otherwise, it will be the same as the AF protocol.

The SINR at *D* is shown as:

$$\gamma_{RDj} = \frac{|g_j|^2}{L_{2j}^2(\sigma_{Dj}^2+I_{Dj})}.K_j\left(|h_j|^2+U_j\right) \quad ; \text{if } \gamma_{RDj} \geq Th_j \tag{4.26}$$

$$\text{else, } \gamma_{RDj} = \frac{a|g_j|^2|h_j|^4+b|g_j|^2|h_j|^2}{c'|h_j|^2+d'|g_j|^2|h_j|^2+e'|g_j|^2+f'}; \text{ if } \gamma_{RDj} < Th_j \tag{4.27}$$

where, Th_j is the threshold SINR for protocol switching for j^{th}relay.

- **Comparison of SINR of AF, DF and Hybrid AF-DF protocols**

The upper bound of SINR for AF protocol is:

$$\gamma_{RDj-AF} = \frac{a|g_j|^2|h_j|^4+b|g_j|^2|h_j|^2}{c'|h_j|^2+d'|g_j|^2|h_j|^2+e'|g_j|^2+f'} < \frac{a|g_j|^2|h_j|^4+b|g_j|^2|h_j|^2}{c'|h_j|^2} = \left(\frac{a}{c'}|g_j|^2\right)\left(|h_j|^2+\frac{b}{a}\right) \quad (4.28)$$

The upper bound is strictly greater than SINR when $d'|g_j|^2|h_j|^2 + e'|g_j|^2 + f' > 0$. Equality holds for $d'|g_j|^2|h_j|^2 + e'^{|g_j|^2} + f' = 0$, which implies noiseless and interference-less conditions. So, the strict upper bound is selected as the communication network is always influenced by noise and interference.

Hence, we obtain,

$$\gamma_{RDj-AF} < \frac{|g_j|^2}{L_{2j}^2(\sigma_{Dj}^2+I_{Dj})}.K_j\left(|h_j|^2+U_j\right) \Rightarrow \gamma_{RDj-AF} < \gamma_{RDj-DF} \quad (4.29)$$

(4.29) shows that the DF mode offers higher SINR compared to the AF mode. Since HDAF uses both AF and DF mode depending upon the threshold, so Hybrid mode offers a judicious trade-off between AF and DF protocol.

- **Channel distribution**

The PDF and CDF of Weibull distribution are defined in (4.30) and (4.31) respectively.

$$f(x) = \begin{cases} \frac{k}{\lambda}\left(\frac{x}{\lambda}\right)^{k-1} e^{-\left(x/\lambda\right)^k}, & x \geq 0 \\ 0, & x < 0 \end{cases} \quad (4.30)$$

$$F(x) = \begin{cases} 1 - e^{-\left(x/\lambda\right)^k}, & x \geq 0 \\ 0, & x < 0 \end{cases} \quad (4.31)$$

where, k is called shape parameter ($k \in (0, \infty)$) and λ is called scale parameter ($\lambda \in (0, \infty)$).

The proposed model developed with Weibull distribution can easily be modified to obtain the other existing models by tuning certain parameters as shown in Table 4.3. Thus, the proposed model is highly flexible as well as adaptable to different situations.

Table 4.3 Parameter tuning to approach existing models

Model	Communication mode	Energy harvesting parameters	Channel distribution
[192]	DF	In TSR, $\beta = \frac{\alpha}{2}, \rho = 0$ In PSR, $\alpha = 0, \beta = \frac{1}{2}$	Nakagami-m
[194]	AF	$\alpha = 0, \beta = \frac{1}{2}$	Nakagami-m and Rayleigh ($k = 2, \lambda = 2\sigma^2$)
[193]	AF	$\alpha = \tau, \beta = \frac{(1-\tau)}{2}, \rho = 0$	FTR (Fluctuating two ray)

4.4.3 Performance Analysis

- **Outage probability (OP) Analysis**

The OP for j^{th} relay can be presented as :

$$P_{outj} = \Pr\left(\gamma_{SRj} \leq \gamma_{th} \ \ or\ \gamma_{RDj} \leq \gamma_{th}\right) = 1 - \Pr\left(\gamma_{SRj} > \gamma_{th}\ ,\ \gamma_{RDj} > \gamma_{th}\right) \tag{4.32}$$

where γ_{th} is the threshold for SINR.

The relay selection can be carried out based on SINR maximization criteria. Since the relays are i.i.d., so the above equation converts to:

$$P_{out} = \prod_{j=1}^{n} \Pr\left(\gamma_{SRj} \leq \gamma_{th} \ \ or\ \gamma_{RDj} \leq \gamma_{th}\right) = \prod_{j=1}^{n} P_{outj} \tag{4.33}$$

Proposition-1:

The OP of DF and AF protocols are given in equations (4.37) and (4.38) respectively.

$$P_{outj-DF} = 1 - \int_{M_j}^{\infty} {}^{k_{hj}}\, e^{-\left\{ p_j + \left(\frac{N_j}{\left(p_j^{\frac{1}{k_{hj}}} + X_j \right)} \right)^{k_{gj}} \right\}} d\, p_j \tag{4.34}$$

$$P_{outj-AF} = 1 - \int_{M_j}^{\infty} {}^{k_{hj}}\, e^{-\left\{ p_j + \left(\frac{(p_j^{\frac{1}{k_{hj}}} + \frac{M_j}{\gamma_{thj}})}{\left(p_j^{\frac{1}{k_{hj}}} - M_j \right)\left(p_j^{\frac{1}{k_{hj}}} + X_j \right)} . N_j \right)^{k_{gj}} \right\}} d\, p_j \tag{4.35}$$

where,

$$M_j = \frac{L_{1j}^2 \gamma_{th}\left((1-\rho_j) I_{Rj} + \sigma_{Rj}^2\right)}{P_s . (1-\rho_j) \lambda_{hj}} \qquad N_j = \frac{L_{1j}^2 L_{2j}^2 \gamma_{th}\left(I_{Dj} + \sigma_{Dj}^2\right)(1-\alpha_j-\beta_j)}{\lambda_{hj}\lambda_{gj}(\eta_{Tj}\alpha_j + \eta_{Pj}\rho_j\beta_j)\, P_s} \qquad X_j = \frac{L_{1j}^2 I_{Rj}}{P_s\, \lambda_{hj}}$$

A formal proof of (4.43) and 4.35 is provided in in Section B.1 of Appendix B

Proposition-2:

The OP of HDAF protocol is given as :

$$P_{outj-Hy} = 1 - \int_{M_j^{k_{hj}}}^{(\gamma_{Hyj}M_j)^{k_{hj}}} e^{-\left\{p_j + \left(\frac{(p_j^{\frac{1}{k_{hj}}} + \frac{M_j}{\gamma_{th}})}{\left(p_j^{\frac{1}{k_{hj}}} - M_j\right)\left(p_j^{\frac{1}{k_{hj}}} + X_j\right)}.N_j\right)^{k_{gj}}\right\}} dp_j - \int_{(\gamma_{Hyj}}^{\infty} e^{-\left\{p_j + \left(\frac{N_j}{\left(p_j^{\frac{1}{k_{hj}}} + X_j\right)}\right)^{k_{gj}}\right\}} dp_j \quad , \text{if } \gamma_{th} < Th_j$$

$$= P_{outj-DF} \quad , \text{if } \gamma_{th} \geq Th_j \tag{4.36}$$

where, $\gamma_{Hyj} = \frac{Th_j}{\gamma_{th}}$.

A formal proof of (4.43) and 4.35 is provided in Section B.2 of Appendix B

It can be noted that when $\gamma_{th} \geq Th_j$, then outage probability for HDAF is equal to OP for DF protocol and when $\gamma_{th} \ll Th_j$, then OP approaches the OP for AF mode, as $\Pr(\gamma_{SRj} \geq Th_j,\ \gamma_{RDj-AF} \leq \gamma_{th},\ \gamma_{RDj-DF} > \gamma_{th})$ tends to zero for low Th_j.

From the expressions of OP of AF, DF and HDAF mode equation (4.40) can be easily proved.

$$P_{outj-DF} \leq P_{outj-Hy} < P_{outj-AF} \tag{4.37}$$

Finally, the overall OP of the system can be derived from equation (4.33).

- **Throughput**

The mathematical description of throughput is shown below:

$$T_{out} = E\left[R(1-\alpha_j-\beta_j)\right] = \sum_{j=1}^{n} R(1-\alpha_j-\beta_j)(1-P_{outj})$$

$$= R\sum_{j=1}^{n}(1-\alpha_j-\beta_j)(1-P_{outj}) \tag{4.38}$$

where, P_{outj} is the outage probability for j^{th} relay, n is the total number of relays. R is the rate of transmission which is equal to, $R = log_2(1+\gamma_{th})$.

- **Proposed solution**

  Solving Algorithm

To solve the optimization problem classically formulated above, Algorithm 1 has been used. For HDAF mode, the following Algorithm is used by the help of Algorithm 2.

Algorithm 1: Pseudo-code of proposed Algorithm
1: **for** $j = 1{:}\,n$
2: Define $s_j = \alpha_j + \beta_j$
3: Calculate constraints of s_j, α_j, ρ_j
4: Calculate M_j, N_j, X_j in terms of s_j, α_j, ρ_j
5: Calculate T_{outj} for the boundary conditions
6: Obtain the optimum condition of throughput by varying α_j and evaluate N_j
7: Simplify the conditions for optimum throughput
8: Evaluate ρ_j for optimum throughput
9: **end for**
10: Calculate $T_{out-max}$ using optimum $\alpha_j, \beta_j, \rho_j$

Algorithm 2: Pseudocode of proposed Algorithm for HDAF mode
1: **If** $\gamma_{th} \geq Th_j$
2: Apply Algorithm 1
3: **Else** $\gamma_{th} < Th_j$
4: Minimize P_{outj} similar to Algorithm 1
6: Obtain the optimum values of $\alpha_j, \beta_j, \rho_j$
7: Calculate $T_{out-max}$ using optimum $\alpha_j, \beta_j, \rho_j$
8: **end if**

The complexity analyses of the proposed model and the existing models have been presented in Table 4.4.

Table 4.4 Time complexity of various models

Model	Time Complexity
Proposed model	$O(n)$
[192]	$O(n)$
[195]	$O(1)$
[194]	$O(1)$

4.4.4 Results and Discussions

This section provides the performance analysis of the proposed scheme. The results are simulated in MATLAB 2021a environment using Monte-Carlo simulation. The parameters used for simulations are listed in Table 4.5.

Table 4.5 Simulation parameters

Symbol	Name of parameter	Value of parameter
R	Transmission rate	2 bps/Hz
η_T	Time switching harvesting efficiency	0.8
η_P	Power splitting harvesting efficiency	0.7
L_1, L_2	Loss factors	1
$\sigma_{Ra}^2, \sigma_{Rc}^2, \sigma_D^2$	Noise variances	0.1W
I_R, I_D	Interference Power	0.01W
α	Time switching fractions	0.2
β		0.3
ρ	Power splitting fraction	0.5

Fig. 4.7 (a) and (b) depict the relation between OP and Throughput versus the number of selected relay nodes. From these figures, it is evident that if the number of relays increases then outage probability decreases and throughput increases. The analytical and simulation results show that the behaviour of the HDAF model has transitioned from AF mode to DF mode for increasing γ_{th} in the region satisfying $\gamma_{th} < Th$ and behaves like DF mode for $\gamma_{th} \geq Th$, which can be easily inferred from (B.29). Fig. 4.8 (a) shows that OP decreases with scale parameters for all protocols. It is also shown that the OP falls rapidly up to $\lambda = 2$, then it falls slowly between 2 to 5. This variation is negligible after $\lambda = 6$. The opposite behaviour is observed for throughput in Fig. 4.8 (b).

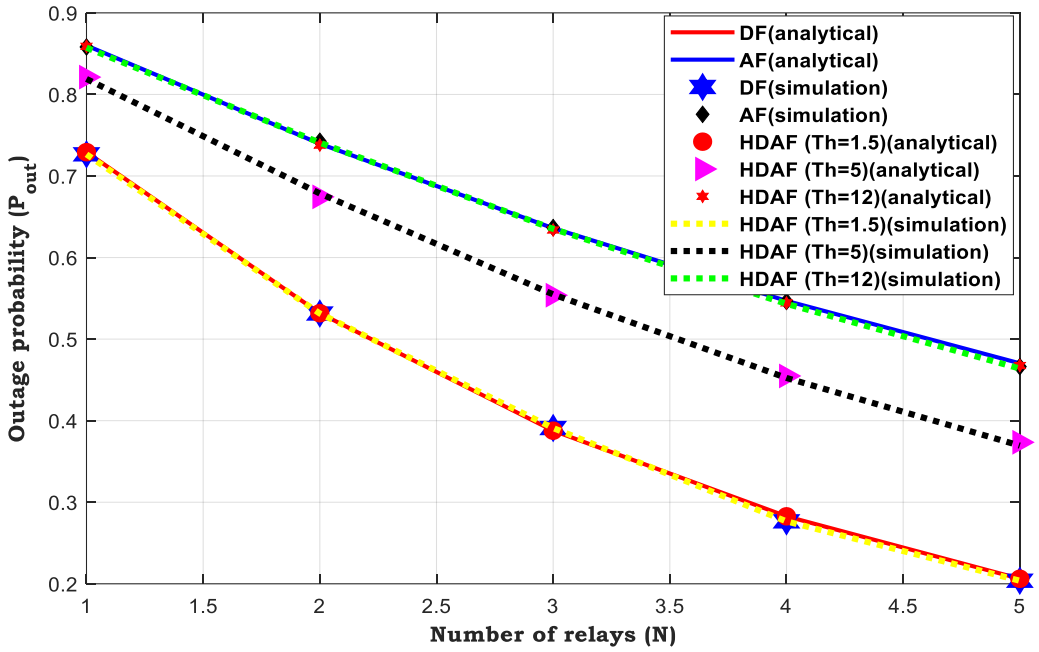

(a)

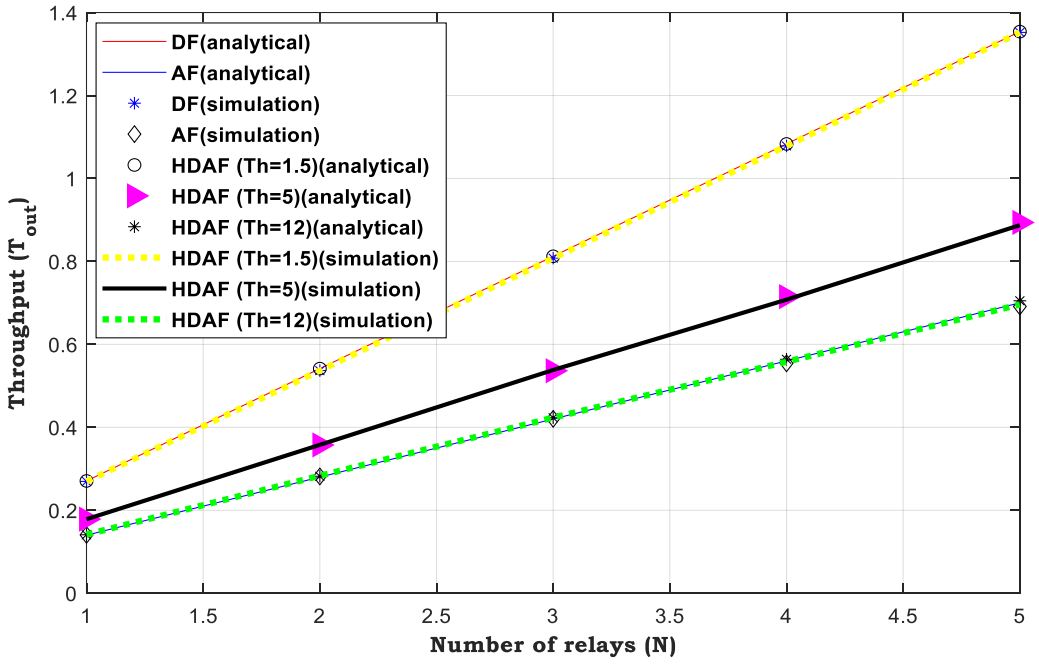

(b)

Fig. 4.7 Performance Analysis for AF, DF and HDAF **(a)** OP versus Number of relays ($P_s = 1W, \gamma_{th} = 3$, Weibull parameters: Shape and Scale parameter=1) **(b)** Throughput versus Number of relays ($P_s = 1W, \gamma_{th} = 3$, Weibull parameters: Shape and Scale parameter=1)

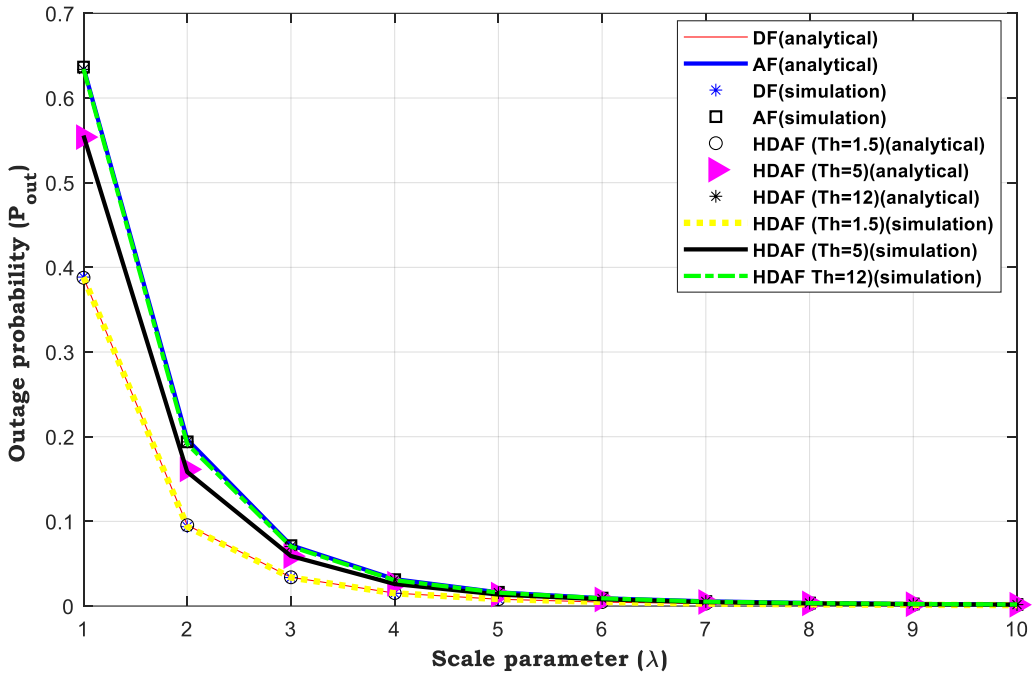

(a)

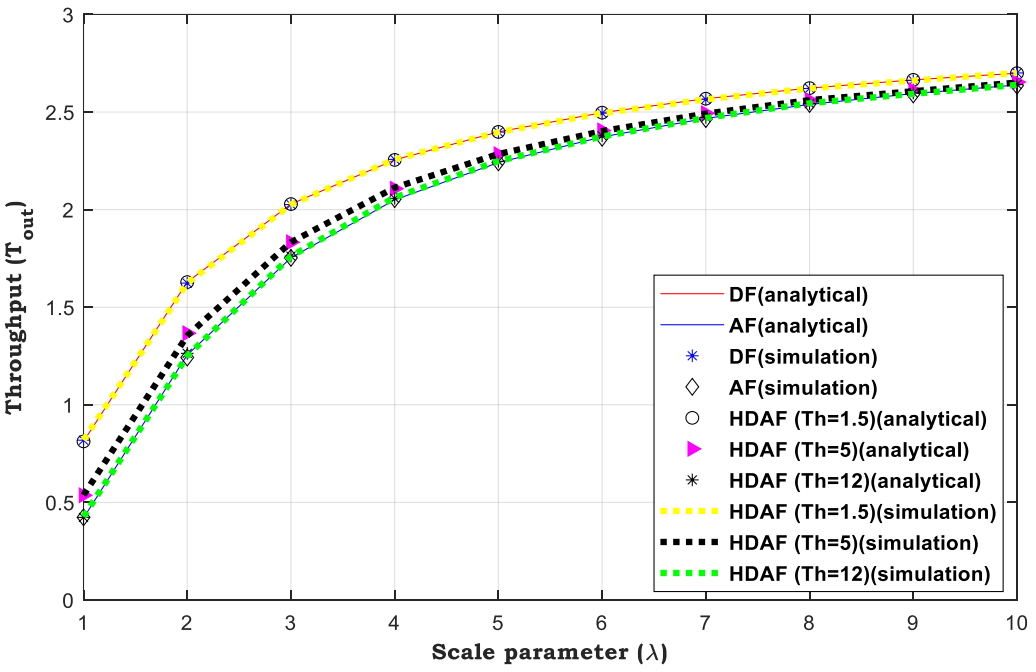

(b)

Fig. 4.8 Performance Analysis for AF, DF and HDAF **(a)** OP versus Weibull Scale parameter ($N = 3, P_s = 1W, \gamma_{th} = 3$, Weibull Shape parameter=1) **(b)** Throughput versus Weibull Scale parameter ($N = 3, P_s = 1W, \gamma_{th} = 3$, Weibull Shape parameter=1)

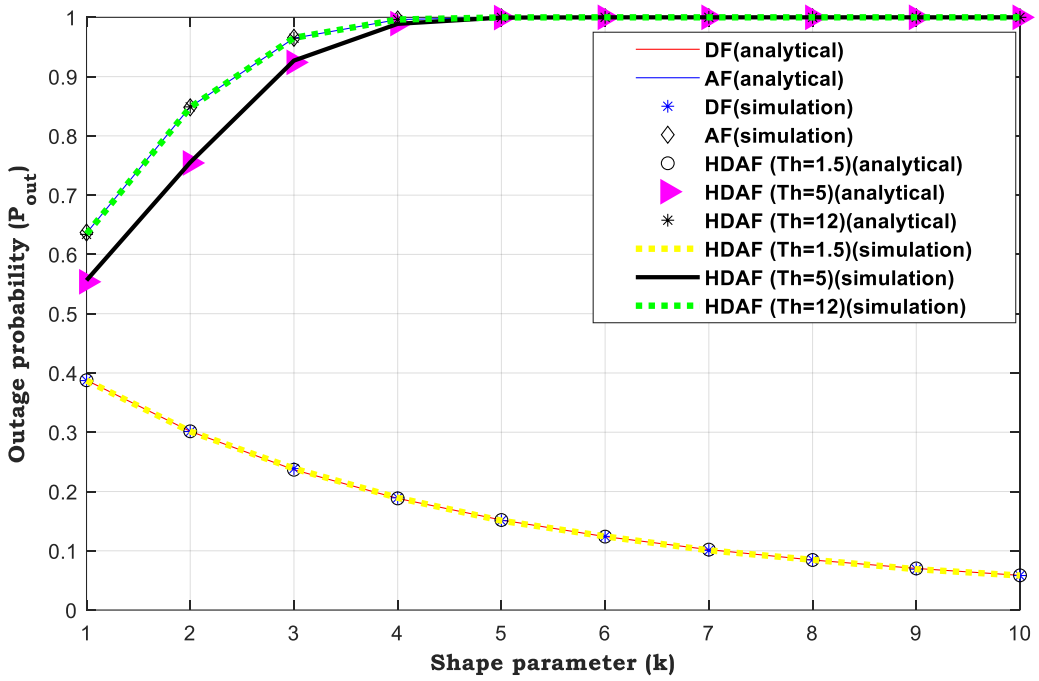

(a)

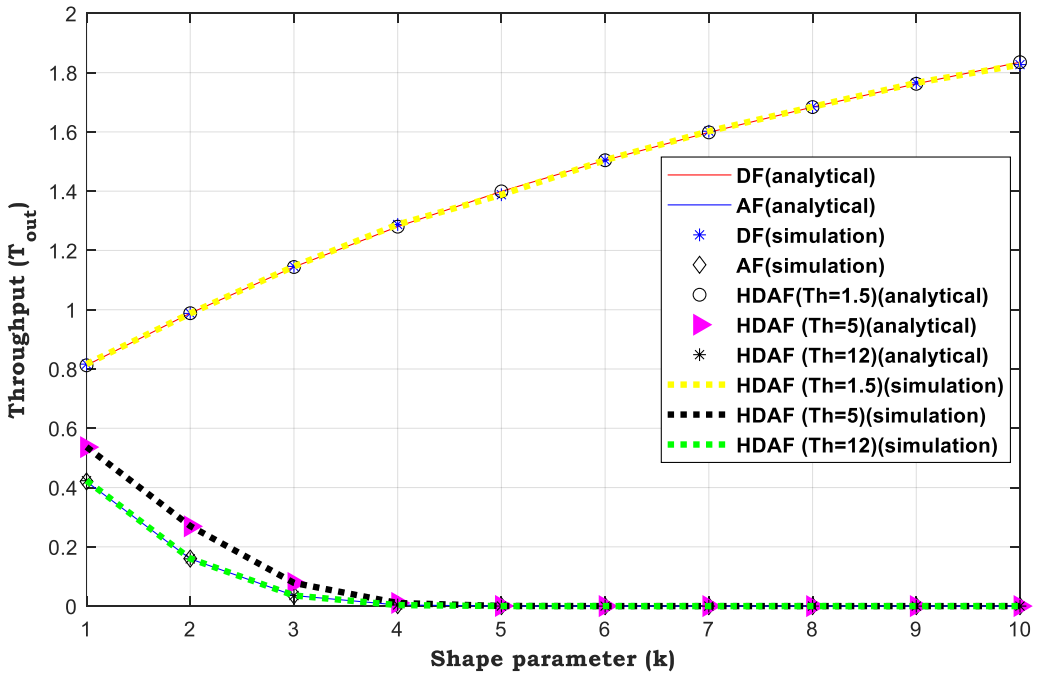

(b)

Fig. 4.9 Performance Analysis for AF, DF and HDAF **(a)** OP versus Weibull Shape parameter ($N = 3, P_s = 1W, \gamma_{th} = 3$, Weibull Scale parameter=1) **(b)** Throughput versus Weibull Shape parameter ($N = 3, P_s = 1W, \gamma_{th} = 3$, Weibull Scale parameter=1)

The performance analysis in terms of Outage and Throughput for different values of Weibull Shape parameter has been shown in Fig. 4.9 (a) and (b) respectively. For Fig. 4.9 (a), the outage probability increases for AF, Hybrid AF-DF with $Th = 5$ and $Th = 12$; whereas, the OP decreases for DF and Hybrid AF-DF with $Th = 1.5$. The opposite behaviour happens for throughput in Fig. 4.9 (b).

Table 4.6 Comparison table

Model	Communication mode	EH protocol	Maximum Throughput (bits/s/Hz)	Percentage improvement of throughput (%)
Proposed model	AF	Hybrid TSR-PSR ($\eta_P = 0$)	3.4385	-
		Hybrid TSR-PSR ($\eta_T = 0$)	2.6293	-
	DF	Hybrid TSR-PSR ($\eta_P = 0$)	3.8174	-
		Hybrid TSR-PSR ($\eta_T = 0$)	3.2071	-
	HDAF	Hybrid TSR-PSR ($\eta_P = 0$)	3.8174	-
		Hybrid TSR-PSR ($\eta_T = 0$)	3.2071	-
[192]	DF	TSR	2.1947	73.94
		PSR	2.7418	16.97
[194]	AF	PSR	2.4156	8.85

It is evident from the above comparison in Table 4.6 that the proposed work offers a noticeable improvement in throughput with respect to the existing models. It is also seen that the throughput performance of the proposed model is much superior to the mentioned existing works considering all the communication modes as highlighted in the table. The above comparison correctly establishes the supremacy of the proposed models over existing ones.

4.5 RELAY SELECTION IN UNTRUSTED ENVIRONMENT WITH A FRIENDLY JAMMER

This section presents an EH-CR network that uses a wireless powered friendly jammer to improve the secrecy performance.

4.5.1 System model for RS in presence of EAV

Fig. 4.10 depicts a network consisting of N sources S_n ,where $n = 1, 2, ...N$ available in the form of transmission towers in an environment such as TV broadcast towers, wireless local area networks or Global System for Mobile (GSM) communication. They operate on orthogonal frequency bands. The relays R_m, where $m = 1, 2, ...M$, harvest energy from S_n and then use that energy to send information to a Base Station BS in the presence of multiple passive EAVs E_k, where $k = 1, 2, ...K$, who wish to intercept the information transmitted from the relays to the BS. This architecture is highly relevant in cognitive radio-based IoT (CIoT) and green communication systems, where opportunistic energy harvesting from licensed or ambient RF signals is essential for sustainable operation. Relays R_m transmit known pilot signals (e.g., for the legitimate receiver BS to estimate CSI). It is assumed that the EAV uses Minimum Mean Square Error (MMSE) estimation for analysing the pilot signals to estimate the CSI of the signal. A friendly jammer J interferes with these EAVs, as illustrated in the figure. It is assumed that all channels undergo Rayleigh fading and that all nodes are equipped with a single antenna.

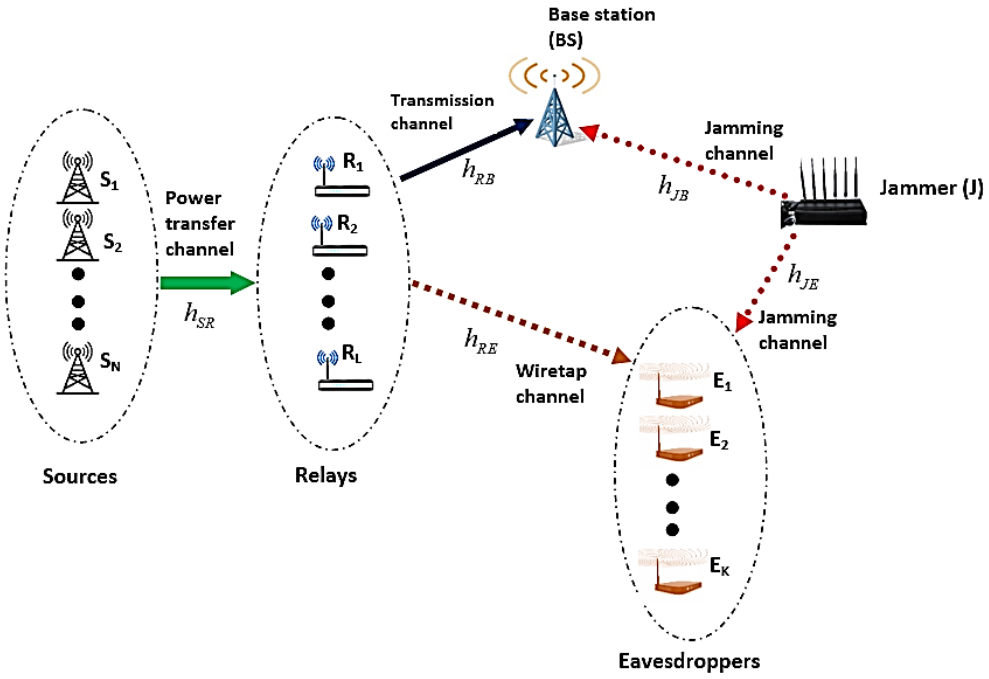

4.10 System Model

4.5.2 Mathematical modelling

Here, Harvest-Use (HU) architecture has been adopted. Once a relay harvests the energy from S_n, it generally uses that energy to transmit the information. Accordingly, the communication technique is deployed in two-phase, energy transfer and information transfer: In the 1st phase i.e. αT, R_m harvests energy from S_n which is expressed as:

$$E_{S_n R_l} = \alpha \eta P_S T \frac{\left|h_{S_n R_l}\right|^2}{d^m_{S_n R_l}} \tag{4.39}$$

where α is fraction of total time for EH and η represents energy conversion efficiency. P_S and T are transmit power of sources and total time block respectively. The distance from S_n to R_m and path loss exponent are expressed as $d_{S_n R_l}$ and *m* respectively.

After EH, a relay node performs CSI estimation to find the best source for harvesting purpose. Here, the best source is selected among *N* sources that allows R_l to use the maximum transmit power to improve the secrecy performance.

➢ Information transmission

During the remaining time slot $(1-\alpha)T$, the best relay R^* is chosen such that channel gain of $R^* - B$ link is maximum

i.e. $h_{R^* B} \square \max_{l=1,2,...L} \left\{\left|h_{R_l B}\right|\right\}$

Now, R^* transmits signal $x(t)$ to the *BS*. Simultaneously, the jammer generates jamming signal $z(t)$ to the EAVs and BS. Signal received at BS is given as:

$$y(t) = \sqrt{\frac{P_{S^* R^*}}{d^m_{R^* B}}} h_{R^* B} x(t) + \sqrt{\frac{P_J}{d^m_{JB}}} h_{JB} z(t) + N \tag{4.40}$$

where d_{JB} is the distance from *J* to *BS*, P_J represents the transmit power of *J*, and *N* is an additive white complex Gaussian noise at *BS*. The instantaneous received SNR at the *BS* is given as:

$$\gamma_B = P_{S^* R^*} \frac{\left|h_{R^* B}\right|^2}{d^m_{R^* B}} = \varsigma \gamma_{S^* R^*} \gamma_{R^* B} \tag{4.41}$$

where $\varsigma = \frac{\alpha \eta P_S}{(1-\alpha)N}$, $\gamma_{S^* R^*} = \frac{\left|h_{S^* R^*}\right|^2}{d^m_{S^* R^*}}$ and $\gamma_{R^* B} = \frac{\left|h_{R^* B}\right|^2}{d^m_{R^* B}}$

The multiple EAVs can overhear the packet transmitted and can attempt to extract *x(t)* without using an active attack. In addition, the EAVs also receive interference signals from *J*; hence, the received signal at E_k is denoted as follows:

$$z_k(t) = \sqrt{\frac{P_{S^*R^*}}{d^m_{R^*E_k}}} h_{R^*E_k} x(t) + \sqrt{\frac{P_J}{d^m_{JE_k}}} h_{JE_k} z(t) + N \tag{4.42}$$

where d_{SE_k} and d_{JE_k} are the distance from S to E_k and from J to E_k respectively. Thus, the instantaneous received SINR at E_k is given by

$$\gamma_{E_k} = \frac{P_{S^*R^*} \left| h_{R^*E_k} \right|^2}{d^m_{R^*E_k} \left[\frac{P_J}{d^m_{JE_k}} \left| h_{JE_k} \right|^2 + N_O \right]} = \varsigma \gamma_{S^*R^*} \tilde{\gamma}_{E_k} \tag{4.43}$$

➢ Secrecy Performance Evaluation

The instantaneous channel capacity of *R*-BS link without interference from *J* is:

$$C_B = W \log_2(1+\gamma_B) \tag{4.44}$$

where *W* is the bandwidth of the system

The instantaneous channel capacity of *R*-E_k link affected by interference from *J* is:

$$C_{E_k} = W \log_2(1+\gamma_{E_k}) \tag{4.45}$$

Thus, the instantaneous secrecy capacity at E_k is:

$$C_{Sec} = [C_B - C_{E_k}]^+ \tag{4.46}$$

$$= \begin{cases} \log_2\left(\frac{1+\gamma_B}{1+\gamma_{E_k}}\right), & \gamma_B > \gamma_{E_k} \\ 0, & \gamma_B \le \gamma_{E_k} \end{cases} \tag{4.47}$$

❒ BEST-NODE SCHEDULING SCHEME

Assuming that all channels are independent, the probability of achieving a successful secure communication between S^* and BS for a single E_k is defined as

$$S_k^{best} = P\left\{C_{Sec_k} > 0\right\} \tag{4.48}$$

In the considered network with multiple EAVs, the information can be transmitted confidentially only when the instantaneous SNR of the BS will be greater than that of any EAV

(this implies that the instantaneous SNR of the BS is greater than the largest EAV among 'K' *EAVs*) i.e., $\gamma_E \square \max_{k=1,...K} \left\{\gamma_{E_k}\right\}$ (4.49)

Thus, the SC for the best-node scheduling scheme as follows:

$$S^{best} = P\left\{\min_{1\le k\le K}\left\{C_{Sec_k}\right\} > 0\right\} \quad (4.50)$$

$$= P\left\{C_{Sec_1} > 0, C_{Sec_2} > 0 ... C_{Sec_N} > 0\right\}$$

$$= \prod_{k=1}^{K} P\left\{C_{Sec_k} > 0\right\}$$

4.5.3 Results and Discussions

For comparison purpose, a conventional round robin scheduling baseline scheme [197] has been used, where each R_m has an equal opportunity to transmit its sensed data to the BS. In this section, the numerical values of the proposed model has been provided in Table 4.7.

Table 4.7 Parameter assumptions

Parameter	Meaning	Default values
R_{th}	Target secrecy threshold	0.1bps/Hz
η_S	Energy conversion efficiency	0.8
α	Power splitting coefficient	0.6
m	Path loss exponent	3

Fig. 4.11 shows the SC of the system versus the distance from R_m to the BS for 'K' *EAVs*. It is observed that the SC for best-node scheduling scheme is higher than that of the round-robin scheduling scheme. Also, when there are more EAVs, their abilities to decode the secret message are improved along with the jamming also increases and the SC improves. Fig. 4.12 highlights the impact of alpha on SOP. The energy harvesting at R_m increases as alpha increases; thus effectively reducing the SOP. It has been observed that SOP of the system with jammer decreases slightly with increasing alpha but the SOP of the system without jammer remains same for all values of alpha. This is because the jammer generates signals that interfere with the *EAV*s; hence, the higher power of the jammer improves the security performance of the system.

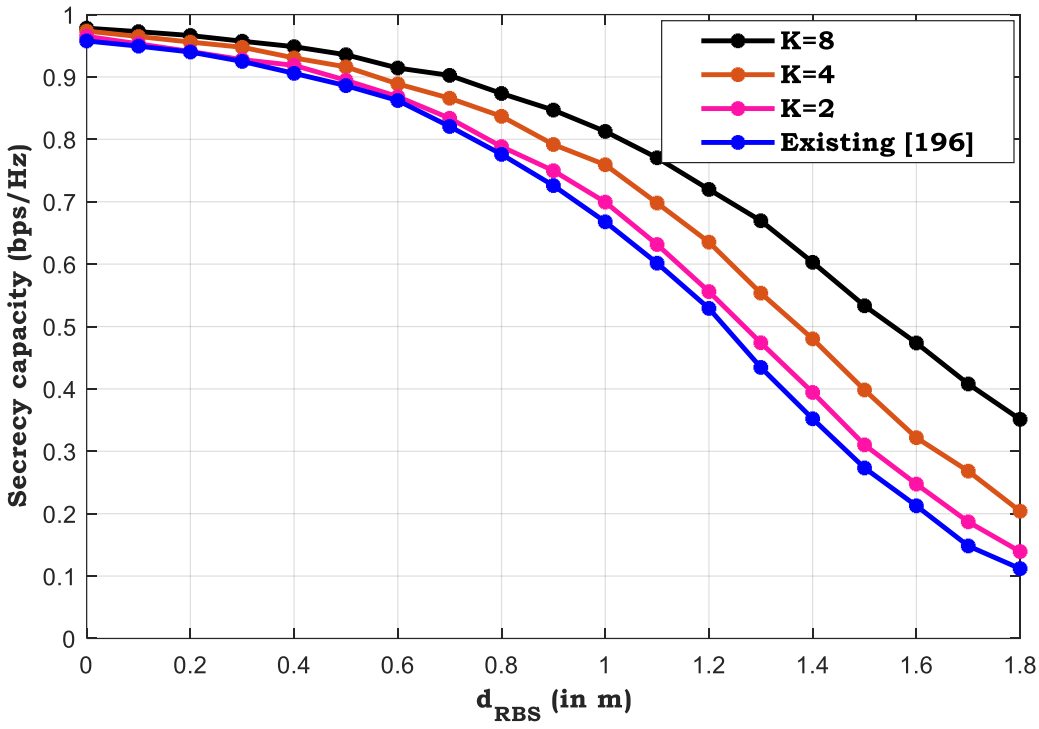

Fig. 4.11 Impact of varying distance and K on SC with $N = 2$, $M = 5$, $\alpha = 0.5$, $\eta = 0.85$, $P_J = 15$ dB

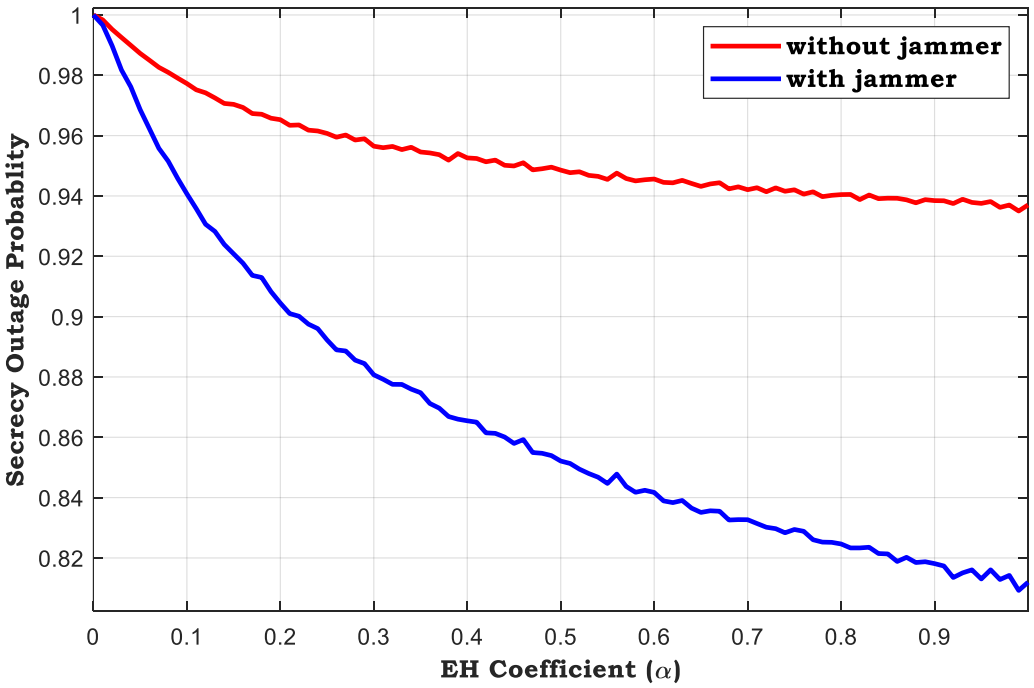

Fig. 4.12 Impact of alpha on SOP with and without the involvement of jammer

Fig. 4.13 depict the SOP versus the SNR with varying M. These plots show a close resemblance between analysis and simulation. It can be inferred from the plots that increasing the number

of '*M*' significantly decreases the SOP of the network, especially in the medium and high-SNR regimes.

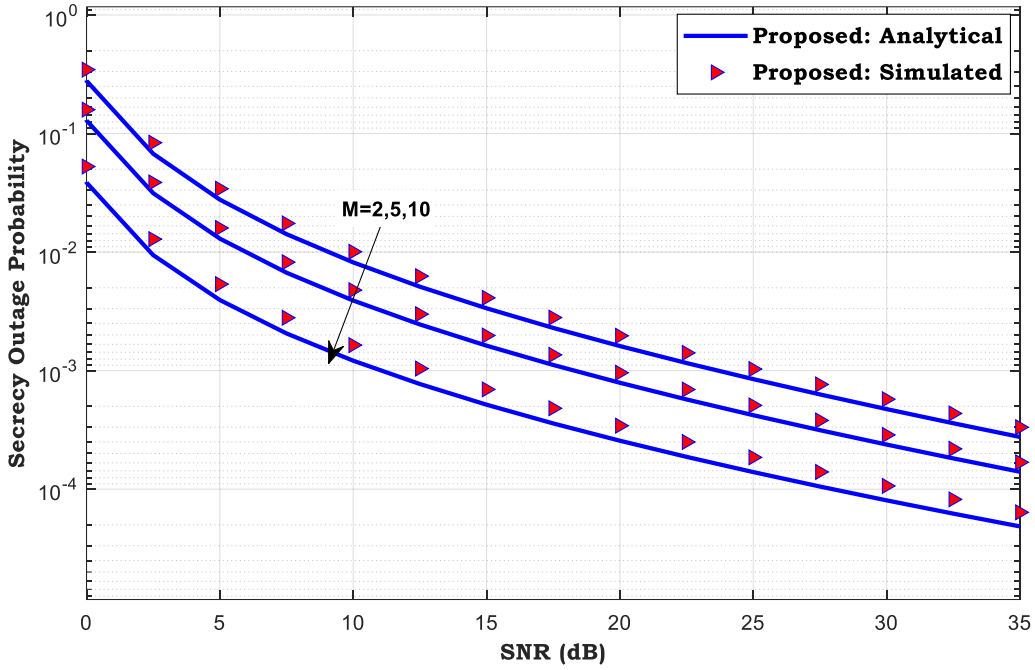

Fig. 4.13 Impact of varying SNR and '*M*' on the SOP with K = 2, N = 2, $\alpha = 0.5$, $\eta = 0.85$, $P_J = 15$ dB

4.6 OVERALL COMPARISON

A critical study and comparison of the above system models with some of the existing relevant state-of-art have been abridged in Table 4.8 and 4.9.

Table 4.8 Comparison table with existing relevant state-of-art

Existing/Proposed Works	Scenario	Relay selection strategy used	Protocol used	Scheme used	Fading channel	Performance metric
Existing Works						
[58]	One-way FD EH relay selection network with DF protocol	OPT-RS, MHE-RS and Minimum self-interference (MSI) relay selection	TSR	DF	Rayleigh	Throughput
[86]	EH two-hop network	Joint time allocation and relay selection algorithm	-	DF	Rayleigh	Throughput

[192]	UAV assisted relay network in IoT	SNR Maximization	TSR,PSR	DF	Nakagami	Throughput
[194]	UAV enabled SWIPT CRN with MRC	-	TSR	AF	Nakagami	OP, SER
[193]	Single Relay Assisted WPCN	-	-	AF	Fluctuating Two Ray Fading	OP and SER
[196]	RRS in Industrial WSNs	Optimal sensor scheduling, Round Robin Scheduling Scheme	-	-	Nakagami	SC, Intercept Probability
Proposed Works						
Proposed Work 1	*Multi-relay cooperative network in interference free scenario*	*MEA-RS and OPT-RS*	*TSR*	*DF*	*Rayleigh*	*Throughput*
Proposed Work 2	*Multi-relay cooperative network in interference-limited environment in absence of EAV*	*Optimal relay selection (ORS) strategy*	*Hybrid TSR-PSR*	*AF, DF, Hybrid AF/DF*	*Weibull*	*Throughput*
Proposed Work 3	*Multi-relay cooperative network with Interference-aided EH in presence of an EAV*	*Best-relay scheduling scheme*	*TSR*	*DF*	*Rayleigh*	*Secrecy*

Table 4.9 Critical Analysis of proposed work with existing works

Performance Metric	**Existing/ Proposed Works**	**Protocol**	**Maximum Throughput (bps/Hz)**	**Secrecy Capacity (bps/Hz)**	**Complexity**
Throughput (bps/Hz) & Complexity Analysis	[58]	TSR	0.913 0.762	-	-
	Proposed Work 1		1.054 1.054		
	[192]	TSR	2.1947	-	*O(n)*
		PSR	2.7418		
		Hybrid TSR-PSR ($\eta_T = 0$)	1.6295		
	[193]			-	*O(1)*
	[194]	PSR	2.4156	-	*O(1)*

	Proposed Work 2	Hybrid TSR-PSR ($\eta_P = 0$)	3.4385	-	*O(n)*
		Hybrid TSR-PSR ($\eta_T = 0$)	2.6293		
		Hybrid TSR-PSR ($\eta_P = 0$)	3.8174		
		Hybrid TSR-PSR ($\eta_T = 0$)	3.2071		
		Hybrid TSR-PSR ($\eta_P = 0$)	3.8174		
		Hybrid TSR-PSR ($\eta_T = 0$)	3.2071		
	[86]	TSR	0.74	-	-
	[85]		0.05	-	-
	Proposed Work 2		1.18	-	
	[45]	PSR	-	-	$O(n^2 log\ n)$
	[44]				$O(n^2 log\ n)$
	Proposed Work 3				$O(L*n+n^2+M^2+M*log_K M)$
Secrecy Capacity (bps/Hz)	[196]	TSR	-	0.61	-
	Proposed Work 3			0.82	

4.7 DISCUSSION

In this chapter, three frameworks have been presented to evaluate the throughput and secrecy performance of RF-powered one-way multi relay networks. In Proposed work 1, the throughput performance of a Multi-Source Multi-Antenna CRN has been observed using two relay-selection techniques. In Proposed work 2, a generalized RF EH system using Hybrid TSR–PSR protocol has been modelled under the Weibull fading channel and the throughput has been analysed for DF, AF and HDAF modes. The proposed model uses the SINR maximization criteria and selects one relay from multiple relays. Comparative analysis shows the improvement in throughput of the proposed model over the existing benchmark models. Proposed work 3 studies the secrecy capacity and the SOP of an EH-CR network with a jammer, multiple beacons, multiple sources, and a base station in the presence of multiple EAVs. In addition, the best-node scheduling scheme has been proposed here to enhance system secrecy performance against eavesdropping attacks.

Chapter 5

RF ENERGY HARVESTING IN TWO-WAY COOPERATIVE RELAY NETWORKS

5.1 OVERVIEW

This Chapter presents the performance analysis of two-way cooperative relay networks in line with Chapters 3 and 4. Initially, the performance of a bidirectional AF multi-relay multi-antenna network system is studied. In the subsequent section, a secure Maximum RF Energy Harvested Antenna Selection (MHE-AS) scheme is presented in a Two-Way Communication (TWC) via two multi-antenna relays with Interference-Aided (IA-EH). Here, the impact of some network parameters, namely EH coefficient, Transmit Power of Sources, Interferer Transmit Power, Global Target Secrecy Rate and number of antennas are examined on the Secrecy Capacity (SC). Lastly, as an extension of this work, a secure transmission scheme in two-way IoT relay network is introduced using IA-EH, where the amount of enhancement in secrecy performance is estimated by exploiting the interference power of CCIs using accumulate-and-forward scheme under both linear and non-linear scenarios.

5.2 BACKGROUND

An Adaptive Relaying Protocol (ARP) was introduced in [23], where the system was investigated over Rician fading channel. This model included a single-antenna relay between the source and destination nodes. To improve the performance of the model described in [23], an adaptive relaying for bidirectional multi-relay multi-antenna system is proposed in both Delay Limited (DL) and Delay Tolerant (DT) transmission over Nakagami faded channel. Similar to One Way Relaying (OWR), due to heavy spectral reuse, TWC systems are also affected by CCI which can be regarded as a constant energy source and has a major role to maximize the SC under EAV attack. In another work [97], the authors obtained the secrecy

performance of a TWC network via two half-duplexes DF relays in presence of an EAV. In contrast to this work, a secure MHE-AS scheme is proposed by incorporating a TWC via two multi-antenna relays in presence of an interferer. The proposed method mainly focuses on boosting the secrecy performance by using a selective antenna which harvests maximum energy from multiple antennas at each relay instead of a single one. The works in [70,80,81,111] involving PLS in EH networks are investigated considering linear EH network. However, in realistic scenario, RF transceivers suffer from various RF impairments such as in-phase/quadrature-phase imbalance, oscillator noise, high-power amplifier nonlinearity etc. that compromises the system secrecy performance. However, the disadvantage associated with this work is that the linear EH model is too idealistic and impractical as this model is unable to demonstrate the nonlinear behaviour of any practical energy harvesting circuit. Moreover, [70,80,81,114] have utilized a separate jammer for maintaining secrecy of the network. In this work, we consider that the source nodes are configured with jamming signal generator to transmit both the message and jamming signals. This scheme does not require extra separate jammers. To address the above challenges, a thorough analysis on the secrecy performance of an untrusted RF-powered IoT relay network is provided under non-linear scenario in presence of CCIs where the relays are collocated with EAVs. Here, the increment in harvested energy with increase in number of frames is observed and the percentage improvement in SC is calculated.

5.3 BIDIRECTIONAL COOPERATIVE NETWORK USING ARP

In this section, a two-way Multi-Relay Multi-Antenna relay network along with its mathematical representation is described in details.

5.3.1 System Model

An adaptive EH protocol for a bidirectional network over Nakagami fading environment has been presented in Fig. 5.1. Here, simultaneous transfer of information and energy takes place between the sources (S_1, S_2) and the relays ($R_1, R_2, \ldots, R_N$) in both directions. The time frame diagram of the proposed scheme is presented in Fig. 5.2. Here, the overall time interval is denoted by T. Energy is harvested from S_1 and S_2 at a time interval αT, where α is the EH coefficient. In the next interval of time $(1-\alpha)T/2$, the source signal splits into two streams. EH by the relay node is done using a fraction of power ρP_S, whereas $(1-\rho)P_S$ is used to decode

the information signal coming from the source nodes. Here, ρ is the power splitting fraction and $0 \leq \rho \leq 1$. In the remaining time interval $(1-\alpha)T/2$, information is forwarded from the relay node to the nodes S_1 and S_2. This architecture is highly applicable to two-way IoT communication systems, such as vehicular-to-infrastructure (V2I) networks, smart meter data exchanges, or disaster recovery networks, where energy sustainability and bidirectional low-latency data exchange are critical. The adoption of Nakagami-mmm fading allows for modeling a wide range of realistic wireless channel conditions, from severe to moderate fading, enhancing the generalizability of the proposed system.

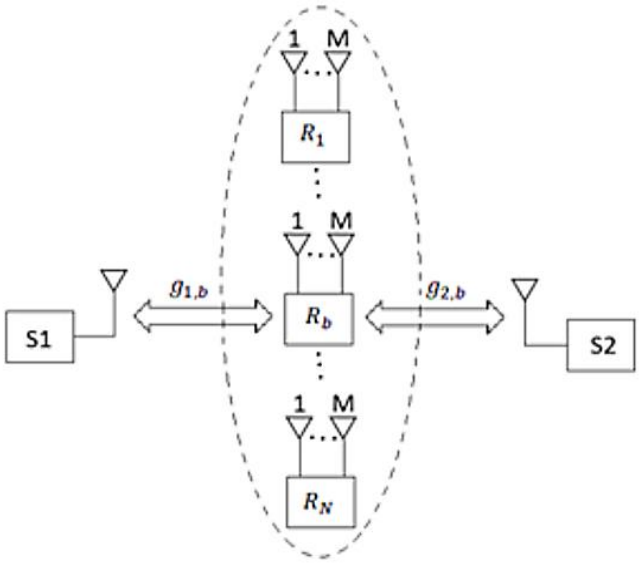

Fig. 5.1 System Model

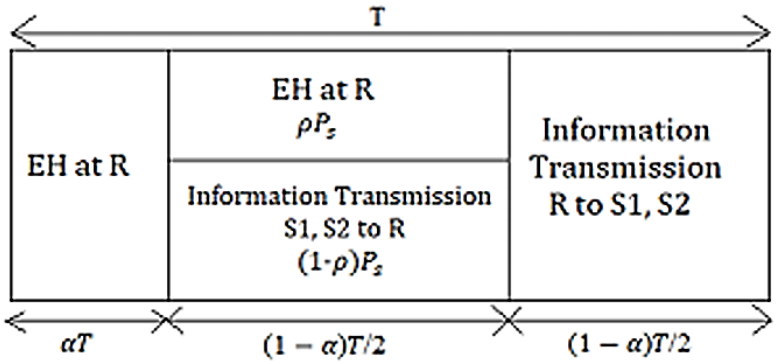

Fig. 5.2 Time Frame Communication

The relevant assumptions are as follows:

- A Nakagami fading channel is employed.

- Power is generated at the relays through EH which takes place through Hybrid TSR-PSR protocol.

5.3.2 Mathematical Modelling

The signal received at the node R_i is calculated as:

$$Y_i = \begin{bmatrix} y_{i,1} \\ y_{i,2} \\ \dots \\ y_{i,M} \end{bmatrix}$$

$$= \begin{bmatrix} \sqrt{P_S} g_{1,i_1} x_1 + \sqrt{P_S} g_{2,i_1} x_2 + n_{i,1}^{[a]} \\ \sqrt{P_S} g_{1,i_2} x_1 + \sqrt{P_S} g_{1,i_1} x_2 + n_{i,2}^{[a]} \\ \dots \\ \sqrt{P_S} g_{1,i_M} x_1 + \sqrt{P_S} g_{1,i_M} x_2 + n_{i,M}^{[a]} \end{bmatrix} = \begin{bmatrix} \sqrt{P_S} g_{1,i_1} + \sqrt{P_S} g_{2,i_1} \\ \sqrt{P_S} g_{1,i_2} + \sqrt{P_S} g_{2,i_2} \\ \dots \\ \sqrt{P_S} g_{1,i_M} + \sqrt{P_S} g_{2,i_M} \end{bmatrix} \begin{bmatrix} x_1 \\ x_2 \end{bmatrix} + \begin{bmatrix} n_{i,1}^{[a]} \\ n_{i,2}^{[a]} \\ .. \\ n_{i,M}^{[a]} \end{bmatrix} \quad (5.1)$$

$$= \begin{bmatrix} \sqrt{P_S} g_{1,i} + \sqrt{P_S} g_{2,i} \end{bmatrix} + n_i^{[a]}$$

where, P_S denotes the transmission power from S_1 and S_2; x_1 and x_2 denote the normalized information signals from S_1 and S_2, respectively; and $n_{i,m}^{[a]} \sim CN(0, \sigma_a^2)$ is the AWGN at the m-th antenna of R_i. Here, g_{1,i_m} , g_{2,i_m} are the Nakagami distribution parameters. The energy harvested at the m-th antenna of the relay node R_i is calculated as:

$$\begin{aligned} E_{HR_{i,m}} &= (\eta_\alpha P_S \left| g_{1,i_m} \right|^2 + \eta_\alpha P_S \left| g_{2,i_m} \right|^2) \alpha T + \\ &(\eta_\rho \rho P_S \left| g_{1,i_m} \right|^2 + \eta_\rho \rho P_S \left| g_{2,i_m} \right|^2)(1-\alpha) T / 2 \\ &= (\eta_\alpha \alpha T + \frac{\eta_\rho \rho (1-\alpha) T}{2})(P_S \left| g_{1,i_m} \right|^2 + P_S \left| g_{2,i_m} \right|^2) \end{aligned} \quad (5.2)$$

where η_α and η_ρ represent the EH efficiency of TS and PS respectively; $0 < \eta_\alpha < 1$ and $0 < \eta_\rho < 1$

Therefore, the power which has been received at the relay node R_i can be computed as:

$$\begin{aligned} P_{R_i} &= \frac{\sum_{m=1}^{M} E_{HR_{i,m}}}{(1-\alpha) T / 2} \\ &= (\frac{2\eta_\alpha \alpha}{1-\alpha} + \eta_\rho \rho)(P_S \sum_{m=1}^{M} \left| g_{1,i_m} \right|^2 + P_S \sum_{m=1}^{M} \left| g_{2,i_m} \right|^2 = k \left(P_S \sum_{m=1}^{M} \left| g_{1,i_m} \right|^2 + P_S \sum_{m=1}^{M} \left| g_{2,i_m} \right|^2 \right) \end{aligned} \quad (5.3)$$

where $k = \left(\frac{2\eta_\alpha \alpha}{1-\alpha} + \eta_\rho \rho \right)$ (5.4)

Here, MHE-RS [58] has been considered. It is also considered that the *n*-th antenna of the *b*-th relay node harvests the maximum amount of energy. The receiver down-converts the RF signal $\sqrt{1-\rho}\, y_{b,n}$ to baseband signal and processes it. After conversion, the baseband signal at the *n*-th antenna is sampled and expressed as:

$$\begin{aligned} \tilde{y}_{b,n} &= \sqrt{1-\rho}\, y_{b,n} + n_{b,n}^{[c]} \\ &= \sqrt{1-\rho P_S}\,(g_{1,b_n} x_1 + g_{2,b_n} x_2) + \sqrt{1-\rho}\, n_{b,n}^{[a]} + n_{b,n}^{[c]} \\ &= \sqrt{1-\rho P_S}\,(g_{1,b_n} x_1 + g_{2,b_n} x_2) + n_{b,n} \end{aligned} \quad (5.5)$$

where $n_{b,n} = \sqrt{1-\rho}\, n_{b,n}^{[a]} + n_{b,n}^{[c]}$ is the AWGN at relay node with variance N_0 and zero mean. The signal received at relay node (which is amplified by a factor μ) is written as:

$$\mu = \frac{x_{b,n}}{\tilde{y}_{b,n}} = \sqrt{\frac{P_b}{(1-\rho)P_S(\left|g_{1,b_n}\right|^2 + \left|g_{2,b_n}\right|^2) + N_O}} \quad (5.6)$$

The received signal at the source S_1 sent by the relay is given by:

$$y_1 = g_{1,b_n} x_{b,n} + n_1 \quad (5.7)$$

Here n_1 represents the AWGN at S_1 with zero mean and variance N_0.

$$\begin{aligned} y_1 &= g_{1,b_n} \beta \tilde{y}_{b,n} + n_1 \\ &= g_{1,b_n} \beta [\sqrt{(1-\rho)P_S}\, g_{1,b_n} x_1 + \sqrt{(1-\rho)P_S}\, g_{2,b_n} x_2 + n_{b,n}] + n_1 \end{aligned} \quad (5.8)$$

S_1 has to extract the signal sent by S_2 from y_1. Since it has the knowledge of its own transmitted symbol S_1, it can perfectly remove the corresponding self-interference term. After that, an estimate of the intended signal x_2 can be obtained as:

$$\hat{x}_2 = \frac{y_1 - \sqrt{(1-\rho)P_S}\,\beta \left|g_{1,b_n}\right|^2 x_1}{(1-\rho)\beta g_{1,b_n} g_{2,b_n}} \quad (5.9)$$

Substituting the value of β, the end-to-end SNR of $\hat{x}_2$ at S_1 can be calculated as:

$$\gamma_{21} = \frac{(1-\rho)\frac{P_S}{N_O}\left|g_{1,b_n} g_{2,b_n}\right|^2}{\left|g_{1,b_n}\right|^2 + (1-\rho)(\frac{P_S}{P_b}\left|g_{1,b_n}\right|^2 + \frac{P_S}{P_b}\left|g_{1,b_n}\right|^2)} \quad (5.10)$$

Putting $P_S / N_O = \gamma_{th}$ and substituting the value of P_b, the above equation is modified to

$$\gamma_{21} = \frac{(1-\rho)\gamma_{th}\left|g_{1,b_n}g_{2,b_n}\right|^2}{\left|g_{1,b_n}\right|^2 + \frac{(1-\rho)}{k}\left(\frac{\left|g_{1,b_n}\right|^2 + \left|g_{2,b_n}\right|^2}{\sum_{m=1}^{M}\left|g_{1,b_n}\right|^2 + \sum_{m=1}^{M}\left|g_{2,b_n}\right|^2}\right)} \tag{5.11}$$

Similarly, the end-to-end SNR of $\hat{x}_1$ at S_2 can be written as:

$$\gamma_{12} = \frac{(1-\rho)\gamma_{th}\left|g_{1,b_n}g_{2,b_n}\right|^2}{\left|g_{2,b_n}\right|^2 + \frac{(1-\rho)}{k}\left(\frac{\left|g_{1,b_n}\right|^2 + \left|g_{2,b_n}\right|^2}{\sum_{m=1}^{M}\left|g_{1,b_n}\right|^2 + \sum_{m=1}^{M}\left|g_{2,b_n}\right|^2}\right)} \tag{5.12}$$

5.3.3 System Performance

The system performance of the network is proposed for both DL and DT transmission.

➢ Delay Limited (DL) Transmission

In DL transmission mode, the throughput is determined by calculating the OP keeping the source transmission rate fixed at R_S bits/s/Hz, where $R_S = \log_2(1+\gamma_{th})$ and γ_{th} is the threshold value of SNR to detect data correctly. Thus, OP at S_1 and S_2 are given as:

$$\begin{aligned} P_{out_1} &= P(\gamma_{21} < \gamma_{th}) \\ P_{out_2} &= P(\gamma_{12} < \gamma_{th}) \end{aligned} \tag{5.13}$$

The achievable throughput at S_1 and S_2 are computed as:

$$\tau_i^{DL} = (1 - p_{out_i}) \times \frac{R_S}{2} \times (1-\alpha) \tag{5.14}$$

where $i \in \{1, 2\}$

➢ Delay Tolerant (DT) Transmission

In DT transmission mode, the ergodic capacity at the destination needs to be evaluated to determine the throughput. Ergodic capacity at S_1 and S_2 are given by

$$C_1 = E_{g_{1,b_n}, g_{2,b_n}} \{\log_2(1+\gamma_{21})\}$$
$$C_2 = E_{g_{1,b_n}, g_{2,b_n}} \{\log_2(1+\gamma_{12})\} \quad (5.15)$$

The achievable throughput at S_1 and S_2 are computed by

$$\tau_i^{DT} = C_i \times \frac{(1-\alpha)}{2} \quad (5.16)$$

where $i \in \{1, 2\}$

5.3.4 Results and Discussions

MATLAB Version 9.1.0.813654 (R2020b) based simulation results are summarized in this section. For simplicity, the distances between sources and relays are normalized to unit value. The parameters used in simulation are listed in Table 5.1 [23].

Table 5.1 Parameter assumptions.

Parameter	Meaning	Default values
η_α	EH efficiency for TS	0.7
η_ρ	EH efficiency for PS	0.7
γ_{th}	SNR threshold	7 dB [23]
P_S / N_O	Source power to noise ratio	0-30 dB
R_S	Source Rate	3 bps/Hz

The impact of SNR on the achievable throughput of the system in DL and DT transmission mode are shown in Fig. 5.3 (a) and (b) respectively. The proposed model is compared with the existing scheme [23]. Since ergodic capacity increases with SNR, the end-to-end SNR for PSP is minimum and for TSP it is maximum as observed from the plots. Hence, throughput in ARP is less than that in TSP. Since effective communication time is more in PSP than ARP or TSP, throughput for PSP is maximum.

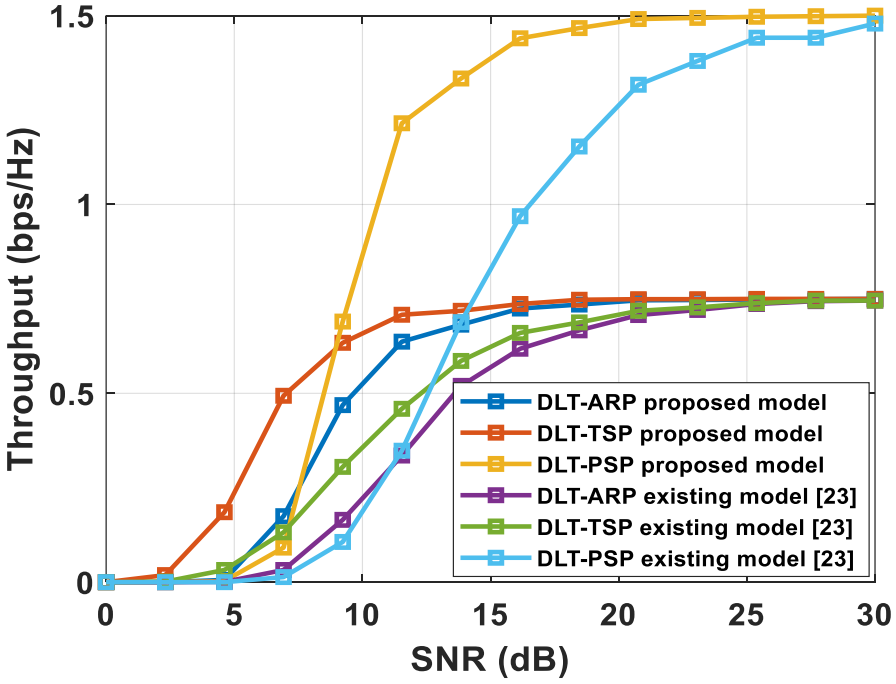

(a)

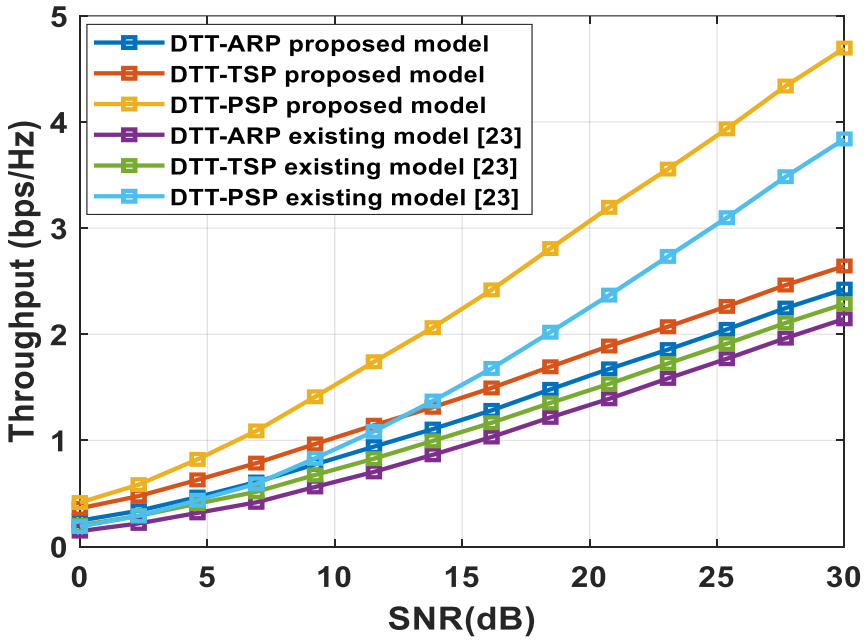

(b)

Fig. 5.3 Throughput vs SNR between the proposed model and the existing model [23] for **(a)** DL transmission mode **(b)** DT transmission mode

Fig. 5.4 (a) and (b) present the effect of variation of number of antennas in the relay nodes on throughput at DL and DT mode respectively.

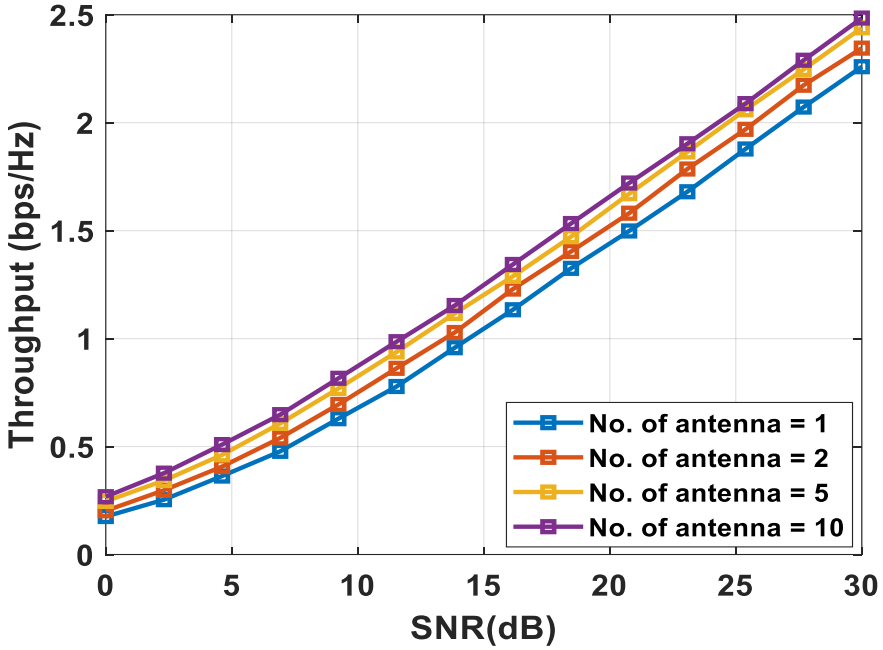

(a)

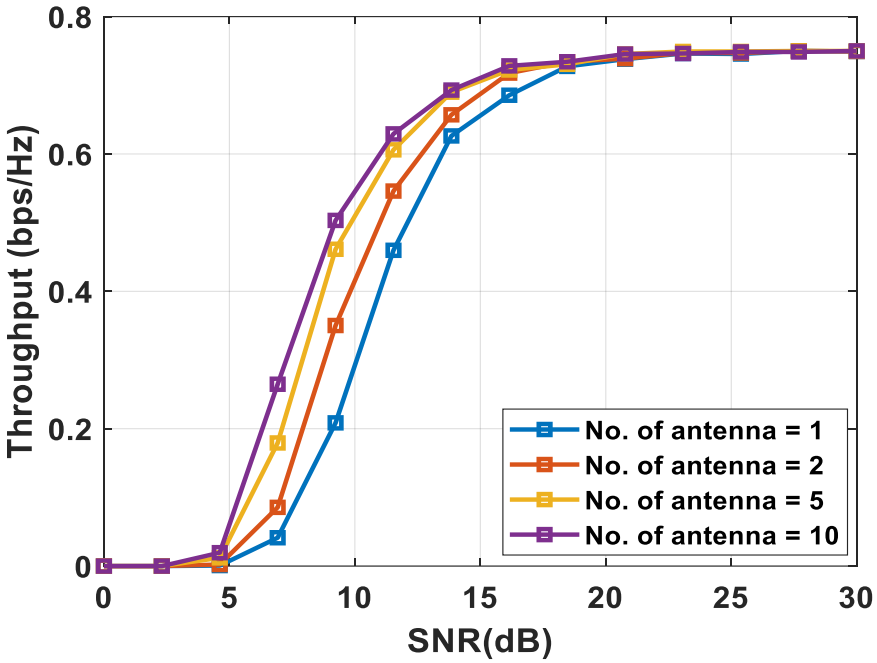

(b)

Fig. 5.4 Throughput vs SNR with the variation of number of antennas in relay nodes for **(a)** ARP-DL transmission **(b)** ARP-DT transmission

For both the cases, ARP has been considered. It is observed that as the number of antennas increases, throughput also increases for a fixed value of SNR. Since in the proposed multi-relay multi-antenna network information is transmitted by the antenna which harvests the maximum amount of energy, the probability that an outage will occur within a specified time period

decreases as the number of antennas increases. As a result, throughput increases with increase in number of antennas. Since there are multiple relay nodes between the end nodes and information transmission occurs via the maximum energy harvesting relay node only; more throughput is achieved in our model compared to the single relay model. A quantitative comparison between the two models is shown in the Table 2.

Table 5.2 Quantitative Analysis of Throughput

Quantity	Proposed	Existing [23]	% Improvement in Throughput
ARP-DLT at Ps/No=15 dB	0.69	0.55	25.45
ARP-TSP at Ps/No=15 dB	0.73	0.62	17.74
ARP-PSP at Ps/No=15 dB	1.38	0.82	68.29
ARP-DTT at Ps/No=15 dB	1.23	0.95	29.47
TSP-DTT at Ps/No=15 dB	1.41	1.07	31.78
PSP-DTT at Ps/No=15 dB	2.25	1.55	45.16

5.4 SECRECY PERFORMANCE OF IA-EH SCHEME IN AN UNTRUSTED SCENARIO

In this section, a single relay two-way relay network is described in details.

5.4.1 System Model

A Two-Way Communication (TWC) with MEH-AS technique is shown in Fig. 5.5 comprising of two sources (S_1 and S_2), two HD, DF relays DFR_1 and DFR_2 equipped with multiple antennas, an Interferer I and an Eavesdropper EAV. The energy-constrained relays collect energy from RF signals of their respective sources as well as from I. After performing Antenna Selection (AS) based on maximum harvested energy, the relays utilize that energy to transmit the data to S_1 and S_2. This system model is highly applicable in secure and energy-efficient IoT scenarios such as smart grid control systems, vehicle-to-vehicle (V2V) communications, or military-grade sensor networks, where bidirectional data exchange, energy sustainability, and secure transmission are paramount. The MEH-AS technique offers enhanced energy utilization without requiring additional power resources, while also contributing to physical layer security by complicating eavesdropping through unpredictable antenna selection.

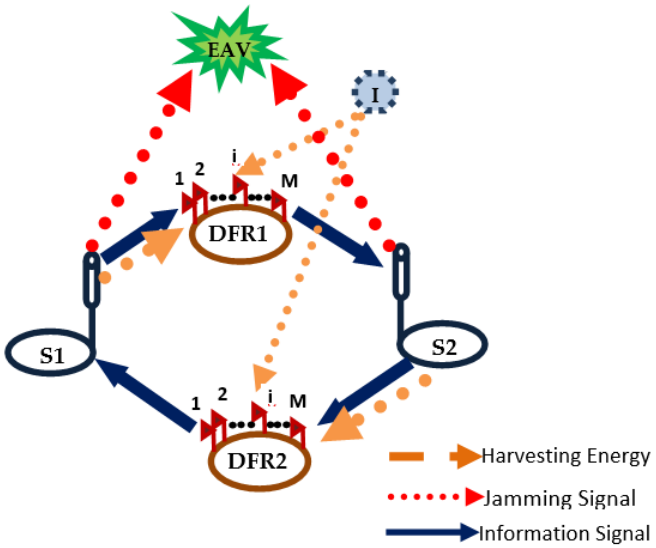

Fig 5.5 System model of TWC with MEH-AS technique

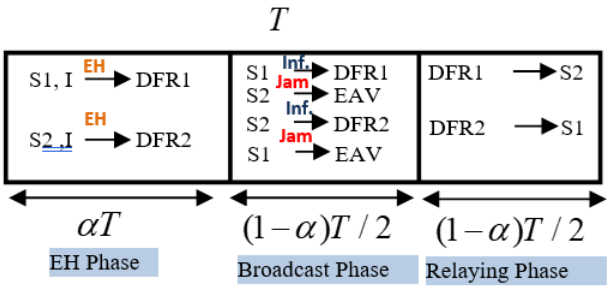

Fig. 5.6 Time frame structure of the system model

The following assumptions have been taken into account:

- Both the relays are deployed at approximately midpoint of S_1 and S_2.
- A single EAV is present in the communication coverage area but not within the loop, i.e, it only intercepts the data of either S_1 or S_2 in the broadcasting phase, but not in the relaying phase due to directional transmit and receive antennas of relays [97].
- Whenever the EAV attempts to overhear the data of S_1 by extracting the message, the signal of S_2 functions as a jamming (or AN) signal and vice versa [38].
- The relays have knowledge on full CSI of the main channels, i.e. S_1-to-DFR_1, DFR_1-to-S_2, S_2-to-DFR_2 and DFR_2-to-S_1.
- All the nodes operate in HD mode [1].
- There is no direct path between S_1 and S_2 due to severe fading [39].
- All channel links being statistically independent and experience Rayleigh fading [19].

The channel coefficients are indicated by $h_{i,j}$ where i, j indicate channel node that follow Rayleigh distribution; i and is the transmitting node and j is the receiving node. Thus, the instantaneous channel gains of these links are denoted by $g_{i,j} = \left|h_{i,j}\right|^2$.

The entire communication is shown in Fig. 5.6. The duration frame T is split into three Time Periods (TP): (a) EH TP αT ; (b) 1st TP $(1-\alpha)T/2$; (c) 2nd TP $(1-\alpha)T/2$. At EH TP, *DFR1* captures energy from the data received from *S1* and *I*. Simultaneously, *DFR2* harvests energy from the data received from *S1* and *I*. During 1st TP, *S1* and *S2* transmit data to *DFR1* and *DFR2* respectively. At this point, as soon as the *EAV* tries to tap the data of *S1* (or *S2*), the signal of *S2* (or *S1*) functions as jamming signal at the *EAV* and degrades the signal strength. At 2nd TP i.e the relaying phase, both the relays decode and then forward the signals to the respective destinations based on MHE-AS scheme with the assistance of directional antennas. At this moment, the EAV is unable to intercept the data relayed by either *DFR1* or *DFR2* presuming it is located at the null of the antennas.

5.4.2 Mathematical modelling

➢ *EH at DFR1 & DFR2*

In the EH phase at the relay nodes, the received signal at each relay node can be calculated as:

$$Y_r = \begin{bmatrix} y_{r1,1} & y_{r2,1} \\ y_{r1,2} & y_{r2,2} \\ \vdots & \vdots \\ y_{r1,M} & y_{r2,M} \end{bmatrix} = \left[(\sqrt{P_{s1}} + \sqrt{P_i})\mathbf{g}_1 \quad (\sqrt{P_{s2}} + \sqrt{P_i})\mathbf{g}_2 \right] \begin{bmatrix} x_1 \\ x_2 \end{bmatrix} + \mathbf{n}_\mathbf{r}^{[a]} \tag{5.17}$$

Thus the energy harvested by both relay nodes can be calculated as :

$$E_{HR_1} = \eta\alpha T \sum_{m=1}^{M} (P_{S1} g_{S1R} + P_I g_{IR_{1M}}) \tag{5.18}$$

$$E_{HR_2} = \eta\alpha T \sum_{m=1}^{M} (P_{S2} g_{S2J} + P_I g_{IR_{2M}}) \tag{5.19}$$

Before decoding, the instantaneous SINRs obtained are:

$$\gamma_{S_1R_{1M}} = \frac{P_{S_1} g_{SR_{1M}}}{P_I g_{IR_{1M}} + N_O} \tag{5.20}$$

$$\gamma_{S_2R_{2M}} = \frac{P_{S_2} g_{SR_{2M}}}{P_I g_{IR_{2M}} + N_O} \tag{5.21}$$

$$\gamma_{S_1E} = \frac{P_{S_1} g_{SR_{1M}}}{P_{S_2} g_{SR_{2M}} + N_O} \tag{5.22}$$

$$\gamma_{S_2E} = \frac{P_{S_2} g_{SR_{2M}}}{P_{S_1} g_{SR_{1M}} + N_O} \tag{5.23}$$

➢ *MHE-AS Scheme*

Both the relays select an antenna from a set of '*M'* antennas and transmit using the best selected antenna i.e. *i-th* antenna that harvests the maximum energy from both S_1, S_2 and *I*. The index of the selected antenna is given by:

$$i_{\Delta}^{*} = \underset{i\in\{1,2,....M\}}{\arg\max}\, E_{HR_{\Delta i}} \tag{5.24}$$

where $\Delta \in \{DFR1, DFR2\}$

Thus, energy harvested by the *i-th* antenna of the relays over the time slot αT can be written as:

$$E_{HR_{i^*_\Delta}} = \eta\alpha T(P_{S1} g_{S1R_{i^*_\Delta}} + P_I g_{IR_{i^*_\Delta}}) \tag{5.26}$$

where $g_{S1R_{i^*_\Delta}} = \underset{i\in\{1,2,....M\}}{\arg\max}\, g_{S1R_{\Delta i}}$

The transmit power of the *i-th* antenna of the relays is given as:

$$P_{R_{i^*_\Delta}} = \frac{E_{HR_{i^*_\Delta}}}{(1-\alpha)(T/2)} \tag{5.27}$$

Thus, the instantaneous SINRs obtained after decoding are given as:

$$\gamma_{R_{i^*1}S_2} = \frac{P_{R_{i^*1}} g_{R_{i^*1}S_2}}{P_I g_{IR_{1M}} + N_O} \tag{5.28}$$

$$\gamma_{R_{i^*2}S_1} = \frac{P_{R_{i^*2}} g_{R_{i^*2}S_1}}{P_I g_{IR_{2M}} + N_O} \tag{5.29}$$

Thus, end-to-end SINR is denoted as:

$$\gamma_{S_1S_2} = \min(\gamma_{S_1R_{1M}}, \gamma_{R_{i1}S_2}) \tag{5.30}$$

$$\gamma_{S_2S_1} = \min(\gamma_{S_2R_{2M}}, \gamma_{R_{i2}S_1}) \tag{5.31}$$

➢ *Secrecy Capacity (SC) Calculation*

The instantaneous SC at the two nodes can be expressed as [97]:

$$\left.\begin{aligned} C_{S_1S_2} &= \frac{1}{2}\log_2(1+\gamma_{S_1S_2}) \\ C_{S_2S_1} &= \frac{1}{2}\log_2(1+\gamma_{S_2S_1}) \end{aligned}\right\} \tag{5.32}$$

$$\left.\begin{aligned} C_{S_1E} &= \frac{1}{2}\log_2(1+\gamma_{S_1E}) \\ C_{S_2E} &= \frac{1}{2}\log_2(1+\gamma_{S_2E}) \end{aligned}\right\} \tag{5.33}$$

Now, the SC of each of the two-way links is expressed as [97]:

$$C_{S1}^{SEC} = [\frac{1}{2}\log_2(1+\gamma_{S_1S_2}) - \frac{1}{2}\log_2(1+\gamma_{S_1E})]^+ \tag{5.34}$$

$$C_{S2}^{SEC} = [\frac{1}{2}\log_2(1+\gamma_{S_2S_1}) - \frac{1}{2}\log_2(1+\gamma_{S_2E})]^+ \tag{5.35}$$

The Global Secrecy Rate (GSR) is expressed as [97]:

$$C_G^{SEC} = \left[\min(C_{S_1}^{SEC}, C_{S_2}^{SEC})\right]^+ \tag{5.36}$$

Now, Secrecy Outage Probability (SOP) can be defined as:

$$SOP = P(C_G^{SEC} < C_{th}) \tag{5.37}$$

5.4.3 Results and Discussions

To calculate the SC performance of the proposed system, simulation have been executed using Matlab version R2020a. The following parameters have been set accordingly as shown in Table 5.3.

Table 5.3 Parameter assumptions

Parameters	Meaning	Default Values
C_{th}	Secrecy Threshold	1 bps/Hz [97]
η	Energy Conversion Efficiency	0.8
α	EH coefficient	0.2
P_{S1}, P_{S2}	Source Transmit Powers	5 dBW [97]
P_I	Peak permissible Interferer Transmit Power	10 dBW
m	Path loss exponent	3

Fig. 5.7 gives a comparison of our proposed scheme with the contrast schemes in terms of EH coefficient.

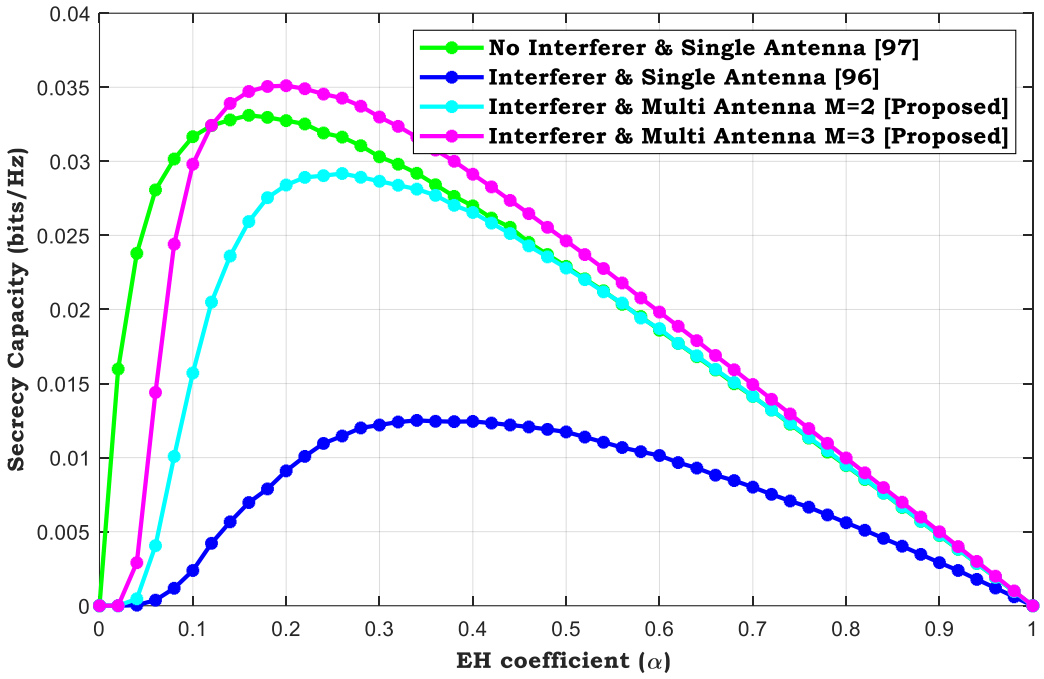

Fig. 5.7 Comparison of SC versus α for three scenarios (in absence of 'I' with M=1 [97], presence of 'I' with M=1 [96] and presence of 'I' with M=2, 3 [proposed])

The performance is significantly better in Interference limited system with single antenna relay [97] upto a certain value of α . It is also observed that for M=3, there exists a crossover point ($\alpha = 0.1$) beyond which the proposed scheme outperforms [97]. Taking a specific value of α i.e $\alpha = 0.3$, the percentage improvement in SC of proposed scheme over [97] and [96] are found to be 13.33% and 61.7% respectively.

In Fig. 5.8, the number of antennas has been varied and their impact on the secrecy capacity performance has been observed. Adding more number of antennas shifts the graph to the left and the system obtains higher secrecy performance at the cost of low EH coefficient i.e. EH time should be kept much less than the broadcast time to achieve the optimal SC. This is because the signal received from *I* provides energy for relay recharge and hence effectively reduces the optimal value of the EH coefficient. Hence peak secrecy can be achieved by not further increasing the EH time but by allocating the time for information transmission as a result of which reliable communication is affected. This indicates a trade-off between reliable communication and secure transmission since by increasing the amount of harvested energy, the available time for information transmission decreases and vice-versa. After M=7, the improvement in secrecy becomes minimal which provides a standard on the maximum number of antennas that can be placed so as to maximize the SC.

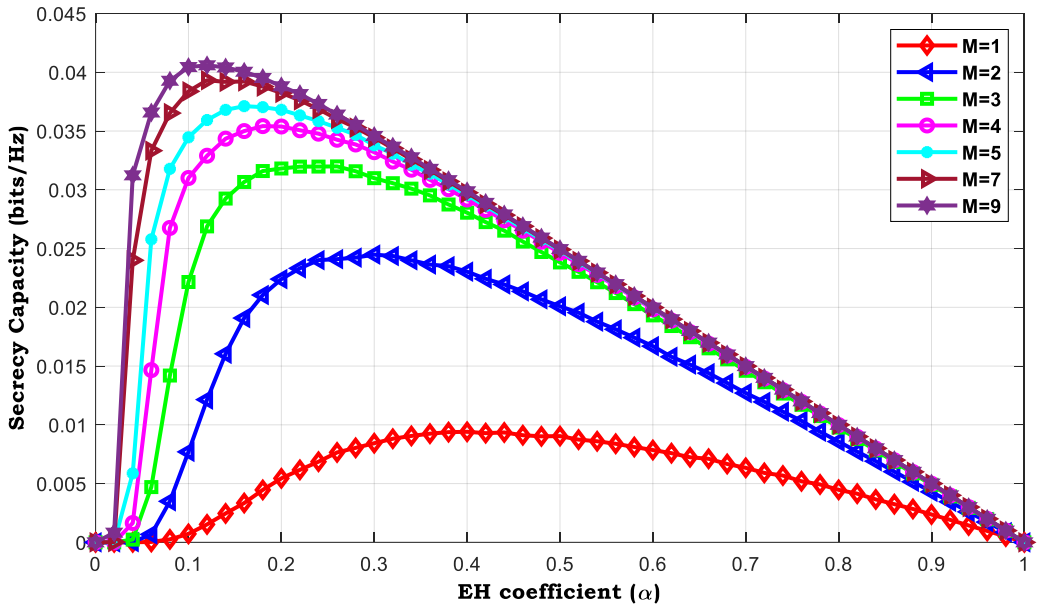

Fig. 5.8 SC versus α for varying M

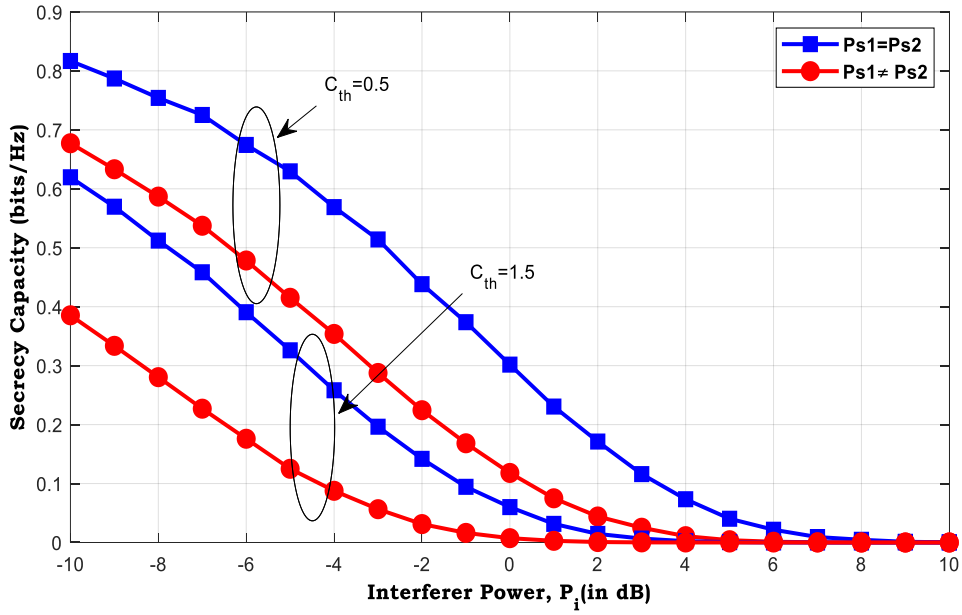

Fig. 5.9 Impact of SC w.r.t. P_I for equal and unequal transmit power of both the sources

Fig. 5.9 highlights a plot of SC versus P_I for equal and unequal transmit power of both the sources with varying C_{th} . It is found that the SC for equal transmission of both the sources is more compared to unequal transmission powers. This is because of the fact that for equal transmit power of *S1* and *S2*, the EAV gets maximum jamming from the sources and

eavesdropping capacity is minimized. Further, there is a performance degradation as Interferer Power is increased and SC goes flat. Flatness is due to good signal quality is received by EAV in broadcast phase since the effect of interference becomes dominant and the deteriorating effects of interference suppresses the gain obtained due to higher harvested energy.

5.5 SECURE TWO-WAY COMMUNICATION WITH IA-EH FOR NON-LINEAR SCENARIO

5.5.1 System model

In this section, the system description and channel modelling are provided in detail.

- ***Network Description***

A two-way IoT environment is considered in this work as shown in Fig. 5.10. A Low Power Wide Area Network (LPWAN) is considered under Rayleigh fading environment with a maximum range of 200 m. It comprises of two static IoT wireless devices (S_1 and S_2) that tries to exchange some confidential information among themselves. As the two sources are located far apart, they require the assistance of relays to support secure communication. The energy-constrained relays are equipped with rechargeable batteries which take part in harvesting energy from the respective RF sources as well as the surrounding CCIs ($I_1, I_2, ..., I_N$). Here, the signals from the surrounding base stations act as interference signals. The relays deployed in this environment are untrusted nodes i.e. apart from being mandatory helpers in communication process, they try to overhear the secret information of the sources. Perfect knowledge of CSI of jamming signals is available at both legitimate sources [101]. Thus, jamming signal gets fully removed from the received signal at the sources. This architecture is highly relevant for urban IoT applications, such as smart home systems, smart metering, or environmental monitoring in low-density areas where low-power, long-range communication is crucial. The adoption of LPWAN allows for energy-efficient communication with minimal overhead, making it well-suited for devices that are either battery-powered or require long battery life, such as sensors or actuators in remote locations. The total time frame structure T is accomplished in three scheduled time phases following TSR protocol [19] as depicted in Fig. 5.11.

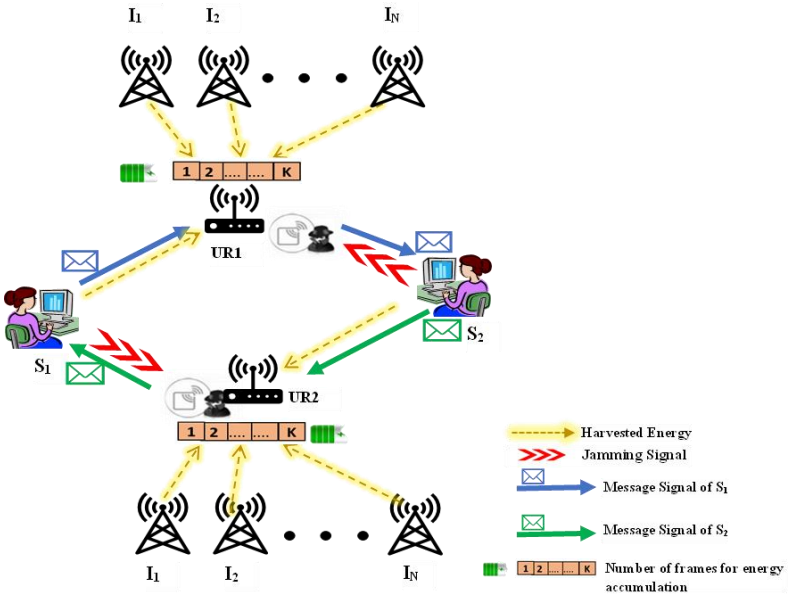

Fig. 5.10 System model of the proposed untrusted TWR network in interference-limited scenario

The following assumptions are considered:

- The untrusted relays are employed at approximately midpoint of both the sources.
- UR1 and UR2 are fitted with directional antennas such that they can intercept the signal of either S_1 or S_2 in the broadcasting phase only, but not in the relaying phase [38].
- All the nodes function in HD mode and configured with a single antenna [1].
- No direct connection exists between the sources due to long distance and strong fading [39].
- All the channel links experience Rayleigh fading [19].

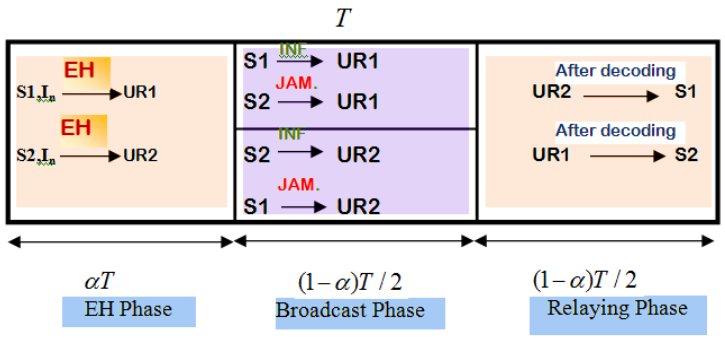

Fig. 5.11 Time frame structure (INF. indicates Information signal and JAM. indicates jamming signal)

➢ *Channel Modelling*

The PDF of channel coefficient and channel gain are expressed as:

$$\left.\begin{aligned} f_{h_{xy}}(x) &= \frac{x}{\sigma^2}\exp(-\frac{x}{2\sigma^2}); x \geq 0 \\ f_{g_{xy}}(x) &= \frac{1}{2\sigma^2}\exp(-\frac{x}{2\sigma^2}); x \geq 0 \end{aligned}\right\} \quad (5.38)$$

Following Rayleigh distribution, the channel gain coefficient between two communication nodes *X* and *Y* is indicated as h_{xy}. Considering the assumption that the channels follow independent and identically Rayleigh distribution (i.i.d.), $g_{xy} = \left|h_{xy}\right|^2$ denotes the channel gains between *X* and *Y*. Thus $\left|h_{S_1R_1}\right|^2, \left|h_{S_2R_2}\right|^2, \left|h_{R_1S_2}\right|^2, \left|h_{R_2S_1}\right|^2, \left|h_{I_1R_1}\right|^2$ and $\left|h_{I_iR_2}\right|^2$ are exponential random variables with parameters $\omega_1, \omega_2, \xi_1, \xi_2, \chi_1, \chi_2$ respectively and $\lambda_1 = \frac{N_O\omega_1}{P_{S_1}}, \lambda_2 = \frac{N_O\omega_2}{P_{S_2}}, \Omega_1 = \frac{N_O\xi_1}{P_{R_1}}, \Omega_2 = \frac{N_O\xi_2}{P_{R_2}}$, $\mu_1 = \frac{N_O\chi_1}{P_{I_i}}, \mu_2 = \frac{N_O\chi_2}{P_{I_i}}$.

5.5.2 Mathematical modelling

In this section, the network is evaluated in the non-linear scenario where the harvested power is saturated to a maximum power value for the high input power at EH circuit.

- ***EH and data communication for 'K' frames in linear scenario***

The received signal at the relays can be expressed as:

$$y_{R_1}^k = \sqrt{P_{S_1}}h_{S_1R_1}^k x_1 + \sum_{i=1}^{N}\sqrt{P_{I_i}}h_{R_1I_i}^k x_I + n_{R_1} \quad (5.39)$$

$$y_{R_2}^k = \sqrt{P_{S_2}}h_{S_2R_2}^k x_2 + \sum_{i=1}^{N}\sqrt{P_{I_i}}h_{R_2I_i}^k x_I + n_{R_2} \quad (5.40)$$

The energy is accumulated in relay's battery up to *K*-th frame as given below:

$$E_{R_{1k}} = \eta\alpha\frac{T}{2}\sum_{k=1}^{K}\left(P_{S_2}g_{S_1R_k} + \sum_{i=1}^{N}P_{I_i}g_{R_kI_i}\right) \quad (5.41)$$

$$E_{R_{2k}} = \eta\alpha\frac{T}{2}\sum_{k=1}^{K}\left(P_{S_2}g_{S1R_{2k}} + \sum_{i=1}^{N}P_{I_i}g_{R_{2k}I_i}\right) \quad (5.42)$$

where $E_{R_{1k}}$ and $E_{R_{2k}}$ are the harvested energy at UR1 and UR2 in *K*-th frame, η is the power conversion efficiency of the harvester. The power transmitted in this duration is given as:

$$P_{R_{1k}} = \eta\alpha\sum_{k=1}^{K}(P_{S_1}g_{S_1R_{1k}} + \sum_{i=1}^{N}P_{I_i}g_{R_{1k}I_i}) \quad (5.43)$$

$$P_{R_{2k}} = \eta\alpha \sum_{k=1}^{K} (P_{S_2} g_{S_2 R_{2k}} + \sum_{i=1}^{N} P_{I_i} g_{R_{2k} I_i}) \tag{5.44}$$

➢ *RF EH for non-linear mode*

In practical scenario, the RF harvester is nonlinear and the DC output power of EH circuit depends on a fixed power saturation threshold P_{th}. The threshold P_{th} depends on the frequency of incoming RF signals and type of the harvesting circuit (linear or non-linear). In general, P_{th} ranges from −30 dB to −5 dB [112]. The received signal at the relays in non-linear mode for 'k' frames can be expressed as:

$$y_{R_1}^k = \sqrt{P_{S_1}} h_{S_1 R_1}^k (x_1 + \eta_1) + \sum_{i=1}^{N} \sqrt{P_{I_i}} h_{R_1 I_i}^k x_I + n_{R_1} \tag{5.45}$$

$$y_{R_2}^k = \sqrt{P_{S_2}} h_{S_2 R_2}^k (x_2 + \eta_2) + \sum_{i=1}^{N} \sqrt{P_{I_i}} h_{R_2 I_i}^k x_I + n_{R_2} \tag{5.46}$$

where η_1 and η_2 are the distortion noises caused by the transmit hardware impairments at S_1 and S_2, respectively; and we can model η_1 and η_2 as circularly symmetric complex Gaussian distribution with zero-mean and variance κ^2, i.e., $\eta_1 \sim CN(0, \kappa^2)$ and $\eta_2 \sim CN(0, \kappa^2)$ where $\kappa^2 \geq 0$ characterizes the level of impairment at the transmitter (3GPP LTE has EVM requirements in the range $\kappa \in [0.08, 0.175]$ [70, Sec. 14.3.4]).

Accordingly, the harvested energy with non-linear circuit at the relay nodes can be obtained as shown below:

$$E_{R_{NL}} = \begin{cases} \eta\alpha T (P_{S1} g_{S1R} + \sum_{i=1}^{N} P_{I_i} g_{RI_i}) & ; P_{S1} g_{S1R} + \sum_{i=1}^{N} P_{I_i} g_{RI_i} \leq P_{th} \\ \eta\alpha T P_{th} & ; P_{S1} g_{S1R} + \sum_{i=1}^{N} P_{I_i} g_{RI_i} > P_{th} \end{cases} \tag{5.47}$$

Thus, the power transmitted by the relays is given as:

$$P_{R_{NL}} = \begin{cases} \eta\alpha (P_{S1} g_{S1R} + \sum_{i=1}^{N} P_{I_i} g_{RI_i}) & ; P_{S1} g_{S1R} + \sum_{i=1}^{N} P_{I_i} g_{RI_i} \leq P_{th} \\ \eta\alpha P_{th} & ; P_{S1} g_{S1R} + \sum_{i=1}^{N} P_{I_i} g_{RI_i} > P_{th} \end{cases} \tag{5.48}$$

Proposition 1. *The closed form expression for accumulated harvested energy can be formulated as:*

$$E_{R_1}^k = \left[\eta\alpha \frac{T}{2} P_{S1} \int_0^\infty \frac{x^K}{\mu_{SR}^K \Gamma(K)} \exp\left(-\frac{x}{\mu_{SR}} \right) dx \right] + \left[P_{I_i} \int_0^\infty \left(\frac{K}{\eta\alpha\mu_{IR}} \right)^{KN} \frac{x^{KN-1}}{\Gamma(KN)} \exp\left(-\frac{Kx}{\eta\alpha \frac{T}{2} \mu_{IR}} \right) dx \right]$$

$$\Rightarrow E_{R_1}^k = \eta\alpha \frac{T}{2} P_{S_1} K \mu_{SR} + \left(\frac{K}{\eta\alpha \frac{T}{2} \mu_{IR}} \right)^{KN} \frac{P_{I_i}}{\Gamma(KN)} \tag{5.49}$$

A formal proof of (5.49) is provided in Section C.1 of Appendix C

5.5.3 SINR estimation

Here the SINR expressions for main channel links during broadcast phase are expressed as:

$$\gamma_{S_1 R_{1k}} = \frac{P_{S_1} g_{S_1 R_{1k}}}{\sum_{i=1}^{N} P_{I_i} g_{I_i R_{1k}} + P_{S_2} g_{S_2 R_{1k}} + N_O} \tag{5.50}$$

$$\gamma_{S_2 R_{2k}} = \frac{P_{S_2} g_{S_2 R_{2k}}}{\sum_{i=1}^{N} P_{I_i} g_{I_i R_{2k}} + P_{S_2} g_{S_2 R_{1k}} + N_O} \tag{5.51}$$

The relays being untrusted, try to intercept the information signals of both the transmitters during broadcasting phase. At this point, whenever relay UR1 tries to overhear the information of S_1, the information signal of S_2 acts as a jamming to the relay and vice versa. The SINRs for the wiretap links are given as:

$$\gamma_{S_2 R_{1k}} = \frac{P_{S_2} g_{S_2 R_{1k}}}{N_O} \tag{5.52}$$

$$\gamma_{S_1 R_{2k}} = \frac{P_{S_1} g_{S_1 R_{2k}}}{N_O} \tag{5.53}$$

where $P_{S_2} g_{S_2 R_{1k}}$ and $P_{S_1} g_{S_1 R_{2k}}$ are the jamming signals from S_1 to UR2 and S_2 to UR1 respectively. At relaying phase, the corresponding SINR at UR1 and UR2 after information decoding is expressed as under:

$$\gamma_{R_{1k} S_2} = \frac{P_{R_{1k}} g_{R_{1k} S_2}}{\sum_{i=1}^{N} P_{I_i} g_{I_i R_{1k}} + N_O} \tag{5.54}$$

$$\gamma_{R_{2k}S_1} = \frac{P_{R_{2k}} g_{R_{2k}S_1}}{\sum_{i=1}^{N} P_{I_i} g_{I_i R_{1k}} + N_O} \tag{5.55}$$

Therefore, the end-to-end SINR for both the paths can be expressed as:

$$\gamma^{k}_{S_1S_2} = \min(\gamma_{S_1R_{1k}}, \gamma_{R_{1k}S_2}) \tag{5.56}$$

$$\gamma^{k}_{S_2S_1} = \min(\gamma_{S_2R_{2k}}, \gamma_{R_{2k}S_1}) \tag{5.57}$$

5.5.4 Performance analysis

The key secrecy performance metrics are considered as SOP and ASC whose closed form expressions are derived below:

➢ *SOP Analysis*

Secrecy Capacity (SC) is the maximum rate of confidential message that is sent from source to destination under the threat of *EAV*s and is determined from the difference between main channel capacity and wiretap channel capacity. The expressions for SC of each of the two-way links from S_1-S_2 and S_2-S_1 is given as [75]:

$$C_{S1}^{SEC} = [\frac{1}{2}\log_2(1+\gamma_{S_1S_2}) - \frac{1}{2}\log_2(1+\gamma_{S_2R_1})]^{+} \tag{5.58}$$

$$C_{S2}^{SEC} = [\frac{1}{2}\log_2(1+\gamma_{S_2S_1}) - \frac{1}{2}\log_2(1+\gamma_{S_1R_2})]^{+} \tag{5.59}$$

where $\gamma_{S_1S_2}$ and $\gamma_{S_2S_1}$ are the SINRs for links S_1-S_2 and S_2-S_1 respectively. Similarly, $\gamma_{S_2R_1}$ and $\gamma_{S_1R_2}$ are SINRs for jamming signals from S_2-*UR1* and S_1-*UR2* respectively.

Global threshold secrecy rate (GSR) C_{th}^{Sec} is expressed as [81]:

$$C_{th}^{Sec} = \left[\min(C_{S_1}^{SEC}, C_{S_2}^{SEC})\right]^{+} \tag{5.60}$$

Secrecy outage occurs when secrecy capacity C_{th}^{SEC} drops below a predetermined threshold R_{th} > 0 (bps/Hz). Therefore, the SOP can be expressed as:

$$SOP = P(C_{th}^{SEC} < R_{th}) \tag{5.61}$$

$$= P(\min(C_{S1}^{SEC}, C_{S2}^{SEC}) < R_{th})$$

$$= 1 - \{P(C_{S1}^{SEC} > R_{th})\}\{P(C_{S2}^{SEC} > R_{th})\}$$

$$= 1 - \{1 - \underbrace{P(C_{S1}^{SEC} < R_{th})}_{P_1}\}\{1 - \underbrace{P(C_{S1}^{SEC} < R_{th})}_{P_2}\}$$

$$= 1 - [1 - P_1][1 - P_2] \tag{5.62}$$

Proposition 2. *The closed form expression for SOP can be formulated as:*

$$SOP = 1 - \left[\left[\exp(-Z) \frac{1}{\Gamma(\mathrm{K})} 2 \sqrt{\left(\frac{A_2 A_3}{\lambda_1 \Omega_1} \right)^{K}} K_K \left(2 \sqrt{\left(\frac{A_2 A_3}{\lambda_1 \Omega_1} \right)} \right) \right]^N \left[\exp(-Y) \frac{1}{\Gamma(\mathrm{K})} 2 \sqrt{\left(\frac{B_2 B_3}{\lambda_2 \Omega_2} \right)^{K}} K_K \left(2 \sqrt{\left(\frac{B_2 B_3}{\lambda_2 \Omega_2} \right)} \right) \right]^N \right] \quad (5.63)$$

A formal proof of (5.63) is provided in Section C.2 of Appendix C

- ***ASC Analysis***

Based on the definition given in [70], ASC is obtained by subtracting the wiretap channel capacity from the legitimate channel capacity.

$$ASC = E\{\log_2(1+x)\} = \int_0^{\infty} \log_2(1+x) f_x(x) dx$$

where, $x \triangleq min(C_{S_1}^{SEC}, C_{S_2}^{SEC})$

$$ASC = \left\{ \log_2(1+x)[F_X(x)-1] \right\}_0^{\infty} - \frac{1}{2\ln 2} \int_0^{\infty} [F_X(x)-1] dx = \frac{1-\alpha}{2\ln 2} \left(\int_0^{\infty} \frac{1-F_{C_{S_1}^{SEC}}(\mathrm{R}_{th})}{1+\mathrm{R}_{th}} dR_{th} + \int_0^{\infty} \frac{1-F_{C_{S_1}^{SEC}}(\mathrm{R}_{th})}{1+\mathrm{R}_{th}} dR_{th} \right) \quad (5.64)$$

where $F_{C_{S_1}^{SEC}}(\mathrm{R}_{th}) = \left\{ P(C_{S_1}^{SEC} < R_{th}) \right\}$ and $F_{C_{S_2}^{SEC}}(\mathrm{R}_{th}) = \left\{ P(C_{S_2}^{SEC} < R_{th}) \right\}$ are the CDFs of $C_{S_1}^{SEC}$ and $C_{S_2}^{SEC}$ respectively.

5.5.5 Results and Discussions

The validation of the proposed system model is carried out through simulation using Matlab 2021b and compared with the existing benchmarks to quantify the secrecy performance improvement. Table 5.4 shows the numerical values of the relevant parameters.

Fig. 5.12 depicts the variation of SOP versus P_S for several values of P_R. Here, signal transmission with equal power from both the transmitters (i.e $P_{S_1} = P_{S_2} = P_S$) is considered. As illustrated in the figure, the SOP performance degrades with increasing value of P_S . The performance of the proposed system is compared with three existing works i.e. *IA TWR Network without jamming [108], Interference-free OWR network with jamming[111] and IA-OWR network with FD* jamming [114]. For a fair comparison, transmit power of the relays are pre-set according to [111] and the impact on SOP is observed. The SOP of the network is found to be more for lower values of P_R and reduces with further increase in P_R .It is also seen that the secrecy performance of the proposed scheme and the other works [114] and [111] with jamming schemes is much better than that of the contrast network without jamming [108]. On

further comparison with OWR networks [111] and [114], it has been observed that the proposed network model achieves the lowest SOP. For $P_S = 15dB$, an SOP value of 10^{-3} is obtained for the proposed model as opposed to 10^{-1} and 10^{0} for [114] and [108] respectively. In addition, a similarity between theoretical and simulation results verifies the correctness of the theoretical derivations with the simulated results.

Table 5.4 Parameter assumptions

Parameter	Meaning	Default values
R_{th}	Target bit rate	1 bps/Hz
η	Energy conversion efficiency for source	0.7 [111]
α	EH coefficient	0.2
m	Path loss exponent	3
P_{S_1}, P_{S_2}	Source Transmit Power	10 dB [111]
N_O	AWGN Power	0.01 W [111]

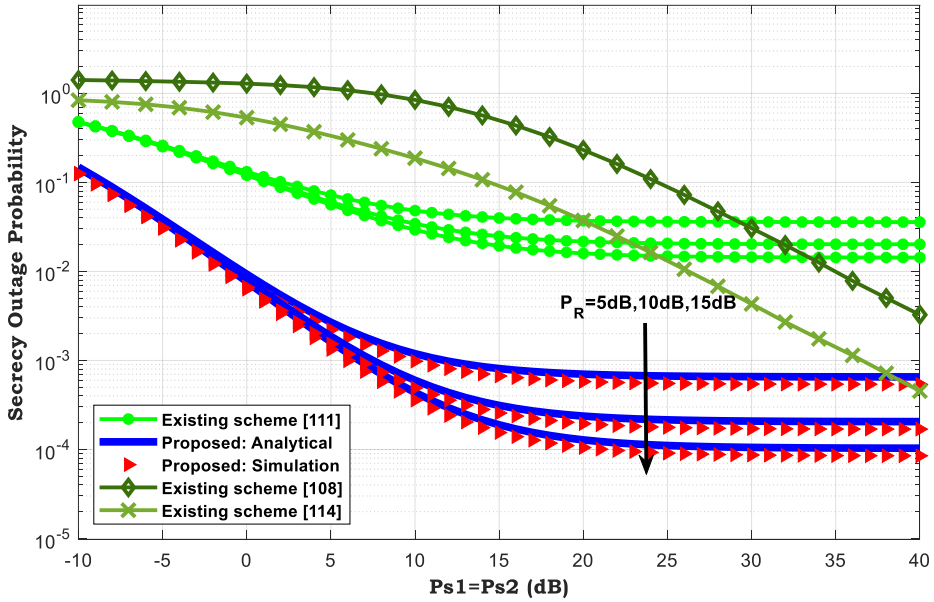

Fig. 5.12 Comparison plot of SOP versus P_S for different values of $P_R = 5,10,15$ dBW

The secrecy performance comparison between the conventional scheme [70] and the proposed system considering non-linear approach is displayed in Fig. 5.13. For a fair comparison with [70], Rayleigh faded channel parameter is set as ($m_1 = m_2 = 1$) and non-linear distortion parameter is considered as 0.08. It clearly shows that the proposed model with energy accumulation significantly outraces the conventional approach. On increasing the number of frames, the accumulated energy at the relays gets increased which contributes to improvement in secrecy performance of the network. But at higher values of P_S i.e. beyond 5dB,

improvement in secrecy is minimal with increase in K. Moreover, the system secrecy capacity saturates when the transmit power is sufficiently high. This reveals the fact that the relay battery has a finite storage capacity because of which the accumulated energy cannot exceed the battery capacity. This study imposes a limitation on the maximum number of allowable frames that can be utilized for energy accumulation to maximize the network security.

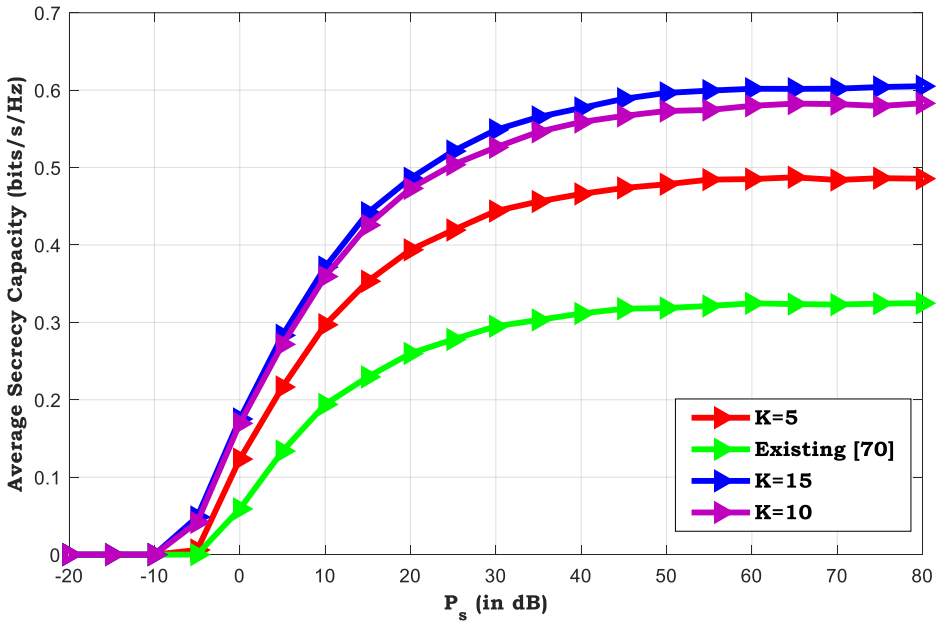

Fig. 5.13 The effect of transmit power on the ASC

Table 5.5 shows a comparison of our scheme with [70] with increasing K in terms of ASC.

Table 5.5 Average secrecy capacity for K=5,10,15 with variation in P_S

Parameter P_S (in dB)	**ASC (in bps/Hz)**			
	[70]	**Proposed**		
		K=5	**K=10**	**K=15**
0	0.06	0.12	0.17	0.175
20	0.25	0.39	0.47	0.486
40	0.31	0.465	0.55	0.576
60	0.32	0.485	0.58	0.62

In Fig. 5.14, the effect of EH coefficient α on the ASC is shown and compared with the existing benchmarks (i.e IA-EH in TWR network [81] and TWR network in interference-free environment [80]).

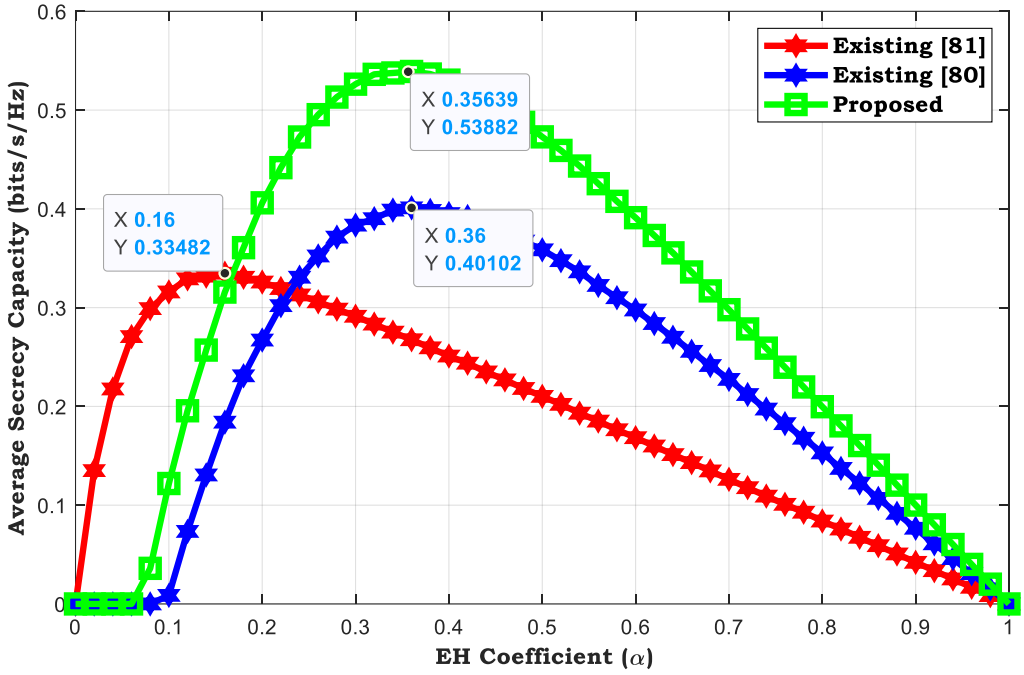

Fig. 5.14 The impact of α on ASC for both trusted and untrusted scenarios

From Fig. 5.15a, b and c, it is seen that the accumulated energy keeps on increasing linearly with 'K' keeping 'N' fixed at 3 and gradually increasing P_S. The variation of E_R / T (in Joules) versus 'K' for $N = 3$ is shown in Table 5.6. From Fig. 5.15c and Fig. 5.15d, as the number of interferers is increased from $N = 3$ to $N = 5$ keeping P_S value fixed at 10dB, a minimal decrease in the value of E_R has been found. Table 5.7 depicts percentage decrease in harvested energy.

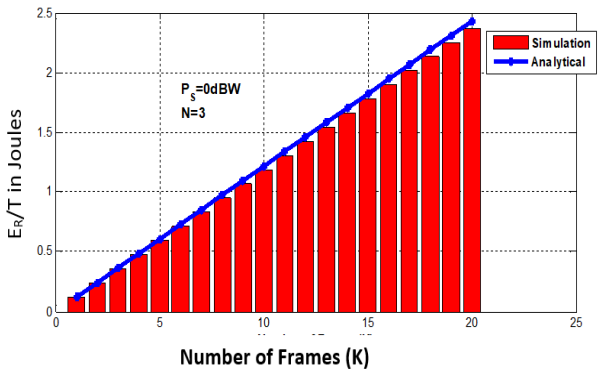

(a)

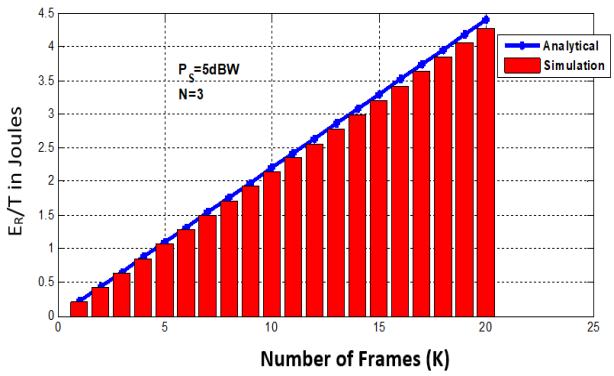

(b)

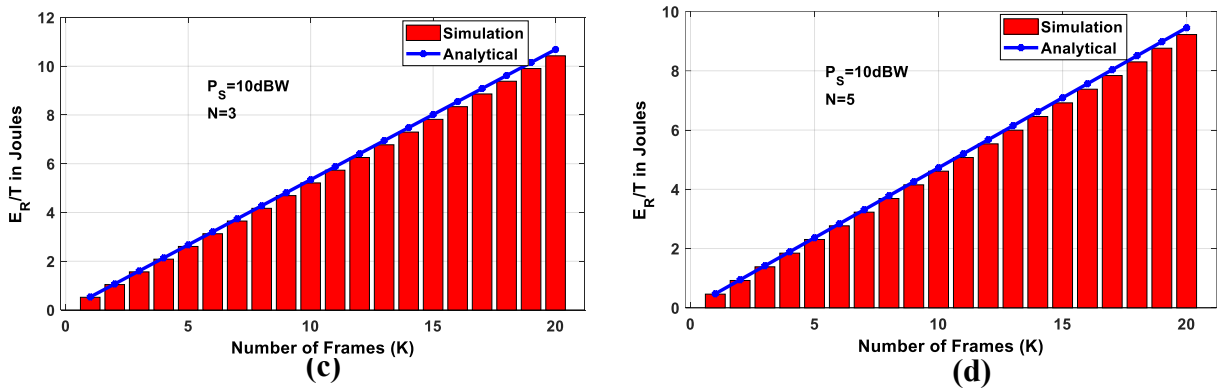

Fig. 5.15 Accumulated harvested energy versus K with variation in source transmit power and number of CCIs

Fig. 5.16 compares the secrecy capacity of the developed network for nonlinear and linear scenarios. It can be observed that the linear approach gives better secrecy than non-linear at relatively low EH coefficient. For $P_{th} = -10dB$, the secrecy is maintained upto $\alpha = 0.57$. On increasing the saturation threshold $P_{th} = -5dB$, maximum secrecy is achieved at $\alpha = 0.35$ beyond which the secrecy falls. An ASC value of 0.3 bps/Hz is obtained for linear EH model at $\alpha = 0.2$, where for $P_{th} = -5dB$ and $P_{th} = -10dB$, the ASC values of 0.2 and 0.12 are obtained at $\alpha = 0.36$ and $\alpha = 0.54$ respectively, for nonlinear scenario. The comparative analysis of the proposed scheme for both the approaches is presented in Table 5.6. For a particular value of α= 0.1, the percentage improvement in ASC of the proposed framework for linear approach over non-linear, at a saturation threshold of -5dB and -10dB is observed as 65% and 88% respectively that falls to 12.8% and 20% at $\alpha = 0.7$. The comparative analysis of the proposed scheme for both the approaches is presented in Table 5.6. For a particular value of α= 0.1, the percentage improvement in ASC of the proposed framework for linear approach over non-linear, at a saturation threshold of -5dB and -10dB is observed as 65% and 88% respectively that falls to 12.8% and 20% at $\alpha = 0.7$. Fig. 5.17 plots the amount of harvested energy versus number of frames 'K' under non-linear scenario, for the Ps value of 0dB. Here, the accumulated energy increases exponentially with increase in 'K'. On comparing with Fig. 5.15 (c) and (d), initially, a significant enhancement in accumulated energy is obtained for linear model as compared to non-linear scheme. The percentage improvement in harvested energy for both linear and non-linear scenarios with respect to the number of frames is calculated and shown in Table 5.7.

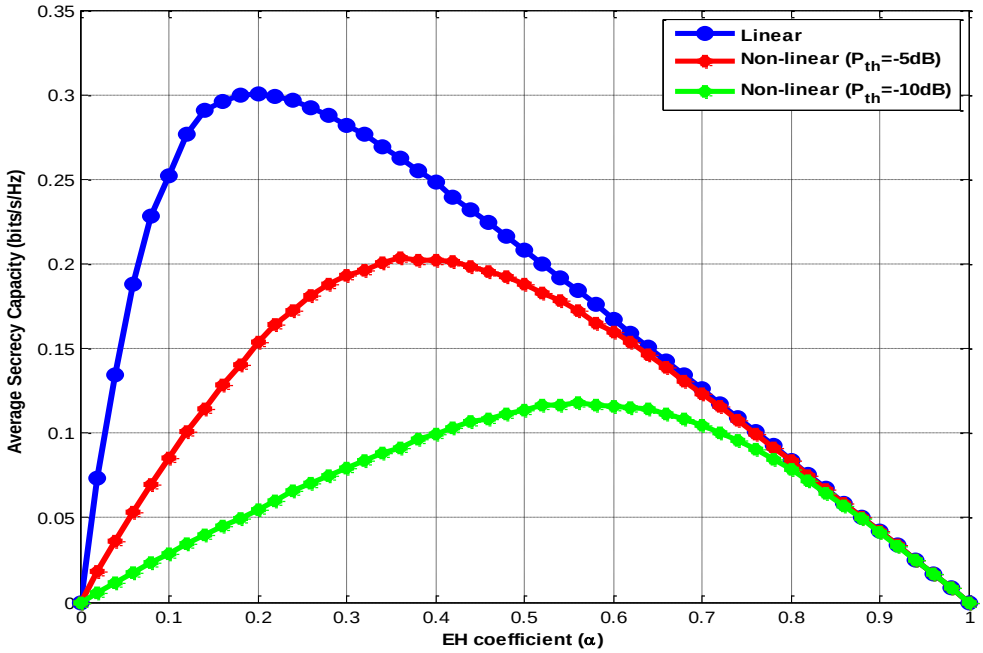

Fig. 5.16 The impact of α on the ASC for nonlinear and linear EH scenarios

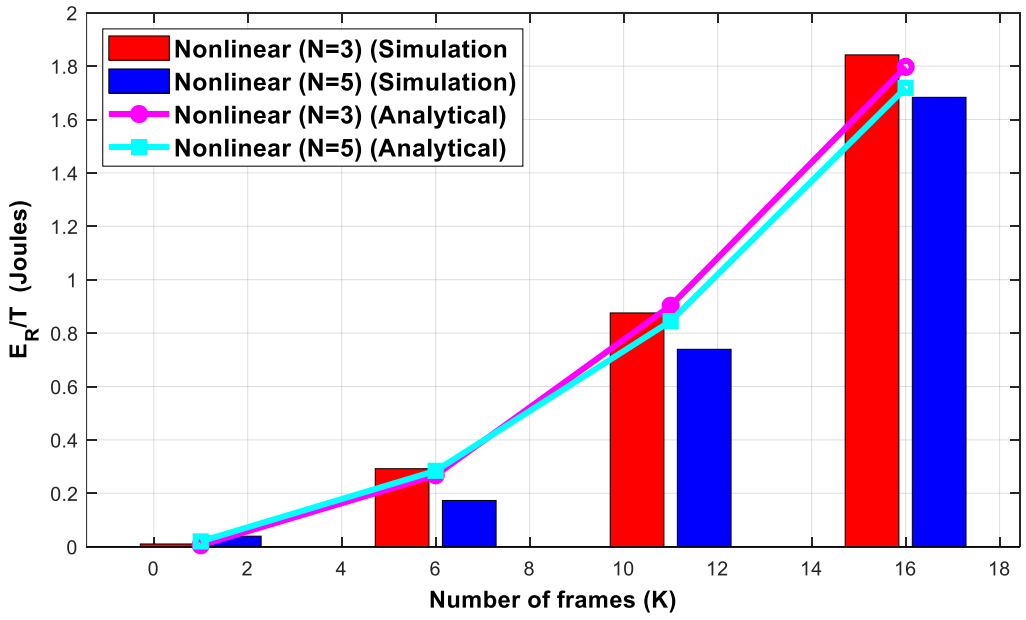

Fig. 5.17 Accumulated Harvested Energy versus K for N=3,5 under nonlinear approach for $P_S = 0dB$

Table 5.6 Comparative secrecy performance analysis for linear and non-linear scenarios

Parameter α	**Average Secrecy Capacity (ASC)**			**% Improvement in ASC**	
	Linear	**Non-Linear**			
		$P_{th} = -5dB$	$P_{th} = -10dB$	**Linear over Non-linear (-5dB)**	**Linear over Non-linear (-10dB)**
0.1	0.25	0.0875	0.03	65	88
0.3	0.28	0.19	0.075	32.14	73.21

0.5	0.22	0.18	0.1125	22.22	48.86
0.7	0.125	0.122	0.109	12.8	20
0.9	0.049	0.048	0.048	2	2.04

Table 5.7 Percentage improvement in accumulated harvested energy for linear and non-linear scenarios

Parameter No. of frames (*K*)	E_R / T ***(For N=3, Ps=0dBW)***		**%Improvement in** E_R / T	E_R / T ***(For N=5, Ps=0dBW)***		**%Improvement in** E_R / T
	Linear	***Non-Linear***		***Linear***	***Non-Linear***	
5	0.6	0.3	50	1.1	0.19	82.72
10	1.2	0.85	29.17	2.1	0.75	64.28
15	1.82	1.8	1.09	3.2	1.7	46.88

5.6 OVERALL COMPARISON

A critical study and comparison of the above three works namely, Proposed Work 1, Proposed Work 2 and Proposed Work 3 are presented in section 5.3, 5.4 and 5.5 respectively with some of the existing relevant state-of-art have been abridged in Table 5.8 and 5.9.

Table 5.8 Comparison table with existing relevant state-of-art

Existing/Proposed Works	**Scenarios**	**CCI Introduced**	**EAV/Untrusted Relay**	**One-way/Two-way**	**Linear/Non-Linear**	**Performance metric**
	Existing Works					
[23]	Single-Antenna TWR network	absence of CCI	EAV absent	Two-way	Linear	Throughput
[96]	Interferer & Single antenna	presence of CCI	No EAV	Two-way	Linear	OP
[97]	No Interferer & single antenna	absence of CCI	Single EAV, DBJ technique	Two-way	Linear	SOP
[70]	untrusted unidirectional relay network with EH	absence of CCI	Untrusted Relay, DBJ technique	One-way	Non-linear	ASC
[111]	Interference-free OWR	absence of CCI	Single EAV	One-way	Linear	SOP

	network with jamming					
[116]	Full-Duplex Cognitive Radio Network	absence of CCI	No EAV	One-way	Nonlinear	BER
[81]	TWR network	presence of CCI	Single EAV, Jamming cancellation	Two-way	linear	ASC
[108]	TW cognitive radio network	absence of CCI	No EAV	Two-way	-	OP
[80]	RF-powered TWR network	absence of CCI	Two-sided EAV (FD) relaying jamming scheme	Two-way	Linear	SR
[79]	EH communication network	absence of CCI	No EAV	One-Way	Linear	Throughput, BER
[114]	EH spectrum sharing network	absence of CCI	Single EAV and FD DBJ	One-way	Non-Linear	OP
Proposed Works						
Proposed Work 1	*ARP for Bidirectional Multi-Relay Multi-antenna Cooperative Network*	*absence of CCI*	*No EAV*	*Two-way*	*Linear*	*Throughput*
Proposed Work 2	*Secure MHE-AS scheme in TWC via Two Multi-Antenna Relays with Interference-aided EH.*	*presence of CCI*	*Single EAV*	*Two-way*	*Linear*	*ESR*
Proposed Work 3	*Interference-assisted RF-powered IoT relay network*	*presence of CCI*	*Untrusted Relays*	*Two-way*	*Nonlinear*	*SOP, ASC, Accumulated Harvested Energy*

Table 5.9 Critical Analysis with existing works

Performance Metrics	**Existing/Proposed Works**		**Throughput (bits/s/Hz)**	**SOP**	**ASC**	**Accumulated Harvested Energy**
Throughput	**[23]**	ARP-DLT ARP-TSP	0.55 0.62	-	-	-

		ARP-PSP ARP-DTT TSP-DTT PSP-DTT	0.82 0.95 1.07 1.55			
	Proposed Work 1	ARP-DLT ARP-TSP ARP-PSP ARP-DTT TSP-DTT PSP-DTT	0.69 0.73 1.38 1.23 1.41 2.25	-	-	-
Secrecy Capacity	**[97]**	TSR	-		0.021	-
	[96]	TSR	-		0.01	
	Proposed Work 2	TSR			0.035	
SOP, ASC & Accumulated Harvested Energy	**[70]**	PSR	-	0.3	K=1: 0.32	-
	Proposed Work 3	TSR	-	0.06	K=5: 0.485	2.45
					K=10: 0.58	5.1
					K=15: 0.62	7.8
	[81]	TSR	-	-	0.38	-
	[80]	TSR	-	-	0.29	-
	Proposed Work 3	TSR	-	-	0.53	-
	[111]	TSR	-	1	-	2.6
	[114]	TSR	-	0.1	-	3.5
	Proposed Work 3	TSR	-	0.001	-	7.68

5.7 DISCUSSION

In this chapter, the system performance of a bidirectional AF HD multi-antenna multi-relay network over the Nakagami fading environment is presented in Proposed Work 1. Here, the impactof different system parameters on the throughput performance of the system is also studied. Next, the Proposed Work 2 with MHE-AS scheme is shown to improve the SC performance significantly as compared to its contrast models where bidirectional communication takes place in presence or absence of CCI and the relays are equipped with a single antenna. Lastly, an IoT environment is designed in Proposed work 3, where the relays collocated with EAVs are equipped with a rechargeable battery so that they can harvest and accumulate the harvested energy from RF signals sent by the sources and CCIs, for stable operation of the network. The obtained results for both linear and non-linear scenarios are compared with each other which gives a useful insight to the network secrecy performance.

Chapter 6

RF ENERGY HARVESTING IN NOMA-ENABLED WIRELESS NETWORKS

6.1 OVERVIEW

The present chapter focuses on analysing the secrecy performance of an RF-powered two-user Cooperative Non-orthogonal Multiple Access (CR-NOMA) in presence of a cluster of CCIs under jamming cancellation scheme. The influence of various network parameters such as the source transmission power, Nakagami-m parameter, Jamming Signal Power and the number of CCIs on the system secrecy performance has been evaluated. Additionally, the impact of power allocation factor for varying transmit power of source on the Ergodic Secrecy Rate (ESR) has been found. In the next section, the performance of an autonomous and energy-efficient RF-powered Multi-Device Diamond Relay Network (MD-DRN) in an IoT environment using an improved Adaptive NOMA (A-NOMA) protocol has been studied. Closed form expressions of Achievable Sum Rate (ASR) and Energy Efficiency (EE) have been derived under Rayleigh fading environment and validated through extensive monte-carlo simulations. In addition, the BER analysis has been carried out and compared with the existing benchmarks. Furthermore, an in-depth analysis on EE with respect to ASR has also been performed. Simulation results demonstrate the effectiveness of our investigated model over the existing state of art and unveil interesting trade-off between EE and ASR.

6.2 BACKGROUND

In conventional NOMA systems, multiple users share the same time-frequency resources by exploiting power domain multiplexing. The Base Station (BS) superimposes the signals of different users with distinct Power Allocation (PA) coefficients, and receivers apply Successive Interference Cancellation (SIC) to recover their intended messages. However, users with poor channel conditions may suffer from degraded performance due to their inability to effectively decode the received signal. To address this limitation, user cooperation can be integrated into NOMA, whereby users with stronger channels assist users with weaker channels by acting as relays. In a typical two-user cooperative NOMA scenario, the system consists of a BS, a strong

user/near user (NU), and a weak user/far user (FU). The cooperation process is generally divided into two phases: Downlink NOMA Transmission and Cooperative Relaying.

Co-channel interference (CCI) in NOMA within a Resource Block (RB) arises due to the simultaneous transmission of multiple users over the same frequency-time resources, which leads to interference among the signals. In NOMA, multiple users share the same RB by superimposing their signals at different power levels. Since users share the same RB, the signals intended for different users overlap in the frequency domain, causing interference. Physical Layer Security (PLS) integrated with EH has been incorporated in NOMA [153], where Secrecy Outage Probability (SOP) plays a significant role. The effect of PLS on the performance of NOMA framework has been studied for both external and internal eavesdropping environment [154] in interference-limited system. In [155], the security performance analysis of NOMA in PLS has been carried out under jamming cancellation technique in interference-free environment. But the influence of EH on the performance of the system has not been addressed. Moreover, the work in [156] have developed UL and DL NOMA scheme in untrusted environment where the influence of EH has not been explored. Addressing the above issues, a secure transmission scheme has been proposed in a CR-NOMA network employing IA-EH. The developed model is focussed on enhancing the system security performance by introducing Jamming cancellation technique to block an EAV that uses Parallel Interference Cancellation (PIC) scheme [22] to intercept the signals of both the users.

Diamond Relay Network (DRN) model has recently attracted considerable attention as an efficient cooperative networking configuration in wireless Ad Hoc networks that offers higher achievable data rates than the conventional relay networks by simultaneous transmission of two symbols to the receiver within only two-time transmission slots thus increasing the multiplexing gain. A single DRN has been proposed in [1] where a pair of relays deployed between transmitter and receiver take part in signal transmission that is similar to combined DL-UL NOMA. In [2], a NOMA-enabled DRN model is deployed in a multi-relay scenario. Here relay selection scheme is applied to obtain higher transmission reliability. The authors in [3] have investigated the security performance of an untrusted diamond network with cooperative jamming scheme. In [4], the sum rate expression followed by optimum power allocation has been analysed in a single DRN but the Bit Error Rate (BER) has not been explored. In [5], BER performance in DL NOMA networks using BPSK modulation has been shown through simulations and real-time tests. Poor error performance in a single DRN has been observed in [6]. Meanwhile, the authors in [7] have improved the error performance of the single DRN earlier designed in [6] using joint maximum likelihood detector (JML).

Although the performance is improved in [7], still an error floor is observed. All of these works have not shown the impact of RF-EH on DRN. Also, the previous works on NOMA-based DRNs was limited to a single-relay scenario and the advantage of EH through multiple relays was not been explored. Since DRN is an efficient cooperative strategy to improve the achievable rate of the network, DRN powered with RF-EH can be an efficient approach to enhance the sum rate and EE of the proposed system. Joint effect of NOMA assisted relaying systems with RF-EH has been studied in [11,12]. In [12], the end-to-end BER has been examined in an RF powered CR-NOMA system with two users. In [13], an EH relay adopting NOMA protocol is designed where the system performance is considered under the impact of Relay Selection (RS). In [14], BER has been explored for downlink NOMA networks using SWIPT. The authors in [15] have examined the OP in NOMA EH AF relay network. The effect of optimizing PA coefficients for the DRN system is investigated in [16]. In [17], the authors have introduced A-NOMA protocol in CR network where the EE of the network is found to be better compared to that of OMA and NOMA. However, EE and BER analysis in RF-powered MD-DRN still remains an unexplored area of research. Motivated by the above investigations, the performance of an RF-powered MD-DRN has been studied in an IoT environment where the relay devices are deployed in a diamond relay topology between transmitter and receiver. In the proposed scheme, the sum rate for OMA and NOMA assisted devices is calculated using CSI, and then the best MA pattern is determined at the receiver based on maximum ASR.

6.3 IA-EH SCHEME FOR CR-NOMA NETWORK

In this section, description of a two-user CR-NOMA network along with its mathematical representation and results have been described in details.

6.3.1 System Model

A system architecture for CR-NOMA has been illustrated in Fig. 6.1. Here a source node *S* transfers superimposed information signals to two users *NU* and *FU* via an intermediate relay *R* using CJ under the impact of a cluster of CCIs ($I_1, I_2, ...I_M$). Here superposition coding is done such that the messages intended to different users are encoded with different power levels. An external jammer *J* transmits jamming signal to block the *EAV*. Here, *EAV* uses PIC scheme to decode NOMA signal. *J* blocks it by sending an Artificial Noise (AN) signal which deteriorates the eavesdropping signal strength. On receiving the source signal, the users

initially detect the jammer signal, removing it and finally decode the information signal. This model is highly applicable to RF-powered IoT communication scenarios, where devices such as *R*, *NU*, and *FU* are assumed to be energy-constrained and are designed to harvest energy from ambient RF signals. In dense wireless environments—such as smart factories, urban sensing systems, or remote environmental monitoring stations—deploying battery-free or battery-assisted IoT nodes reduces maintenance overhead and enhances scalability. The integration of NOMA allows the simultaneous servicing of multiple users on the same frequency band, which is crucial in such spectrum-limited settings.

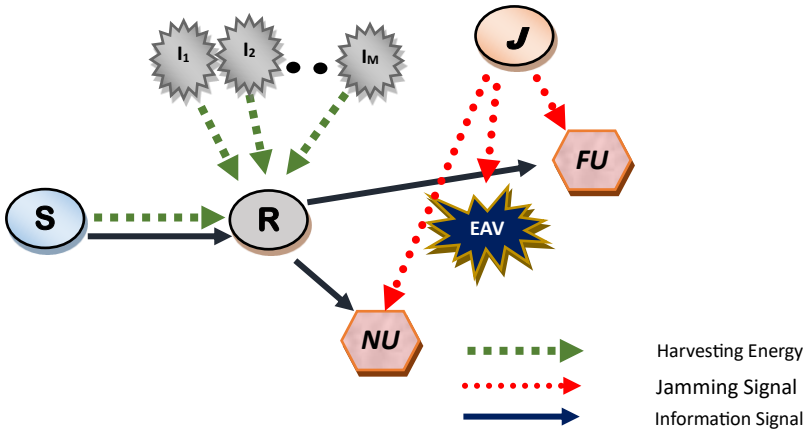

Fig. 6.1 Network Architecture of EH based NOMA

The following assumptions have been considered:

- *S* is a conventional node with constant power supply.
- Direct path between *NU* and *FU* is non-existent due to high attenuation.
- *S* and *R* are NOMA-assisted users that can transmit superimposed information to other users.
- Each node is configured with a single omni-directional antenna.
- *NU* is present near *R* as compared to *FU*; mean channel strength for $R \rightarrow NU$ is stronger compared to $R \rightarrow FU$.
- Both *NU* and *FU* are aware of the knowledge of jamming signal. SIC occurs at *R* for UL and at nearest user *NU* for DL.

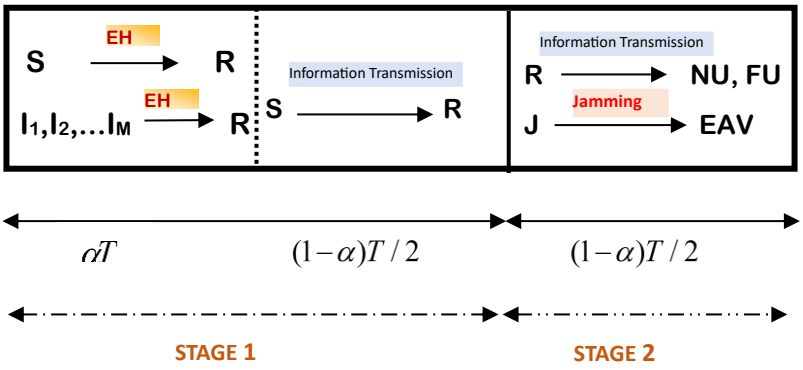

Fig. 6.2 Time frame

6.3.2 Channel Model

All the interferer links at *R* suffer from Nakagami-m fading. Thus, the power of summation of *M* identical CCI signals at *R* follows gamma distribution as:

$$f_{I_R}(x) = \frac{1}{\Gamma(\mathrm{M}\, m_{I_R})}\left(\frac{m_{I_R}}{\Omega_{I_R}}\right)^{Mm_{I_R}} x^{Mm_{I_R}-1} \exp\left(-\frac{m_{I_R} x}{\Omega_{I_R}}\right)$$

where m_{I_R} and Ω_{I_R} are the fading and $\Gamma(.)$ is the Gamma function.

All the wireless links apart from the CCI links are subjected to independent non-selective block Rayleigh fading whose channel coefficients for $S \to R$, $R \to NU$, $R \to FU$, $J \to EAV$ are denoted as h_{SR}, h_{RD_1}, h_{RD_2}, h_{JE}. Then, the average power of the channel gain is exponentially distributed. Here D_1 and D_2 represents NU and FU respectively.

6.3.3 Time Frame Description

The total two path communication has been shown based on TSR protocol [19] in two stages as represented in Fig. 6.2. Total duration frame *T* is split into two stages. During STAGE 1, *R* collects RF energy from the signals emitted from *S* and additional energy from CCIs as depicted from Fig. 6.1. Next, *S* broadcasts superimposed signals $'s_1'$ and $'s_2'$ to *R*. At STAGE 2, SIC occurs at *R* during uplink transmission following which *R* sends the decoded message signal to both *NU* and *FU*. At the same time, *J* creates artificial interference at the nodes to block the *EAV*. On receiving the signal, *FU* removes the jamming signal and decodes its own signal s_2; whereas *NU* being the nearest user, performs SIC to cancel s_2 and obtain its own signal s_1.

6.3.4 Mathematical Analysis

➢ *Energy Harvesting at R*

In the EH phase αT , *R* harvests energy from *S* and CCIs given as:

$$E_R = \eta\alpha T(P_S \left|h_{SR}\right|^2 + I_R) \tag{6.1}$$

where $I_R = \sum_{i=1}^{M} P_i \left|h_{RI_i}\right|^2$; α is the EH coefficient; η represents network energy conversion efficiency; P_S is the Source transmission power and P_I is the transmit power of the CCIs

The corresponding transmit power is:

$$P_R = \frac{E_R}{(1-\alpha)\,\mathrm{T}/\,2} \tag{6.2}$$

Next, *S* broadcasts superimposed signals $'s_1'$ and $'s_2'$ to relay *R* which can be expressed as:

$$y_R = \sqrt{\alpha_1 P_S}\, s_1 + \sqrt{\alpha_2 P_S}\, s_2 \tag{6.3}$$

where α_1 and α_2 denote NOMA power factor allocation coefficients for *NU* and *FU* respectively,

It is assumed that, $\alpha_1 < \alpha_2$ due to long distance of *FU*

and $\alpha_1 + \alpha_2 = 1$ (6.4)

➢ *Information Processing at R, D1 and D2*

Assuming D_1 to be *NU* and *D2* to be *FU*, applying NOMA principle, the SINR at *R* to decode $'s_1'$ by treating $'s_2'$ as noise is given as:

$$\gamma_R^{s_1} = \frac{a_1\rho_S \left|h_{RD_1}\right|^2}{a_2\rho_S \left|h_{RD_1}\right|^2 + \sum_{i=1}^{M} \rho_I \left|h_{RI_i}\right|^2 + 1} \tag{6.5}$$

where $\left|h_{RD_1}\right|$ and $\left|h_{RI_i}\right|$ represents mean channel power from R to NU and R to CCIs respectively.

where $\rho_S = \frac{P_S}{N_O}$; $\rho_I = \frac{P_I}{N_O}$

After perfect SIC, the SINR at *R* to decode $'s_2'$ is given as:

$$\gamma_R^{s_2} = \frac{a_2 \rho_S \left|h_{RD_1}\right|^2}{\sum_{i=1}^{M} \rho_I \left|h_{RI_i}\right|^2 + 1} \tag{6.6}$$

Now, treating $'s_1'$ as interference, *NU* decodes symbol $'s_2'$ by cancelling $'s_1'$ with SIC. Thus, the received SINR for $'s_2'$ at *NU* is:

$$\gamma_{D_1}^{s_2} = \frac{a_2 \rho_R \left|h_{RD_2}\right|^2}{a_1 \rho_R \left|h_{RD_1}\right|^2 + \sum_{i=1}^{M} \rho_I \left|h_{RI_i}\right|^2 + 1} \tag{6.7}$$

SINR after SIC at *NU* to decode $'s_1'$

$$\gamma_{D_1}^{s_1} = \frac{a_1 \rho_R \left|h_{RD_1}\right|^2}{\sum_{i=1}^{M} \rho_I \left|h_{RI_i}\right|^2 + 1} \tag{6.8}$$

Treating $'s_1'$ as IUI, SINR at *FU* to recover its own signal is given as:

$$\gamma_{D_2}^{s_2} = \frac{a_2 \rho_R \left|h_{RD_2}\right|^2}{\sum_{i=1}^{M} \rho_I \left|h_{RI_i}\right|^2 + 1} \tag{6.9}$$

PIC is carried out at *EAV* to decode the superimposed signal of *S* from *R*. Hence the received SINR at *EAV* to detect the signals of *NU* and *FU* is:

$$\gamma_E^{s_1} = \frac{a_1 \rho_R \left|h_{RD_1}\right|^2}{\rho_J \left|h_{JE}\right|^2 + \sum_{i=1}^{M} \rho_I \left|h_{RI_i}\right|^2 + 1} \tag{6.10}$$

$$\gamma_E^{s_2} = \frac{a_2 \rho_R \left|h_{RD_2}\right|^2}{\rho_J \left|h_{JE}\right|^2 + \sum_{i=1}^{M} \rho_I \left|h_{RI_i}\right|^2 + 1} \tag{6.11}$$

The end-to-end SINR for both the paths is computed as:

$$\gamma_{SD_1}^{1} = \min(\gamma_R^{s_1}, \gamma_{D_1}^{s_1}) \tag{6.12}$$

$$\gamma_{SD_2}^2 = \min(\gamma_R^{s_2}, \gamma_{D_2}^{s_2}) \tag{6.13}$$

- ***SOP and ESR Analysis***

Following [157], the ESR of *NU* and *FU* are obtained as follows:

$$C_S^{D1} = \left\{ \log_2 \left[\frac{1+\gamma_{SD_1}^{s_1}}{1+\gamma_E^{s_1}} \right] \right\}^+$$
$$C_S^{D2} = \left\{ \log_2 \left[\frac{1+\gamma_{SD_2}^{s_2}}{1+\gamma_E^{s_2}} \right] \right\}^+ \tag{6.14}$$

where $[x]^+ = \max(x, 0)$

The probability of the given SR remaining below a predetermined secrecy rate is known as the SOP which is expressed as:

$$P_{out}^{\text{sec}} = P(C_S^{D1} < R_1 \quad or \quad C_S^{D2} < R_2) \tag{6.15}$$

where R_1 is threshold secrecy rate of *NU* and R_2 is threshold secrecy rate of *FU*.

6.3.5 Results and Discussions

The effectiveness of the developed model has been investigated through simulation using Matlab 2021b. The relevant parameters are set according to Table 6.1.

Table 6.1 Parameter Setting

Parameter	Meaning	Default Values
R_1, R_2	Bit Rates for *NU* and *FU*	2,0.2 bits/s/Hz
η	Energy conversion efficiency	0.8
α	EH coefficient	0.2
α_1, α_2	PA coefficients	0.2,0.8 [155]
P_S	Source transmit power	10dBW
P_I	Interferer transmit power	1dBW
P_J	Jamming Power	20dB

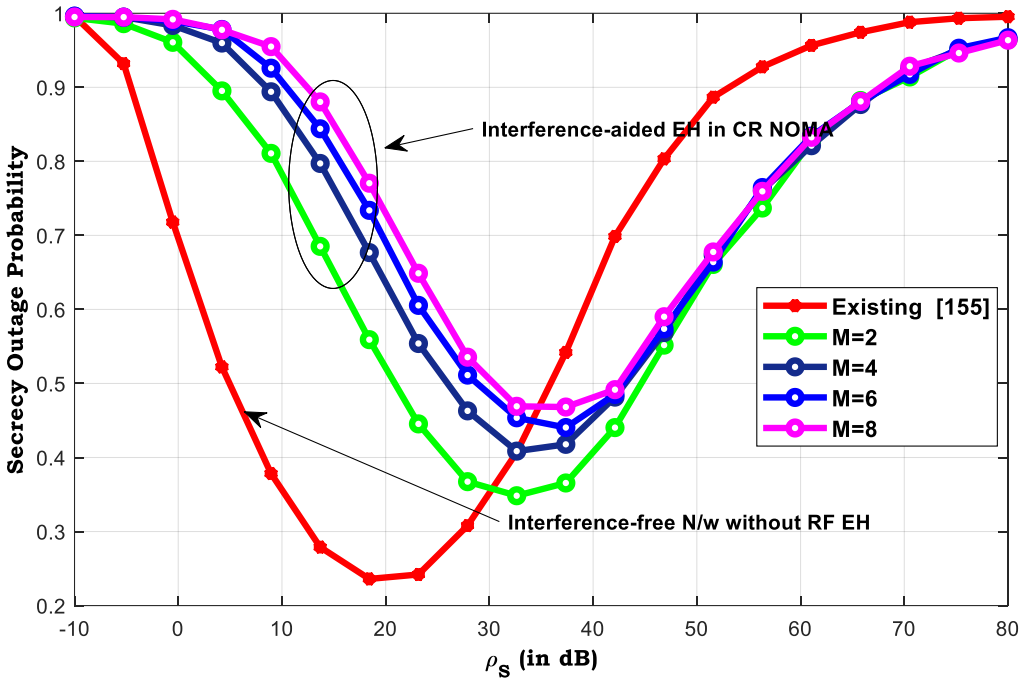

Fig. 6.3 Comparison of SOP versus ρ_S with varying number of CCIs

Fig. 6.3 highlights a comparison plot of the developed model with the contrast model [155] for several values of *M*. It is found that the secrecy performance is significantly better in [155] upto a certain value of ρ_S . It is shown that when the additional energy from CCI is introduced, the SOP falls upto some optimal value of ρ_S and then after a certain crossover point we observe a noticeable improvement in secrecy performance for our model. In addition, the gap between the SOP curves decreases with increasing *M* and at high SINR, the gap between the plots becomes negligible indicating lesser impact of change in *M* beyond 6. The highlighted portion in Table 6.2 depicts the improvement in SOP of our developed model over the existing model. From Table 6.2, the percentage improvement in SOP of proposed scheme (*M*=2) outperforms that of [155] by 27.08% at $\rho_S = 0dB$ which decreases to 9.69% at $\rho_S = 20dB$. Beyond 30dB, a significant improvement in secrecy performance is obtained for our developed network compared to the existing one.

Table 6.2 Percentage Improvement in SOP

Parameter	**SOP**					**%Improvement in SOP**			
ρ_S	Existing [155]	M=2	M=4	M=6	M=8	Proposed (M=2) over [155]	M=4 over M=2	M=6 over M=4	M=8 over M=6
0	0.7	0.96	0.9849	0.985	0.9854	27.08	2.4	0.01	0.04
20	0.22	0.52	0.62	0.69	0.72	9.69	16.13	10.14	4.34

40	0.6	0.4	0.45	0.47	0.49	33.33	13.04	4.25	4.08
60	0.95	0.8	0.81	0.816	0.818	15.78	1.23	0.73	0.5
80	1	0.97	0.972	0.975	0.976	2	0.21	0.31	0.1

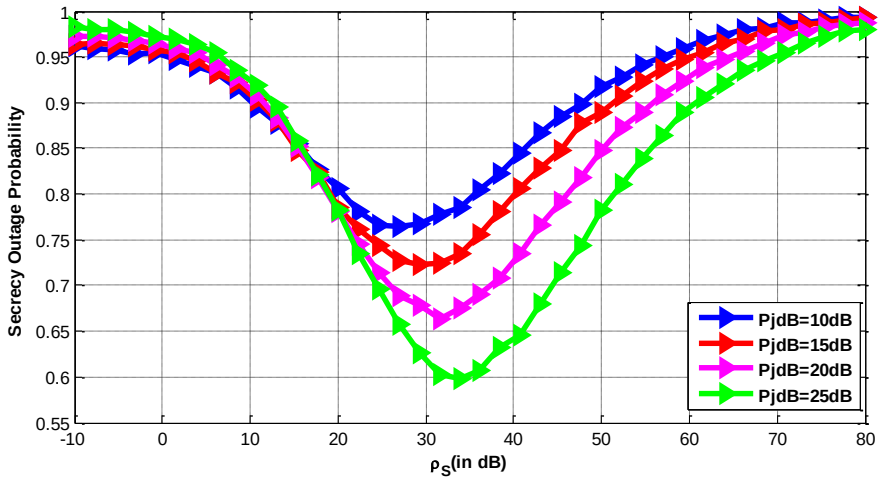

Fig. 6.4 SOP as a function of ρ_S for different values of jamming power

The impact of ρ_S on SOP for different levels of P_J has been discussed in Fig. 6.4. We observe that for a fixed ρ_S in each curve, with increasing value of P_J, initially the SOP falls guaranteeing higher secrecy. This is because with increasing P_J, *EAV* receives more interference from *J* due to which EAV capacity decreases. This in turn increases the secrecy capacity and SOP falls. Also, the optimum value of ρ_S where SOP is minimum shifts to the right with increasing P_J. After a certain optimal ρ_S, the *EAV* channel capacity increases for a fixed P_J. At low to moderate SNRs, the jamming power is typically sufficient to significantly suppress the eavesdropper's channel capacity. As the source transmission power increases, the legitimate receiver benefits more than the eavesdropper, resulting in an increased secrecy capacity and hence a reduced SOP. At high SNR, both the legitimate and eavesdropping channels improve due to stronger received signals. Since the jamming power remains constant, its relative impact on the eavesdropper diminishes as the signal power increases. Consequently, the capacity of the eavesdropper channel C_e begins to rise more noticeably. As C_e increases, the gap between C_m and C_e narrows, and in some cases, the secrecy capacity may decrease or even drop to zero. This leads to a higher probability of secrecy outage, indicating that the system becomes more vulnerable to information leakage at high transmission powers unless jamming power is also adaptively increased.

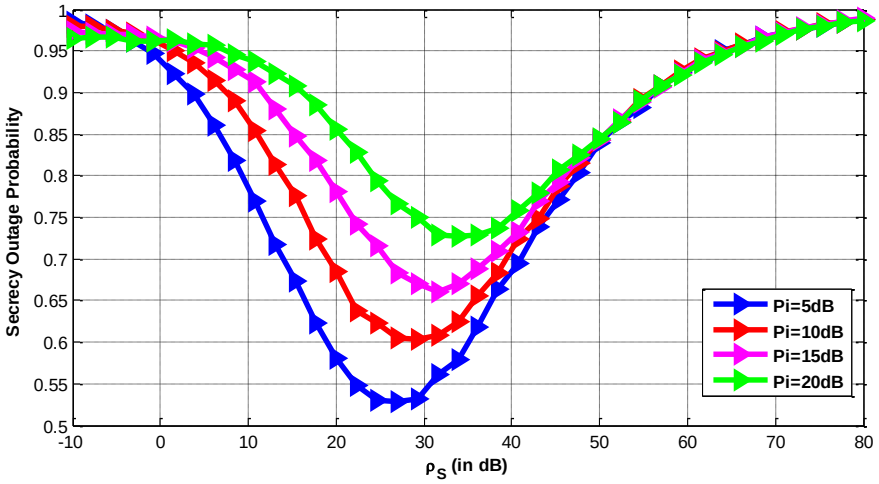

Fig. 6.5 SOP performance for different values of interferer power

Fig. 6.5 illustrates the plot of SOP versus ρ_S for varying P_I. As P_I increases, the SOP increases and the secrecy performance of the system degrades. Initially with increasing values of P_I, the transmit power based on harvesting also increases. But simultaneously, the effect of interference from the cluster of interferer nodes also increases which have a dominant effect thus increasing SOP. So, at higher values of ρ_S, the SINR at each relay node is near about constant and become independent of P_I.

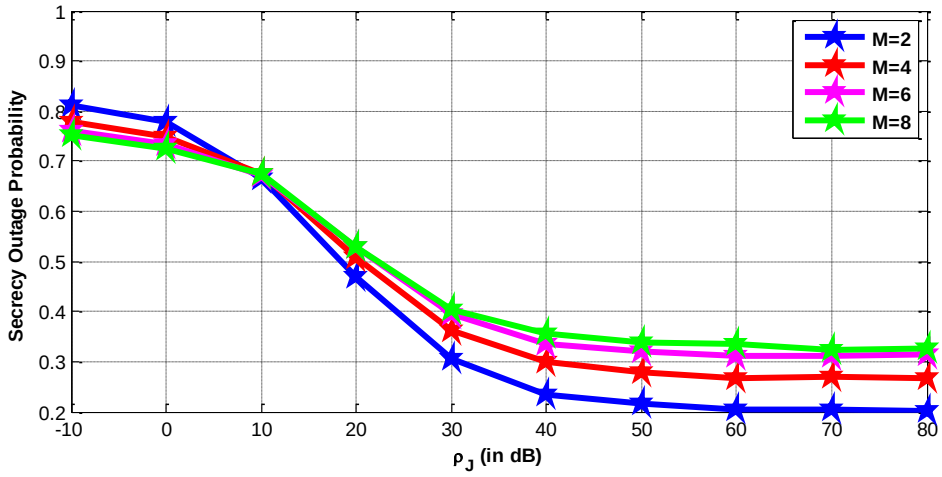

Fig. 6.6 SOP versus Transmit Power of Jammer for various values of M

In Fig. 6.6, we observe a change in SOP for increasing *M*. Initially the SOP is more for lower value of *M* and then gradually goes down at high transmit power, SOP falls and becomes almost independent of ρ_J. At high value of ρ_J, the channel capacity of the EAV becomes poor and the SOP plot gradually decreases. For a fixed ρ_J in the low SINR range, EAV is able to successfully

intercept the source signal as a result of which SOP is higher. But with increase in jamming power level, the secrecy capacity increases and SOP curve goes down. Moreover, as we increase the number of CCIs from (M=2 to 8), the value of SOP decreases due to increased opportunity for *R* to harvest more energy from both *S* and CCIs. But, after a certain value of ρ_J i.e. beyond 10dB the SOP curve for higher CCI becomes comparatively more and then becomes almost independent of ρ_J because of greater interference effect imposed on the jammer.

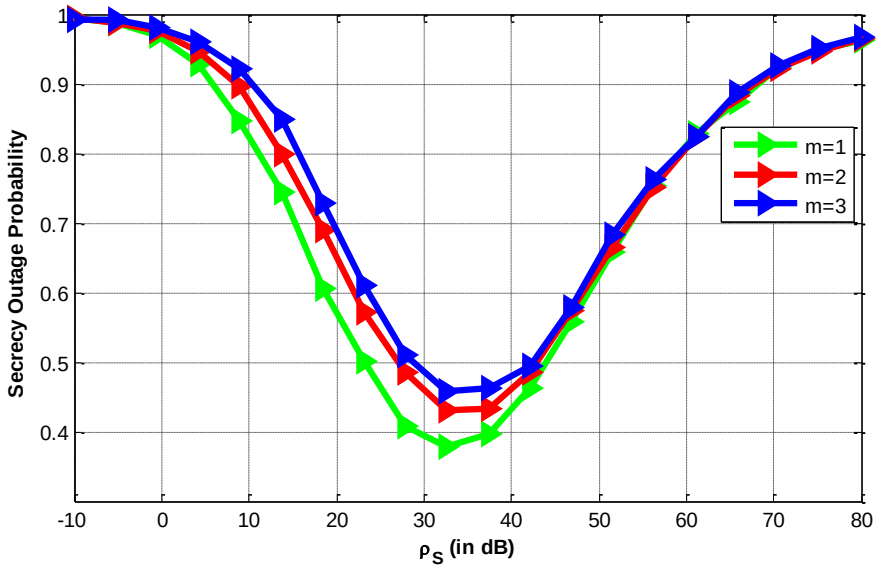

Fig. 6.7 SOP versus ρ_S for different values of Nakagami parameter

Fig. 6.7 illustrates the plot of SOP versus ρ_S for several values of Nakagami-m parameter (m=1,2,3). The network performance worsens with increasing 'm'.

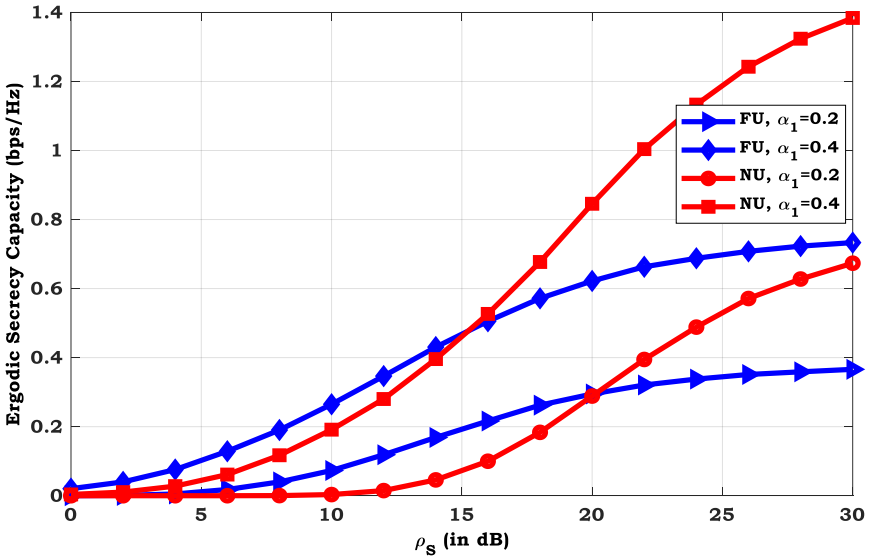

Fig 6.8 ESR versus ρ_S for both *NU* and *FU*

To highlight the impact of α_1 on ESR for both *NU* and *FU*, Fig. 6.8 plots ESR versus ρ_S for varying α_1. Increasing α_1 improves ESR for both the users. It is also observed that ESR for *NU* is much better than that of *FU*. Less power allocation factor α_1 indicates more power allocated to *FU*, thus C_S^{D1} increases initially. But due to longer distance from *R*, transmission power loss becomes more in *FU* as evident from Equation (6.4).

6.4 RF-POWERED MULTI-DEVICE DIAMOND RELAY IoT NETWORK USING A-NOMA

In this section, description of diamond relay IoT network using A-NOMA along with its mathematical representation and results have been described in details.

6.4.1 System Model

An RF-powered IoT relay network is shown in Fig. 6.9. The network consists of a base station transmitter ***T***, '*N*' RF-powered IoT relay devices represented as $\boldsymbol{D_n} = \{D_1, D_2, ...D_K, ...D_N\}$ and a Receiver ***R***. The relays can be any wearable device, smartphone, camera, sensor etc that harvest RF energy from ***T*** and utilize it for downlink information reception as well as uplink information transmission. The battery of the n^{th} relay is denoted as $\boldsymbol{p_n}$. NOMA protocol is implemented by ***K*** devices located far away from ***T*** with different allocated power factors represented as $\boldsymbol{D_k}$ where $k = \{1, 2, ..., K\}$; whereas OMA is implemented by the rest ***N-K*** devices deployed closer to ***T*** that require less power for communication represented as $\boldsymbol{D_m}$ where $m = \{K+1, K+2, ..., N\}$. Accordingly, the network is modelled in a diamond relay topology and the devices are grouped into two groups based on channel conditions between ***T*** and $\boldsymbol{D_n}$. $\boldsymbol{D_k}$ operate in the same bandwidth ***B*** whereas $\boldsymbol{D_m}$ communicates over different bands $\boldsymbol{B_m}$. We also assume that $\boldsymbol{D_n}$ and ***R*** are fitted with SIC receivers. Employing (TSR) [19], the entire time frame τ in Fig. 6.10 is divided into three-time phases: in the 1st phase, $\boldsymbol{D_n}$ harvest energy from ***T***. In the next phase, ***T*** multicasts superimposed signals to $\boldsymbol{D_n}$. $\boldsymbol{D_k}$ implements SIC to decode their desired signals. $\boldsymbol{D_m}$ uses OMA to decode their respective signals. In the 3rd time slot, ***R*** receives two copies of superimposed signals from $\boldsymbol{D_k}$ and $\boldsymbol{D_m}$, calculates the sum rate and finally selects the protocol with the maximum sum rate. Here we have not considered end-to-

end delay for the devices. Here, Rayleigh fading has been applied whose CDF and PDF are defined respectively as:

$$F_{|h_{i,j}|^2}(x) = 1 - e^{-\frac{x}{\Omega^2_{i,j}}} \tag{6.1}$$

$$\text{and } f_{|h_{i,j}|^2} = \frac{1}{\Omega^2_{i,j}} e^{-\frac{x}{\Omega^2_{i,j}}} dx \tag{6.2}$$

where $|h_{i,j}|^2$ are random independent variables with i and j as source and destination nodes, and $\Omega^2_{i,j}$ is the channel mean power with $\Omega^2_{i,j} = E[|h_{i,j}|^2]$.

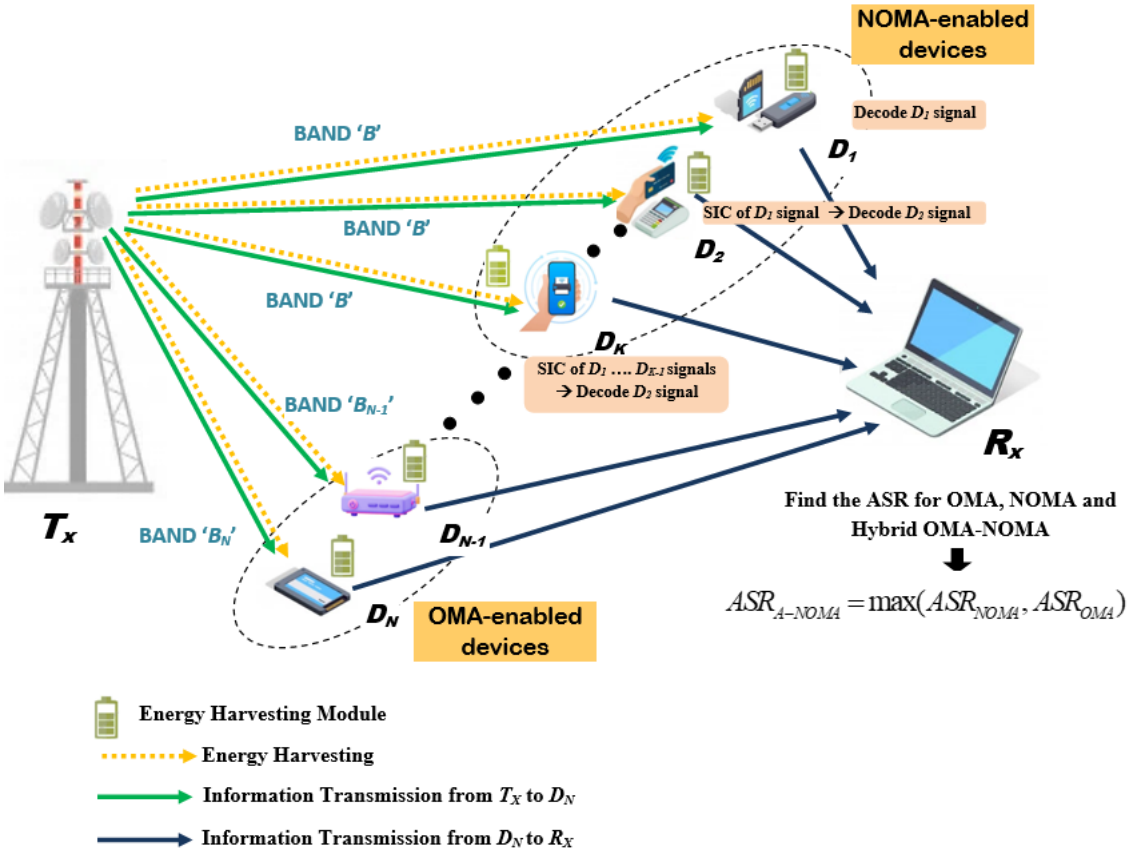

Fig. 6.9 System Configuration of MD-DRN using A-NOMA

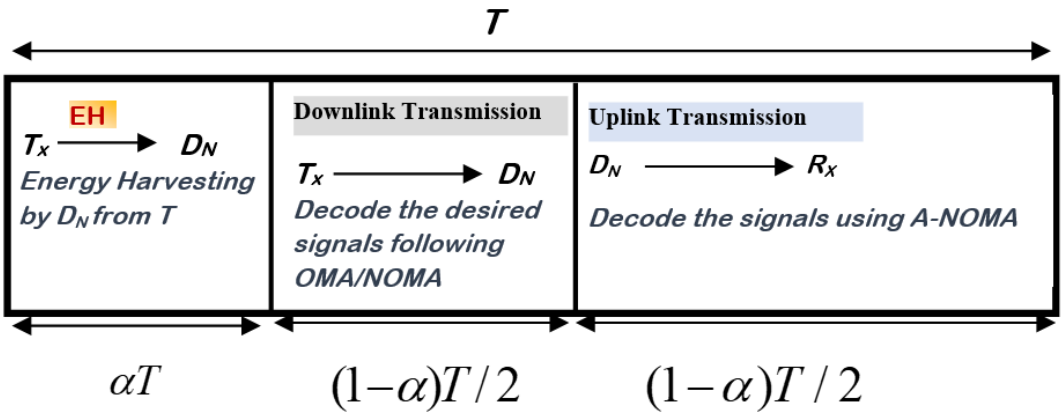

Fig. 6.10 Frame Structure

6.4.2 Workflow of A-NOMA

To understand the concept of A-NOMA and for simplicity, a 4-device scenario has been considered as shown in Fig. 6.11. Fig. 6.12 depicts the workflow of A-NOMA. The CSI of all the links is collected at T_x. Initially, CSI estimates the distance between T_x and the relay devices. Accordingly, power and resource allocation are done based on far and near distances. In order to support the diamond relay topology in a 4-device IoT network, it is assumed that the 1st node is at a distance of 2.5 m, 2nd node at 2m, 3rd node at 1.5 m and the nearest node at 1m from T_x. Three devices located far away from T_x employ NOMA protocol (Band 6) while the nearest device located near T_x transmits data in a separate frequency band with OMA protocol (Band 3). In the 1st group for RF-powered NOMA, the farthest node D_1 will decode a single packet. D_2 implements SIC to decode the multiplexed packets in descending order, i.e., first x_1 and then x_2. Similarly, D_3 obtains its desired signal x_3 after decoding and subtracting x_1 and x_2. The nearest user D_4 follows OMA protocol to decode its signal. At R_x, we determine the appropriate Multiple Access (MA) pattern by selecting the best protocol between OMA and NOMA to obtain the maximum sum rate.

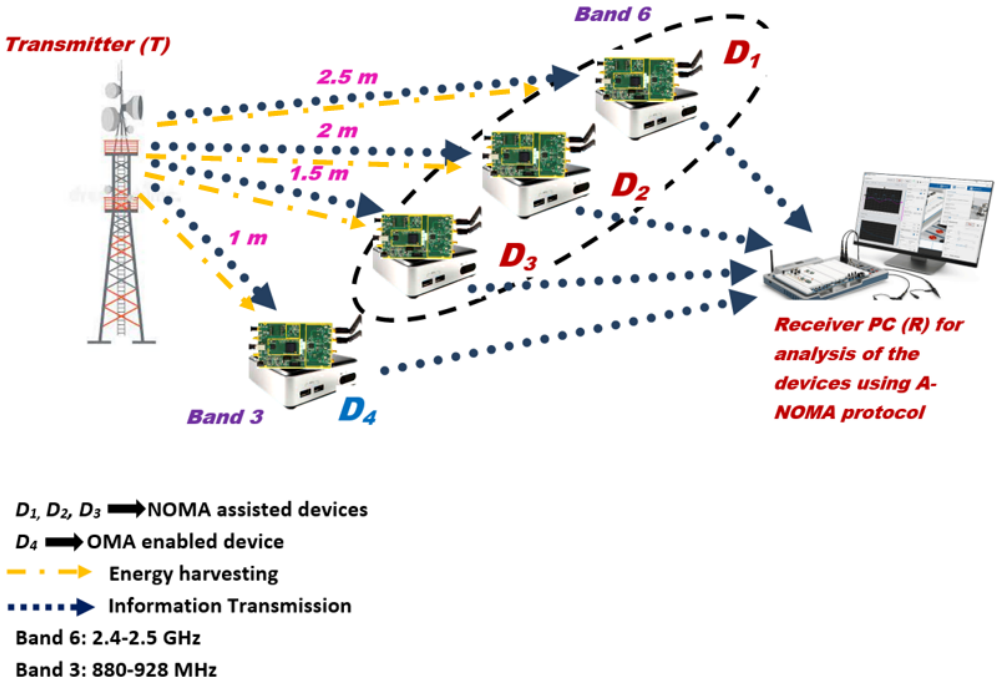

Fig. 6.11 System Configuration of 4-device DRN using A-NOMA

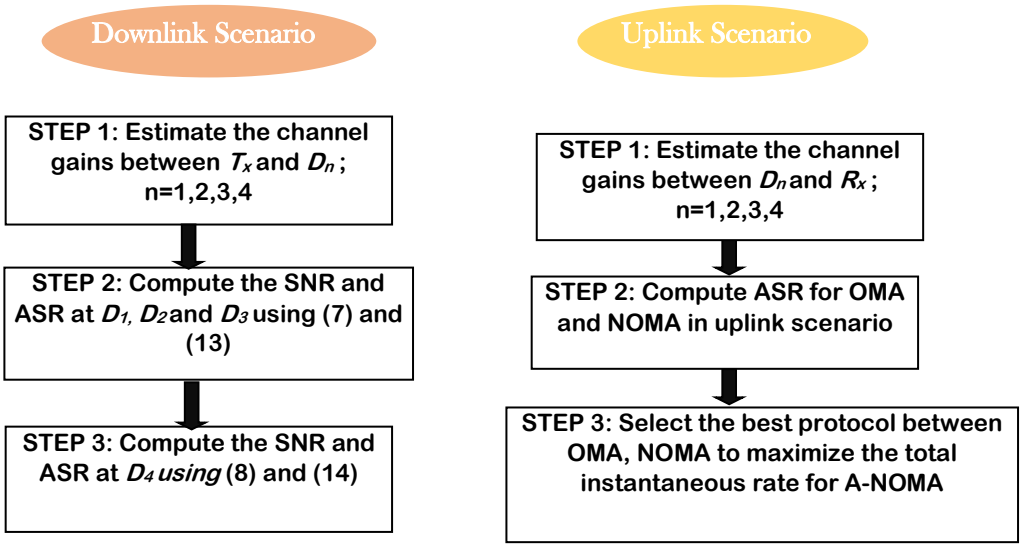

Fig. 6.12 Workflow of A-NOMA

6.4.3 Mathematical Modelling

- ***Energy Harvesting by D_n***

In the EH slot, the energy harvested by $\boldsymbol{D_n}$ is expressed as:

$$E_{D_n} = \sum_{n=1}^{N} \eta \alpha P_T \left| h_{TD_n} \right|^2 \tau / 2 \tag{6.16}$$

where P_T is the total power transmitted by $\boldsymbol{T_x}$, α is the EH coefficient, η is energy conversion efficiency, $\left| h_{TD_n} \right|^2$ is the channel mean power from $\boldsymbol{T_x}$ to n^{th} *relay*

The power transmitted by $\boldsymbol{D_n}$ is:

$$P_{D_n} = \sum_{n=1}^{N} \eta \alpha P_T \left| h_{TD_n} \right|^2 \tag{6.17}$$

- ***Communication in DL scenario***

In the 1st time slot, $\boldsymbol{T}$ multicasts data packets consisting of $x_1, x_2, ..., x_l, .., x_N$ to $\boldsymbol{D_n}$ given as

$$t = \sqrt{P_T} \sum_{n=1}^{N} \sqrt{\alpha_n} x_n \tag{6.18}$$

where x_n denotes modulated symbol of n^{th} relay ; α_n is the allocated power factor to n^{th} relay $\sum_{n=1}^{N} \alpha_n = 1$ and $0 > \alpha_1 > \alpha_2 > ..... > \alpha_N > 1$; n_n is the Additive White Gaussian Noise with zero mean and variance N_O.

The received signal at $\boldsymbol{D_n}$ is given as:

$$y_{D_n} = \left| h_{TD_n} \right|^2 \sqrt{P_T} \sum_{n=1}^{N} \sqrt{\alpha_n p_n} x_n + n_n \tag{6.19}$$

where $n = 1, 2, ..., N$, p_n is the battery of *n-th relay devices*

Out of '$\boldsymbol{N}$' devices, the first $\boldsymbol{K}$ devices are NOMA-functioned, and the rest $\boldsymbol{N}$-$\boldsymbol{K}$ devices are OMA-functioned. To obtain the desired signal of *k-th relay*, SIC process is applied. Using (6.19), the SNR for *k-th relay* is expressed as [128]:

$$\gamma_k^{Downlink} = \frac{\alpha_k \rho_{D_k} \left| h_{D_k R} \right|^2}{\sum_{i=1}^{K-1} \alpha_i \rho_{D_i} \left| h_{D_i R} \right|^2 + 1} \tag{6.20}$$

Now, for **'*N-K*'** devices with OMA functionality, the SNR is given as:

$$\gamma_m^{Downlink} = \rho_{D_m} \alpha_m^{'} \left| h_{D_m R} \right| \tag{6.21}$$

➢ *Communication in UL scenario*

In the 3rd slot, $\boldsymbol{R_x}$ receives two copies of superimposed signals from $\boldsymbol{D_k}$ and $\boldsymbol{D_m}$. SIC is applied to decode the signals of the first '***K***' NOMA-enabled devices. In uplink mode, the farthest device located far from $\boldsymbol{T_x}$ is now the nearest device from $\boldsymbol{R_x}$. Accordingly, the strongest device's signal is decoded first (reverse order with respect to the downlink) i.e. D_1 will be decoded first at $\boldsymbol{R_x}$ followed by $D_2, D_3, ..., D_K$. Accordingly, the SNR for *k-th relay* is expressed as:

$$\gamma_k^{Uplink} = \frac{\alpha_k \rho_T \left| h_{TD_k} \right|^2}{\sum_{i=1}^{K-1} \alpha_i \rho_T \left| h_{TD_i} \right|^2 + 1} \tag{6.22}$$

For ***N-K*** devices with OMA functionality, the SNR is given as:

$$\gamma_m^{Uplink} = \frac{P_T \left| h_{TD_m} \right|^2}{N_O} \tag{6.23}$$

where $m = K+1, K+2, ..., N$ and $\rho_T = P_T / N_O$

6.4.4 Performance Analysis

In this section, the key secrecy performance metrics of our investigated system i.e., ASR, BER and EE are derived.

➢ ASR calculation

ASR signifies the transmission capacity [117] which guarantees the highest spatial reuse under a maximum outage constraint. ASR for the overall network is given as:

$$ASR_{A-NOMA} = R_{Total_{Downlink}} + C_{Total_{Uplink}} \tag{6.24}$$

When NOMA is employed, the ASR for *k-th* relay can be expressed as follows:

$$R_k = \begin{cases} \mathrm{B}\log_2 \left(1 + \dfrac{\alpha_k \rho_T \left| h_{TD_k} \right|^2}{\sum_{i=1}^{K-1} \alpha_i \rho_T \left| h_{TD_i} \right|^2 + 1} \right) & ; \quad k < K \\ B\log_2 \left(1 + \rho_T \alpha_K \left| h_{TD_k} \right| \right); & k = K \end{cases} \tag{6.25}$$

The total ASR for '*K*' devices is

$$R_{Total_{Downlink}}^{NOMA} = \sum_{k=1}^{K} R_k \tag{6.26}$$

Similarly, the ASR for OMA can be formulated as:

$$R_m = B_m \log_2 \left(1+\gamma_m\right) \tag{6.27}$$

The aggregate ASR of DL OMA can be written as:

$$R_{Total_{Downlink}}^{OMA} = \sum_{m=K+1}^{N} R_m \tag{6.28}$$

Combining (6.26) and (6.28), the ASR for DL scenario is expressed as:

$$R_{Total_{Downlink}} = R_{Total_{Downlink}}^{NOMA} + R_{Total_{Downlink}}^{OMA} \tag{6.29}$$

Now, for UL mode, ASR for *k-th device* using NOMA and OMA protocols is formulated as under:

$$C_k = \mathrm{B}\log_2 \left(1+\frac{\alpha_k^{'}\rho_{D_k}\left|h_{D_kR}\right|^2}{\sum_{i=1}^{K-1}\alpha_i^{'}\rho_{D_i}\left|h_{D_iR}\right|^2+1} \right) \tag{6.30}$$

where $\rho_{D_K} = P_{D_K} / N_O$ represents the transmit power from D_K

and $C_m = B_m \log_2 \left(1+\rho_{D_m}\alpha_m^{'}\left|h_{D_mR}\right|\right)$ (6.31)

Combining (6.30) and (6.31), the overall ASR in UL scenario is expressed as:

$$C_{Total_{uplink}} = C_k + C_m \tag{6.32}$$

Finally, ASR for NOMA and OMA DRNs are described as:

$$ASR_{NOMA} = R_{Total_{Downlink}}^{NOMA} + C_{Total_{Uplink}}^{NOMA} \tag{6.33}$$

$$ASR_{OMA} = R_{Total_{Downlink}}^{OMA} + C_{Total_{Uplink}}^{OMA} \tag{6.34}$$

Next step is to determine the best multiple access pattern. The best protocol between OMA and NOMA is selected to maximize the total instantaneous rate for A-NOMA.

$$ASR_{A-NOMA} = \max(ASR_{NOMA}, ASR_{OMA}) = [ASR_{NOMA} - ASR_{OMA}]^{+} \tag{6.35}$$

$$= \int_0^{\infty} \sum_{k=1}^{K} f(\gamma_k^{NOMA}(\mathrm{k})) \times \sum_{m=K+1}^{N} \frac{e^{-\frac{\gamma_m^{OMA}(m)}{\bar{\gamma}_m^{OMA}(m)}}}{\bar{\gamma}_m^{OMA}(m)} d\gamma_m^{OMA}(m)\, \mathrm{d}\gamma_k^{NOMA}(\mathrm{k})$$

where $f(\gamma_k^{NOMA}(\mathrm{k})) = \max_{i \le q \le K}\left(\frac{N_O}{P_{D_i}\alpha_q - P_{D_i}\sum_{j=1}^{q-1}\alpha_j}\right) \times \exp\left(-\max_{i \le q \le K}\left(\frac{N_O \gamma_k^{NOMA}(\mathrm{k})}{P_{D_i}\alpha_q - P_{D_i}\sum_{j=1}^{q-1}\alpha_j}\right)\right)$ (6.36)

and $[x,0]^+ = \max(x,0)$

Taking the help of [187] as well as (4) and (5) from [143], and after some tedious calculations using (6.36), we obtain the closed form expression of ASR for A-NOMA network given as:

$$ASR_{A-NOMA} = \left(1 - \sum_{k=1}^{K}\sum_{m=K+1}^{N}\binom{K}{k}\binom{N}{m}(-1)^{k+m-2} \times \sqrt{\frac{4k\upsilon_k N_O}{\alpha_k \xi \lambda_{TD_k}}} K_1\left(\frac{4km\upsilon_k N_O}{\alpha_k \xi \lambda_{TD_k}}\right)\right)$$
$$\times\left(1 - \sum_{m=K+1}^{N}\frac{1}{(m-1)!}\left((m-1)! - 2\left(\frac{\alpha_m}{P_{D_m}}\right)^{\frac{m}{2}} \mathrm{K}_m\left(2\sqrt{\frac{\alpha_m}{P_{D_m}}}\right)\right) \times \frac{(N-1)!}{(m-1)!(N-m)!} e^{-m\beta}(1-e^{-\beta})^{N-m} + (1-e^{-\beta})\right) \quad (6.36)$$

where $K_{\mathrm{K}}(*)$ is the modified Bessel function of second kind with order K, and $v_k = N!/(N-k)!(k-1)!$

A formal proof of (6.36) is provided in Appendix D

➢ *BER analysis*

From [148], the end-to-end BER analysis can be expressed as:

$$P_n^{e2e}(e) = \frac{P_1^{e2e}(e) + P_2^{e2e}(e) + ... + P_N^{e2e}(e)}{N} \quad (6.37)$$

where $P_1^{e2e}(e), P_2^{e2e}(e), ..., P_N^{e2e}(e)$ represents e2e BER of $x_1, x_2, ..., x_N$ symbols respectively.

The overall BER of A-NOMA network for both UL and DL scenarios can be expressed as:

$$BER_{A-NOMA} = P(ASR_{ANOMA} < ASR_{th}) \quad (6.38)$$

where ASR_{th} is a fixed threshold rate

➢ **EE calculation**

The EE can be calculated as the overall ASR of the network (in bps/Hz) divided by the total power consumption of the network. It is mathematically expressed as:

$$EE = \frac{ASR_{A-NOMA}}{\sum_{n=1}^{N} P_n + P_C} \quad (6.39)$$

where P_C is the circuit power consumption

Putting the value of ASR_{A-NOMA} , we get (6.40) as follows:

$$EE = \frac{1}{\sum_{n=1}^{N} P_n + P_C} \left(\left(1 - \sum_{k=1}^{K} \sum_{m=K+1}^{N} \binom{K}{k} \binom{N}{m} (-1)^{k+m-2} \times \sqrt{\frac{4km\upsilon_m N_O}{\alpha_m \xi \lambda_{SR}}} K_1 \left(\frac{4km\upsilon_m N_O}{\alpha_m \xi \lambda_{TD_m}} \right) \right) \times \left(1 - \sum_{m=K+1}^{N} \frac{1}{(m-1)!} \left((m-1)! - 2 \left(\frac{\alpha_m}{P_{D_m}} \right)^{\frac{m}{2}} K_m \left(2\sqrt{\frac{\alpha_m}{P_{D_m}}} \right) \times \frac{(N-1)!}{(m-1)!(N-m)!} e^{-m\beta} (1 - e^{-\beta})^{N-m} + (1 - e^{-\beta}) \right) \right) \right) \quad (6.40)$$

6.4.5 Results and Discussions

In this section, the effectiveness of the developed model has been investigated through simulation using Matlab 2021 over Intel i5, 4GHz processor. The relevant parameters are set according to Table 6.3.

Table 6.3 Parameter settings

Parameters	Value
Fixed Transmit Power	0 dB
Noise power	-174 dBm
Modulation	BPSK [148]
No. of devices	2,3,4
Circuit Power consumption	1 W
Power allocation for 3-device DRN	$a_1 = 0.18, a_2 = 0.27, a_3 = 0.55$ [148]
Power allocation for 4-device DRN	$a_1 = 0.12, a_2 = 0.16, a_3 = 0.24, a_3 = 0.48$ [148]

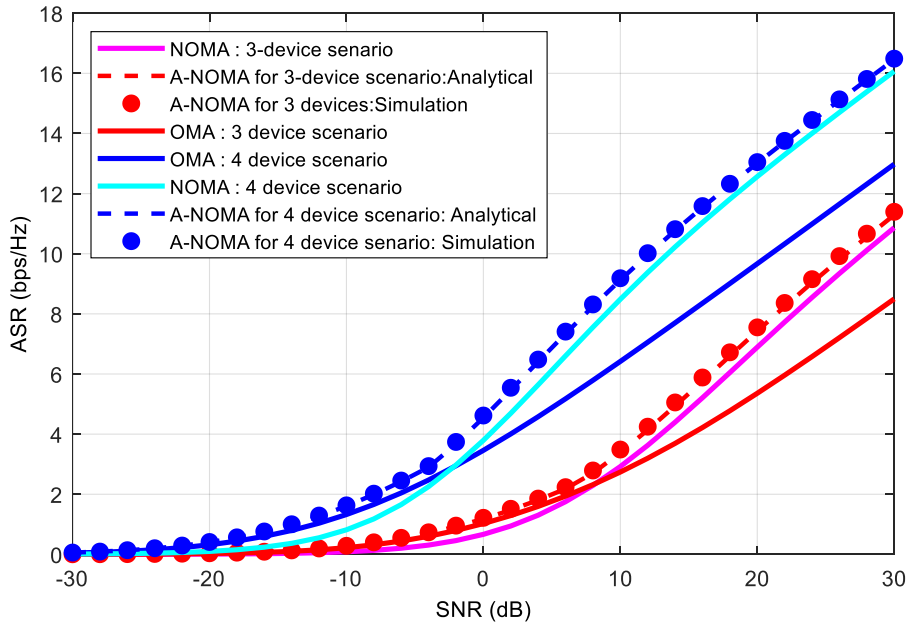

Fig. 6.13 Comparison of OMA, NOMA and A-NOMA in terms of ASR for 3-device and 4-device DRN

Fig. 6.13 highlights ASR comparison of the proposed scheme for RF powered OMA, NOMA and A-NOMA in an '***N***' device DRN where ***N***=3,4. A close similarity between theoretical and simulation results has been observed. For a fair and logical comparison, the system model has been devised using OMA and NOMA protocols and then in terms of ASR. On comparing, it is observed that ASR for the proposed RF powered network employing A-NOMA is much better than the RF powered OMA and NOMA DRN. From the figure, it is found that 4-device DRN system gives better sum rate than 3-device DRN. At $P_S = 10dB$, ASR is 3.6bps/Hz for 3-device network that rises to 9bps/Hz for 4-device network.

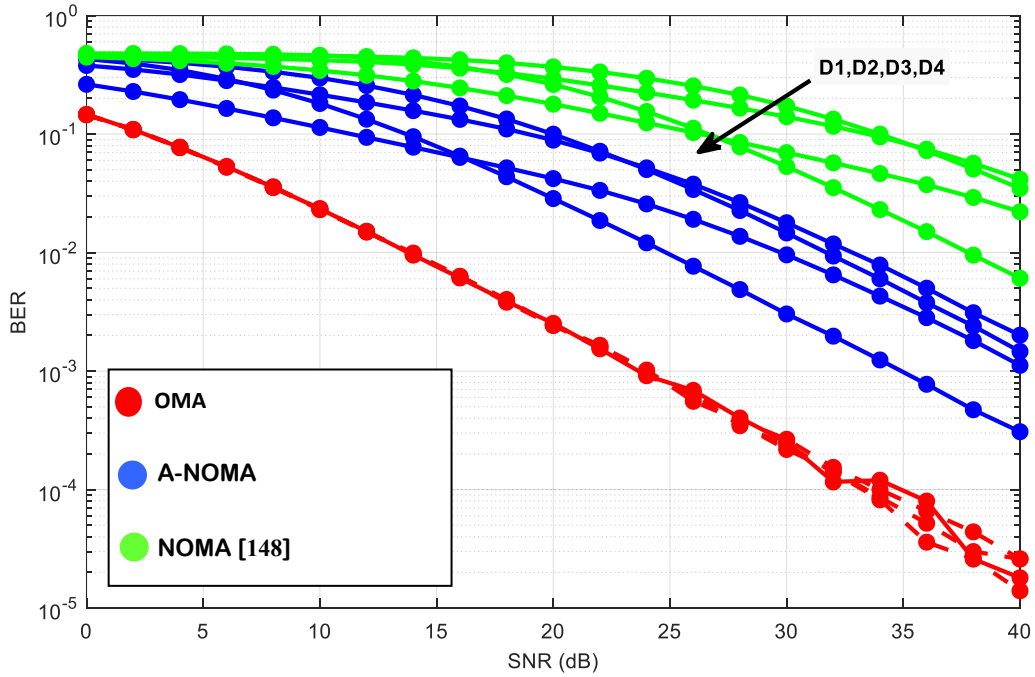

Fig. 6.14 Comparison of OMA, NOMA [148] and A-NOMA in terms of BER in 4-device network

In Fig. 6.14, the BER performance of the investigated DRN using A-NOMA scheme in a 4-device scenario has been compared with the existing OMA and NOMA protocols [148]. The selection of power allocation factors for a 4D DRN is based on the analysis of BER in DL NOMA utilizing BPSK modulation, as reported in [148]. In order to provide a fair comparison, we have assumed D_1 as the farthest device and D_4 as the device closer to T. From the plots, the BER performance of A-NOMA is found to be less than NOMA, but more than OMA. This can be explained as follows: The BER plots for N=1,2, 3 and 4 using OMA technique are similar, since there is no asymmetrical power allocation applied in OMA; whereas, when NOMA is

applied, the difference of the BER curves of all the devices is noticeable. This is due to the fact that for OMA, each device is assigned a single orthogonal block that is free of any interference from other devices; whereas using NOMA protocol, the devices are sharing the same transmission power, which lowers the SNR and energy per symbol. As a result, there is more interference between the devices and more incorrect bits. Hence, the BER performance is high and the system reliability in NOMA is compromised. For the case of A-NOMA, the relay devices are divided into two groups in the diamond relay topology model of the network. Thus, the interference among 'N' devices is comparatively less than NOMA and the BER performance decreases.

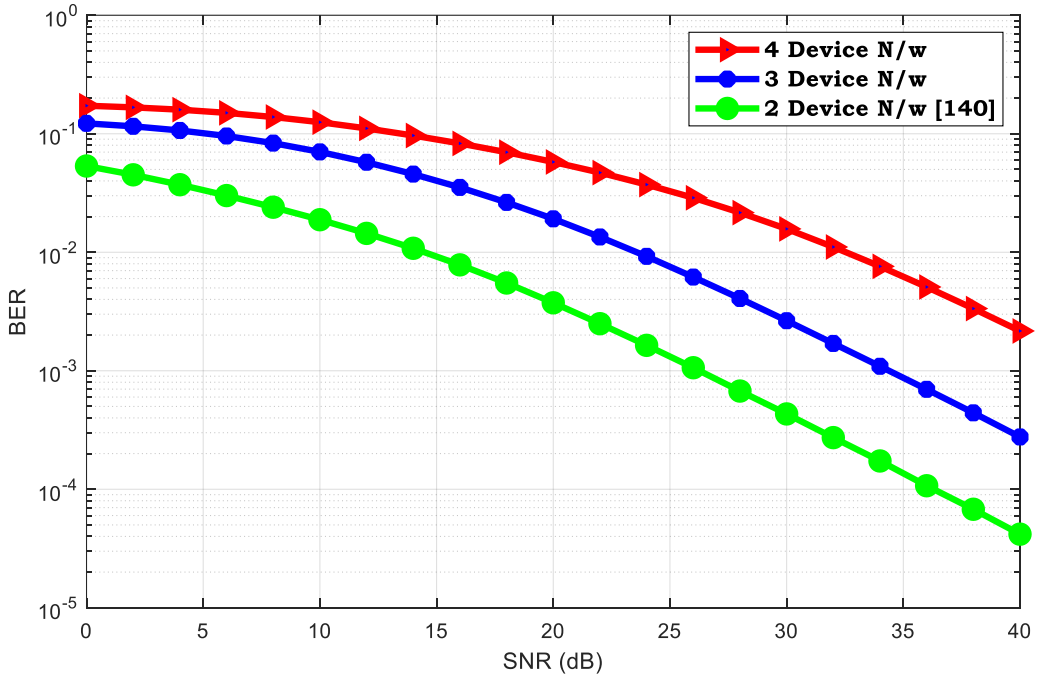

Fig. 6.15 BER performance of our proposed MD-DRN using A-NOMA for N=2,3,4

Fig. 6.15 compares the BER performance for ***N***=2,3,4. Here [140] represents Single DRN using NOMA where the concept of EH has not been addressed. For a fair comparison, the model in [140] has been devised using A-NOMA and then compared. It is observed that BER value increases with increasing ***N***. From the analysis, it can be concluded that superposing the signals of more than 2 devices on a single orthogonal block leads to severe degradation in BER. Hence, the system reliability is compromised. This is because the same transmission power is being divided among the devices resulting in lesser energy per symbol and lower SNR thus leading to high interference among the devices and more erroneous bits. For $P_S = 20dB$, a BER value

of 0.003 is obtained for the proposed model with a single DRN as opposed to 0.02 and 0.057 for 3-device and 4-device DRNs respectively.

Fig. 6.16 shows a comparison between conventional non-RF A-NOMA network [141] and RF-powered A-NOMA in terms of EE with respect to ASR (i.e. SE). As depicted from the figure, in the low SE region, EE rises, becomes maximum and then gradually reduces in the high SE region signifying an EE-SE trade-off. It can be clearly understood from the figure that the proposed adaptive scheme provides better efficiency within a certain SE region. It is evident from the figure that initially upto a certain value of ASR, [141] gives better efficiency. After a certain crossover point, an upsurge in EE is observed upto a certain range of ASR beyond which the EE performance falls. At lower levels of ASR, energy efficiency tends to improve with increasing SE. This is because the energy used for transmitting data is spread over a smaller bandwidth, allowing more bits to be transmitted for the same amount of energy. As SE increases, the system may reach an optimal point where the trade-off between bandwidth and energy use is balanced. At this point, the system is efficiently using both energy and bandwidth. Beyond this optimal point, further increasing SE can lead to diminishing returns in EE. This is often due to increased complexity in signal processing, higher power requirements for maintaining signal quality and the need for more sophisticated (and energy-intensive) techniques to handle higher data rates or finer modulation schemes.

From Table 6.4, for $ASR_{A-NOMA} = 0.75 bps/Hz$, the maximum EE for the developed scheme is found to be 55 Mbits/s/Hz/J, whereas the maximal EE for benchmark scheme is 38 Mbits/s/Hz/J for $ASR_{A-NOMA} = 0.5 bps/Hz$. Upto $ASR_{A-NOMA} = 1.5 bps/Hz$, better EE is obtained for the developed scheme as compared to its contrast part. Highlighted part indicates improvement of the proposed work compared to the conventional scheme. For a particular value of ASR= 0.85bps/Hz, the percentage enhancement in EE of our proposed system over [141] is 28.4% beyond which the efficiency reduces.

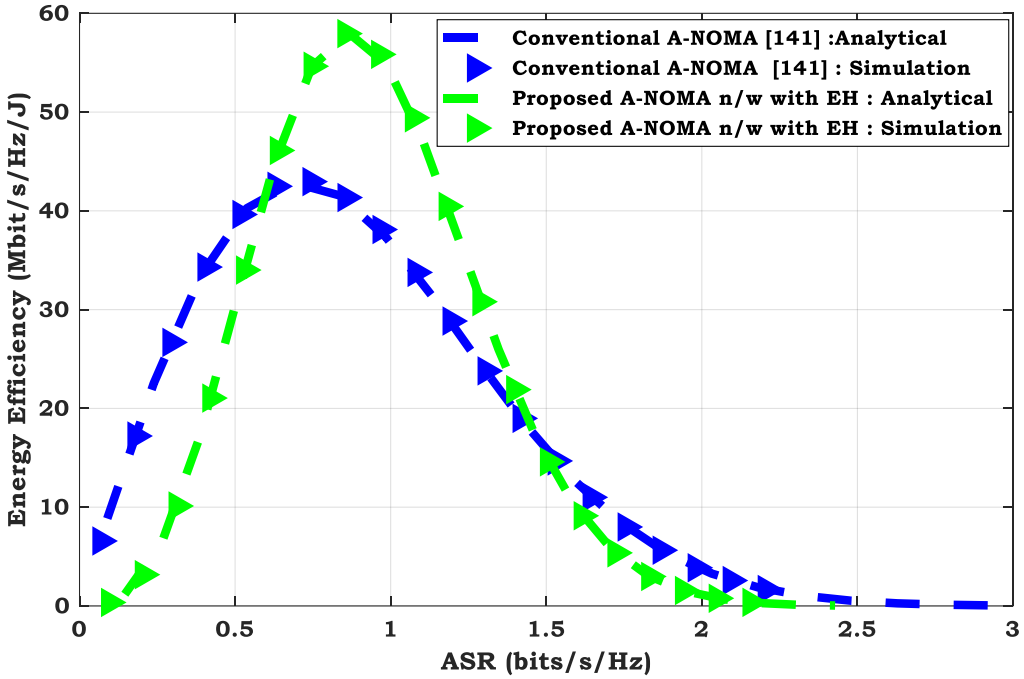

Fig. 6.16 Comparative plot of EE versus ASR for Conventional A-NOMA [141] and proposed RF powered A-NOMA

Table 6.4 Percentage Improvement in EE with respect to ASR

Parameter ASR (bps/Hz)	Energy Efficiency (Mbit/s/Hz/J)		% Improvement in EE
	Conventional A-NOMA [141]	Proposed RF powered A-NOMA	
0.5	38	30	21
0.75	43	55	**21.86**
0.85	41.5	58	**28.4**
2	1.9	1.4	26.31

Fig. 6.17 plots EE comparison for existing OMA, NOMA [139] and proposed A-NOMA with respect to ASR. Among the three scenarios, A–NOMA achieves a remarkable performance gain as compared to OMA and NOMA signifying that our proposed scheme is much more energy and spectrally efficient than the existing schemes. It is also found that initially with increase of SE, the optimal achievable EE gradually rises to the maximum point and after attaining the maximum EE, the network suffers a sudden decrease in EE with further increase in ASE. When ASE is 2 bps/Hz, the proposed network with A-NOMA achieves 67.56% and 12.7% EE gain over the conventional OMA and NOMA functioned networks respectively. In addition, a close resemblance between theoretical and simulation result has been observed for our proposed model which verify the correctness of our theoretical derivations with the simulated results.

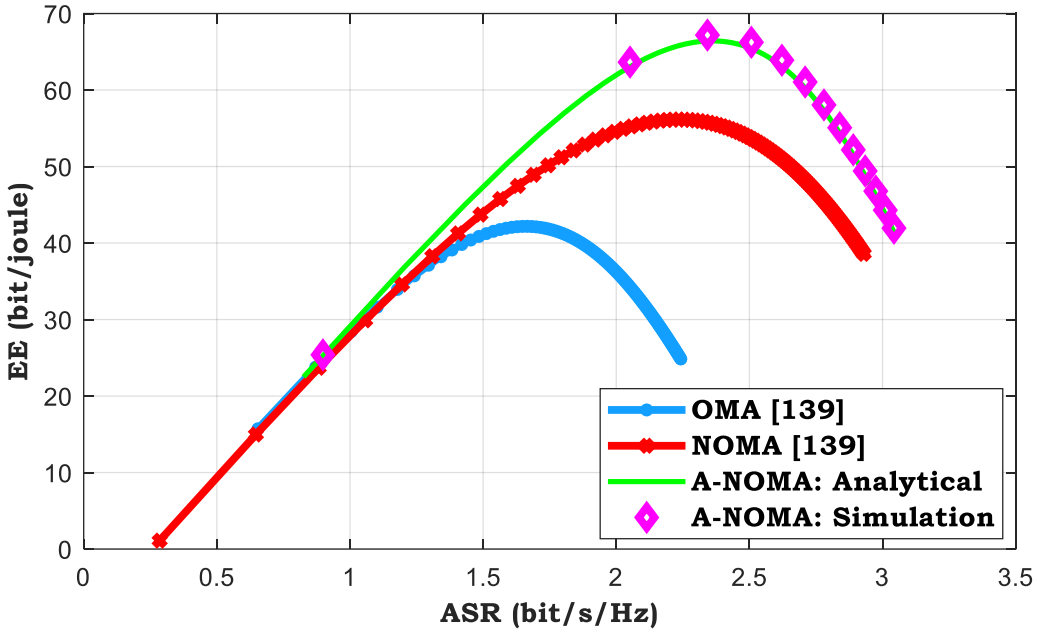

Fig. 6.17 EE versus ASR for both OMA and NOMA and our proposed RF powered A-NOMA

6.5 OVERALL COMPARISON

A critical study and comparison of the above works namely, Proposed Work 1 and Proposed Work 2 are presented in section 6.3 and 6.4 respectively with some of the existing relevant state-of-art have been abridged in Table 6.5 and 6.6.

Table 6.5 Comparison table with some existing relevant state-of-art

References	**Scenario**	**Protocol used**	**Performance metric**
Existing Works			
[151]	Multi-relay Single DRN in IoT	NOMA	ASR
[144]	Single DRN	NOMA	ASR
[143]	Single DRN	NOMA	BER
[135]	SWIPT assisted Single DRN in IoT	NOMA	ASR
[150]	Single DRN	NOMA	ASR
[141]	Cooperative Relay Network	A-NOMA	ASR, EE
[155]	NOMA in PLS under jamming cancellation technique in interference-free environment	NOMA	SOP
Proposed Works			
Proposed Work 1	***Interference-aided RF powered Cooperative NOMA Network***	***NOMA***	***SOP, ESC***
Proposed Work 2	***RF-powered MD-DRN***	***RF-powered A-NOMA***	***ASR, BER, EE***

Table 6.6 Critical Analysis of proposed work with existing works

Performance metric used	Existing/Proposed works	SOP	ESR	ASR	BER	EE
SOP & ESR	[14]	0.85	0.9		0.7	-
	Proposed Work 1	0.65	1.4		0.2	
ASR	[26]	-	-	0.85	-	-
	[27]			0.65		
	[28]			0.93		
	[29]			0.39		
	Proposed Work 2			1.4		
BER	Single DRN [5]	-	-	-	0.2	-
	[17]				0.7	
	Proposed Work 2				0.85	
EE	[28]	-	0.9	-	-	41.5
	Proposed Work 2		1.6			58

6.6 DISCUSSION

In Proposed Work 1, the performance of CR-NOMA network with Interference-aided RF EH has been improved by introducing a secure jamming cancellation scheme in the presence of an eavesdropper. Here, the security performance of the existing model [13] has been improved through our developed model. The performance of an RF-powered MD-DRN has been investigated using an upgraded A-NOMA protocol in Proposed Work 2. In this framework, the IoT relays are deployed in a diamond relay topology and are empowered by ambient RF energy for sustainable operation of the network. Firstly, theoretical derivations have been carried out and validated using Monte-Carlo simulation. Using the expressions, overall ASR has been evaluated in a 3-device and 4-device scenario and compared with the existing conventional OMA and NOMA protocols. BER comparison criteria has been used to evaluate the performance of the overall network in terms of communication reliability. Lastly, an in-depth analysis on the network performance in terms of EE with respect to ASR has also been performed.

Chapter 7

RF-POWERED RECHARGEABLE WIRELESS SENSOR NETWORK FOR LR-WPAN

7.1 OVERVIEW

This chapter explores the feasibility of Radio Frequency Wireless Power Transfer (RF-WPT) using an advanced energy measurement system consisting of PowerSpot® RF module in Low-Rate Wireless Personal Area Network (LR-WPAN) for industrial monitoring applications. The main focus is to design an intelligent industrial WSN to make the sensors autonomous in any industrial environment. In other words, it is required to develop an RF-powered Rechargeable WSN (R-WSN) and study its performance in terms of battery recharging time, harvested energy and Network Lifetime (NL). To meet this objective, firstly, measurement is carried out to monitor the effect of antenna gain on the recharging time for three widely used on-board rechargeable batteries. Moreover, the variation in recharging time for the batteries is recorded using patch and dipole antennas with respect to distance, depth of discharge and number of RF transmitters. Using these measurement values, a realistic virtual WSN environment has been created in Netsim v13.1 and subsequently the simulated values of energy consumption are processed in MATLAB 2022b to compare NL and throughput with Non-Rechargeable WSN (NR-WSN). Finally, the percentage improvement in harvested RF energy has been calculated and compared with some of the existing state-of-art.

7.2 BACKGROUND

Industrial IoT (IIoT) consist of ultra-low battery-powered automated smart sensors to sense, collect, process, and communicate temporal events in industrial systems [190, 191]. Classic IIoT sensor nodes (motes) are mostly equipped with non-rechargeable batteries that perform

energy-intensive network operations [191]. For stable network operation, the sensor batteries require frequent recharging/replacement after a specific time, which is expensive in terms of both labour and cost. Also, the battery lifetime of the sensor motes must be monitored continuously for better maintenance. Being a key enabler in the evolution of Industry 4.0, energy is a vital component in smart production environment. Thus, energy management is an important aspect to be considered when improvement in lifetime of sensor nodes is concerned [193]. This has motivated robust research into the development of RF-EH technique of acquiring energy from either ambient sources or other dedicated sources and further utilizing the harnessed energy (electrically converted) to power the sensor motes and improve their operational capability and lifetime. RF-WPT technology has emerged as viable attractive green technology to power the sensors in smart factory, where ambient RF cannot deliver sufficient energy to power the sensors. The application of wireless recharge mechanisms to WSNs, referred to as R-WSN [6], consists of multiple sensors that harvest energy emitted by single or multiple wireless power transmitters to recharge their batteries or super-capacitors. One of the commercially available evaluation kits allowing wireless energy transmission is the Bluetooth-enabled PowerSpot RF Wireless Power Development Module (P1110-EVAL-PS) [11] to charge various sensors and multiple consumer devices using the harvested RF power. In [177], the total harvested energy was typically modelled by the linear model. However, in practice, EH circuits produce a non-linear end-to-end WPT. In [178], a non-linear EH model was built on a logistic function that reflects the dynamics of RF energy conversion efficiency for various input power levels. Contrary to [178], the authors in [179] proposed a quadratic RF-EH efficiency model that obtained better results. Meanwhile, the authors in [180] designed a piecewise linear approximation model and obtained better performance but they did not analyzed the battery recharging time. To the best of our knowledge, none of the above-mentioned articles have analysed the battery recharging time and NL for any R-WSN in IIoT environment using RF-WPT. So, this study is presented in subsequent section.

7.3 FLOW OF PROPOSED WORK

The logical flow of the proposed work is presented in Fig. 7.1.

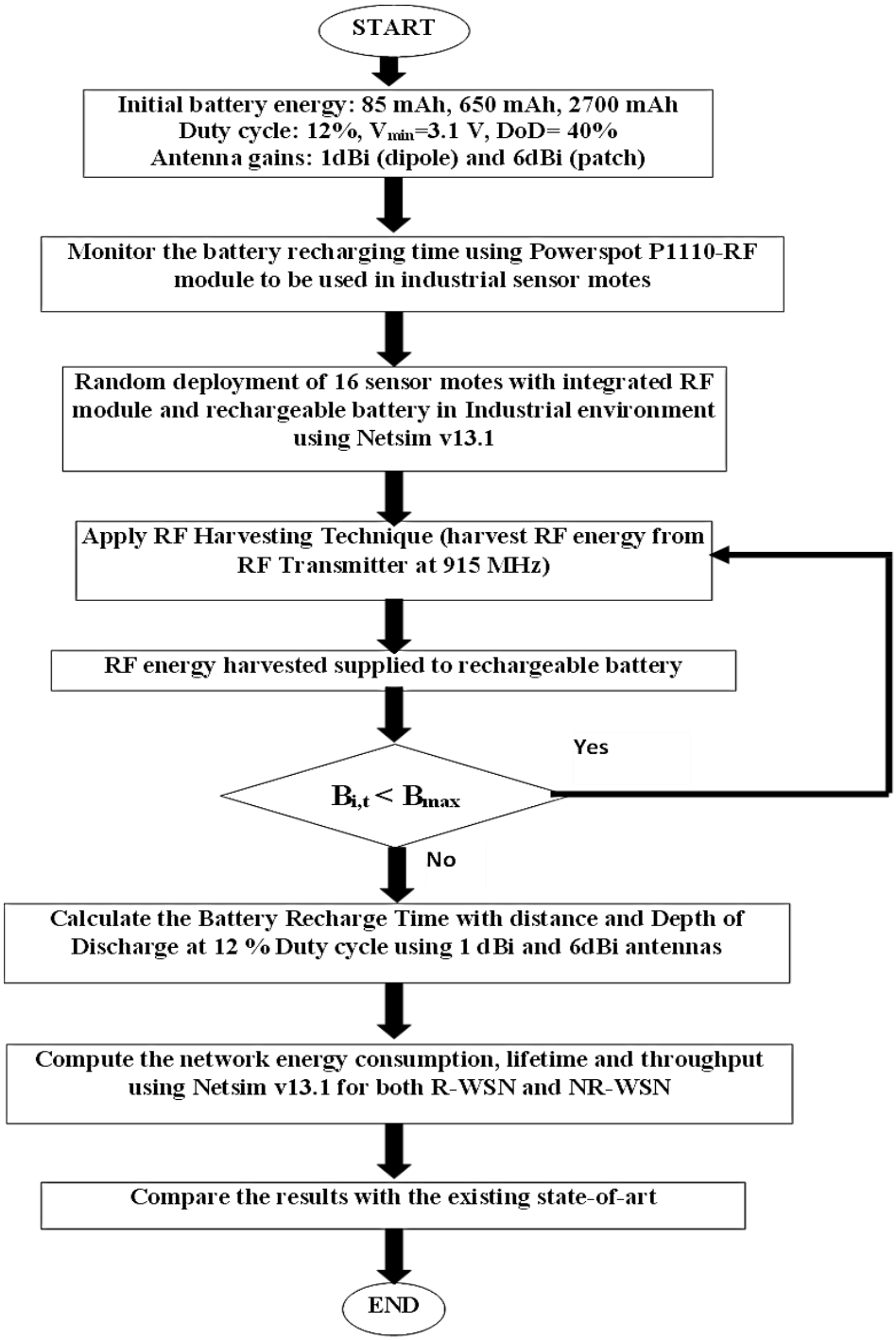

Fig. 7.1 Flow chart of the proposed work

7.4 NETWORK MODEL

Fig. 7.2 presents an R-WSN based on LR-WPAN architecture deployed for environmental monitoring in an industrial warehouse (30 x 40 m^2).

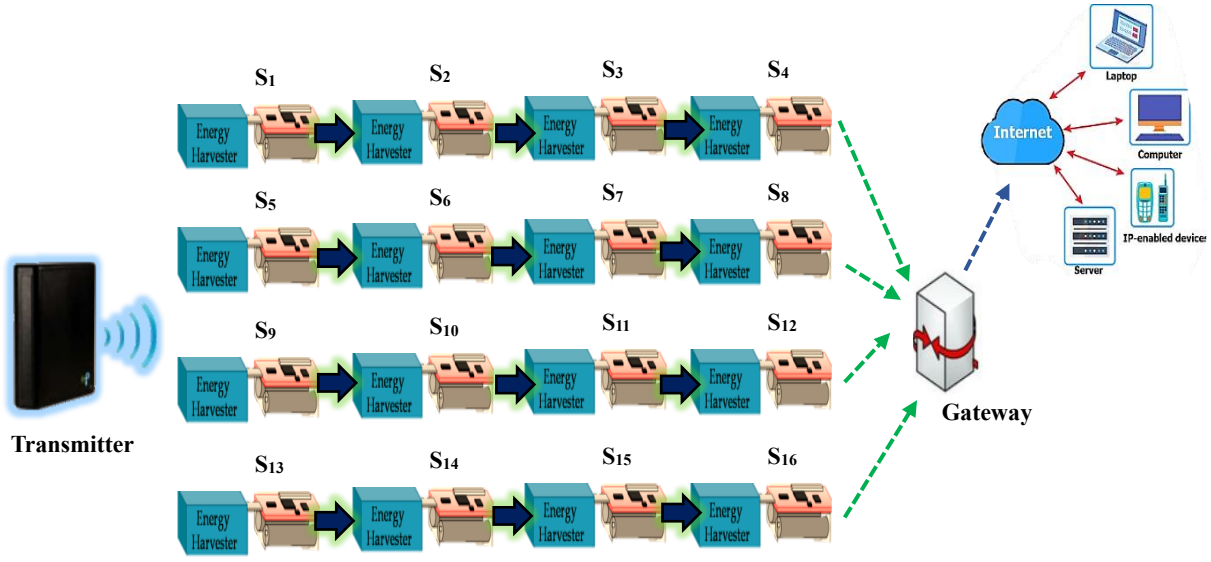

Fig. 7.2 Proposed framework for R-WSN in LR-WPAN

Here sixteen sensor motes ($S_1,....,S_{16}$), say Zolertia mote (also known as Z1 mote [187]) working at 915 MHz radios are installed at different locations in the warehouse and they report data to an Access Point (AP) within a period of 4 seconds. Using Internet connection, the data received at AP gets stored in a database that runs on a remote server which can be accessed by the user anytime using special Java-based application. For simplicity, it is assumed that there is only one transmitter located at a depot within the monitoring area of the WSN. Each mote comprises of a wireless EH module (P1110), an energy storage module (preferably a rechargeable battery), and a sensor module. To keep the sensor motes working perpetually, they are assumed to have EH capabilities. Each Z1 mote has an onboard rechargeable battery (i.e., Li-ion or AAA) that stores energy charged by the EH module. The harvesting module powers the sensor module using an Analog-to-Digital converter (ADC). The motes adopt TI MSP430 as an MCU and TI CC2420 as an RF transceiver that is responsible for data transmission and reception. The sensed data is sent periodically to a cloud platform through the Internet and then to GSM mobile or Wi-fi router. The user observes the data using monitoring and control application running on their Personal Computer or mobile phone. The assumptions for the constructed network model are listed below:

- The amount of the available RF energy is the same throughout the WSN.
- The motes are static and homogeneous with same initial battery energy and same hardware. They transmit/receive similar number of packets and are distributed in the industry to monitor variables, such as humidity, temperature, sound, luminosity etc.
- Each of the energy constrained motes are powered by rechargeable batteries and fitted with an RF harvester that harvest energy from a dedicated power beacon.
- Multiple sensor motes are managed by one gateway.
- The rechargeable batteries of the sensor nodes are subjected to recharge via radiative WPT.

7.5 MEASUREMENT METHODOLOGY

In this section, a detailed description of measurement tools and procedure is given to calculate the battery charging time of on-board rechargeable batteries. RF module P1110-EVAL-PS is used for measurement of battery recharging time. Software tools used for modelling and simulation are Netsim v13.1 and Matlab R2022b. Measurements are taken at different distance and DoD is varied using vertically polarized PCB dipole (1 dBi) and patch (6.1 dBi) antennas.

7.5.1 Measurement tools

Table 7.1 shows the specifications of three widely used rechargeable test batteries to drive the sensor motes i.e. one Li-ion 2032 coin cell battery (Bat 1), a single AA Lithium Manganese Li-Mn (Bat 2), and 3 AAA Nickle Metal hydride (Ni-MH) in series (Bat 3). The developed model (shown in Figure 7.2) is tested by selecting all the three batteries one at a time and the performance is analysed using Netsim modeller tool. The runtime of a battery is dictated by the battery capacity expressed in milliampere per hour (mAh) or amp hours (Ah). Z1 motes can be powered by any one of the given three batteries [175]. Figure 7.3 depicts the Evaluation Board (EVB) to charge the on-board batteries [11].

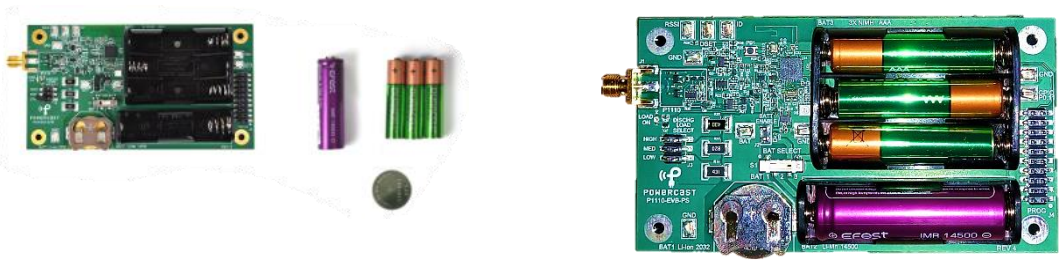

Fig 7.3 Powerspot Development Board with battery holder for harvesting energy to charge the on-board batteries [11]

Table 7.1 Various on-board rechargeable battery specifications [11]

Battery type	NiMH 900mAh 10.5mm x 44.5mm	Li-MN 650mAh 14mm x 50mm	Li-ion coin cell 85mAh 20mm x 3.2mm
Make	Duracell	EFest	Route JD
Model no.	DX2400	IMR14500	PD2032C1

Characteristics of a single storage element

Nominal voltage (V)	1.2	3.6	3.7
Current rating (mAh)/ Capacity	900mAh	650mAh	85mAh
Self-discharge (per month)	30	<10	<10
Charge–discharge efficiency (%)	66	95	99.9
Memory effect	No	No	No
Charging method	Trickle/Pulse	Pulse	Pulse
Charging Time (in hours)	4-9	4-5	2-3
Recharge cycles	1000	1200	1200

7.5.2. Block diagram of WPT model

Fig. 7.4 depicts the block diagram of the WPT model. Left part of the diagram depicts power beacon (TX91501-3W-ID) and the right part shows a sensor mote powered by P1110-EVAL-PS power harvester [11]. The WPT system consists of RF energy transfer channel and data communication channel. There is no interference between these channels as they use different frequency bands.

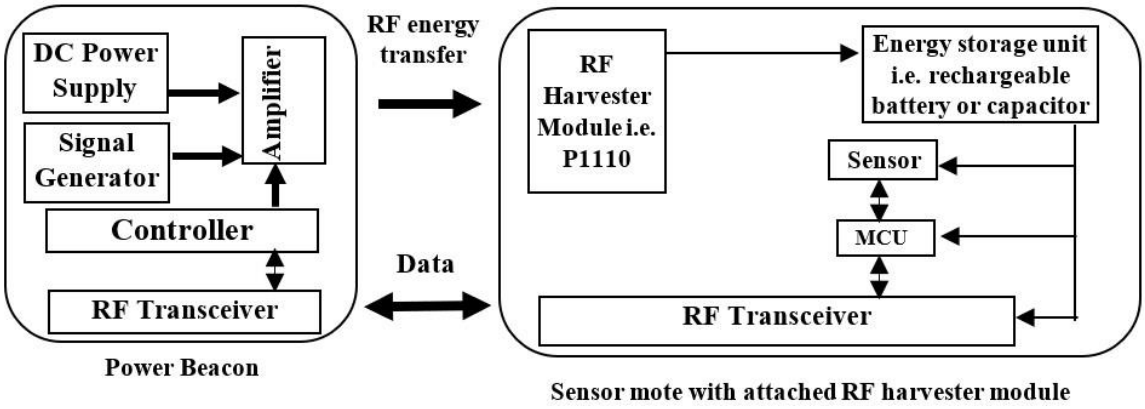

Fig. 7.4 Block Diagram

The RF energy that is harvested by the P1110 RF module gets stored in a rechargeable battery or capacitor. An internal RF sensor in this module measures the received power using ADC. The beacon and EVB exchange information by means of IEEE 802.15.4 standard [175] on the 2.4 GHz ISM band that provides a communication range of approximately 20-50 m indoors. Main function of the power beacon is to wirelessly supply RF energy to any battery-driven sensor mote by means of WPT. The beacon is connected to a power grid. It consists of a signal generator that generates a weak continuous wave RF source signal and feeds it to the amplifier. The weak RF signal is amplified by the amplifier and the transmit antenna emits a high-power signal. The amplifier consumes DC power from the power supply and performs DC-to-RF conversion. In the sensor mote, the harvester receives RF signal from the power beacon through the receive antenna and performs RF-to-DC conversion by using a rectifier. The DC power is then stored in the storage module i.e., a rechargeable battery.

7.5.3. Measurement procedure

Fig. 7.5 shows the experimental set up for the determination of battery charging time using Powerspot Development module consisting of a transmitter TX91501-3W and the EVB. The former is a wireless dedicated 915 MHz transmitter with 26 MHz bandwidth and 3 Watts Equivalent Isotopically Radiated Power (EIRP) fitted with an inbuilt patch antenna (8 dBi gain). The latter is a power harvester EVB with onboard rechargeable batteries which can harvest energy from RF signal radiated by the transmitter to provide intermittent/pulsed power output. In the current setting, the operation of Z1 mote has not been considered as the main focus is on battery charging time using P1110-EVAL-PS module. P1110 IC converts 915MHz

RF received using a dipole or patch antenna to DC and stores it in any one of the selected onboard rechargeable batteries. The harvester collects the RF input power in the range of −5 to +20 dBm. EVB includes the circuitry required to activate the Powerspot transmitter via Bluetooth Low Energy (BLE) communication.

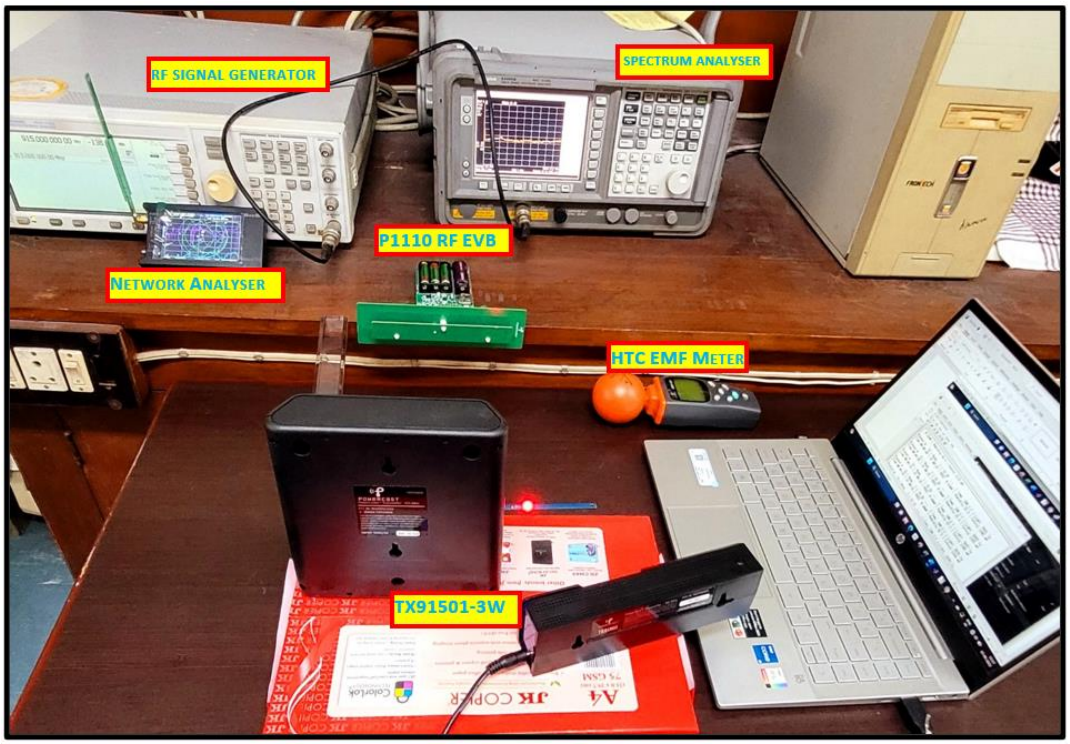

Fig. 7.5 Experiment Setting for monitoring Battery Recharge Time at 915 MHz

Circuitry on the board monitors the Received Signal Strength Indication (RSSI) of the RF field received from the Powerspot transmitter, the amount of current supplied to recharge the selected battery and the voltage of the selected battery being recharged. Via Bluetooth, the data is transmitted to a smartphone and is displayed in the Powerspot Dev app. A sliding switch on the EVB allows the user to select any one of the three batteries. The Li-ion battery is connected to BAT 1 pin, LiMn to Bat 2 and AAA to Bat 3. When any battery voltage goes below a predetermined threshold (3.1V), the selected battery will recharge again and the cycle will repeat. When the charge threshold >=3.1 is achieved, P1110 enables the voltage output. The output voltage from P1110 is applied to the BAT pin. The RSSI is monitored using RSSI Pin on the board or from Powerspot Dev app in smartphone. After reaching the max voltage of 3.6 V or 3.7 V, P1110 shut off its output and prevents the battery from getting overcharged. During the experiment, the transmitter is fixed at a position and the harvester board is varied with 10 steps (10 cm, 20 cm, 30 cm and so on). To find out the battery recharge time, measurement is taken at different distances using dipole antenna attached to the harvester circuit as shown in

Fig. 7.5. Similar experiment is carried out with patch antenna. As per the recharge time, the batteries can be used in Z1 motes. Initially, the battery recharge time for Bat 1 with a capacity of 85 mAh and nominal voltage of 3.6 V is monitored. The process is repeated with the other on-board batteries and compared with respect to distance and DoD.

7.6 SIMULATION NETWORK SCENARIO OF THE PROPOSED MODEL

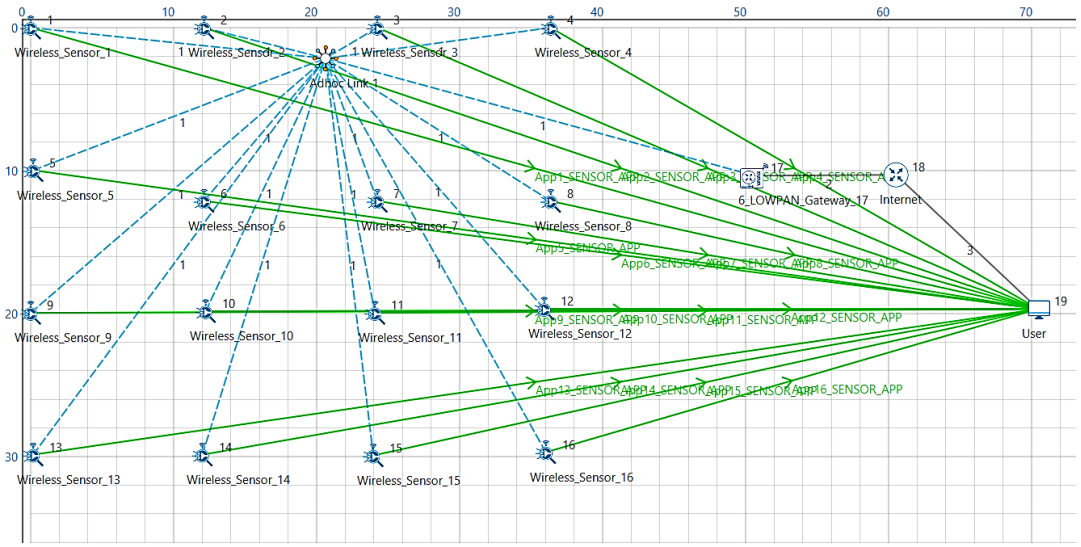

Fig. 7.6 RF simulation module implementation using NETSIM modeller tool comprising of 16 battery-operated RF-powered sensor motes

9.6.1 Simulation model and network setup

To test the feasibility and performance of the proposed R-WSN described in Fig. 7.2, a virtual IIoT scenario is created using NETSIM in Fig. 7.6 comprising of similar rechargeable sensor motes with P1110 EH module for monitoring environmental parameters. Z1 mote requires 36 mJ at 3.6 V of harvested voltage to turn on the mote for initialization of the uC MSP430F2617 and data communication. Z1 can be powered in several ways: Battery-powered (using AA or AAA or Li-ion coin cell in the battery-holder) or USB powered. It is flexible in the sense that it can switch to any battery as per the required application. The measured and processed data from the sensor motes is transmitted to the Gateway. Finally, the transmitted data is forwarded

to the user through Internet. Simulation is carried out in Netsim modeller to find the network energy consumption. The sixteen RF-powered Z1 motes can operate as both with (Rechargeable) or without (Non-rechargeable) RF harvesting feature. For real-time IIoT applications, the harvested power needs to be deterministic and consistent and proper placement of RF source and sensor motes are required to obtain fixed amount of harvested power. In this network, if the battery voltage of any sensor falls below a critical minimum voltage level (V_{min}) i.e., 3.1 V then, it is considered to be 'non-operational' and requires re-powering by EH.

9.6.2 Design and implementation

To model the circuit described in Fig. 7.2, the sensor battery/energy model (that is a part of WSN/IoT networks) in the Netsim simulator has been used. The energy model is user-configurable and can be found in the ZigBee Interface properties of the sensor motes. The network performance has been analysed in terms of energy consumption by entering the specifications of all the three batteries one at a time. Energy consumption is calculated individually for each battery. Based on the simulations and calculations done, NetSim provides a detailed Battery Model Metrics table which provides energy consumption of each mote with respect to Transmission, Reception, Idle Mode, Sleep Mode. NetSim also supports an abstract EH model where a specified amount of energy (calculated from recharging current and voltage specified) is added to the remaining energy of the node periodically to replenish the battery energy.

7.7 THEORETICAL ANALYSIS

A R-WSN is considered that comprises of a set of rechargeable homogeneous sensor motes $S = \{s_1, s_2, ...s_n\}$ deployed in a rectangular area $L \times L$ for environmental monitoring; n is the total number of sensor motes. The coordinate of i^{th} sensor mote s_i is taken as (x_i, y_i). The energy of the RF transmitter is assumed to be infinite and is located at a depot within the monitoring area of the network. Sensor s_i comprises of a sensing module, a processing unit, an RF transceiver, an EH module, rechargeable battery for storage and a power management unit. Sensory data is generated by s_i with a data rate of R_i and fed to the processing unit. After processing, the data is forwarded to the gateway via single-hop or multi-hop communication

using the transceiver unit. $B_{i,t}$ represents the remaining energy of s_i at some time point t, and $B_{\max}$ is the maximum energy level of each sensor mote. When $B_{i,t} <= B_{\max}$, then s_i starts harvesting energy from the RF transmitter to continue operation of the network. For NR-WSN, when $B_{i,t} <= B_{\max}$, then s_i becomes non-operational.

➢ Battery Charging Time

The Friis free space equation according to omnidirectional WPT model is given as [15]

$$P_R = \frac{P_T \Delta \eta_t |h|^2 |s|^2}{d^\beta} \tag{7.1}$$

where P_R represents the power received by a sensor mote; P_T is the power transmitted by the RF transmitter; s is the transmitted signal, and h is the channel coefficient between the beacon and harvester. $|s|^2$ and $|h|^2$ denote the powers of s and h respectively. β is the path loss exponent, d indicates distance between the transmitter and harvester board. η and Δ are the transmitter efficiency and the large-scale propagation effect parameter, respectively.

$$\Delta = \frac{G_T G_R}{L_P}\left(\frac{\lambda}{4\pi}\right)^2 \tag{7.2}$$

Here Δ is dependent on transmitter and receiver antenna gains (G_T and G_R), wavelength of transmitted signal (λ) and polarization loss (L_p)

Let θ represent the charging orientation angle between transmitter and sensor. According to directional WPT model [15], the Friis free space equation is expressed as:

$$P_R = \frac{P_T A_R A_T \Delta \eta_t |h|^2 |s|^2 (\cos\theta + c)}{d^\beta} \tag{7.3}$$

where A_R and A_T represent effective power receiving area and the maximum power transferring area of sensor and transmitter, respectively; c is a constant.

The RF EH circuit converts the received RF input power to DC output power. The efficiency of the P1110 EH module used here is approximately 80% at 915 MHz given as:

$$\eta_{EH} = \frac{P_{DC}}{P_R} \tag{7.4}$$

where P_{DC} indicates DC output power

The harvested energy by the harvesting circuitry is expressed as:

$$E_H = P_{DC} T_{Bat} \tag{7.5}$$

where T_{Bat} is the time to recharge the battery as expressed below:

$$T_{Bat} = \frac{E_H}{\sum_{n=1}^{N} \left(\eta P_{T,n} G_{T,n} G_R \left(\frac{\lambda}{4\pi d_n} \right)^2 \right)} \tag{7.6}$$

Now, E_H amount of harvested energy is transferred to a rechargeable battery with a certain capacity and voltage and stored to power the sensor motes. Thus, the expression for battery recharging time is given as:

$$T_{Bat} = \frac{C_B D_B V_B^2}{2\sum_{n=1}^{N} \left(\eta P_{T,n} G_{T,n} G_R \left(\frac{\lambda}{4\pi d_n} \right)^2 \right)} \tag{7.7}$$

where V_B is the charging voltage, C_B is the battery capacity and D_B is the DoD of the battery. From (7.7), the recharging time is inversely proportional to the gain of antenna, number of transmitters and directly proportional to the battery capacity, voltage, distance and DoD.

➢ Energy Consumption (E_C)

The E_C of a sensor mote occurs during four modes: idle listening (E_{Idle}) and sleep mode (E_{Sleep}), data transmission (E_{T_X}) and data reception (E_{R_X}). The sum of all the consumed energies give the total energy consumed by a mote. E_{T_X} depends on the amount of data transmitted by one node to other motes. In the reception mode, the amount of data received by the sensor motes from the gateway is a measure of the total energy consumed. In idle mode, the motes consume energy by turning their transceivers in “ON” position without any data transmission or reception. During sleep mode, the sensors turn off their receiver and the energy consumption

is negligible, hence ignored in calculation. The following equation is used to compute energy consumption [182].

$$E = V \times I \times \tau^{ON} \tag{7.8}$$

where 'I' is current drawn at different modes in the mote components, 'V' represents the battery voltage of the mote (voltage is 3.6 V for Z1 mote), and 'τ^{ON}' is the duration when the node is ON.

The energy consumed during transmission is expressed as:

$$E_{Tx} = V \times I_{Tx} \times \tau_{Tx} = V \times I_{Tx} \times \frac{l_{beacon}}{R} \tag{7.9}$$

where l_{beacon} represents length of beacon packet and R is the data rate

Energy consumption in reception mode is given as:

$$E_{Rx} = V \times I_{Rx} \times \tau_{Rx} = V \times I_{Rx} \times \frac{l_{beacon}}{R} \tag{7.10}$$

where I_{Rx} denotes current drawn during data reception and τ_{Rx} is the receiving time. For idle mode, the energy consumed during is given as:

$$E_{Idle} = V \times I_{Idle} \times \tau_{Idle} \tag{7.11}$$

where I_{Idle} is the idle-mode current and τ_{Idle} represents time in idle mode

The energy consumed by a single sensor mote is calculated as:

$$E_C = E_{Tx} + E_{Rx} + E_{Idle} \tag{7.12}$$

➢ Network Lifetime (NL)

In WSN, the time duration from starting time to the time instant when the network becomes non-functional defines the NL as expressed [183]:

$$T_{Net} = \frac{E_{initial} - E_W}{E_C + \chi.E_S} \tag{7.13}$$

where T_{Net} = Average Network Lifetime (in days)

$E_{initial}$ = Initial Network Energy (Joules)

E_W = Expected wasted (unused) energy in the network when it dies (Joules)

E_C is the energy consumed by the network / day (Joules)

E_S is the expected energy consumption (Joules)

χ is packet arrival rate

❒ Initial network energy $E_{Initial}$ calculation:

It is assumed that each mote operates with a single AA LiMn (Bat 2) rechargeable battery. The initial energy of a single AA 3.7 V battery having capacity 650 mAh in joules is obtained as 0.65 Ah × 3.7 x 3600 = 8658 J. Thus, initial energy of the whole network with 16 Bat 2-driven motes is obtained as 8560 J × 16 = 138,528 J. Similarly, the initial energy of the network with the other two test batteries (Bat 1 and Bat 3) has been obtained as presented in Table 7.2.

❒ Unused network energy E_W calculation

It is assumed that the battery State-of-Charge (SoC) becomes 'zero' for NR-WSN when the maximum rated energy of the battery is reduced to 70%. Here, one sensor mote has maximum energy of 8658 J. Then 70% of 8658 J = 6060.59 J. Thus, when the battery energy reaches less than 6060.59 J, each sensor mote is considered "non-operational". For the entire network, the expected wasted energy when the network dies is 6060.59 J × 16 = 96969.59 J.

If any mote energy goes below the predefined threshold level, the battery re-charging for the motes occurs autonomously for R-WSN. After battery charging using RF harvesting, when the battery SoC of the energy constrained motes is more than 70%, they become operational and automatically participates in the network. Thus, NL becomes infinite (ideally) and network never dies completely. In traditional NR-WSNs, very low duty cycle (say < 5%) is kept by the designers to save the power consumption of WSN motes. But, in RF-EH, as the nodes are not energy limited, the duty cycle can be increased. Here, 5% DoD and 12% duty cycle has been considered for R-WSN i.e. the network sends one message after every 8.3 s to the gateway node for better monitoring in industrial application.

Table 7.2 On-board battery energy calculation

Sl.No	Parameters	1 WSN			Whole Network (comprising of 16 WSNs)		
		Bat3	Bat2	Bat1	Bat3	Bat2	Bat1
1	Initial energy (in J)	34992	8658	1101.6	559,872	138,528	17,625.6
2	Unused or wasted energy (in J)	24494.4	6060.59	771.12	391910.4	96,969.6	12,337.9

Let the expected energy consumption by a sensor mote be 16 mW or 16 mJ/s. For 16 motes, it becomes 16 mW×16 = 256 mW or 256 mJ/s. The number of secs-rounds in one day is 24 h × 60 min × 60 s = 86,400 s. For 1 % duty cycle, a sensor mote is powered up for 864 s out of 86,400 s in 24 h. Thus, the expected energy consumed by a single mote E_{S_1} is 16 mJ/s × 864 s = 13.82 J/ day. For 16 motes, E_S becomes 13.82 J × 16 = 221.184 J/ day. Thus, the NL is calculated as given in (7.13). Using the same procedure as 1% duty cycle, the NL for various duty cycles (5%, 10%,…) is calculated and shown in Table 7.3.

Table 7.3 Duty cycle versus Network Lifetime

Duty Cycle (in %)	Energy consumption/day for 1 WSN (in J/day)	Energy consumption/day for of the network (comprising of 16 WSNs) (in J/day)	Network lifetime (no. of days)		
			Bat 1	Bat 2	Bat 3
1	13.82	221.184	24.59	187.934	253.18
5	69.12	1105.92	4.92	37.58	151.88
10	138.24	2211.84	2.46	18.79	76.07
12	162.12	2593.92	2.03	16.23	64.75
20	276.48	4423.68	1.19	9.39	27.97
50	691.2	11059.2	0.5	3.75	5.06

➢ THROUGHPUT

Throughput is defined as the rate of successful transmission of data (in bps/Hz) within the network for a specific duration of simulation time. It is expressed as:

Throughput = SRP x packet size/Ts (7.14)

where SRP is successful reception of data packets and Ts is the simulation time.

7.8 PERFORMANCE EVALUATION

In this section, the recharging time is evaluated by varying the DoD for all the batteries. The distance between the RF transmitter and EVB is not shortened by less than 10 cm during

measurement. Table 7.4 shows the measurement results of Recharge Time versus DoD for Bat 1, 2 and 3 at 915 MHz and 10 cm distance.

Table 7.4 Test results of Recharge Time versus DoD at 10 cm distance

Battery Type	**Parameters**	**Patch**	**Dipole**
	Received RF Power (mW)	8.12	2.56
	Harvested DC Power (mW)	5.33	1.43
	Conversion Efficiency (in %)	65.7	55.7
	DoD (in %)	**Recharging Time (in hours)**	
Bat 1	5	0.24	0.37
	10	0.43	0.84
	15	0.56	1.05
	20	0.67	1.18
	25	0.76	1.28
	30	0.85	1.41
	35	0.91	1.55
	40	0.97	1.69
Bat 2	5	0.6	1.70
	10	1.52	2.33
	15	1.62	2.86
	20	1.87	3.30
	25	2.09	3.68
	30	2.32	4.05
	35	2.47	4.36
	40	2.65	4.7
Bat 3	5	0.97	1.95
	10	1.68	2.76
	15	1.89	3.38
	20	2.19	3.90
	25	2.46	4.5
	30	2.70	4.82
	35	2.90	5.2
	40	3.08	5.51

The recharging time values with varying distance (in cm) for Bat 1, 2 and 3 using patch and dipole antennas at 915 MHz and 5% DoD are listed in Table 7.5. It is evident that recharging time increases with increasing distance. Moreover, recharging time is faster with patch antenna compared to dipole. In addition, Bat 1 gives the shortest recharging time value at 10 cm distance with 6.1 dBi patch antenna at 5% DoD as compared to Bat 2 and 3. For Bat 1, the shortest charging time is found to be 0.24 hrs (14.4 minutes) at a distance of 10 cm and the longest charging time is determined as 0.672 hrs (40.32 minutes) at a distance of 50 cm for 6.1 dBi Patch antenna. Moreover, the shortest recharging time is determined as 0.36 hrs (21.6 minutes) at a distance of 10 cm and the longest charging time is found as 1.92 hrs at a distance of 50 cm

for 1 dBi Dipole antenna. Similarly, the recharging time for Bat 2 and 3 are also recorded and shown in Table 7.5.

Table 7.5 Recharging time versus Distance

Distance (in cm)	Recharging time (in hrs)					
	Bat 1		Bat 2		Bat 3	
	Patch	Dipole	Patch	Dipole	Patch	Dipole
10	0.24	0.32	0.6	0.72	0.97	2.88
20	0.312	0.44	0.96	2.64	3.84	11.04
30	0.432	0.72	1.93	5.04	8.4	20.88
40	0.6	1.2	3.12	8.64	13.5	35.76
50	0.672	1.92	4.56	13.92	18.72	50.2

Table 7.6 shows the variation in recharging time with increase in number of transmitters for Bat 1, 2 and 3 using PCB patch and dipole. Due to resource constraint, only two transmitters are used in this work. It is observed that the recharging time is faster with increase in number of transmitters. Using 6.1 dBi PCB patch, the recharging time for Bat 1 is found to be 0.672 hrs (40.32 minutes) for N=1 that reduces to 0.432 hrs (25.92 minutes) for N=2. Meanwhile, the recharging time using 1 dBi PCB dipole for Bat 1 is found to be 1.92 hrs for N=1 that decreases to 0.96 hrs (57.6 minutes) for N=2. Similarly, the recharge time for Bat 2 and 3 are also recorded and shown in Table 7.6.

Table 7.6 Recharging time for Bat 1, 2 and 3 for single and double RF transmitters at 50 cm distance and 5% DoD

No. of Transmitters (N)	Recharging time (in hrs)					
	Patch			Dipole		
	Bat 1	Bat 2	Bat 3	Bat 1	Bat 2	Bat 3
1	0.672	4.56	18.72	1.92	13.92	50.6
2	0.432	2.64	9.04	0.96	6.72	15.08

To evaluate the performance of the overall WSN using Bat 1, 2 and 3, a simulation environment is designed as shown in Fig. 7.6 using NETSIM comprising of a set of 16 WSN nodes, one gateway, one router and one user application. The 16 sensor nodes are uniformly deployed in the network area and the initial energy for each node is varied according to the battery specifications given in Table 7.1. Physical quantity like temperature, light, humidity etc. is

sensed by a sensing agent in the industrial environment that sends data to all the motes. The simulation parameters are listed in Table 7.7.

Table 7.7 Simulation parameters

Performance Parameters	Values
Simulation Time	10000
Frequency	915 MHz
Sensor mote	Z1 mote
No. of sensors	16
Initial battery capacity	1101 J, 8658 J, 34992 J
Recharging Current (mA)	50
Transmitting Current (mA)	8.8
Idle Mode Current (mA)	3.3
Receiving Current (mA)	9.6
Voltage (V)	3.7
Mobility model	No mobility
No. of sink (gateways)	1
Type of harvesting source	RF
Area of deployed nodes	30 x 40 m^2
Transmission rate	250 kbps
Data size	800 bits
Duty cycle (%)	12

Two sets of simulation results are obtained in the pre-analysis, for only battery-powered i.e. NR-WSN and another with included EH feature i.e. R-WSN. Tables 7.8 and 7.9 shows the simulated results generated in NETSIM using Bat 1.

Table 7.8 Results for NR-WSN using Bat 1 without EH feature (NR-WSN)

Device Name	Consumed energy(mJ)	Remaining Energy(mJ)	Harvested Energy(mJ)	Transmitting energy(mJ)	Receiving energy(mJ)	Idle energy(mJ)
WIRELESS_SENSOR_1	1101600	0	0	24312.8331	23470.78487	1053816.382033
WIRELESS_SENSOR_2	1101600	0	0	24312.8331	23470.78487	1053816.382033
WIRELESS_SENSOR_3	1101600	0	0	24312.8331	23470.78487	1053816.382033
WIRELESS_SENSOR_4	1101600	0	0	24312.8331	23470.78487	1053816.382033
WIRELESS_SENSOR_5	1101600	0	0	24312.8331	23470.78487	1053816.382033
WIRELESS_SENSOR_6	1101600	0	0	24312.8331	23470.78487	1053816.382033
WIRELESS_SENSOR_7	1101600	0	0	24312.8331	23470.78487	1053816.382033
WIRELESS_SENSOR_8	1101600	0	0	24312.8331	23470.78487	1053816.382033
WIRELESS_SENSOR_9	1101600	0	0	24312.8331	23470.78487	1053816.382033
WIRELESS_SENSOR_10	1101600	0	0	24312.8331	23470.78487	1053816.382033
WIRELESS_SENSOR_11	1101600	0	0	24312.8331	23470.78487	1053816.382033
WIRELESS_SENSOR_12	1101600	0	0	24312.8331	23470.78487	1053816.382033
WIRELESS_SENSOR_13	1101600	0	0	24312.8331	23470.78487	1053816.382033
WIRELESS_SENSOR_14	1101600	0	0	24312.8331	23470.78487	1053816.382033
WIRELESS_SENSOR_15	1101600	0	0	24312.8331	23470.78487	1053816.382033
WIRELESS_SENSOR_16	1101600	0	0	24312.8331	23470.78487	1053816.382033

Table 7.9 Results for R-WSN using Bat 1 with EH feature (R-WSN)

Device Name	Consumed energy(mJ)	Remaining Energy(mJ)	Harvested Energy(mJ)	Transmitting energy(mJ)	Receiving energy(mJ)	Idle energy(mJ)
WIRELESS_SENSOR_1	3014622.019	62886273.879	64799295.89	67397.6475	53149.85061	2894074.521
WIRELESS_SENSOR_2	3014622.019	62886273.879	64799295.89	67397.6475	53149.85061	2894074.521
WIRELESS_SENSOR_3	3014622.019	62886273.879	64799295.89	67397.6475	53149.85061	2894074.521
WIRELESS_SENSOR_4	3014622.019	62886273.879	64799295.89	67397.6475	53149.85061	2894074.521
WIRELESS_SENSOR_5	3014622.019	62886273.879	64799295.89	67397.6475	53149.85061	2894074.521
WIRELESS_SENSOR_6	3014622.019	62886273.879	64799295.89	67397.6475	53149.85061	2894074.521
WIRELESS_SENSOR_7	3014622.019	62886273.879	64799295.89	67397.6475	53149.85061	2894074.521
WIRELESS_SENSOR_8	3014622.019	62886273.879	64799295.89	67397.6475	53149.85061	2894074.521
WIRELESS_SENSOR_9	3014622.019	62886273.879	64799295.89	67397.6475	53149.85061	2894074.521
WIRELESS_SENSOR_10	3014622.019	62886273.879	64799295.89	67397.6475	53149.85061	2894074.521
WIRELESS_SENSOR_11	3014622.019	62886273.879	64799295.89	67397.6475	53149.85061	2894074.521
WIRELESS_SENSOR_12	3014622.019	62886273.879	64799295.89	67397.6475	53149.85061	2894074.521
WIRELESS_SENSOR_13	3014622.019	62886273.879	64799295.89	67397.6475	53149.85061	2894074.521
WIRELESS_SENSOR_14	3014622.019	62886273.879	64799295.89	67397.6475	53149.85061	2894074.521
WIRELESS_SENSOR_15	3014622.019	62886273.879	64799295.89	67397.6475	53149.85061	2894074.521
WIRELESS_SENSOR_16	3014622.019	62886273.879	64799295.89	67397.6475	53149.85061	2894074.521

Table 7.10 presents a detailed analysis on the total energy consumption of the network driven by Bat 1 for NR-WSN and R-WSN scenarios. It is found that the transmission mode energy consumed by the network driven by Bat 1 is 11149.42109 mJ for NR-WSN, whereas it is 12294.82967 mJ for R-WSN. The receiving mode energy consumed is 26462.86184 mJ without harvesting and 29065.52955 mJ with EH. In idle mode, energy consumption for NR-WSN is 114,175 mJ and for R-WSN is 2,208,608 mJ. Sleep energy consumption in both cases is zero. Finally, the total sum of all energies consumed in all modes of operation for NR-WSN and R-WSN is 17625600 mJ and 48233952.3 mJ respectively using Bat 1. It can be observed that although the total network energy consumption increases, at the same time the remaining energy does increase from 0 to 64799.295 J.

Table 7.10 Network Energy Consumption for NR-WSN and R-WSN using Bat 1

Packets Generated	Parameters	NR-WSN (A) (in mJ)	R-WSN (B) (in mJ)	Improvement Factor (B/A)
10000	Remaining Energy	0	62886273.88	NA
	Harvested Energy	0	64799295.89	NA
	Transmitting mode energy consumed	24312.8331	67397.6475	2.77
	Receiving mode energy consumed	23470.78487	53149.85061	2.26
	Idle mode energy consumed	1053816.382	2894074.521	2.74
	Total Energy Consumption (1 sensor)	1101600	3014622.019	2.73
	Network Energy Consumption (16 sensors)	17625600	48233952.3	2.73

Similarly, Tables 7.11 and 7.12 present a detailed analysis on the total energy consumption of the network driven by Bat 2 and 3 respectively for both the scenarios. Energy consumption of the entire network driven by rechargeable Li-ion battery, LiMn AA and 3 AAA is increased by 2.73, 3.46 and 1.00 times with RF harvesting. With addition of harvested energy in the battery, the remaining energy for Bat 1, 2 and 3 is found to be 62886.273 J, 45284.922 J and 89900.888 J respectively.

Table 7.11 Network Energy Consumption for NR-WSN and R-WSN using Bat 2

Packets Generated	Parameters	NR-WSN (A)	R-WSN (B)	Improvement Factor (B/A)
10000	Remaining Energy	0	45284922.22	NA
	Harvested Energy	0	66599271.68	NA
	Transmitting mode energy consumed	39499.46914	138514.0865	3.50
	Receiving mode energy consumed	32343.60269	89393.6576	2.76
	Idle mode energy consumed	8586156.928	29744441.71	3.46
	Total Energy Consumption (mJ)	8658000	29972349.46	3.46

Table 7.12 Network Energy Consumption for NR-WSN and R-WSN using Bat 3

Packets Generated	Parameters	NR-WSN (A)	R-WSN (B)	Improvement Factor (B/A)
10000	Remaining Energy	25101629.101703	89900888.189864	3.58
	Harvested Energy	0	64799291.362509	NA
	Transmitting mode energy consumed	134680.677481	134646.316201	0.99
	Receiving mode energy consumed	108858.17088	108938.63808	1.00
	Idle mode energy consumed	9646832.049846	9646818.21807	0.99
	Total Energy Consumption (mJ)	9890370	9890403.172301	1.00

7.9 RESULTS AND DISCUSSIONS

Fig. 7.7 highlights a plot of Recharging time (t_C) versus DoD for Bat 1, 2 and 3 at a fixed distance of 40 cm using PCB patch and dipole antennas respectively. From Fig 7.7 (a) and (b), a close resemblance is observed between the measured and simulated values for both patch and dipole antennas. It is found that the recharging time increases with increase in DoD. Table 7.13 presents the % deviation calculation in recharging time of a single sensor mote driven by Bat 1, 2 and 3 using Patch antenna at varying distances (in cm) and DoD (in %). The shortest recharging time is found to be 0.24 hrs (14.4 mins) for Bat 1 at a distance of 10 cm. The %

deviation is lowest for Bat 3 (0.12) at a distance of 50 cm and 5% DoD and highest for Bat 1 (6.06) at a distance of 100 cm and 20% DoD as highlighted in blue colour.

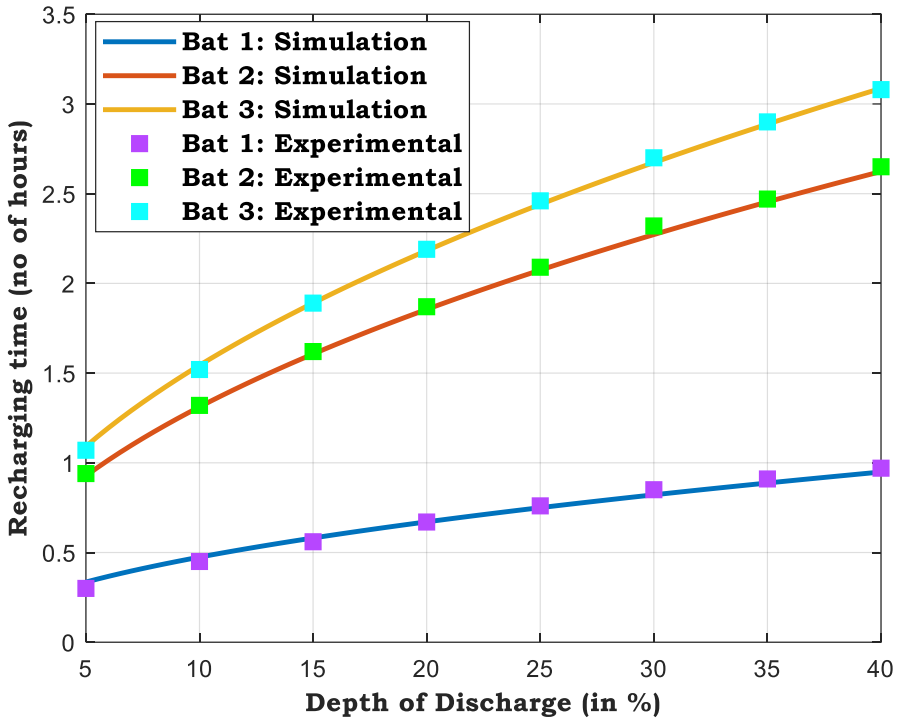

(a)

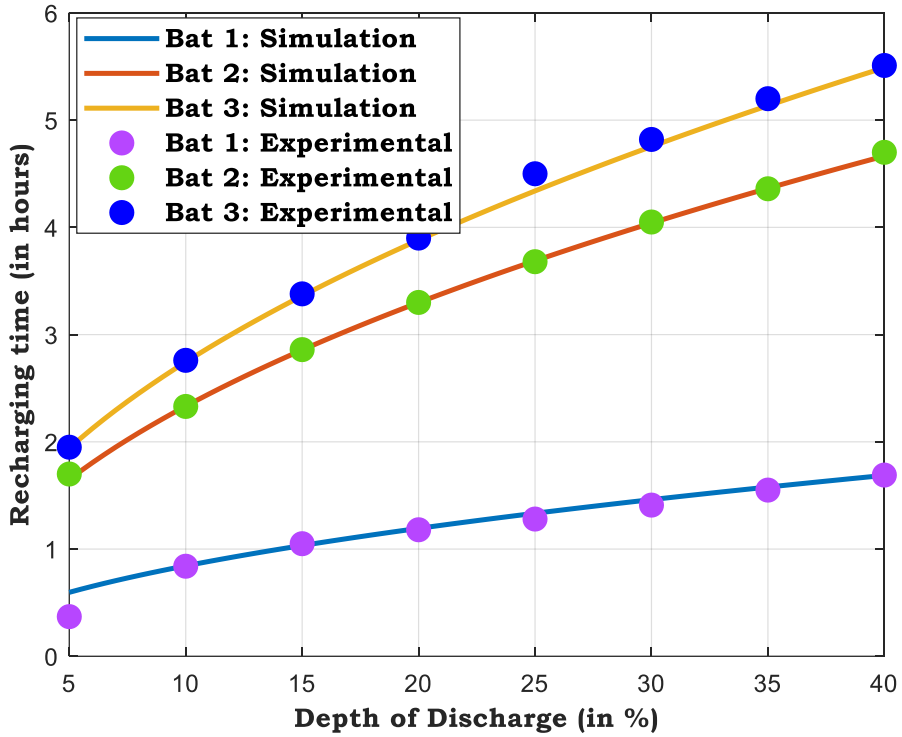

(b)

Fig. 7.7 Recharging time versus DoD **(a)** Patch Antenna **(b)** Dipole Antenna

Table 7.13 Percentage deviation calculation in recharging time of a single sensor mote driven by Bat 1, 2 and 3 using Patch antenna at varying distances (in cm) and DoD (in %)

Distance (in cm)	Battery Type	Recharging time (in hrs)								
		DoD 5%			DoD 10%			DoD 20%		
		Measured	Simulated	% Deviation	Measured	Simulated	% Deviation	Measured	Simulated	% Deviation
10	Bat 1	0.24	0.239	0.416	0.432	0.42	2.7	0.69	0.67	3.1
	Bat 2	0.6	0.591	1.5	1.52	1.554	1.87	1.85	1.87	2.67
	Bat 3	0.97	0.964	0.62	1.68	1.56	1.56	2.12	2.024	0.95
20	Bat 1	0.312	0.309	0.96	0.862	0.84	2.5	1.73	1.68	2.9
	Bat 2	0.96	0.954	0.625	4.26	4.2	1.41	8.376	8.16	2.57
	Bat 3	3.84	3.85	0.25	17.38	17.28	0.57	33.96	33.6	1.06
50	Bat 1	0.672	0.661	1.63	1.25	1.22	2.12	2.592	2.52	2.78
	Bat 2	4.56	4.584	0.52	9.24	9.12	1.29	18.22	18	1.18
	Bat 3	18.74	18.72	0.12	37.63	37.44	0.6	75.8	74.88	1.20
100	Bat 1	7.52	7.2	4.25	11.04	10.8	4.34	15.84	14.88	6.06
	Bat 2	18.72	21.84	3.19	31.68	30.24	4.54	44.88	42.72	5.34
	Bat 3	25.68	25.2	1.84	36.48	35.52	2.63	52.56	50.4	4.10

The effect of antenna gains on the recharging time for Bat 1, 2 and 3 at different distances is shown in Fig. 7.8. Based on the charging time values given in Table 7.5, the % improvement in recharging time with increasing distance has been calculated for Bat 1, 2 and 3 with respect to antenna gains. For a fixed distance of 10 cm, it was found that patch antenna shortened the recharging time by 25.34%, 16.67% and 66.32% for Bat 1, 2 and 3 respectively compared to dipole antenna. On further increasing the distance to maximum 50 cm, the recharging time for patch antenna is improved by 65%, 67.24% and 62.96% for Bat 1, 2 and 3 respectively as compared to dipole. Based on the charging time values given in Table 7.6, the percentage improvement in recharging time with increasing number of RF transmitters has been calculated for Bat 1, 2 and 3 with respect to antenna gains as depicted in Fig. 7.9. It is found that dual RF transmitters decrease the recharging time by 35.7%, 42.1% and 51.7% for Bat 1, 2 and 3 respectively compared to single RF transmitter using 6.1 dBi patch.

Fig. 7.10 compares the impact of transmit power on the harvested energy for proposed and existing baseline models (linear [177], constant-linear (CL) [180] and constant-linear-constant (CLC) [180]). Accordingly, the percentage improvement in harvested energy for the proposed work over the existing works has been presented in Table 7.14. For a fixed transmit power of 28 dBm, the % improvement of our work over Linear [177], CL [180] and CLC [180] is 99.3%, 89.3% and 84 % respectively.

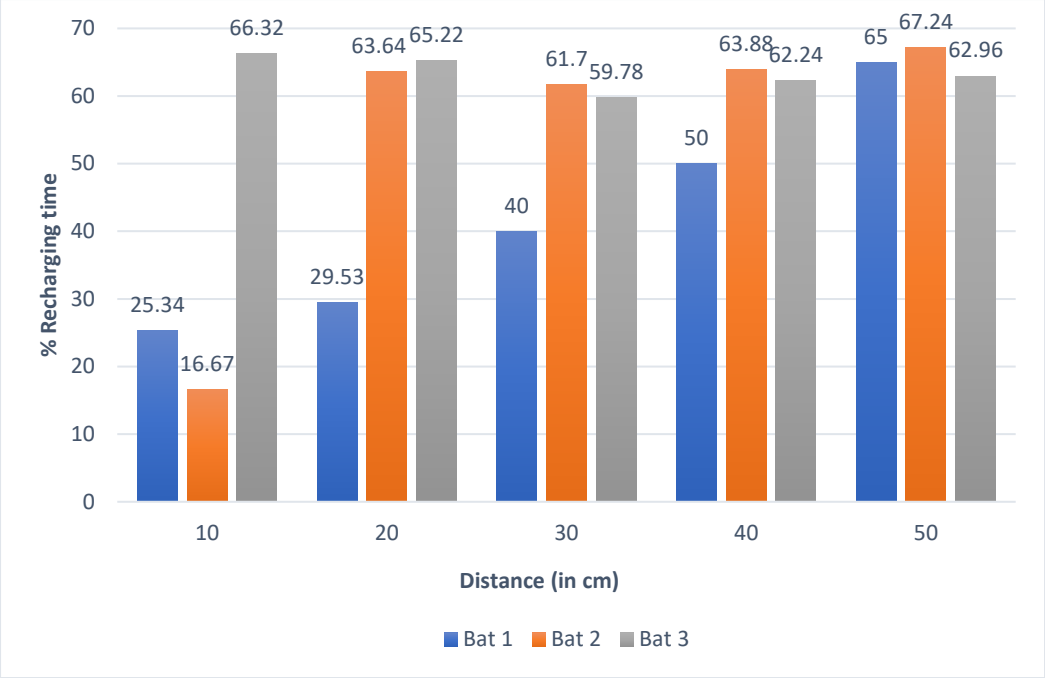

Fig. 7.8 Effect of antenna gain on recharging time for Bat 1, 2 and 3 at different distance expressed as percentage

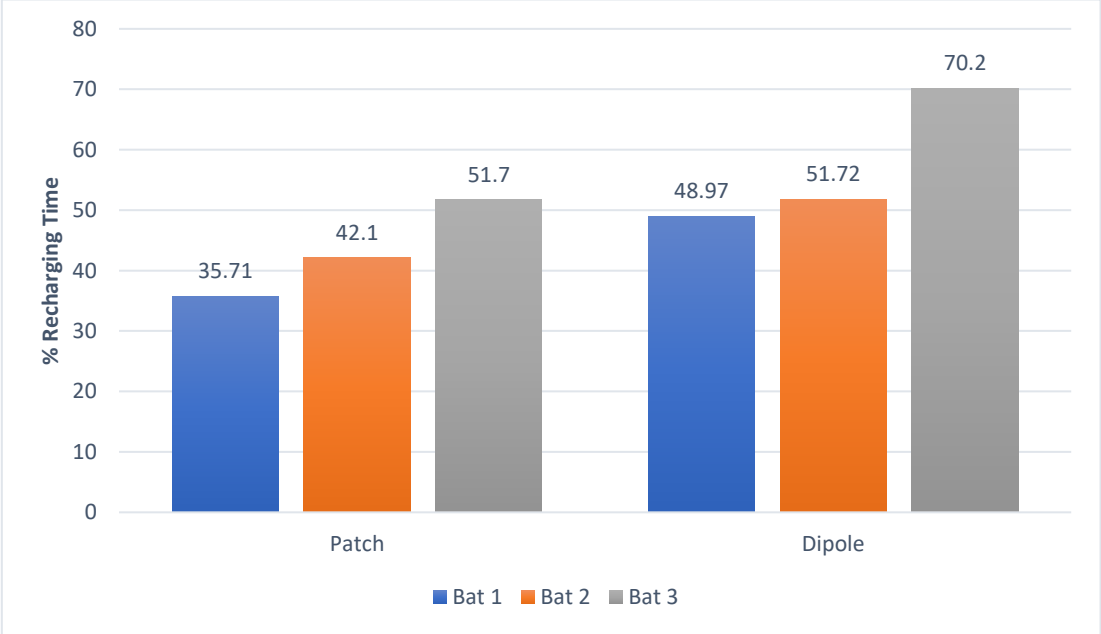

Fig. 7.9 Percentage improvement in Recharging time for Bat 1, 2 and 3 for single and dual RF transmitters with 6.1 dBi patch

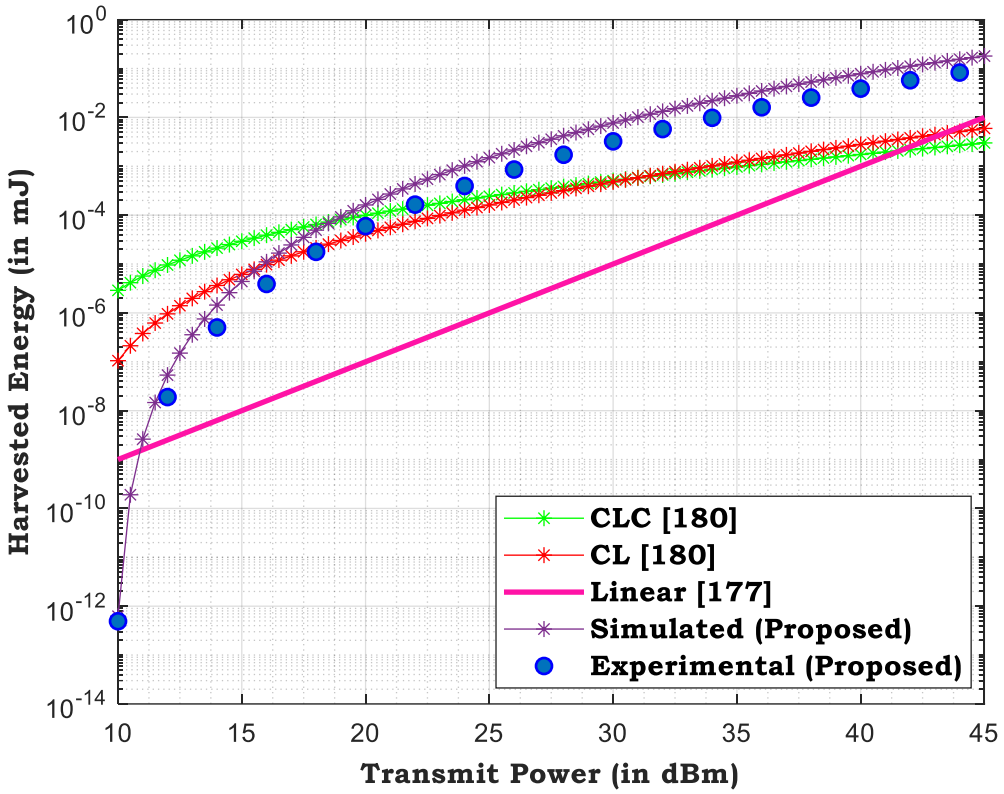

Fig. 7.10 Comparison of harvested energy for proposed and existing works

Table 7.14 Percentage improvement in harvested energy

Parameter	Harvested power (in mJ)				% Harvested energy		
Transmit power (in dBm)	[180] CLC	[180] CL	[177] Linear	Proposed	Proposed over [180] CLC	Proposed over [180] CL	Proposed over Linear [177]
26	2.9×10^{-5}	6.1×10^{-6}	10^{-7}	4.3×10^{-6}	85.2 (deterioration)	29.5 (deterioration)	97.6
27	9.9×10^{-5}	4.2×10^{-5}	10^{-6}	1.6×10^{-4}	38.13	73.75	99.35
28	2.4×10^{-4}	1.6×10^{-4}	10^{-5}	1.5×10^{-3}	84	89.3	99.33
29	5.1×10^{-4}	4.8×10^{-4}	10^{-4}	7.7×10^{-3}	93.4	93.7	98.75
31	0.011	0.003	0.001	0.078	85.9	96.15	98.7

Figs. 7.11, 7.12 and 7.13 highlight the comparison of Throughput and NL for NR-WSN and R-WSN using Bat 1, 2 and 3. The average transmitted power from source is 3W EIRP and the harvested energy is approx. 2.97 J. The average network throughput for NR-WSN with Bat 1, 2 and 3 is 162.64, 162.48 and 162.19 Kbps respectively. For Bat 1, beyond 34 hrs, the throughput goes below 162.64 Kbps and keeps on decreasing as is evident from Fig. 7.11. Similarly for Bat 2 and 3, after 245 hrs and 1031 hrs, the throughput goes below 162.48 and 162.19 Kbps because the sensor node battery SoC decreases continuously with time. From Fig. 7.11, the NL for Bat 1 is around 59 hrs. This means that network is operational for 59 divided

by 24 hrs i.e. 2.45 days approximately. After 2.45 days, the network throughput goes down and the network becomes non-operational.

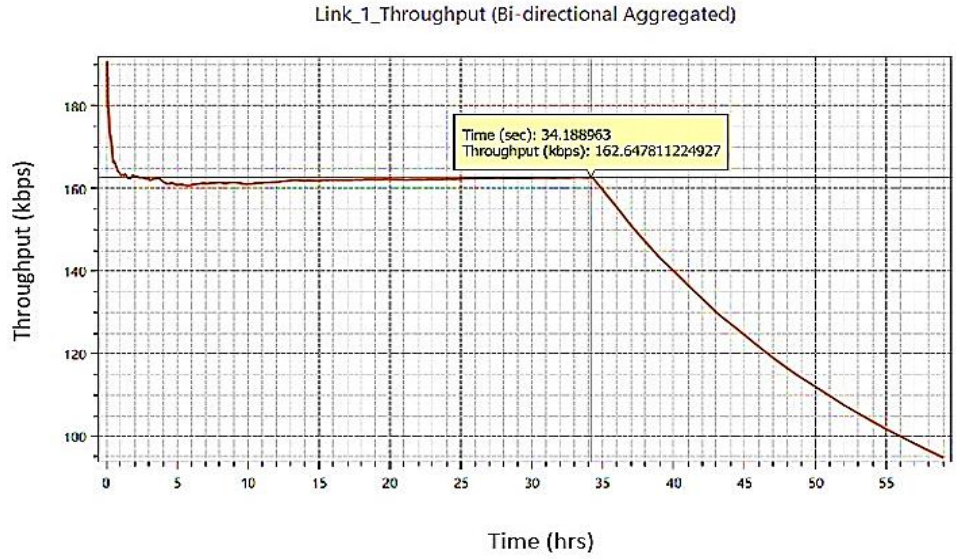

(a)

(b)

Fig. 7.11 Comparison plot of Throughput and Network Lifetime with Bat 1 **(a)** NR-WSN **(b)** R-WSN

Similarly, from Figs. 7.12 and 7.13 the network lifetime for Bat 2 and 3 is around 390 hrs and 1559 hrs respectively. This means that network is operational for 16.25 days and 64.95 days approximately. The average network throughput for R-WSN using Bat 1, 2 and 3 is 175.88,

174.87 and 165.07 Kbps upto 10,000 hrs (416 days i.e. 1.13 years). Following the limitation of the simulation software which cannot show simulation beyond 10,000, the maximum limit is shown up to 10,000 only. The network throughput is increased up to 1.08, 1.07 and 1.02 times for Bat 1, 2 and 3 with RF Harvesting.

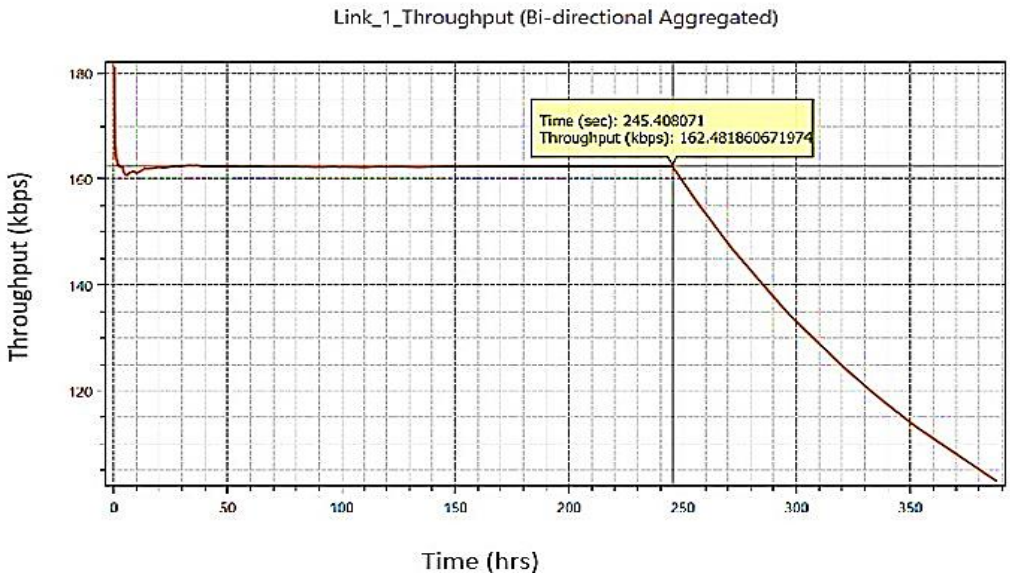

(a)

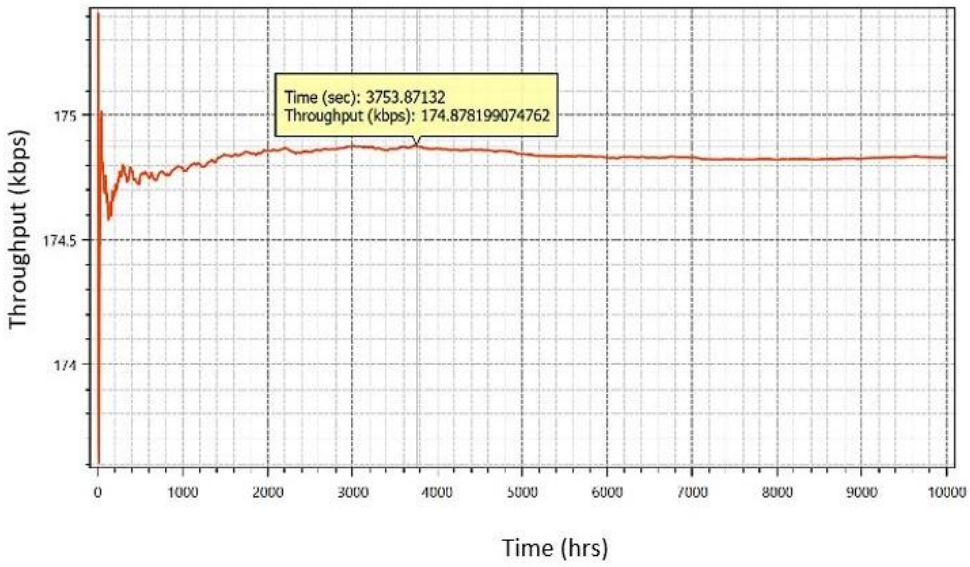

(b)

Fig 7.12 Comparison plot of Throughput and Network Lifetime with Bat 2 **(a)** NR-WSN **(b)** R-WSN

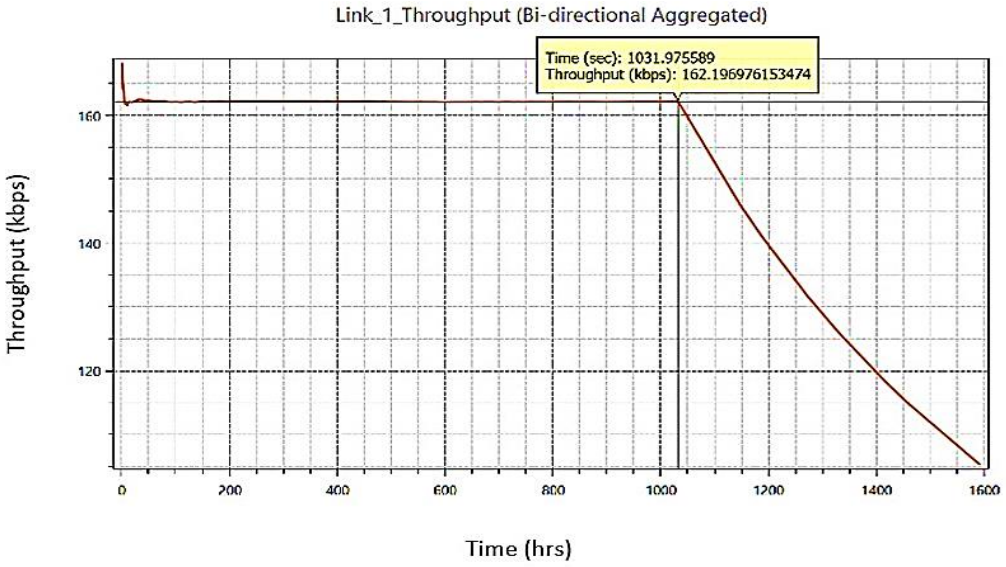

(a)

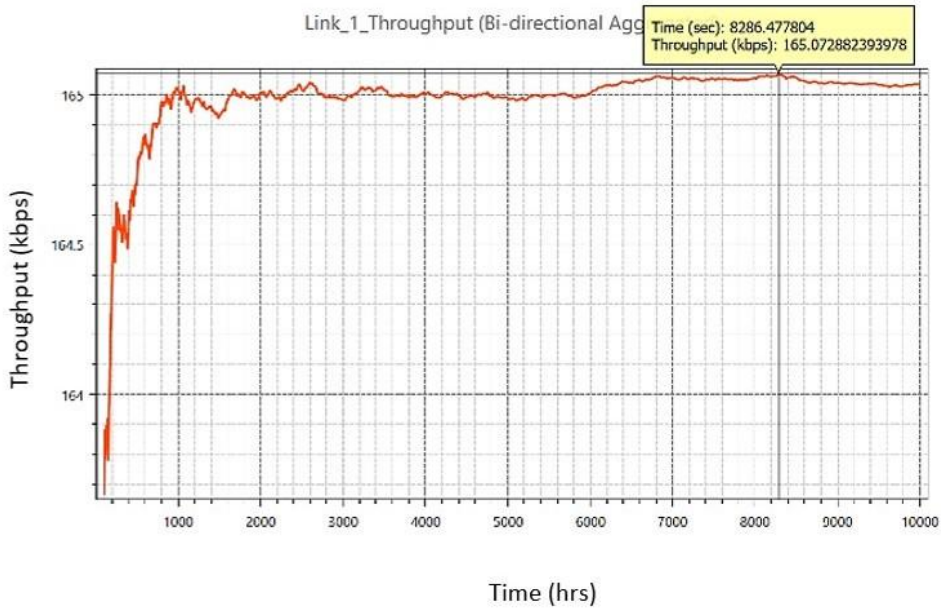

(b)

Fig. 7.13 Comparison plot of Throughput and Network Lifetime with Bat 3 **(a)** NR-WSN **(b)** R-WSN

The key findings from the analysis are summarised below:

- Bat 1 gives the shortest recharging time value at 10 cm distance with 6dBi patch antenna at 5% DoD as compared to Bat 2 and 3. The recharging time for Bat 1 (Li-ion coin cell) is much faster (14.4 minutes) using 6.1 dBi patch at 10 cm as compared to Li-Mn (Bat 2) and 3 AAA (Bat 3).

- 6.1 dBi patch shortens the recharging time by 65%, 67.24 and 63% for Bat 1, 2 and 3 respectively as compared to 1 dBi dipole.
- Dual RF transmitters reduce the recharging time by 35.7%, 42.1% and 51.7% for Bat 1, 2 and 3 respectively compared to single RF transmitter with 6.1 dBi patch.
- The energy consumption for RF powered WSN driven by Li-ion battery, LiMn AA and 3 AAA is increased by 2.73, 3.46 and 1.00 times. At the same time, the remaining energy for Bat 1, 2 and 3 is found to be 62886.273, 45284.922 J and 89900.888 J respectively. Thus, a conclusion can be made that with EH, the lifetime of a wireless sensor node can be extended with proper selection of correct parameters.
- The network lifetime @ 12% duty cycle and 5% DoD is extended up to 1.13 years and higher (ideally, up to infinite time) as compared to only 2.45, 16.45 and 66.67 days by RF harvesting. Besides, the network throughput is increased up to 1.08, 1.07 and 1.02 times for Bat 1, 2 and 3 with RF Harvesting.

7.10 DISCUSSION

This chapter investigates the impact of RF-WPT on a battery driven R-WSN for IIoT application to enhance the throughput and network lifetime. P1110 Power harvester® Receiver IC converts RF energy into DC power and charges the onboard batteries. The simulation findings show that RF-EH can extend the network's life span to a theoretically unlimited amount of time. In addition, from the analysis, RF harvesting can be considered a cost-efficient technique as the battery of the sensor nodes need not be changed regularly to maintain the network operation. The performance of the proposed model is compared with existing state-of-art network models. The results obtained prove the superiority of the proposed model in terms of harvested energy.

Chapter 8
CONCLUSION AND FUTURE WORKS

8.1 CONCLUDING REMARKS

With the emergence of 5G+, the proliferation of RF signals will provide abundant opportunities for harvesting energy from the surrounding environment. This will lead to the development of ultralow power and even energy-autonomous IoT devices, revolutionizing the way we interact with technology. In this research, different relay selection strategies have been applied for better reception reliability in one-way and two-way relay networks with IA-EH. Moreover, research has been carried out to augment the performance of NOMA-assisted network by integration of RF-EH technology. In addition, the impact of RF-EH in IIoT scenario has been demonstrated to enhance the throughput and network lifetime of the designed R-WSN.

The throughput performance of EH from an interferer in a CRN has been investigated in DL transmission mode in Chapter 3. It is seen that initially the throughput is more due to the extra acquired energy while harvesting energy from the interferer compared to the case where the interference is treated as an undesired in EH phase. Moreover, the throughput of the protocols strictly depends on the location of relay, position of interference and energy conversion efficiency. The results of simulation also show that as the interferer is closer to relay and destination, more energy is harvested at relay and less interference is imposed on relay and destination so that the throughput of the network increases. Results also show that after a certain distance, the detrimental effect of interference outweighs the benefits of energy harvested from interferer. In the next framework, a novel approach for hybrid CIoT network has been implemented in the presence of an EAV where an SNR-based HDAF relay has been implemented for analysing the security of the network under dissimilar fading environments. Secrecy performance of each of the relaying schemes has been evaluated in terms of power splitting factor and channel variances. It is also observed that the proposed relaying scheme maximizes the SR of the network as compared to the existing schemes. Results also show the impact of EAV position on SR at different channel mean power values. Also, it can be observed that severe fading over desired link provides more secure communication over main link.

Comparative study of all the fading models shows that weibull fading gives better secrecy and higher EE than the other fading models. More precisely, the secrecy performance as well as EE of the developed model has been found to be better in weibull/rayleigh environment as compared to the other fading environments (rayleigh/ weibull, hoyt/rayleigh, rayleigh/hoyt). Also, the effect of fading parameters on the SEE performance for HDAF relay has been investigated. On further extending the model to interference-limited environment in untrusted scenario, the SR of the system has been effectively enhanced as compared to interference-free environment. Results demonstrate that as distance between EAV and interferer increases, STP increases due to increased jamming. This study provides a benchmark on the maximum amount of interferer power that can be harvested so as to maximize the security performance.

A simulation model of the HD DF network has been presented using accumulate-and-forward scheme in Chapter 4. From the calculations it can be seen that there has been considerable improvement in throughput compared to any multi-source (single antenna) or any multi-relay. The different criteria for relay-selection have also been explored, like maximum energy accumulated and optimal relay, and the throughput variations for the same are observed. Next, a generalized RF energy harvesting system model with the Hybrid TSR–PSR protocol under Weibull fading channel has been introduced using DF, AF and HDAF modes. Here OP and throughput have been calculated. Along with this, the throughput optimization has been carried out to find the maximum achievable throughput. Integral form expressions for OP and throughput have been simulated using MATLAB and compared with analytical results to establish the correctness of the proposed model. The comparative analysis shows an improvement in throughput of the proposed model over the existing benchmark models.

In Chapter 5, the system performance of a bidirectional AF HD multi-antenna multi-relay network over the Nakagami fading environment in terms of OP, throughput and ergodic capacity for DL and DT transmission modes has been evaluated. The impact of different system parameters on the performance of the proposed model has also been studied. Next, a secure MHE-AS scheme has been incorporated in TWC via Two Multi-Antenna Relays with IA-EH. Here, the relays harvest energy from both the sources as well as CCI, and after performing antenna selection, utilize that energy to decode the signals and forward it to the respective nodes. The proposed model with MHE-AS scheme improves the secrecy performance significantly as compared to its contrast models where bidirectional communication takes place in presence or absence of CCI. Results demonstrate that (i) a trade-off has been observed for the secrecy capacity. The presence of CCI increases the secrecy performance of the considered protocol at the cost of reliable communication (ii) the secrecy performance is improved when

both the sources transmit information with equal power (iii) From the findings, it is found that the presence of CCI creates a flooring effect on the system performance. In addition, this study provides a constraint on the maximum number of antennas that needs to be installed at a particular relay so to maximize the secrecy performance. The results presented can be helpful for designing a multi-antenna relay network for bidirectional communication in untrusted scenario for secured data transmission with IA-EH. The proposed model has been extended to two-way untrusted scenario where an IoT environment has been designed. Here the relays collocated with EAVs are equipped with a rechargeable battery so that they can harvest and accumulate the harvested energy from RF signals sent by the sources and CCIs for stable operation of the network. Theoretical derivations have been carried out and validated via Monte-Carlo simulation results. Using the derived expressions, SOP performance has been evaluated in terms of source transmit power, threshold secrecy rate and number of frames. Comparative analyses with the existing conventional schemes depict superiority of our model in terms of energy accumulation and secrecy. The impact of EH coefficient and number of frames on the SC has also been examined. Moreover, the amount of harvested energy versus number of frames in terms of source transmission power and number of CCIs has been analysed for both linear and non-linear scenarios. The obtained results for both the scenarios have been compared with each other which gives a useful insight to the network secrecy performance. Lastly, the effect of saturation threshold value on the secrecy capacity for non-linear approach has also been depicted. The results of this paper illustrate how the accumulated energy alongwith exploitation of the radiated energy from CCIs contributes to improvement in secrecy performance of a bidirectional IoT Relay network. More precisely, this study provides a guideline on the maximum number of frames that can be utilized for energy accumulation in any interference-limited environment to obtain a desired level of secrecy.

In Chapter 6, the secrecy performance of CR-NOMA network with IA-EH has been investigated by introducing a secure jamming cancellation scheme in the presence of an EAV. Results demonstrate that (i) there exists an optimal value of ρ_S for SOP curves with varying P_I and P_J (ii) the security performance is initially improved due to addition of extra energy from CCIs, but at high ρ_J, a performance degradation has been observed due to dominant interfering effect after exceeding a certain threshold. From the findings, it is also seen that increasing α_1 increases ESR of both near and far users. Our findings may serve as a constraint on the utilization of maximum number of CCI nodes that will prove to be beneficial for secrecy performance improvement of the network. In the subsequent framework, the performance of

an RF-powered MD-DRN has been investigated using an upgraded A-NOMA protocol. From the observations, it has been found that a 4-device DRN system gives a better sum rate than a 3-device DRN. At $P_S = 10dB$, ASR is found to be 3.6 bps/Hz for a 3-device network that rises to 9 bps/Hz for a 4-device network. With an increase in the number of relay devices, the BER value increases. For $P_S = 10dB$, a BER value of 0.19 is obtained for the proposed model with a single DRN as opposed to 0.7 and 0.98 for 3-device and 4-device DRNs respectively. With a greater number of devices, the BER value for the A-NOMA protocol is comparatively less than that of NOMA, thus providing much better system reliability. Upto a certain range of ASR, the proposed adaptive scheme provides better efficiency than the conventional non-RF A-NOMA scheme. At a fixed ASR of 0.85 bps/Hz, the percentage improvement in EE of our developed system over the existing scheme is found to be 28.4%. Additionally, our proposed network with RF-enabled A-NOMA achieves upto 67.56% and 12.7% EE gain over the conventional OMA and NOMA functioned networks, respectively, for ASE=2 bps/Hz.

The impact of RF-EH on a battery driven R-WSN for IIoT application has been depicted in Chapter 7 to enhance the throughput and NL using P1110 Power harvester® Receiver module. It was found that Bat 1 gives the shortest recharging time value at 10 cm distance with 6.1 dBi patch antenna at 5% DoD as compared to Bat 2 and 3. The recharging time for Bat 1 (Li-ion coin cell) is much faster (14.4 minutes) using 6.1 dBi patch at 10 cm as compared to Li-Mn (Bat 2) and 3 AAA (Bat 3). More precisely, 6.1 dBi patch shortens the recharging time by 65%, 67.24 and 63% for Bat 1, 2 and 3 respectively as compared to 1 dBi dipole. Dual RF transmitters reduce the recharging time by 35.7%, 42.1% and 51.7% for Bat 1, 2 and 3 respectively compared to single RF transmitter with 6.1 dBi patch. The energy consumption for RF powered WSN driven by Li-ion battery, LiMn AA and 3 AAA is increased by 2.73, 3.46 and 1.00 times. At the same time, the remaining energy for Bat 1, 2 and 3 is found to be 62886.273 J, 45284.922 J and 89900.888 J respectively. Thus, a conclusion can be made that with EH, the lifetime of a wireless sensor node can be extended with proper selection of correct parameters. The NL @ 12% duty cycle and 5% DoD is extended up to 1.13 years and higher (ideally, up to infinite time) as compared to only 2.45, 16.45 and 66.67 days by RF harvesting. Besides, the network throughput is increased up to 1.08, 1.07 and 1.02 times for Bat 1, 2 and 3 with RF-EH. The proposed system model can be a reference for new RF-powered IIoT designs and can be relevant for planning and deploying IEEE 802.15.4 based sensor networks with appropriate battery system and specific performance demands.

8.2 FUTURE SCOPE

The power consumption of portable gadgets, implantable medical devices (IMDs) and WSNs has reduced significantly with the ongoing progression in low-power electronics and the swift advancement in nano and microfabrication. The recent emergence in IoT, Industry 4.0, and 5G communication has resulted in a demand for using self-powered, ultra-low powered, and maintenance-free devices and circuits. In this context, the area of RF-EH for wireless networks has been progressed significantly over the last decades. Despite the highlighted possibilities for RF-EH in wireless networks, there exist a number of open research challenges and future research directions for the new entrants working into RF energy harvesting domain. This work could have been extended further as discussed below:

The secrecy performance of bi-directional relaying in untrusted scenario using CR-NOMA may be well-though-out as alternative interesting investigation track. In addition, the performance of our proposed model can be observed using full duplex relays where the effect of positions of the selected relays can be examined. Further extension of this work may include game theory approach for power allocation in DRN under the influence of multiple interfering signals. Furthermore, some relaying strategies can be combined with deep learning algorithms and intelligent reflecting surface (IRS) for more efficient results. Also, the impact of RF-WPT on a battery-less R-WSN can be observed for IIoT application where it can be shown that that RF-WPT allows the implementation of battery-free WSNs where the lifetime is no longer limited by battery lifespan, but rather by the lifespans of the electronic components. The solutions for enhancing the performance of RF-powered wireless communication using ambient backscatter technology may be another interesting future topic.

APPENDIX

Appendix A

A.1 Proof of (3.43)

The CDF of the S-R link is given as:

$$\mathrm{F}_{\gamma_{SR}}(\gamma_{th}) = \mathrm{P}(\gamma_{SR} < \gamma_{th}) = P\left(\frac{(1-\beta)(\rho p_S)g_{SR}}{(1-\beta)p_D g_{RD}+1} < \gamma_{th}\right)$$

$$= P\left(\frac{(1-\beta)\rho p_S X_1}{(1-\beta)p_D X_2+1} < \gamma_{th}\right)$$

$$= \int_0^{\infty} \mathrm{F}_{X_1}\left(\frac{\gamma_{th}(p_D X_2+1)}{p_S}\right) f_{X_2}(x_2)dx_2$$

$$= \left[1-\frac{1}{\psi_X(\gamma_{th}+\psi_X^{-1})}\exp\left(-\frac{\gamma_{th}\lambda_{X_1}}{p_S}\right)\right] \quad \text{(A.1)}$$

$$\mathrm{P}(\gamma_{SR} \geq \gamma_{th}) = \left[\frac{1}{\psi_X(\gamma_{th}+\psi_X^{-1})}\exp\left(-\frac{\gamma_{th}\lambda_{X_1}}{p_S}\right)\right] \quad \text{(A.2)}$$

where $\psi_X = \frac{\rho_D}{\rho_S}\frac{m_x}{m_y}$; $\rho_S = \frac{P_S}{N_O}$; $\rho_D = \frac{P_D}{N_O}$

$$C_{\gamma_{RD}}^{AF} = \mathrm{E}\{\ln(1+\gamma_{RD})\} \quad \text{(A.3)}$$

$$= \mathrm{E}\left\{\ln\left(1+\frac{\mu^2(1-\beta)(\rho P_S)g_{sr}g_{rd}}{(\mu^2 g_{rd}+1)N_o}\right)\right\}$$

$$= \mathrm{E}\left\{\ln(1+\frac{X_{AF}Y_{AF}}{Y_{AF}+1})\right\}$$

$$\overset{(a)}{\geq} \ln\left(1+\exp\left(\mathrm{E}\left\{\ln(\frac{X_{AF}Y_{AF}}{Y_{AF}+1})\right\}\right)\right)$$

$$= \ln\left(1+\exp\left(\overbrace{\mathrm{E}\{\ln[X_{AF}Y_{AF}]\}}^{\varphi_1} - \overbrace{\mathrm{E}\{\ln[\mathrm{Y}_{AF}+1]\}}^{\varphi_2}\right)\right) \quad \text{(A.4)}$$

where $X_{AF} = \frac{(1-\beta)(\rho P_S)\mathrm{g}_{SR}}{N_O}$ and $Y_{AF} = \mu^2 g_{RD}$ are exponential random variables with mean $\lambda_{X_{AF}} = \frac{(1-\beta)(\rho P_S)\Omega_{SR}}{N_O}$ and $\lambda_{Y_{AF}} = \mu^2\Omega_{RD}$; Using (4.352.1)] and (4.331.2) of [185], φ_1 and φ_2 can be calculated, respectively as

$$\varphi_1 = -2\Phi - \ln\left(\frac{1}{\lambda_{X_{AF}}\lambda_{Y_{AF}}}\right) \text{and } \varphi_2 = -\exp(\lambda_{Y_{AF}}^{-1})Ei\left(-\frac{1}{\lambda_{Y_{AF}}}\right) \quad \text{(A.5)}$$

where Φ is the Euler's constant [9.73].

Putting the value of φ_1 and φ_2 from (A.5) to (A.4) we have,

$$C_{\gamma_{\mathrm{RD}}}^{AF}=\ln\left(1+\exp\left(-2\phi-\ln\left(\frac{1}{\lambda_{X_{AF}}\lambda_{Y_{AF}}}\right)\right)+\exp(\lambda_{Y_{AF}}^{-1})Ei\left(-\frac{1}{\lambda_{Y_{AF}}}\right)\right) \tag{A.6}$$

where $Ei(.)$ is the exponential integral

Capacity of EAV Channel is given as:

$$=P\left(g_{sr}<\frac{R_{th}}{X_2}\frac{g_{rd}}{g_{re}}\Big|_{Y_2}\right)=P\left(g_{sr}<\frac{R_{th}}{X_2}Y_2\right)=\int_0^{\infty}F_{g_{sr}}\left(\frac{R_{th}}{X_2}y_2\right).f_{Y_2}(y_2)dy_2=\int_0^{\infty}(1-e^{\frac{R_{th}Y_2}{X_2g_{sr}}}).\frac{\lambda_{re}\lambda_{rd}}{(\lambda_{rd}+y_2\lambda_{re})^2}dy_2 \tag{A.7}$$

After some simplification and manipulation:

$$C_{\gamma_{\mathrm{RE}}}^{AF}=1-\frac{\lambda_{RD_{AF}}R_{th}}{X_2\lambda_{RE_{AF}}\lambda_{SR}}\exp\left(\frac{\lambda_{RD_{AF}}R_{th}}{a_1\lambda_{RE_{AF}}\lambda_{SR}}\right)Ei\left(-\frac{\lambda_{RDAF}R_{th}}{a_1\lambda_{RE_{AF}}\lambda_{SR}}\right)-\frac{\lambda_{RE_{AF}}}{\lambda_{RD_{AF}}} \tag{A.8}$$

The SC of HDAF relay when operating in AF mode is given as:

$$C_S^{AF}=C_{RD}^{AF}-C_{RE}^{AF}=\ln\left(1+\exp\left(-2\phi-\ln\left(\frac{1}{\lambda_{X_{AF}}\lambda_{Y_{AF}}}\right)\right)+\exp(\lambda_{Y_{AF}}^{-1})Ei\left(-\frac{1}{\lambda_{Y_{AF}}}\right)\right) \tag{A.9}$$
$$-\left(1-\frac{\lambda_{RD_{AF}}R_{th}}{X_2\lambda_{RE_{AF}}\lambda_{SR}}\exp\left(\frac{\lambda_{RD_{AF}}R_{th}}{a_1\lambda_{RE_{AF}}\lambda_{SR}}\right)Ei\left(-\frac{\lambda_{RDAF}R_{th}}{a_1\lambda_{RE_{AF}}\lambda_{SR}}\right)-\frac{\lambda_{RE_{AF}}}{\lambda_{RD_{AF}}}\right)$$

The SC of HDAF relay when operating in DF mode is given as:

$$C_{\gamma_{RD}}^{DF}=\mathrm{E}\{\ln(1+\gamma_{RD})\} \tag{A.10}$$

$$=\mathrm{E}\left\{\ln\left(1+\frac{\eta\beta(1-\beta)\rho P_S g_{sr}g_{rd}}{(\eta\beta g_{sr}+(1-\beta))N_o}\right)\right\}$$

$$=\mathrm{E}\left\{\ln(1+\frac{X_{DF}Y_{DF}}{Y_{DF}+1})\right\} \tag{A.11}$$

$$\overset{(a)}{\geq}\ln\left(1+\exp\left(\mathrm{E}\left\{\ln(\frac{X_{DF}Y_{DF}}{Y_{DF}+1})\right\}\right)\right)$$

$$=\ln\left(1+\exp\left(\overbrace{\mathrm{E}\{\ln[X_{DF}Y_{DF}]\}}^{\varphi_1}-\overbrace{\mathrm{E}\{\ln[\mathrm{Y}_{DF}+1]\}}^{\varphi_2}\right)\right)$$

where $X_{DF}=\frac{(1-\beta)(\rho P_S)g_{SR}}{N_O}$ and $Y_{DF}=\frac{\eta\beta g_{rd}}{(1-\beta)}$ are exponential random variables with means

$\lambda_{X_{DF}}=\frac{(1-\beta)(\rho P_S)\Omega_{SR}}{N_O}$ and $\lambda_{Y_{DF}}=\frac{\eta\beta\Omega_{rd}}{(1-\beta)}$

Capacity of EAV Channel is given as:

$$C_{\gamma_{\mathrm{RE}}}^{DF}=P\left(\frac{(1-\beta)(\rho P_S)g_{sr}g_{re}}{P_D\,g_{rd}}<R_{th}\right)=P\left(\frac{X_3g_{sr}g_{re}}{g_{rd}}<R_{th}\right) \tag{A.12}$$

$$=P\left(g_{sr}<\frac{R_{th}}{X_3}\frac{g_{rd}}{g_{re}}\Big|_{Y_3}\right)=P\left(g_{sr}<\frac{R_{th}}{X_3}Y_3\right)=\int_0^{\infty}F_{g_{sr}}\left(\frac{R_{th}}{X_3}y_3\right).f_{Y_3}(y_3)dy_3=\int_0^{\infty}(1-e^{\frac{R_{th}Y_3}{X_3g_{sr}}}).\frac{\lambda_{re}\lambda_{rd}}{(\lambda_{rd}+y_3\lambda_{re})^2}dy_3$$

After some simplification and manipulation:

$$C_{\gamma_{\mathrm{RE}}}^{DF}=\left(1-\frac{\lambda_{RD_{DF}}R_{th}}{X_3\lambda_{RE_{DF}}\lambda_{SR}}\exp\left(\frac{\lambda_{RD_{DF}}R_{th}}{a_1\lambda_{RE_{DF}}\lambda_{SR}}\right)Ei\left(-\frac{\lambda_{RD_{DF}}R_{th}}{a_1\lambda_{RE_{DF}}\lambda_{SR}}\right)-\frac{\lambda_{RE_{DF}}}{\lambda_{RD_{DF}}}\right) \tag{A.13}$$

Similarly, the SC of HDAF relay when operating in DF mode is given as:

$$C_S^{DF}=C_{\gamma_{RD}}^{DF}-C_{\gamma_{RE}}^{DF}=\ln\left(1+\exp\left(-2\phi-\ln\left(\frac{1}{\lambda_{X_{DF}}\lambda_{Y_{DF}}}\right)\right)+\exp(\lambda_{Y_{DF}}^{-1})Ei\left(-\frac{1}{\lambda_{Y_{DF}}}\right)\right) \tag{A.14}$$

$$-\left(1-\frac{\lambda_{RD_{DF}}R_{th}}{X_3\lambda_{RE_{DF}}\lambda_{SR}}\exp\left(\frac{\lambda_{RD_{DF}}R_{th}}{a_1\lambda_{RE_{DF}}\lambda_{SR}}\right)Ei\left(-\frac{\lambda_{RD_{DF}}R_{th}}{a_1\lambda_{RE_{DF}}\lambda_{SR}}\right)-\frac{\lambda_{RE_{DF}}}{\lambda_{RD_{DF}}}\right)$$

Thus substituting (A.9), (A.14) in (3.38) , closed form equation for (3.43) is obtained. Putting (3.43) in (3.46), closed form equation for (3.48) is obtained.

A.2 Proof of (3.45):

The pdf of main and wiretap links for Weibull fading takes the following form :

$$f_{\gamma_{RD}}(\gamma_{RD})=\frac{v_m}{2}\left(\frac{1}{u_o}\Gamma(1+\frac{2}{v_m})\right)^{\frac{v_m}{2}}u^{v_m/2-1}\times\exp\left\{-\left[\frac{u}{u_o}\Gamma(1+\frac{2}{v_m})\right]\right\}^{\frac{v_m}{2}} \tag{A.15}$$

$$f_{\gamma_{\mathrm{RE}}}(\gamma_{RE})=\frac{v_e}{2}\left(\frac{1}{w_o}\Gamma(1+\frac{2}{v_e})\right)^{\frac{v_e}{2}}w^{v_e/2-1}\times\exp\left\{-\left[\frac{w}{w_o}\Gamma(1+\frac{2}{v_e})\right]\right\}^{\frac{v_e}{2}} \tag{A.16}$$

where v_m is the fading factor of the main channel and $\Gamma(.)$ is the gamma function, defined as:

$$\Gamma(x)=\int_0^\infty t^{x-1}\exp(-t)dt$$

v_e is the fading factor of the EAV channel

Corresponding to (A.15) and (A.16), the CDFs take the following form:

$$F_{\gamma_{RD}}(\gamma_{RD})=1-\exp\left(-\left[\frac{\gamma_{RD}}{\overline{\gamma}_{RD}}\Gamma\left(1+\frac{2}{v_m}\right)\right]^{v_m/2}\right)$$

(A.17)

$$F_{\gamma_{RE}}(\gamma_{RE})=1-\exp\left(-\left[\frac{\gamma_{RE}}{\overline{\gamma}_{RE}}\Gamma\left(1+\frac{2}{v_e}\right)\right]^{v_e/2}\right) \tag{A.18}$$

The SR of the channel is defined as follows:

$$C_{S_{WEIBULL}}^{AF}=\int_0^\infty\int_{\gamma_{RE_{AF}}}^\infty\log_2\left(\frac{1+\gamma_{RD_{AF}}}{1+\gamma_{RE_{AF}}}\right)f_{\gamma_{RD_{AF}}}(\gamma_{RD_{AF}})f_{\gamma_{RE_{AF}}}(\gamma_{RE_{AF}})d\gamma_{RD_{AF}}d\gamma_{RE_{AF}} \tag{A.19}$$

Substituting (3.27),(3.29),(A.17) and (A.18) into (A.19), we have:

$$C_{S_{WEIBULL}}^{AF}=\frac{v_m v_e}{4}\left[\frac{1}{\bar{\gamma}_{RD_{AF}}}\Gamma\left(1+\frac{2}{v_m}\right)\right]^{v_m/2}\left[\frac{1}{\bar{\gamma}_{RE_{AF}}}\Gamma\left(1+\frac{2}{v_m}\right)\right]^{v_e/2}\times\int_0^{\infty}\int_{\gamma_{RE_{AF}}}^{\infty}\log_2\left(\frac{1+\gamma_{RD_{AF}}}{1+\gamma_{RE_{AF}}}\right)\gamma_{RD_{AF}}^{(v_m/2)-1}\exp\left(-\left[\frac{\gamma_{RD_{AF}}}{\bar{\gamma}_{RD_{AF}}}\Gamma\left(1+\frac{2}{v_m}\right)\right]^{\frac{v_m}{2}}\right)\times$$

$$\gamma_{RE_{AF}}^{(v_e/2)-1}\exp\left(-\left[\frac{\gamma_{RE_{AF}}}{\bar{\gamma}_{RE_{AF}}}\Gamma\left(1+\frac{2}{v_e}\right)\right]^{\frac{v_e}{2}}\right)d\gamma_{RD_{AF}}d\gamma_{RE_{AF}} \tag{A.20}$$

After converting to single integral form, we have,

$$C_{S_{WEIBULL}}^{AF}=\frac{2}{v_m}\log_2\left(1+\frac{\gamma_{RD_{AF}}^{v_m/2}}{\gamma_{RE_{AF}}^{v_e/2}}\right)-\int_0^1\log_2\left(1+\frac{2\Gamma(2/v_m)\{[1+(\gamma_{RD_{AF}}/\gamma_{RE_{AF}})^{v_m/2}]^{2/v_m}-1\}}{2\Gamma(2/v_m)+a\gamma_{RD_{AF}}(-\ln t)^{2/v_m}}\right)dt \tag{A.21}$$

$$C_{S_{WEIBULL}}^{AF}=\int_1^{\infty}\log_2(z)f_Z(z)dz \tag{A.22}$$

According to probability theory, we have:

$$f_Z(z)=\int_0^{\infty}\gamma_{RE}f_{\gamma_{RD}}(\gamma_{RE}z)f_{\gamma_{RE}}(\gamma_{RE})d\gamma_{RE}$$

Accordingly, the CDF is formulated as:

$$F_Z(z)=\int_0^z f_Z(t)dt=\int_0^z\int_0^{\infty}\gamma_{RE}f_{\gamma_{RD}}(\gamma_{RE}t)f_{\gamma_{RE}}(\gamma_{RE})d\gamma_{RE}$$

$$=\int_0^{\infty}f_{\gamma_{RE}}(\gamma_{RE})\left[\int_0^{\gamma_{RE}z}f_{\gamma_{RD}}(y)dy\right]d\gamma_{RE}=\int_0^{\infty}f_{\gamma_{RE}}(\gamma_{RE})F_{\gamma_{RD}}(\gamma_{RE}z)d\gamma_{RE} \tag{A.23}$$

With several transformations, we obtain:

$$F_Z(z)=\frac{v_e}{2}(H_1-H_2) \tag{A.24}$$

$$H_1=\int_0^{\infty}\gamma_{RE_{AF}}^{(v_e/2)-1}\left[\frac{1}{\bar{\gamma}_{RE_{AF}}}\Gamma\left(1+\frac{2}{v_e}\right)\right]^{\frac{v_e}{2}}\times\exp\left(-\left[\frac{\gamma_{RE_{AF}}}{\bar{\gamma}_{RE_{AF}}}\Gamma\left(1+\frac{2}{v_e}\right)\right]^{\frac{v_e}{2}}\right)d\gamma_{RE_{AF}}\approx\frac{2}{v_e} \tag{A.25}$$

$$H_2=\int_0^{\infty}\gamma_{RE_{AF}}^{(v_e/2)-1}\exp\left(-\left[\frac{\gamma_{RE_{AF}}z}{\bar{\gamma}_{RE_{AF}}}\Gamma\left(1+\frac{2}{v_e}\right)\right]^{\frac{v_m}{2}}\right)\times\left[\frac{1}{\bar{\gamma}_{RE_{AF}}}\Gamma\left(1+\frac{2}{v_e}\right)\right]^{\frac{v_e}{2}}\exp\left(-\left[\frac{\gamma_{RE_{AF}}}{\bar{\gamma}_{RE_{AF}}}\Gamma\left(1+\frac{2}{v_e}\right)\right]^{\frac{v_m}{2}}\right)d\gamma_{RE_{AF}}$$

$$=\frac{2}{v_e}\int_0^{\infty}\exp\left(-t-\left[\frac{v_e\Gamma(2/v_m)z}{v_m\Gamma(2/v_e)r}\right]^{\frac{v_m}{2}}t^{\frac{v_m}{v_e}}\right)dt \tag{A.26}$$

Thus , $F_Z(z)=1-\int_0^{\infty}\exp\left[-t-\left(\frac{z}{r}\right)^{\frac{v_m}{2}}t\right]dt=1-\frac{1}{1+(z/r)^{v_m/2}}$ (A.27)

Thus, SC of HDAF relay when operating in AF mode is given as:

$$C_{S_{WEIBULL}}^{AF}=\int_1^{\infty}\log_2(z)f_Z(z)dz=\frac{1}{\ln 2}\int_1^{\infty}\frac{dz}{z[1+(z/r)^{v_m/2}]}\approx\frac{2}{v_m}\log_2(1+r^{v_m/2}) \tag{A.28}$$

Similarly, the SC of HDAF relay when operating in DF mode is given as:

$$C_{S_{WEIBULL}}^{DF} = \frac{2}{v_m}\log_2(1+r^{v_m/2}) \tag{A.29}$$

Thus substituting (A.28), (A.29) in (3.38) , closed form equation for (3.45) is obtained. Putting (3.45) in (3.46), closed form equation for (3.48) under Weibull faded environment is obtained.

A.3 Proof of (3.44):

The pdf of S-R link for Hoyt fading takes the following form :

$$f_{\gamma_{SR}}(\gamma_{th}) = \frac{(1+q_m^2)}{2q_m\overline{\gamma}_{RD}}\exp\left(-\frac{(1+q_m^2)^2\gamma_{th}}{4q_m^2\overline{\gamma}_{RD}}\right)I_O\left(\frac{1-q_m{}^4}{4q_m^2\overline{\gamma}_{RD}}\gamma_{th}\right) \tag{A.30}$$

where $I_O(.)$ is the modified Bessel function of the first kind and zero order, $\overline{\gamma}_{RD} = \mathrm{E}\{\gamma_{RD}\}$ and $q \in [0,1]$

$$F_{\gamma_{SR}}(\gamma_{th}) = Q\left(\alpha(q_1)\sqrt{\frac{\gamma_{th}}{\overline{\gamma}_1}}, \beta(q_1)\sqrt{\frac{\gamma_{th}}{\overline{\gamma}_1}}\right) - Q\left(\beta(q_1)\sqrt{\frac{\gamma_{th}}{\overline{\gamma}_1}}, \alpha(q_1)\sqrt{\frac{\gamma_{th}}{\overline{\gamma}_1}}\right) \tag{A.31}$$

$$\begin{cases} \alpha(q) = \dfrac{\sqrt{1-q^4}}{2q}\sqrt{\dfrac{1+q}{1-q}} \\ \beta(q) = \dfrac{\sqrt{1-q^4}}{2q}\sqrt{\dfrac{1-q}{1+q}} \end{cases}$$

For Rayleigh faded channel, the capacity per unit bandwidth using Optimum Rate Adaptation (ORA) policy is calculated as:

$$P(C_S > R_S) = \frac{\overline{\gamma}_{RD}}{\overline{\gamma}_{RD} + 2^{R_S}\overline{\gamma}_{RE}}\exp\left(-\frac{2^{R_S}-1}{\overline{\gamma}_{RD}}\right) \tag{A.32}$$

Now, for a Hoyt faded channel, the capacity per unit bandwidth is calculated as:

$$C_S^{AF} = \frac{\log_2(e)}{\pi}\int_0^{\pi} e^{1/\gamma(\theta,q)}E_1\left(\frac{1}{\gamma(\theta,q)}\right)d\theta \tag{A.33}$$

where $\gamma(\theta,q) \approx \overline{\gamma}(1-\dfrac{1-q^2}{1+q^2}\cos\theta)$

$$C_{S_{HOYT}}^{AF} = \frac{1}{\pi^2}\int_0^{\pi}\int_0^{\pi}\exp\left(-\frac{2^{R_{th}}-1}{\overline{\gamma}_{RD_{AF}}(1-\in_{RD_{AF}}\cos\theta_{RD_{AF}})}\right)\times\frac{\overline{\gamma}_{RD_{AF}}(1-\in_{RD_{AF}}\cos\theta_{RD_{AF}})}{\overline{\gamma}_{RD}(1-\in_{RD_{AF}}\cos\theta_{RD_{AF}}) + 2^{R_S}\overline{\gamma}_{RE}(1-\in_{RE}\cos\theta_{RE_{AF}})}d\theta_{RE_{AF}}d\theta_{RD_{AF}} \tag{A.34}$$

where q_m and q_e represent the Hoyt shape parameters for the desired and EAV links. Eccentricities associated with both Hoyt distributions as $\in_{RD} = \dfrac{1-q_m^2}{1+q_m^2}$ and $\in_{RE} = \dfrac{1-q_e^2}{1+q_e^2}$

$$C_{S_{HOYT}}^{AF} = \frac{1}{\pi}\int_0^{\pi}\exp\left(-\frac{2^{R_{th}}-1}{\overline{\gamma}_{RD_{AF}}(\theta)}\right)\times\frac{\overline{\gamma}_{RD_{AF}}(\theta)}{\overline{\gamma}_{RD_{AF}}(\theta)+2^{R_{th}}\overline{\gamma}_{RE_{AF}}}\frac{1}{\sqrt{1-\left(\dfrac{q_e 2^{R_S}\overline{\gamma}_{\mathrm{RE}_{AF}}}{\overline{\gamma}_{\mathrm{RD}_{AF}}(\theta)+2^{R_S}\overline{\gamma}_{\mathrm{RE}_{AF}}}\right)^2}}d\theta \tag{A.35}$$

Thus, SC of HDAF relay when operating in AF mode is given as:

$$C_{S_{HOYT}}^{AF} = \frac{\overline{\gamma}_{RD_{AF}}}{\overline{\gamma}_{RD_{AF}} + \overline{\gamma}_{RE_{AF}}} \frac{1}{\sqrt{1-\left(\frac{q_e \overline{\gamma}_{\mathrm{RE}_{AF}}}{\overline{\gamma}_{\mathrm{RD}_{AF}} + \overline{\gamma}_{\mathrm{RE}_{AF}}}\right)^2}} \quad \text{(A.36)}$$

Similarly, the secrecy capacity of HDAF relay when operating in DF mode is given as:

$$C_{S_{HOYT}}^{DF} = \frac{\overline{\gamma}_{RD_{DF}}}{\overline{\gamma}_{RD_{DF}} + \overline{\gamma}_{RE_{DF}}} \frac{1}{\sqrt{1-\left(\frac{q_e \overline{\gamma}_{\mathrm{RE}_{DF}}}{\overline{\gamma}_{\mathrm{RD}_{DF}} + \overline{\gamma}_{\mathrm{RE}_{DF}}}\right)^2}} \quad \text{(A.37)}$$

Thus substituting (A.36), (A.37) in (3.38) , closed form equation for (3.44) is obtained. Putting (3.44) in (3.46), closed form equation for (3.48) under Hoyt faded environment is obtained.

Appendix B

B.1 Proof of (4.34) and (4.35)

For deriving the OP for DF protocol, the SINR of DF is put into the expression of OP
By using equations (4.19)-(4.22), the resultant expression of OP for j^{th} relay is obtained which is shown in equation (B.1).

$$P_{outj} = 1 - \Pr\left(P_j|h_j|^2 > \gamma_{th} \ , Q_j\left(|h_j|^2 + U_j\right)|g_j|^2 > \gamma_{th}\right)$$

$$= 1 - \Pr\left(|h_j|^2 > \frac{\gamma_{th}}{P_j} \ , |g_j|^2 > \frac{\gamma_{th}}{Q_j\left(|h_j|^2 + U_j\right)}\right)$$

$$= 1 - \int_{\frac{\gamma_{th}}{P_j}}^{\infty} f_{|h_j|^2}(z)\left[\Pr\left(|g_j|^2 > \frac{\gamma_{th}}{Q_j\left(z_j + U_j\right)}\right)\right] dz$$

$$= 1 - \int_{\frac{\gamma_{th}}{P_j}}^{\infty} f_{|h_j|^2}(z)\left[1 - \Pr\left(|g_j|^2 \leq \frac{\gamma_{th}}{Q_j(z_j+U_j)}\right)\right] dz \quad \text{(B.1)}$$

Putting the PDF and CDF of the Weibull distribution equation (B.2) is obtained.

$$P_{outj} = 1 - \frac{K_{hj}}{{\lambda_{hj}}^{k_{hj}}} \int_{\frac{\gamma_{th}}{P_j}}^{\infty} {z_j}^{k_{hj}-1} \ e^{-\left\{\left(\frac{z_j}{\lambda_{hj}}\right)^{k_{hj}} + \left(\frac{\gamma_{th}}{Q_j \lambda_{gj}\left(z_j+U_j\right)}\right)^{k_{gj}}\right\}} dz_j \quad \text{(B.2)}$$

Substitution of $p_j = \left({z_j}/{\lambda_{hj}}\right)^{k_{hj}}$ into equation (B.3) can be derived.

$$P_{outj} = 1 - \int_{\left(\frac{\gamma_{th}}{P_j \lambda_{hj}}\right)}^{\infty} {}^{k_{hj}} \; e^{-\left\{ p_j + \left(\frac{\gamma_{th}}{Q_j \lambda_{gj} \lambda_{hj}} \cdot \frac{1}{\left(p_j \frac{1}{k_{hj}} + \frac{U_j}{\lambda_{hj}} \right)} \right)^{k_{gj}} \right\}} dp_j \quad \text{(B.3)}$$

Now, using (4.18), (4.19), (4.22) and (4.24), (B.4)-(B.6) are formulated.

$$\frac{\gamma_{th}}{P_j \lambda_{hj}} = \frac{\gamma_{th}\left((1-\rho_j) I_{Rj} + \sigma_{Rj}^2\right)}{{L_{1j}}^2 P_S . (1-\rho_j) \lambda_{hj}} = M_j \quad \text{(B.4)}$$

$$\frac{\gamma_{th}}{Q_j \lambda_{gj} \lambda_{hj}} = \frac{\gamma_{th}\left(I_D + \sigma_D^2\right)(1-\alpha_j-\beta_j)}{\lambda_{hj} \lambda_{gj} (\eta_{Tj} \alpha_j + \eta_{Pj} \rho_j \beta_j) {L_{1j}}^2 {L_{2j}}^2 P_S} = N_j \quad \text{(B.5)}$$

$$\frac{U_j}{\lambda_{hj}} = \frac{I_{Rj}}{L_{1j}^2 P_S \lambda_{hj}} = X_j \quad \text{(B.6)}$$

Equations (B.3)-(B.6) lead to equation (B.7).

$$P_{outj} = 1 - \int_{M_j}^{\infty} {}^{k_{hj}} \, e^{-\left\{ p_j + \left(\frac{N_j}{\left(p_j \frac{1}{k_{hj}} + X_j \right)} \right)^{k_{gj}} \right\}} d\, p_j \quad \text{(B.7)}$$

Equation (B.7) shows the OP of j^{th} relay in DF protocol.

Outage probability for AF protocol

For deriving the outage probability for DF protocol, the SINR of DF is put into the expression of outage probability. The alternative expression of outage probability for j^{th}relay is shown in equation (B.8).

$$P_{outj} = \Pr\left(\gamma_{SRj} \le \gamma_{th}\right) + \Pr\left(\gamma_{SRj} > \gamma_{th} \;,\; \gamma_{RDj} \le \gamma_{th}\right) \quad \text{(B.8)}$$

Putting (4.19) in $\Pr\left(\gamma_{SRj} \le \gamma_{thj}\right)$ equation (B.9) is obtained.

$$\Pr\left(\gamma_{SRj} \le \gamma_{th}\right) = \Pr\left(\frac{\left(1-\rho_j\right) P_s}{L_{1j}^2 (\sigma_{jR}^2 + \left(1-\rho_j\right) I_{jR})} |h_j|^2 \le \gamma_{th} \right)$$

$$= \Pr\left(|h_j|^2 \le \gamma_{th} . \frac{L_{1j}^2 [(1-\rho_j)\sigma_{jR}^2 + I_{jR}]}{(1-\rho_j) P_s}\right) \quad \text{(B.9)}$$

The constants in equations (19)-(22) are modified into equations (B.10)-(B.13).

$$c = c' \gamma_{th} \quad \text{(B.10)}$$

$$d = d' \gamma_{th} \quad \text{(B.11)}$$

$$e = e' \gamma_{th} \quad \text{(B.12)}$$

$$f = f' \gamma_{th} \quad \text{(B.13)}$$

Therefore, equation (B.14) is obtained.

$$\Pr(\gamma_{SRj} \le \gamma_{th}) = \Pr\left(|h_j|^2 \le \frac{d}{a}\right) = \int_{z=0}^{\frac{d}{a}} f_{|h_j|^2}(z)dz \quad \text{(B.14)}$$

The equation (B.15) shows the expression for $\Pr(\gamma_{SRj} > \gamma_{th},\ \gamma_{RDj} \le \gamma_{th})$.

$$\Pr(\gamma_{SRj} > \gamma_{th},\ \gamma_{RDj} \le \gamma_{th})$$

$$= \Pr\left(\frac{(1-\rho_j)P_s}{L_{1j}^2[\sigma_{jR}^2 + (1-\rho_j)I_{jR}]}|h_j|^2 > \gamma_{th}, \frac{a|g_j|^2|h_j|^4 + b|g_j|^2|h_j|^2}{c'|h_j|^2 + d'|g_j|^2|h_j|^2 + e'|g_j|^2 + f'} \le \gamma_{th}\right)$$

$$= \Pr\left(|h_j|^2 > \gamma_{th}.\frac{L_{1j}^2[(1-\rho_j)\sigma_{jR}^2 + I_{jR}]}{(1-\rho_j)P_s}, |g_j|^2\left\{a|h_j|^4 + b|h_j|^2 - \gamma_{th}d'|h_j|^2 - \gamma_{th}e'\right\}\right.$$

$$\left. \le \gamma_{th}(c'|h_j|^2 + f')\right)$$

$$= \Pr\left(|h_j|^2 > \frac{d}{a}\ , |g_j|^2\left\{a|h_j|^4 + b|h_j|^2 - d|h_j|^2 - e\right\} \le \left(c|h_j|^2 + f\right)\right) \quad \text{(B.15)}$$

From equations (17), (18), (20), (21), (B.11), (B.12),$\frac{b}{a} = \frac{e'}{d'} = \frac{e}{d}$. Thus,

$$\left\{a|h_j|^4 + b|h_j|^2 - d|h_j|^2 - e\right\} = a\left(|h_j|^2 - \frac{d}{a}\right)\left(|h_j|^2 + \frac{b}{a}\right) \quad \text{(B.16)}$$

If,$|h_j|^2 > \frac{d}{a}$, then the right-hand side of the equation (A.16) will be positive. The equation (A.15) leads to equation (A.17).

$$\Pr(\gamma_{SRj} > \gamma_{th}\ ,\ \gamma_{RDj} \le \gamma_{th})$$

$$= \Pr\left(|h_j|^2 > \frac{d}{a}\ , |g_j|^2 \le \frac{\left(c|h_j|^2 + f\right)}{a\left(|h_j|^2 - \frac{d}{a}\right)\left(|h_j|^2 + \frac{b}{a}\right)}\right)$$

$$= \int_{z_j=\frac{d}{a}}^{\infty} f_{|h_j|^2}(z_j) Pr\left(|g_j|^2 \le \frac{cz_j + f}{a\left(z_j - \frac{d}{a}\right)\left(z_j + \frac{b}{a}\right)}\right) dz_j \quad \text{(B.17)}$$

By putting the p.d.f. and c.d.f. of Weibull distribution and using $\Pr(\gamma_{SRj} > \gamma_{th}\ ,\ \gamma_{RDj} \le \gamma_{th})$ leads to:

$$P_{outj} = \int_{z_j=0}^{\frac{d}{a}} f_{|h_j|^2}(z_j)dz_j + \int_{z=\frac{d}{a}}^{\infty} f_{|h_j|^2}(z_j)\left[1 - e^{-\left(\frac{cz_j + f}{a\left(z_j - \frac{d}{a}\right)\left(z_j + \frac{b}{a}\right)}.\frac{1}{\lambda_{gj}}\right)^{k_{gj}}}\right] dz_j$$

$$P_{outj} = 1 - \int_{z_j=\frac{d}{a}}^{\infty} f_{|h_j|^2}(z_j) e^{-\left(\frac{cz_j + f}{a\left(z_j - \frac{d}{a}\right)\left(z_j + \frac{b}{a}\right)}.\frac{1}{\lambda_{gj}}\right)^{k_{gj}}} dz_j$$

$$P_{outj} = 1 - \int_{z_j=\frac{d}{a}}^{\infty} \frac{k_{hj}}{\lambda_{hj}} \left(\frac{z_j}{\lambda_{hj}}\right)^{k_{hj}-1} e^{-\left(z_j/\lambda_{hj}\right)^{k_{hj}}} e^{-\left(\frac{cz_j+f}{a\left(z_j-\frac{d}{a}\right)\left(z_j+\frac{b}{a}\right)}\cdot\frac{1}{\lambda_{gj}}\right)^{k_{gj}}} dz_j$$

$$= 1 - \frac{k_{hj}}{\lambda_{hj}^{k_{hj}}} \int_{z=\frac{d}{a}}^{\infty} z_j^{k_{hj}-1} e^{-\left\{\left(z_j/\lambda_{hj}\right)^{k_{hj}} + \left(\frac{cz_j+f}{a\left(z_j-\frac{d}{a}\right)\left(z_j+\frac{b}{a}\right)}\cdot\frac{1}{\lambda_{gj}}\right)^{k_{gj}}\right\}} dz_j$$

(B.18)

Now using $cz_j + f = c\left(z_j + \frac{f}{c}\right) = c(z_j + \frac{d}{a\gamma_{th}})$ and $p_j = \left(z_j/\lambda_{hj}\right)^{k_{hj}}$ equation (B.19) can be obtained.

$$P_{outj} = 1 - \int_{\left(\frac{d}{a\lambda_{hj}}\right)^{k_{hj}}}^{\infty} e^{-\left\{p_j + \left(\frac{(p_j^{\frac{1}{k_{hj}}} + \frac{d}{a\lambda_{hj}\gamma_{th}})}{\left(p_j^{\frac{1}{k_{hj}}} - \frac{d}{a\lambda_{hj}}\right)\left(p_j^{\frac{1}{k_{hj}}} + \frac{b}{a\lambda_{hj}}\right)}\cdot\frac{c}{a\lambda_{gj}\lambda_{hj}}\right)^{k_{gj}}\right\}} d\,p_j \quad \text{(B.19)}$$

Now, using (4.25) and (B.10)-(B.11), (B.20)-(B.22) are formulated.

$$\frac{d}{a\lambda_{hj}} = \frac{L_{1j}{}^2\gamma_{th}\left((1-\rho_j)I_{Rj}+\sigma_{Rj}^2\right)}{P_S.(1-\rho_j)\lambda_{hj}} = M_j \quad \text{(B.20)}$$

$$\frac{c}{a\lambda_{gj}\lambda_{hj}} = \frac{L_{1j}{}^2 L_{2j}{}^2\gamma_{th}\left(I_D+\sigma_D^2\right)(1-\alpha_j-\beta_j)}{\lambda_{hj}\lambda_{gj}(\eta_{Tj}\alpha_j+\eta_{Pj}\rho_j\beta_j)\,P_s} = N_j \quad \text{(B.21)}$$

$$\frac{b}{a\lambda_{hj}} = \frac{L_{1j}{}^2 I_{Rj}}{P_S\,\lambda_{hj}} = X_j \quad \text{(B.22)}$$

Equations (B.20)-(B.22) lead to equation (B.23).

$$P_{outj} = 1 - \int_{M_j{}^{k_{hj}}}^{\infty} e^{-\left\{p_j + \left(\frac{(p_j^{\frac{1}{k_{hj}}} + \frac{M_j}{\gamma_{th}})}{\left(p_j^{\frac{1}{k_{hj}}} - M_j\right)\left(p_j^{\frac{1}{k_{hj}}} + X_j\right)}.N_j\right)^{k_{gj}}\right\}} d\,p_j \quad \text{(B.23)}$$

(B.23) shows the OP of j^{th} relay in AF protocol.

(B.7) and (B.23) are in very similar forms with the same constants. Therefore, the AF and DF in the proposed model can be analysed similarly.

B.2 Proof of (4.36)

Outage probability for HDAF protocol

Outage probability for j^{th} relay for HDAF is given in (B.24).

$$P_{outj} = \underbrace{\Pr(\gamma_{SRj} \le \gamma_{th}, \gamma_{SRj} \ge Th_j) + \Pr(\gamma_{SRj} > \gamma_{th}\ ,\ \gamma_{RDj-DF} \le \gamma_{th}, \gamma_{SRj} \ge Th_j)}_{\textbf{DF component}} +$$

$$\underbrace{\Pr(\gamma_{SRj} \le \gamma_{th}, \gamma_{SRj} < Th_j) + \Pr(\gamma_{SRj} > \gamma_{th}\ ,\ \gamma_{RDj-AF} \le \gamma_{th}, \gamma_{SRj} < Th_j)}_{\textbf{AF component}} \quad \text{(B.24)}$$

Let us define, $\gamma_{Hyj} = \frac{Th_j}{\gamma_{th}}$. (B.25)

I. If $\gamma_{th} \ge Th_j$, i.e., $\gamma_{Hyj} \le 1$, (B.26)-(B.29) are obtained.

$$\Pr(\gamma_{SRj} \le \gamma_{th}, \gamma_{SRj} \ge Th_j) = \Pr(Th_j \le \gamma_{SRj} \le \gamma_{thj}). \quad \text{(B.26)}$$

$$\Pr(\gamma_{SRj} > \gamma_{th}\ ,\ \gamma_{RDj-DF} \le \gamma_{th}, \gamma_{SRj} \ge Th_j) = \Pr(\gamma_{SRj} > \gamma_{th}\ ,\ \gamma_{RDj-DF} \le \gamma_{thj}). \quad \text{(B.27)}$$

$$\Pr(\gamma_{SRj} \le \gamma_{th}, \gamma_{SRj} < Th_j) = \Pr(\gamma_{SRj} < Th_j). \quad \text{(B.28)}$$

$$\Pr(\gamma_{SRj} > \gamma_{th}\ ,\ \gamma_{RDj-AF} \le \gamma_{th}, \gamma_{SRj} < Th_j) = 0. \quad \text{(B.29)}$$

Putting the values of (B.26) -(B.29) into (B.24), OP can be written as equation (B.30).

$$P_{outj} = \Pr(Th_j \le \gamma_{SRj} \le \gamma_{th}) + \Pr(\gamma_{SRj} < Th_j) + \Pr(\gamma_{SRj} > \gamma_{th}\ ,\ \gamma_{RDj-DF} \le \gamma_{th})$$
$$= \Pr(\gamma_{SRj} \le \gamma_{th}) + \Pr(\gamma_{SRj} > \gamma_{th}\ ,\ \gamma_{RDj-DF} \le \gamma_{th})$$
$$= P_{outj-DF} \quad \text{(B.30)}$$

So, if $\gamma_{th} \ge Th_j$ ($\gamma_{Hyj} \le 1$), then the OP of the HDAF protocol is equal to the OP of the DF protocol.

II. If $\gamma_{th} < Th_j$, i.e., $\gamma_{Hyj} > 1$,

$$\Pr(\gamma_{SRj} \le \gamma_{th}, \gamma_{SRj} \ge Th_j) = 0. \quad \text{(B.31)}$$

$$\Pr(\gamma_{SRj} > \gamma_{th}\ ,\ \gamma_{RDj-DF} \le \gamma_{th}, \gamma_{SRj} \ge Th_j) = \Pr(\gamma_{SRj} \ge Th_j\ ,\ \gamma_{RDj-DF} \le \gamma_{th}). \quad \text{(B.32)}$$

$$\Pr(\gamma_{SRj} \le \gamma_{th}, \gamma_{SRj} < Th_j) = \Pr(\gamma_{SRj} \le \gamma_{th}). \quad \text{(B.33)}$$

$$\Pr(\gamma_{SRj} > \gamma_{th}\ ,\ \gamma_{RDj-AF} \le \gamma_{th}, \gamma_{SRj} < Th_j) = \Pr(\gamma_{th} < \gamma_{SRj} < Th_j,\ \gamma_{RDj-AF} \le \gamma_{th}). \quad \text{(B.34)}$$

Putting the values of (B.31) -(B.34) into (B.24), OP can be written as equation (B.35).

$$P_{outj} = \Pr(\gamma_{SRj} \le \gamma_{th}) + \Pr(\gamma_{SRj} \ge Th_j\ ,\ \gamma_{RDj-DF} \le \gamma_{th})$$
$$+ \Pr(\gamma_{th} < \gamma_{SRj} < Th_j,\ \gamma_{RDj-AF} \le \gamma_{th})$$
$$= \Pr(\gamma_{SRj} \le \gamma_{th}) + \Pr(\gamma_{SRj} > \gamma_{th}\ ,\ \gamma_{RDj-AF} \le \gamma_{th})$$
$$+ [\Pr(\gamma_{SRj} \ge Th_j,\ \gamma_{RDj-DF} \le \gamma_{th}) - \Pr(\gamma_{SRj} \ge Th_j,\ \gamma_{RDj-AF} \le \gamma_{th})]$$
$$= P_{outj-AF} - [\Pr(\gamma_{SRj} \ge Th_j,\ \gamma_{RDj-AF} \le \gamma_{th}) - \Pr(\gamma_{SRj} \ge Th_j,\ \gamma_{RDj-DF} \le \gamma_{th})] \quad \text{(B.35)}$$

$$\Pr(\gamma_{SRj} \ge Th_j,\ \gamma_{RDj-AF} \le \gamma_{th}) = \Pr\left(\gamma_{SRj} \ge \gamma_{th}.\frac{Th_j}{\gamma_{th}},\ \gamma_{RDj-AF} \le \gamma_{th}\right)$$

$$= \Pr\left(|h_j|^2 \geq \frac{d}{a}.\frac{Th_j}{\gamma_{th}} \ , |g_j|^2 \left\{ a|h_j|^4 + b|h_j|^2 - d|h_j|^2 - e \right\} \leq \left(c\,|h_j|^2 + f \right) \right)$$

$$= \Pr\left(|h_j|^2 \geq \frac{d}{a}.\gamma_{Hyj} \ , |g_j|^2 \left\{ a|h_j|^4 + b|h_j|^2 - d|h_j|^2 - e \right\} \leq \left(c\,|h_j|^2 + f \right) \right)$$

Now, as $\gamma_{Hyj} > 1$, therefore $|h_j|^2 \geq \frac{d}{a}.\gamma_{Hyj} > \frac{d}{a}$.

$$\Pr(\gamma_{SRj} \geq Th_j,\ \gamma_{RDj-AF} \leq \gamma_{th}) = \int_{z_j=\gamma_{Hyj}.\frac{d}{a}}^{\infty} f_{|h_j|^2}(z_j) Pr\left(|g_j|^2 \leq \frac{cz_j+f}{a\left(z_j-\frac{d}{a}\right)\left(z_j+\frac{b}{a}\right)} \right) dz_j \qquad \text{(B.36)}$$

Putting the parameters of Weibull distribution in equation (B.14), equation (B.37) is obtained.

$$\Pr(\gamma_{SRj} \geq Th_j,\ \gamma_{RDj-AF} \leq \gamma_{th}) = \int_{z_j=\gamma_{Hyj}.\frac{d}{a}}^{\infty} \frac{k_{hj}}{\lambda_{hj}} \left(\frac{z_j}{\lambda_{hj}} \right)^{k_{hj}-1} e^{-\left(z_j/\lambda_{hj}\right)^{k_{hj}}} [1 - e^{-\left(\frac{cz_j+f}{a\left(z_j-\frac{d}{a}\right)\left(z_j+\frac{b}{a}\right)}.\frac{1}{\lambda_{gj}} \right)^{k_{gj}}}] dz_j \qquad \text{(B.37)}$$

Substituting $p_j = \left(z_j/\lambda_{hj}\right)^{k_{hj}}$ in equation (B.37), equation (B.38) is obtained.

$$\Pr(\gamma_{SRj} \geq Th_j,\ \gamma_{RDj-AF} \leq \gamma_{th})$$

$$= \int_{\left(\frac{d}{a\lambda_{hj}}.\gamma_{Hyj}\right)^{k_{hj}}}^{\infty} e^{-p_j} d\,p_j - \int_{\left(\frac{d}{a\lambda_{hj}}.\gamma_{Hyj}\right)^{k_{hj}}}^{\infty} e^{-\left\{ p_j + \left(\frac{(p_j^{\frac{1}{k_{hj}}} + \frac{d}{a\lambda_{hj}\gamma_{th}})}{\left(p_j^{\frac{1}{k_{hj}}} - \frac{d}{a\lambda_{hj}}\right)\left(p_j^{\frac{1}{k_{hj}}} + \frac{b}{a\lambda_{hj}}\right)}.\frac{c}{a\lambda_{gj}\lambda_{hj}} \right)^{k_{gj}} \right\}} dp_j$$

$$= e^{-\left(\frac{d}{a\lambda_{hj}}.\gamma_{Hyj}\right)^{k_{hj}}} - \int_{\left(\frac{d}{a\lambda_{hj}}.\gamma_{Hyj}\right)^{k_{hj}}}^{\infty} e^{-\left\{ p_j + \left(\frac{(p_j^{\frac{1}{k_{hj}}} + \frac{d}{a\lambda_{hj}\gamma_{th}})}{\left(p_j^{\frac{1}{k_{hj}}} - \frac{d}{a\lambda_{hj}}\right)\left(p_j^{\frac{1}{k_{hj}}} + \frac{b}{a\lambda_{hj}}\right)}.\frac{c}{a\lambda_{gj}\lambda_{hj}} \right)^{k_{gj}} \right\}} dp_j \qquad \text{(B.38)}$$

Using (B.20)-(B.22), equation (B.39) is obtained.

$$\Pr(\gamma_{SRj} \geq Th_j,\ \gamma_{RDj-AF} \leq \gamma_{th}) = e^{-(\gamma_{Hyj}M_j)^{k_{hj}}} - \int_{(\gamma_{Hyj}M_j)^{k_{hj}}}^{\infty} e^{-\left\{ p_j + \left(\frac{(p_j^{\frac{1}{k_{hj}}} + \frac{M_j}{\gamma_{th}})}{\left(p_j^{\frac{1}{k_{hj}}} - M_j\right)\left(p_j^{\frac{1}{k_{hj}}} + X_j\right)}.N_j \right)^{k_{gj}} \right\}} dp_j \qquad \text{(B.39)}$$

$$\Pr(\gamma_{SRj} \geq Th_j,\ \gamma_{RDj-DF} \leq \gamma_{th}) = \Pr\left(\gamma_{SRj} \geq \gamma_{th}.\frac{Th_j}{\gamma_{th}},\ \gamma_{RDj-DF} \leq \gamma_{th} \right)$$

$$= \Pr\left(|h_j|^2 > \frac{\gamma_{th}}{P_j}.\frac{Th_j}{\gamma_{th}}\ , |g_j|^2 \le \frac{\gamma_{th}}{Q_j(|h_j|^2+U_j)}\right) = \int_{\gamma_{Hyj}.\frac{\gamma_{th}}{P_j}}^{\infty} f_{|h_j|^2}(z)\ \Pr\left(|g_j|^2 \le \frac{\gamma_{th}}{Q_j(z_j+U_j)}\right)dz \quad \text{(B.40)}$$

Putting the PDF and CDF. of Weibull distribution equation (B.41) is obtained.

$$\Pr(\gamma_{SRj} \ge Th_j,\ \gamma_{RDj-DF} \le \gamma_{th}) = \frac{K_{hj}}{{\lambda_{hj}}^{k_{hj}}} \int_{\gamma_{Hyj}.\frac{\gamma_{th}}{P_j}}^{\infty} {z_j}^{k_{hj}-1}\ e^{-\left(\frac{z_j}{\lambda_{hj}}\right)^{k_{hj}}} [1 - e^{-\left\{\left(\frac{\gamma_{th}}{Q_j\lambda_{gj}(z_j+U_j)}\right)^{k_{gj}}\right\}}]dz_j \quad \text{(B.41)}$$

Substitution of $p_j = \left({z_j}/{\lambda_{hj}}\right)^{k_{hj}}$ into equation (B.42) can be derived.

$$\Pr(\gamma_{SRj} \ge Th_j,\ \gamma_{RDj-DF} \le \gamma_{th})$$

$$= \int_{\left(\gamma_{Hyj}.\frac{\gamma_{th}}{P_j\lambda_{hj}}\right)^{k_{hj}}}^{\infty} e^{-p_j}dp_j$$

$$- \int_{\left(\gamma_{Hyj}.\frac{\gamma_{th}}{P_j\lambda_{hj}}\right)^{k_{hj}}}^{\infty} e^{-\left\{p_j+\left(\frac{\gamma_{th}}{Q_j\lambda_{gj}\left(p_j^{\frac{1}{k_{hj}}}\lambda_{hj}+U_j\right)}\right)^{k_{gj}}\right\}}dp_j$$

$$= e^{-\left(\gamma_{Hyj}.\frac{\gamma_{th}}{P_j\lambda_{hj}}\right)^{k_{hj}}} - \int_{\left(\gamma_{Hyj}.\frac{\gamma_{th}}{P_j\lambda_{hj}}\right)^{k_{hj}}}^{\infty} e^{-\left\{p_j+\left(\frac{\gamma_{th}}{Q_j\lambda_{gj}\left(p_j^{\frac{1}{k_{hj}}}\lambda_{hj}+U_j\right)}\right)^{k_{gj}}\right\}}dp_j \quad \text{(B.42)}$$

Using (B.4) -(B.6), (B.43) is formulated.

$$Pr(\gamma_{SRj} \ge Th_j,\ \gamma_{RDj-DF} \le \gamma_{th}) = e^{-(\gamma_{Hyj}.M_j)^{k_{hj}}} - \int_{(\gamma_{Hyj}M_j)^{k_{hj}}}^{\infty} e^{-\left\{p_j+\left(\frac{N_j}{\left(p_j^{\frac{1}{k_{hj}}}+\ X_j\right)}\right)^{k_{gj}}\right\}}d\,p_j \quad \text{(B.43)}$$

Combining (B.23), (B.4) -(B.6), (B.20) -(B.22),

$$P_{outj} = P_{outj-AF} - [Pr(\gamma_{SRj} \ge Th_j,\ \gamma_{RDj-AF} \le \gamma_{th}) - Pr(\gamma_{SRj} \ge Th_j,\ \gamma_{RDj-DF} \le \gamma_{th})]$$

$$= [1 - \int_{M_j^{k_{hj}}}^{\infty} e^{-\left\{p_j + \left(\frac{(p_j^{\frac{1}{k_{hj}}} + \frac{M_j}{\gamma_{th}})}{\left(p_j^{\frac{1}{k_{hj}}} - M_j\right)\left(p_j^{\frac{1}{k_{hj}}} + X_j\right)}.N_j\right)^{k_{gj}}\right\}} dp_j$$

$$+ \int_{(\gamma_{Hyj}M_j)^{k_{hj}}}^{\infty} e^{-\left\{p_j + \left(\frac{\left(p_j^{\frac{1}{k_{hj}}} + \frac{M_j}{\gamma_{th}}\right)}{\left(p_j^{\frac{1}{k_{hj}}} - M_j\right)\left(p_j^{\frac{1}{k_{hj}}} + X_j\right)}.N_j\right)^{k_{gj}}\right\}} dp_j$$

$$- \int_{(\gamma_{Hyj}M_j)^{k_{hj}}}^{\infty} e^{-\left\{p_j + \left(\frac{N_j}{\left(p_j^{\frac{1}{k_{hj}}} + X_j\right)}\right)^{k_{gj}}\right\}} d\,p_j$$

$$= 1 - \int_{M_j^{k_{hj}}}^{(\gamma_{Hyj}M_j)^{k_{hj}}} e^{-\left\{p_j + \left(\frac{(p_j^{\frac{1}{k_{hj}}} + \frac{M_j}{\gamma_{th}})}{\left(p_j^{\frac{1}{k_{hj}}} - M_j\right)\left(p_j^{\frac{1}{k_{hj}}} + X_j\right)}.N_j\right)^{k_{gj}}\right\}} dp_j -$$

$$\int_{(\gamma_{Hyj}M_j)^{k_{hj}}}^{\infty} e^{-\left\{p_j + \left(\frac{N_j}{\left(p_j^{\frac{1}{k_{hj}}} + X_j\right)}\right)^{k_{gj}}\right\}} dp_j \qquad \text{(B.44)}$$

Therefore if $\gamma_{Hyj} \leq 1$ then, $P_{outj} = P_{outj-DF}$; else

$$P_{outj} = 1 - \int_{M_j^{k_{hj}}}^{(\gamma_{Hyj}M_j)^{k_{hj}}} e^{-\left\{p_j + \left(\frac{(p_j^{\frac{1}{k_{hj}}} + \frac{M_j}{\gamma_{th}})}{\left(p_j^{\frac{1}{k_{hj}}} - M_j\right)\left(p_j^{\frac{1}{k_{hj}}} + X_j\right)}.N_j\right)^{k_{gj}}\right\}} dp_j -$$

$$\int_{(\gamma_{Hyj}M_j)^{k_{hj}}}^{\infty} e^{-\left\{p_j + \left(\frac{N_j}{\left(p_j^{\frac{1}{k_{hj}}} + X_j\right)}\right)^{k_{gj}}\right\}} dp_j \qquad \text{(B.45)}$$

From equation (B.45), it is noted that if $\gamma_{Hyj} \leq 1$, then the system behaves like DF and when γ_{Hyj} is sufficiently large, then the system approaches AF.

Appendix C

C.1 Proof of (5.49)

This appendix furnishes the steps to obtain closed form expression of accumulated harvested energy in multiple frames. We recall from (5.41), $E_{R_1}^k$ can be expressed as:

$$\begin{aligned} E_{R_1}^k &= \eta\alpha \frac{T}{2} \sum_{k=1}^{K} \left(P_{S1} g_{S1R_k} + \sum_{i=1}^{N} P_{I_i} g_{R_k I_i} \right) \\ &= \eta\alpha \frac{T}{2} \sum_{k=1}^{K} P_{S1} g_{S1R_k} + \eta\alpha \frac{T}{2} \sum_{k=1}^{K} \sum_{i=1}^{N} P_{I_i} g_{R_k I_i} \\ &= \eta\alpha \frac{T}{2} P_{S1} \sum_{k=1}^{K} g_{S1R_k} + \eta\alpha \frac{T}{2} P_{I_i} \sum_{k=1}^{K} \sum_{i=1}^{N} g_{R_k I_i} \end{aligned} \tag{C.1}$$

Since, $g_{S_1R_{1k}}$ is an exponential random variable, $\sum_{k=1}^{K} g_{S_1R_{1k}}$ follows gamma distribution. From (3.351.3) of [185] and (13) of [111], the harvesting energy for '*K*' frames at each relay in closed-form expression can be obtained from (5.41).

C.2 Proof of (5.63)

This appendix provides the details for obtaining SOP. From (5.62), we compute P_1 and P_2.

$$\begin{aligned} \mathrm{P}_1 &= P(C_{S1}^{SEC} < R_{th}) \\ &= P\left\{ \frac{1}{2} \log_2 \left(\frac{1+\gamma_{S_1S_2}}{1+\gamma_{S_2R_1}} \right) < R_{th} \right\} \\ &= P\left\{ \frac{1}{2} \log_2 \left(\frac{1+\phi}{1+\psi} \right) < R_{th} \right\} = P\left\{ \phi < 2^{2R_{th}} (1+\Psi) - 1 \right\} \\ &= \int_0^{\infty} \left(\int_0^{2^{2R_{th}}(1+\Psi)-1} f_{\phi}(\phi) d\phi \right) f_{\Psi}(\Psi) d\Psi \\ &= \int_0^{\infty} P\{\phi < R_{th}(1+\Psi) - 1\} f_{\Psi}(\Psi) d\Psi \\ &= \int_0^{\infty} F_{\phi}(R_{th}(1+\Psi) - 1)) f_{\Psi}(\Psi) d\Psi \end{aligned} \tag{C.2}$$

where $\phi = \gamma_{S_1S_2}$ and $\psi = \gamma_{S_2R_1}$

Now, $\gamma_{S_1S_2} = \min(\gamma_{S_1R_1}, \gamma_{R_1S_2})$

Thus, $F_{\gamma_{S_1S_2}}(\gamma_{th}) = F_{\gamma_{S_1R_1}}(\gamma_{th}) + F_{\gamma_{R_1S_2}}(\gamma_{th}) - F_{\gamma_{S_1R_1}}(\gamma_{th}) F_{\gamma_{R_1S_2}}(\gamma_{th})$ (C.3)

and

$$F_{\gamma_{S_2S_1}}(\gamma_{th}) = F_{\gamma_{S_2R_2}}(\gamma_{th}) + F_{\gamma_{R_2S_1}}(\gamma_{th}) - F_{\gamma_{S_2R_2}}(\gamma_{th}) F_{\gamma_{R_2S_1}}(\gamma_{th}) \tag{C.4}$$

Taking CDF of $\gamma_{S_1R_1}$, we have,

$$F_{\gamma_{S_1R_1}}(\gamma_{th}) = P(\gamma_{S_1R_1} < \gamma_{th})$$

$$= P\left\{\left(\frac{P_{S_1} g_{S_1R_1}}{P_{S_2} g_{S_2R_2} + \sum_{i=1}^{N} P_{I_i} g_{I_iR_1} + N_O}\right) < \gamma_{th}\right\}$$

$$= P\left\{\left(\frac{P_{S_1} A_1}{P_{S_2} A_2 + P_I A_3 + N_O}\right) < \gamma_{th}\right\}$$

$$= P\left\{\left(\frac{P_{S_1} A_1}{A' + N_O}\right) < \gamma_{th}\right\}$$

$$= \int_0^{\infty} F_{A_1}\left\{\frac{\gamma_{th}(A' + N_O)}{P_{S_1}}\right\} f_{A'}(a')da'$$

$$= 1 - \exp\left(\frac{\gamma_{th}(A' + N_O)}{P_{S_1}}\right)\left(\frac{P_{S_1}\lambda_{A_1}}{P_{S_1}\lambda_{A_1} + \gamma_{th}P_{S_2}\lambda_{A_2}}\right)\left(\frac{P_{S_1}\lambda_{A_1}}{P_{S_1}\lambda_{A_1} + \gamma_{th}P_I\lambda_{A_3}}\right)^N \quad \text{(C.5)}$$

Differentiating the above equation, we obtain the PDF of $\gamma_{S_1R_1}$ given as:

$$f_{\gamma_{S_1R_1}}(\gamma_{th}) = 1 - \exp(M_1\gamma_{th})[(M_1.M_2.M_3) - \left\{(P_{S_1}P_{S_2}\lambda_{A_1}\lambda_{A_2}).\frac{M_3}{M_2}\right\} - \{N.(P_{S_1}P_{S_2}\lambda_{A_1}\lambda_{A_2}).M_2.M_3\}] \quad \text{(C.6)}$$

Next, for a single frame i.e. K=1, we recall from (5.54),

$$\gamma_{R_1S_2} = \frac{P_{R_1} g_{R_1S_2}}{\sum_{i=1}^{N} P_{I_i} g_{I_iR_1} + N_O}$$

$$= \frac{X}{1+W}$$

$$F_{\gamma_{R_1S_2}}(\gamma_{th}) = P(\gamma_{R_1S_2} < \gamma_{th})$$

$$= P(X < (1+W)\gamma_{th})$$

$$= \int_0^{\infty} F_X(\gamma_{th} + \gamma_{th}w) f_w(w)dw$$

Now, $f_w(w) = \frac{(\mu_1)^N}{(N-1)!} w^{N-1} \exp(-\mu_1 w)$

$$F_X(\gamma_{th} + \gamma_{th}w) = 1 - \exp(-\lambda_1(\gamma_{th} + \gamma_{th}w))$$

$$\therefore F_{\gamma_{R_1S_2}}(\gamma_{th}) = 1 - \frac{(\mu_1)^N}{(N-1)!}\exp(-\mu_1 w)\int_0^{\infty} w^{N-1}\exp(-(\mu_1 + \Omega_1\gamma_{th})w)\,\mathrm{dw}$$

$$\Rightarrow F_{\gamma_{R_1S_2}}(\gamma_{th}) = u_1[1 - (\xi_1)^N \exp(-u_2\gamma_{th})(\xi_1 + u_3\gamma_{th})^{-N}] \quad \text{(C.7)}$$

After some simplification and modifications, taking help of (24) in [28], we obtain (C.8) as:

$$F_{\gamma_{R_1S_2}}(\gamma_{th}) = 1 - \left(\frac{\alpha_2}{\gamma_{th} + \alpha_2}\right)^N \exp(-\Omega_1\gamma_{th}) \quad \text{(C.8)}$$

where $\alpha_1 = \frac{\mu_1}{\lambda_1}$; $\mu_1 = \frac{N_O\chi_1}{P_{R_1}}$ and $\lambda_1 = \frac{N_O\omega_1}{P_{S_1}}$

Thus, putting (C.5) and (C.7) in (C.3) and after some simplifications we get (C.9) as shown below:

$$F_{\gamma_{S_1S_2}}(\gamma_{th}) = F_{\gamma_{S_1R_1}}(\gamma_{th}) + F_{\gamma_{R_1S_2}}(\gamma_{th}) - F_{\gamma_{S_1R_1}}(\gamma_{th})F_{\gamma_{R_1S_2}}(\gamma_{th})$$

$$= 1 - \left(\frac{\alpha_1}{\gamma_{th}+\alpha_1}\right)^N \left(\frac{\alpha_2}{\gamma_{th}+\alpha_2}\right)^N \exp(-\frac{\gamma_{th}}{\Xi}) \quad \text{(C.9)}$$

where

$$\Xi = \frac{(1/\lambda_{A_1})(1/\Omega_1)}{(1/\lambda_{A_1})+(1/\Omega_1)}$$

Putting (C.8) and (C.9) in (C.2) we get

$$\mathrm{P}_1 = \int_0^\infty F_\phi(\gamma_{th}(1+\Psi)-1))f_\Psi(\Psi)d\psi$$
$$= \int_0^\infty \left[1-\exp(-P)\cdot\left\{\begin{matrix}1-\exp(\mathrm{Z}_1\gamma_{th})[(\mathrm{Z}_1.\mathrm{Z}_2.\mathrm{Z}_3) \\ -\left((P_{S_1}P_{S_2}\lambda_{A_1}\lambda_{A_2}).\frac{Z_3}{Z_2}\right)-\{N.(P_{S_1}P_{S_2}\lambda_{A_1}\lambda_{A_2}).\mathrm{Z}_2.\mathrm{Z}_3\}]\end{matrix}\right\}\right]d\psi \quad \text{(C.10)}$$

where $P = 1-\left(\frac{\alpha_1}{\Delta+\alpha_1}\right)^N \left(\frac{\alpha_2}{\Delta+\alpha_2}\right)^N \exp(-\frac{\Delta}{\Xi})$

and $\Delta = \gamma_{th}(1+\Psi)-1$

After some modification and simplification we obtain (C.11):

$$P_1 = \left[1-\exp(-Z)\frac{1}{\Gamma(\mathrm{K})}2\sqrt{\left(\frac{A_2A_3}{\lambda_1\Omega_1}\right)^K}K_K\left(2\sqrt{\left(\frac{A_2A_3}{\lambda_1\Omega_1}\right)}\right)\right]^N \quad \text{(C.11)}$$

where $K_K(*)$ is the "modified Bessel function of second kind with order K, $A_1 = \gamma_{S_1R_{1K}}$, $A_2 = 2^{2R_{th}}(1+A_1)-1$

Similarly,

$$P_2 = \left[1-\exp(-Y)\frac{1}{\Gamma(\mathrm{K})}2\sqrt{\left(\frac{B_2B_3}{\lambda_2\Omega_2}\right)^K}K_K\left(2\sqrt{\left(\frac{B_2B_3}{\lambda_2\Omega_2}\right)}\right)\right]^N \quad \text{(C.12)}$$

where $K_K(*)$ is the "modified Bessel function of second kind with order K", $B_1 = \gamma_{S_2R_{2K}}$, $B_2 = 2^{2R_{th}}(1+B_1)-1$

Putting equation (C.11) and (C.12) in (5.62), we get the closed form expression of SOP for multiple frames.

Appendix D

Proof of (6.36)

From Equation (6.22), we have,

$$\gamma_k^{UL} = \frac{\alpha_k P_{D_k} \left| h_{D_k R} \right|^2}{\sum_{i=1}^{K-1} \alpha_i P_{D_i} \left| h_{D_i R} \right|^2 + N_O} \tag{D.1}$$

$$\gamma_k^{UL} = \frac{\gamma_U}{1 + I_N} \tag{D.2}$$

I_N denotes sum of '*N*' statistically independent but not necessarily identically distributed (i.n.i.d) exponential random variables, each with mean $\mu_m = \frac{P_t}{\sigma^2} \Omega_{D_i R}$. Thus, the PDF of I_N is obtained as:

$$f_{I_N}(\gamma) = \sum_{m=1}^{v(A)} \sum_{n=1}^{\tau_m(A)} \chi_{m,n}(A) \frac{\mu_{\langle m \rangle}^{-n}}{(n-1)!} \gamma^{n-1} \exp\left\{ -\frac{\gamma}{\mu_{\langle m \rangle}} \right\} \tag{D.3}$$

where $A = diag(\mu_1, \mu_2, ..., \mu_N)$, $v(A)$ denotes number of distinct diagonal elements of *A*, $\mu_{\langle 1 \rangle} > \mu_{\langle 2 \rangle} > ... > \mu_{\langle v(A) \rangle}$ are the distinct diagonal elements, $\tau_m(A)$ denotes multiplicity of μ, and $\chi_{m,n}(A)$ is the (m, n)th characteristic coefficient of *A*.

The PDF of γ_k^{UL} is then obtained as

$$f_{\gamma_k^{UL}}(\gamma) = \frac{1}{\overline{\gamma}_U} \exp\left(-\frac{\gamma}{\overline{\gamma}_U} \right) \sum_{m=1}^{v(A)} \sum_{n=1}^{\tau_m(A)} \chi_{m,n}(A) \times \left[\left(1 + \frac{\mu_{\langle m \rangle}}{\overline{\overline{\gamma}_U}} \gamma \right)^{-n} + n\mu_{\langle m \rangle} \left(1 + \frac{\mu_{\langle m \rangle}}{\overline{\overline{\gamma}_U}} \gamma \right)^{-n-1} \right] \tag{D.4}$$

where the approach in [186, Chapter 6] is used to obtain (D.4). On integrating (31), the CDF of γ_k^{UL} is obtained as:

$$F_{\gamma_k^{UL}}(\gamma) = \sum_{m=1}^{v(A)} \sum_{n=1}^{\tau_m(A)} \chi_{m,n}(A) \left(1 + \frac{\mu_{\langle m \rangle}}{\overline{\overline{\gamma}_U}} \gamma \right)^{-n} \exp\left\{ -\frac{\gamma}{\overline{\overline{\gamma}_U}} \right\} \tag{D.4}$$

If the signals are i.i.d., the CDF of γ_k^{UL} reduces to

$$F_{\gamma_k^{UL}}(\gamma) = 1 - \left(1 + \frac{\mu_{\langle m \rangle}}{\overline{\overline{\gamma}_U}} \gamma \right)^{-N} \exp\left\{ -\frac{\gamma}{\overline{\overline{\gamma}_U}} \right\} \tag{D.5}$$

Using a similar approach as (D,4), the PDF of OMA in UL is expressed as:

$$f_{\gamma_m^{UL}}(\gamma) = 1 - \sum_{m=1}^{v(B)} \sum_{n=1}^{\tau_m(B)} \frac{\chi_{m,n}(B)}{(n-1)!} \times 2 \left(\frac{\gamma}{\overline{\overline{\gamma_g v_{\langle m \rangle}}}} \right)^{\frac{n}{2}} K_n \left(2 \sqrt{\frac{\gamma}{\overline{\overline{\gamma_g v_{\langle m \rangle}}}}} \right) \tag{D.6}$$

Putting the value of PDF and CDF of γ_k^{UL} and γ_m^{UL} in Equation (6.35) we obtain (6.36).

REFERENCES

1. Lu, X., Wang, P., Niyato, D., Kim, D. I., & Han, Z. (2014). Wireless networks with RF energy harvesting: A contemporary survey. *IEEE Communications Surveys & Tutorials*, *17*(2), 757-789.
2. Khuntia, P., Hazra, R., & Goswami, P. (2021). A bidirectional relay-assisted underlay device-to-device communication in cellular networks: An IoT application for FinTech. *IEEE Internet of Things Journal, 10*(3), 2174-2182.
3. Son, P. N., & Kong, H. Y. (2017). Co-channel interference energy harvesting for decode-and-forward relaying. *Wireless Personal Communications*, *95*, 3629-3652.
4. Makki, B., Chitti, K., Behravan, A., & Alouini, M. S. (2020). A survey of NOMA: Current status and open research challenges. *IEEE Open Journal of the Communications Society*, *1*, 179-189.
5. Yadav, C. B. K., & Dash, D. (2024). A novel data collection and partial charging scheme using multiple mobile vehicles in wireless rechargeable sensor networks. *Arabian Journal for Science and Engineering*, 1-21.
6. Lee, D., Lee, C., Jang, G., Na, W., & Cho, S. (2022). Energy-efficient directional charging strategy for wireless rechargeable sensor networks. *IEEE Internet of Things Journal, 9*(19), 19034-19048.
7. Alabsi, A., Hawbani, A., Wang, X., Al-Dubai, A., Hu, J., Aziz, S. A., ... & Alsamhi, S. H. (2024). Wireless power transfer technologies, applications, and future trends: a review. *IEEE Transactions on Sustainable Computing*.
8. Zhao, N., Zhang, S., Yu, F. R., Chen, Y., Nallanathan, A., & Leung, V. C. (2017). Exploiting interference for energy harvesting: A survey, research issues, and challenges. *IEEE Access*, *5*, 10403-10421.
9. Shaik, R. H., & Naidu, R. (2019). Performance evaluation of energy harvesting based DF system over Nakagami-m fading channels in the presence of co-channel interferences. *Physical Communication*, *36*, 100758.
10. Rahman, A. B., & Kader, M. F. (2023). A new energy harvesting scheme for multi-relay cooperative networks. *Digital Signal Processing*, *133*, 103846.
11. Powercast Corporation, (2015). [Online].
    Available: http://www.powercastco.com/products/development-kits/#P1110-EVAL-PS

12. T. Company., “NetSim.” [Online]. Available: http://www.tetcos.com/index.html.
13. Niotaki, K., Carvalho, N. B., Georgiadis, A., Gu, X., Hemour, S., Wu, K., ... & Shinohara, N. (2023). RF energy harvesting and wireless power transfer for energy autonomous wireless devices and RFIDs. *IEEE Journal of Microwaves, 3*(2), 763-782.
14. Khan, N. U., & Khan, F. U. (2019, November). RF energy harvesting for portable biomedical devices. In *2019 22nd International Multitopic Conference (INMIC)* (pp. 1-6). IEEE.
15. Sharma, P., & Singh, A. K. (2023). A survey on RF energy harvesting techniques for lifetime enhancement of wireless sensor networks. *Sustainable Computing: Informatics and Systems, 37*, 100836.
16. Khan, N. U., Khan, F. U., Farina, M., & Merla, A. (2024). RF energy harvesters for wireless sensors, state of the art, future prospects and challenges: a review. Physical and Engineering Sciences in Medicine, 1-17.
17. Ojo, F. K., Akande, D. O., & Salleh, M. F. M. (2019). An overview of RF energy harvesting and information transmission in cooperative communication networks. *Telecommunication Systems, 70*, 295-308.
18. Van der Meulen, E. C. (1968). Transmission of information in a T-terminal discrete memoryless channel. University of California, Berkeley.
19. Nasir, A. A., Zhou, X., Durrani, S., & Kennedy, R. A. (2013). Relaying protocols for wireless energy harvesting and information processing. *IEEE Transactions on Wireless Communications, 12*(7), 3622-3636.
20. Xiao, R., Liu, Y., Yang, H., Shen, J., & Yan, C. (2018, December). Performance analysis of hybrid protocol based two-way Decode-and-Forward relay networks. In *2018 IEEE 4th International Conference on Computer and Communications (ICCC)* (pp. 146-151). IEEE.
21. Rabie, K. M., Adebisi, B., & Alouini, M. S. (2016, December). Wireless power transfer in cooperative DF relaying networks with log-normal fading. *In 2016 IEEE Global Communications Conference (GLOBECOM)* (pp. 1-6). IEEE.
22. Al-Habob, A. A., Salhab, A. M., Zummo, S. A., & Alouini, M. S. (2018, April). A modified time-switching relaying protocol for multi-destination relay networks with SWIPT. In 2018 *IEEE Wireless Communications and Networking Conference (WCNC)* (pp. 1-6). IEEE.

23. Nguyen, T. N., Minh, T. H. Q., Tran, P. T., & Voznak, M. (2018). Adaptive energy harvesting relaying protocol for two-way half-duplex system network over Rician fading channels. *Wireless Communications and Mobile Computing*, 2018.
24. Khafagy, M., Ismail, A., Alouini, M. S., & Aissa, S. (2013). On the outage performance of full-duplex selective decode-and-forward relaying. *IEEE Communications Letters, 17*(6), 1180-1183.
25. Ozfatura, M. E., ElAzzouni, S., Ercetin, O., & ElBatt, T. (2019). Optimal throughput performance in full-duplex relay assisted cognitive networks. *Wireless Networks, 25*, 1931-1947.
26. Zhong, K., & Fu, L. (2021, September). Optimal throughput of the full-duplex two-way relay system with energy harvesting. In *2021 IEEE 94th Vehicular Technology Conference (VTC2021-Fall)* (pp. 1-6). IEEE.
27. Wang, D., Zhang, R., Cheng, X., & Yang, L. (2016). Capacity-enhancing full-duplex relay networks based on power-splitting (PS-) SWIPT. *IEEE Transactions on Vehicular Technology, 66*(6), 5445-5450
28. Laneman, J. N., Tse, D. N., & Wornell, G. W. (2004). Cooperative diversity in wireless networks: Efficient protocols and outage behavior. *IEEE Transactions on Information theory, 50*(12), 3062-3080.
29. Nasir, A. A., Zhou, X., Durrani, S., & Kennedy, R. A. (2014, June). Throughput and ergodic capacity of wireless energy harvesting based DF relaying network. In *2014 IEEE international conference on communications (ICC)* (pp. 4066-4071). IEEE.
30. Atapattu, S., Jiang, H., Evans, J., & Tellambura, C. (2015, June). Time-switching energy harvesting in relay networks. In *2015 IEEE International conference on communications (ICC)* (pp. 5416-5421). IEEE.
31. Boujemâa, H. (2011). Static hybrid amplify and forward (AF) and decode and forward (DF) relaying for cooperative systems. *Physical Communication, 4*(3), 196-205.
32. Peng, C., Li, F., & Liu, H. (2017). Optimal power splitting in two-way decode-and-forward relay networks. *IEEE Communications Letters, 21*(9), 2009-2012.
33. Nguyen, T. N., Minh, T. H. Q., Tran, P. T., Voznak, M., Duy, T. T., Nguyen, T. L., & Tin, P. T. (2019). Performance enhancement for energy harvesting based two-way relay protocols in wireless ad-hoc networks with partial and full relay selection methods. *Ad hoc networks*, *84*, 178-187.

34. Nguyen, T. N., Tran, D. H., Van Chien, T., Phan, V. D., Voznak, M., Tin, P. T., ... & Poor, H. V. (2022). Security–reliability tradeoff analysis for SWIPT-and AF-based IoT networks with friendly jammers. *IEEE Internet of Things Journal, 9*(21), 21662-21675.
35. Yang, F., Wei, W., & Huo, N. (2020, December). Performance Analysis of Energy-efficient HDAF Relaying Communication Based on SWIPT in Wireless Sensor Networks. In *2020 IEEE 6th International Conference on Computer and Communications (ICCC)* (pp. 802-807). IEEE.
36. Shannon, C. E. (1961, January). Two-way communication channels. In *Proceedings of the Fourth Berkeley Symposium on Mathematical Statistics and Probability, Volume 1: Contributions to the Theory of Statistics* (Vol. 4, pp. 611-645). University of California Press.
37. Nguyen, T. N., Tran, P. T., & Voznak, M. (2020). Wireless energy harvesting meets receiver diversity: A successful approach for two-way half-duplex relay networks over block Rayleigh fading channel. *Computer Networks, 172*, 107176.
38. Sun, L., Zhang, T., Li, Y., & Niu, H. (2012). Performance study of two-hop amplify-and-forward systems with untrustworthy relay nodes. *IEEE Transactions on Vehicular Technology*, *61*(8), 3801-3807.
39. Liu, W., Zhou, X., Durrani, S., & Popovski, P. (2015). Secure communication with a wireless-powered friendly jammer. *IEEE Transactions on Wireless Communications*, *15*(1), 401-415.
40. Tran, H. Q. (2024). PSR versus TSR relaying protocols: Leveraging full-duplex DF and energy harvesting for SWIPT in NOMA Systems. *Wireless Personal Communications, 134*(1), 293-318.
41. Ye, Y., Shi, L., Chu, X., Zhang, H., & Lu, G. (2019). On the outage performance of SWIPT-based three-step two-way DF relay networks. *IEEE Transactions on Vehicular Technology, 68*(3), 3016-3021.
42. Shi, L., Ye, Y., Hu, R. Q., & Zhang, H. (2019). System outage performance for three-step two-way energy harvesting DF relaying. *IEEE Transactions on Vehicular Technology, 68*(4), 3600-3612.
43. Shah, S. T., Choi, K. W., Hasan, S. F., & Chung, M. Y. (2016). Throughput analysis of two-way relay networks with wireless energy harvesting capabilities. *Ad Hoc Networks, 53*, 123-131.

44. Khanikar, K., Sinha, R., & Bhattacharjee, R. (2017). Incorporating primary user interference for enhanced spectrum sensing. *IEEE Signal Processing Letters*, *24*(7), 1039-1043.
45. Alhamad, R., & Boujemaa, H. (2020). Cooperative spectrum sensing with energy harvesting. *Telecommunication Systems*, *74*(1), 35-43.
46. Gurjar, D. S., Nguyen, H. H., & Tuan, H. D. (2019). Wireless information and power transfer for IoT applications in overlay cognitive radio networks. *IEEE Internet of Things Journal, 6*(2), 3257-3270.
47. Ghosh, S., Acharya, T., & Maity, S. P. (2020). On outage analysis in SWIPT enabled bidirectional D2D communications using spectrum sharing in cellular networks. *IEEE Transactions on Vehicular Technology, 69*(9), 10167-10176.
48. Pejoski, S., Hadzi-Velkov, Z., & Schober, R. (2017). Optimal power and time allocation for WPCNs with piece-wise linear EH model. *IEEE Wireless Communications Letters, 7*(3), 364-367.
49. Xiong, K., Wang, B., & Liu, K. R. (2017). Rate-energy region of SWIPT for MIMO broadcasting under nonlinear energy harvesting model. *IEEE Transactions on Wireless Communications, 16*(8), 5147-5161.
50. Anwar, A., Shah, S. T., Hasan, S. F., & Shin, D. R. (2018, December). SWIPT-based three-step multiplicative amplify-and-forward two-way relay networks with non-linear energy conversion model. In *2018 IEEE 4th International Conference on Computer and Communications (ICCC)* (pp. 152-157). IEEE.
51. Parvez, S., Kumar, D., & Bhatia, V. (2020, February). On performance of SWIPT enabled two-way relay system with non-linear power amplifier. In *2020 National Conference on Communications (NCC)* (pp. 1-6). IEEE.
52. Bletsas, A., Khisti, A., Reed, D. P., & Lippman, A. (2006). A simple cooperative diversity method based on network path selection. *IEEE Journal on selected areas in communications, 24*(3), 659-672.
53. Kader, M. F., Shahab, M. B., & Shin, S. Y. (2017, January). Cooperative spectrum sharing with energy harvesting best secondary user selection and non-orthogonal multiple access. In *2017 international conference on computing, networking and communications (ICNC)* (pp. 46-51). IEEE.
54. Andrawes, A., Nordin, R., & Ismail, M. (2019). Wireless energy harvesting with cooperative relaying under the best relay selection scheme. Energies, 12(5), 892.

55. Kader, M. F. (2020). Interference aided cooperative SWIPT for cellular IoT networks towards 5G and beyond. *Physical communication, 43*, 101223.
56. Do, N. T., Nguyen, Q. B. V., & An, B. (2015, October). A relay selection protocol for wireless energy harvesting relay networks. In *2015 International conference on advanced technologies for communications (ATC)* (pp. 243-247). IEEE.
57. Soysa, M., Suraweera, H. A., Tellambura, C., & Garg, H. K. (2012). Partial and opportunistic relay selection with outdated channel estimates. *IEEE Transactions on Communications*, *60*(3), 840-850.
58. Nguyen, X. X., & Do, D. T. (2017). Maximum harvested energy policy in full-duplex relaying networks with SWIPT. *International Journal of Communication Systems, 30*(17), e3359.
59. Altubaishi, E. S., & Shen, X. (2012, June). A novel distributed fair relay selection strategy for cooperative wireless system. In *2012 IEEE International Conference on Communications (ICC)* (pp. 4160-4164). IEEE.
60. Zou, Y., Zhu, J., & Jiang, X. (2019). Joint power splitting and relay selection in energy-harvesting communications for IoT networks. *IEEE Internet of Things Journal, 7*(1), 584-597.
61. Huang, J., Mukherjee, A., & Swindlehurst, A. L. (2013). Secure communication via an untrusted non-regenerative relay in fading channels. *IEEE Transactions on Signal Processing, 61*(10), 2536-2550.
62. Chen, X., Lei, L., Zhang, H., & Yuen, C. (2015). Large-scale MIMO relaying techniques for physical layer security: AF or DF?. *IEEE Transactions on Wireless Communications, 14*(9), 5135-5146.
63. Zou, Y., Zhu, J., Wang, X., & Leung, V. C. (2015). Improving physical-layer security in wireless communications using diversity techniques. *IEEE Network, 29*(1), 42-48.
64. Wyner, A. D. (1975). The wire-tap channel. *Bell system technical journal, 54*(8), 1355-1387.
65. He, X., & Yener, A. (2008, November). Two-hop secure communication using an untrusted relay: A case for cooperative jamming. In *IEEE GLOBECOM 2008-2008 IEEE Global Telecommunications Conference* (pp. 1-5). IEEE.
66. Gurrala, K. K., & Das, S. (2017). Performance study of hybrid decode–amplify–forward (HDAF) relaying scheme for physical layer security in wireless cooperative network. *International Journal of Communication Systems, 30*(8), e3182.

67. Jameel, F., Javed, M. A., Jayakody, D. N., & Hassan, S. A. (2018). On secrecy performance of industrial internet of things. *Internet Technology Letters, 1*(2), e32.
68. Ouyang, N., Jiang, X. Q., Bai, E., & Wang, H. M. (2017). Destination assisted jamming and beamforming for improving the security of AF relay systems. *IEEE Access, 5*, 4125-4131.
69. Lei, H., Dai, Z., Park, K. H., Lei, W., Pan, G., & Alouini, M. S. (2018). Secrecy outage analysis of mixed RF-FSO downlink SWIPT systems. *IEEE Transactions on Communications, 66*(12), 6384-6395.
70. Tuan, V. P., & Kong, H. Y. (2020). Secrecy capacity analysis of untrusted relaying energy-harvesting systems with hardware impairments. *Annals of Telecommunications, 75,* 397-405.
71. Srinivasan, M., & Kalyani, S. (2018). Secrecy capacity of $\kappa-\mu $ shadowed fading channels. *IEEE Communications Letters, 22*(8), 1728-1731.
72. Singh, R., Soni, S. K., Raw, R. S., & Kumar, S. (2017). A new approximate closed-form distribution and performance analysis of a composite Weibull/log-normal fading channel. *Wireless Personal Communications, 92*, 883-900.
73. Sinha, R., & Jindal, P. (2017, February). A study of physical layer security with energy harvesting in single hop relaying environment. In *2017 4th international conference on signal processing and integrated networks (SPIN)* (pp. 530-533). IEEE.
74. Qin, D., & Zhou, T. (2022). Energy efficiency in cognitive cooperative amplify and forward networks. *Sustainable Energy, Grids and Networks, 32*, 100923.
75. Mamaghani, M. T., Kuhestani, A., & Wong, K. K. (2018). Secure two-way transmission via wireless-powered untrusted relay and external jammer. *IEEE Transactions on Vehicular Technology, 67*(9), 8451-8465.
76. Chen, H., Liu, J., Zhai, C., & Zheng, L. (2010, April). Performance analysis of SNR-based hybrid decode-amplify-forward cooperative diversity networks over Rayleigh fading channels. In *2010 IEEE Wireless Communication and Networking Conference* (pp. 1-6). IEEE.
77. Bai, Z., Jia, J., Wang, C. X., & Yuan, D. (2015). Performance analysis of SNR-based incremental hybrid decode-amplify-forward cooperative relaying protocol. *IEEE Transactions on Communications, 63*(6), 2094-2106.
78. Bi, Y., & Chen, H. (2016). Accumulate and jam: Towards secure communication via a wireless-powered full-duplex jammer. *IEEE Journal of Selected Topics in Signal Processing, 10*(8), 1538-1550.

79. Long, M., & Chen, Y. (2019). Performance analysis of energy harvesting communications using multiple time slots. *IET Communications, 13*(3), 289-296.
80. Song, X., Zhu, J., Zhang, R., Peng, M., & Xu, S. (2023). Adaptive secure transmission for two-way energy harvesting relay networks with two-sided eavesdropping. *Transactions on Emerging Telecommunications Technologies, 34*(2), e4696.
81. Thakur, C., & Chattopadhyay, S. (2020, October). Secrecy performance of an improved interference-aided RF energy harvesting scheme in two-way multi-antenna relay network. In *2020 IEEE Applied Signal Processing Conference (ASPCON*) (pp. 123-127). IEEE.
82. Tabataba, F. S., Rouhani, P., & Koolivand, M. (2021). Energy efficiency optimization for amplify and forward relay networks with channel estimation errors. *Telecommunication Systems*, *76*, 541-552.
83. Yang, M., Kuo, Y., Chen, J., Yang, L., & Lv, L. (2017, September). Optimal time-switching relaying protocol for wireless-powered DF relay networks. *In 2017 IEEE 86th Vehicular Technology Conference (VTC-Fall)* (pp. 1-5). IEEE.
84. Kader, M. F., Uddin, M. B., Islam, A., & Shin, S. Y. (2019). Cooperative non-orthogonal multiple access with SWIPT over Nakagami-m fading channels. *Transactions on Emerging Telecommunications Technologies, 30*(5), e3571.
85. Rahman, A. B., & Kader, M. F. (2020, June). Best relay transmission aided energy harvesting in a multi relay cooperative network. In *2020 IEEE Region 10 Symposium (TENSYMP)* (pp. 106-109). IEEE.
86. Wei, X., & Zhu, Q. (2022). Joint optimization of energy harvesting and information transmission for trapped user. *Wireless Networks*, *28*(7), 2937-2950.
87. Nguyen, N. P., Duong, T. Q., Ngo, H. Q., Hadzi-Velkov, Z., & Shu, L. (2016). Secure 5G wireless communications: A joint relay selection and wireless power transfer approach. *IEEE access*, *4*, 3349-3359.
88. Y Gu, Y., & Aissa, S. (2014, June). Interference aided energy harvesting in decode-and-forward relaying systems. In *2014 IEEE international conference on communications (ICC)* (pp. 5378-5382). IEEE.
89. Gu, Y., & Aissa, S. (2015). RF-based energy harvesting in decode-and-forward relaying systems: Ergodic and outage capacities. *IEEE Transactions on Wireless Communications, 14*(11), 6425-6434.

90. Zeng, W., Tang, D., Zhao, S., Liu, G., & Huang, G. (2017, December). Energy diversity and opportunistic energy harvesting based cooperative communication with SWIET under RF interference. In *2017 3rd IEEE International Conference on Computer and Communications (ICCC)* (pp. 1046-1051). IEEE.
91. Ng, D. W. K., Lo, E. S., & Schober, R. (2013). Wireless information and power transfer: Energy efficiency optimization in OFDMA systems. *IEEE Transactions on Wireless Communications, 12*(12), 6352-6370.
92. Ahmed, I., Ikhlef, A., Schober, R., & Mallik, R. K. (2014). Power allocation for conventional and buffer-aided link adaptive relaying systems with energy harvesting nodes. *IEEE Transactions on Wireless Communications, 13*(3), 1182-1195.
93. L Elmorshedy, L., Leung, C., & Mousavifar, S. A. (2016, May). RF energy harvesting in DF relay networks in the presence of an interfering signal. In *2016 IEEE international conference on communications (ICC)* (pp. 1-6). IEEE.
94. Ojo, F. K., & Salleh, M. F. M. (2019). Energy efficiency optimization for SWIPT-enabled cooperative relay networks in the presence of interfering transmitter. *IEEE Communications Letters, 23*(10), 1806-1810.
95. Xing, H., Wong, K. K., Nallanathan, A., & Zhang, R. (2016). Wireless powered cooperative jamming for secrecy multi-AF relaying networks. *IEEE Transactions on Wireless Communications, 15*(12), 7971-7984.
96. Shukla, M. K., Yadav, S., & Purohit, N. (2017). Cellular multiuser two-way relay network with cochannel interference and channel estimation error: Performance analysis and optimization. *IEEE Transactions on Vehicular Technology, 67*(4), 3431-3446.
97. Sharma, S., Roy, S. D., & Kundu, S. (2017, November). Two way secure communication with two half-duplex DF relay. In *TENCON 2017-2017 IEEE Region 10 Conference* (pp. 869-874). IEEE.
98. Liang, H., Zhong, C., Lin, H., Li, Y., & Zhang, Z. (2020). Optimization and analysis of wireless powered multi-antenna two-way relaying systems. *IEEE Transactions on Communications, 68*(4), 2048-2060.
99. Toan, H. V., Bao, V. N. Q., & Le, K. N. (2018). Performance analysis of cognitive underlay two-way relay networks with interference and imperfect channel state information. *EURASIP Journal on Wireless Communications and Networking, 2018*, 1-10.

100. Kuhestani, A., & Mohammadi, A. (2016). Destination-based cooperative jamming in untrusted amplify-and-forward relay networks: resource allocation and performance study. *IET Communications, 10*(1), 17-23.

101. V Gupta, V., Kalamkar, S. S., & Banerjee, A. (2017, December). On secure communication using RF energy harvesting two-way untrusted relay. In *GLOBECOM 2017-2017 IEEE Global Communications Conference* (pp. 1-7). IEEE.

102. Okandeji, A. A., Khandaker, M. R., Wong, K. K., Zheng, G., Zhang, Y., & Zheng, Z. (2017). Secure full-duplex two-way relaying for SWIPT. *IEEE Wireless Communications Letters, 7*(3), 336-339.

103. Lee, K., Hong, J. P., Choi, H. H., & Quek, T. Q. (2018). Wireless-powered two-way relaying protocols for optimizing physical layer security. *IEEE Transactions on Information Forensics and Security, 14*(1), 162-174.

104. Ha, D. H., Nguyen, T. N., Tran, M. H., Li, X., Tran, P. T., & Voznak, M. (2020). Security and reliability analysis of a two-way half-duplex wireless relaying network using partial relay selection and hybrid TPSR energy harvesting at relay nodes. *IEEE Access, 8*, 187165-187181.

105. Xu, S., Song, X., Gao, Y., Li, S., Cao, J., & Xie, Z. (2021). Secrecy-enhancing design for two-way energy harvesting cooperative networks with full-duplex relay jamming. *China Communications, 18*(5), 273-284.

106. Tung, N. T., Nam, P. M., & Tin, P. T. (2021). Performance evaluation of a two-way relay network with energy harvesting and hardware noises. *Digital Communications and Networks, 7*(1), 45-54.

107. Jiang, X., Li, P., Shang, Y., Zou, Y., Li, B., & Yan, P. (2024). Improving Physical Layer Security for Distributed Antenna Systems with a Friendly Jammer. *IEEE Transactions on Communications*.

108. Ghosh, S., Maity, S. P., & Acharya, T. (2023). On outage analysis in overlay CCRN with RF energy harvesting and co-channel interference. *Wireless Personal Communications, 129*(2), 993-1007.

109. Ye, Y., Li, Y., Wang, D., & Lu, G. (2017, May). Power splitting protocol design for the cooperative NOMA with SWIPT. In *2017 IEEE International Conference on Communications (ICC)* (pp. 1-5). IEEE.

110. Ye, Y., Li, Y., Wang, Z., Chu, X., & Zhang, H. (2018). Dynamic asymmetric power splitting scheme for SWIPT-based two-way multiplicative AF relaying. *IEEE Signal Processing Letters, 25*(7), 1014-1018.

111. Sharma, S., Dhar Roy, S., & Kundu, S. (2020). Secure communication with energy harvesting multiple half-duplex DF relays assisted with jamming. *Wireless Networks, 26*, 1151-1164.
112. Wang, S., Xia, M., Huang, K., & Wu, Y. C. (2017). Wirelessly powered two-way communication with nonlinear energy harvesting model: Rate regions under fixed and mobile relay. *IEEE Transactions on Wireless Communications, 16*(12), 8190-8204.
113. Li, X., Liu, M., Deng, D., Li, J., Deng, C., & Yu, Q. (2019). Power beacon assisted wireless power cooperative relaying using NOMA with hardware impairments and imperfect CSI. *AEU-International Journal of Electronics and Communications, 108*, 275-286.
114. Ho-Van, K., & Do-Dac, T. (2023). Joint effects of non-linear energy harvesting, primary interference, and full-duplex destination-assisted jamming on spectrum sharing networks. *Wireless Networks, 29*(1), 221-234.
115. Jia, X., Guo, Y., Hao, Z., & Cao, S. (2022). Age of information and energy efficiency of amplify-and-forward relay-assisted Internet of Things with nonlinear energy harvesting and imperfect channel state information over Nakagami-fading channels. *Transactions on Emerging Telecommunications Technologies, 33*(11), e4586.
116. Babaei, M., Aygölü, Ü., Başaran, M., & Durak-Ata, L. (2020). BER performance of full-duplex cognitive radio network with nonlinear energy harvesting. *IEEE Transactions on Green Communications and Networking, 4*(2), 448-460.
117. Vu, T. H., Nguyen, T. V., & Kim, S. (2021). Cooperative NOMA-enabled SWIPT IoT networks with imperfect SIC: Performance analysis and deep learning evaluation. *IEEE Internet of Things Journal, 9*(3), 2253-2266.
118. Nguyen, M. T., Vu, T. H., & Kim, S. (2022). Performance analysis of wireless powered cooperative NOMA-based CDRT IoT networks. *IEEE Systems Journal, 16*(4), 6501-6512.
119. Bisen, S., Shaik, P., & Bhatia, V. (2021). On performance of energy harvested cooperative NOMA under imperfect CSI and imperfect SIC. *IEEE Transactions on Vehicular Technology, 70*(9), 8993-9005.
120. Aghababaiyan, K., & Maham, B. (2018). QoS-aware downlink radio resource management in OFDMA-based small cells networks. *IET Communications, 12*(4), 441-448.

121. Wang, R., & Brown, D. R. (2014, November). Throughput maximization in wireless powered communication networks with energy saving. In *2014 48th Asilomar Conference on Signals, Systems and Computers* (pp. 516-520). IEEE.
122. Marcano, A. S., & Christiansen, H. L. (2017, June). A novel method for improving the capacity in 5G mobile networks combining NOMA and OMA. In *2017 IEEE 85th Vehicular Technology Conference (VTC Spring)* (pp. 1-5). IEEE.
123. Saito, Y., Kishiyama, Y., Benjebbour, A., Nakamura, T., Li, A., & Higuchi, K. (2013, June). Non-orthogonal multiple access (NOMA) for cellular future radio access. In *2013 IEEE 77th vehicular technology conference (VTC Spring)* (pp. 1-5). IEEE.
124. Ding, Z., Yang, Z., Fan, P., & Poor, H. V. (2014). On the performance of non-orthogonal multiple access in 5G systems with randomly deployed users. *IEEE signal processing letters, 21*(12), 1501-1505.
125. Rabie, K. M., Adebisi, B., Yousif, E. H., Gacanin, H., & Tonello, A. M. (2017). A comparison between orthogonal and non-orthogonal multiple access in cooperative relaying power line communication systems. IEEE access, 5, 10118-10129.
126. Liu, Q., Lv, T., & Lin, Z. (2018). Energy-efficient transmission design in cooperative relaying systems using NOMA. *IEEE Communications Letters, 22*(3), 594-597.
127. Yue, X., Liu, Y., Kang, S., & Nallanathan, A. (2017). Performance analysis of NOMA with fixed gain relaying over Nakagami-$ m $ fading channels. *IEEE access, 5*, 5445-5454.
128. Dai, L., Wang, B., Ding, Z., Wang, Z., Chen, S., & Hanzo, L. (2018). A survey of non-orthogonal multiple access for 5G. *IEEE communications surveys & tutorials, 20*(3), 2294-2323.
129. Al-Imari, M., Xiao, P., Imran, M. A., & Tafazolli, R. (2014, August). Uplink non-orthogonal multiple access for 5G wireless networks. *In 2014 11th international symposium on wireless communications systems (ISWCS)* (pp. 781-785). IEEE.
130. Zhang, N., Wang, J., Kang, G., & Liu, Y. (2016). Uplink nonorthogonal multiple access in 5G systems. *IEEE Communications Letters, 20*(3), 458-461.
131. Wei, X., Al-Obiedollah, H., Cumanan, K., Zhang, M., Tang, J., Wang, W., & Dobre, O. A. (2020, June). Resource allocation technique for hybrid TDMA-NOMA system with opportunistic time assignment. In *2020 IEEE International Conference on Communications Workshops (ICC Workshops)* (pp. 1-6). IEEE.

132. Mahmood, A., Zeeshan, M., & Ashraf, T. (2021). A new hybrid CDMA–NOMA scheme with power allocation and user clustering for capacity improvement. *Telecommunication Systems, 78*(2), 225-237.

133. Ni, Z., Chen, Z., Zhang, Q., & Zhou, C. (2019, September). Analysis of RF energy harvesting in uplink-NOMA IoT-based network. In *2019 IEEE 90th vehicular technology conference (VTC2019-Fall)* (pp. 1-5). IEEE.

134. Khennoufa, F., Abdellatif, K., & Kara, F. (2022). Bit error rate evaluation of relay-aided cooperative NOMA with energy harvesting under imperfect SIC and CSI. *Physical Communication, 52*, 101630.

135. Rauniyar, A., Engelstad, P., & Østerbø, O. (2020, December). Exploiting SWIPT for IoT NOMA-based diamond relay networks. In MobiQuitous 2020-17th EAI International Conference on Mobile and Ubiquitous Systems: Computing, Networking and Services (pp. 137-146).

136. Rauniyar, A.; Engelstad, P. E.; Østerbø, O. N.: Performance analysis of RF energy harvesting and information transmission based on NOMA with interfering signal for IoT relay systems. *IEEE Sensors Journal 19*(17), 7668-7682 (2019)

137. Hoang, T. M., Tan, N. T., Hoang, N. H., & Hiep, P. T. (2019). Performance analysis of decode-and-forward partial relay selection in NOMA systems with RF energy harvesting. *Wireless networks*, *25*, 4585-4595.

138. Bariah, L., Muhaidat, S., & Al-Dweik, A. (2019). Error probability analysis of NOMA-based relay networks with SWIPT. *IEEE Communications Letters, 23*(7), 1223-1226.

139. Demirkol, B., Aldababsa, M., Toka, M., & Kucur, O. (2022). Performance analysis of antenna selection scheme in dual-hop NOMA HD and FD energy harvesting relay networks. *AEU-International Journal of Electronics and Communications, 143*, 154031.

140. Ghosh, S., Al-Dweik, A., & Alouini, M. S. (2023). On the performance of end-to-end cooperative NOMA-based IoT networks with wireless energy harvesting. *IEEE Internet of Things Journal, 10*(18), 16253-16270.

141. Alhamad, R. (2021). Adaptive NOMA/OMA for wireless communications. *Signal, Image and Video Processing, 15*(7), 1469-1475.

142. Wan, D., Wen, M., Yu, H., Liu, Y., Ji, F., & Chen, F. (2016, December). Non-orthogonal multiple access for dual-hop decode-and-forward relaying. In *2016 IEEE Global Communications Conference (GLOBECOM)* (pp. 1-6). IEEE.

143. Wan, D., Wen, M., Ji, F., Yu, H., & Chen, F. (2018). On the achievable sum-rate of NOMA-based diamond relay networks. *IEEE Transactions on Vehicular Technology, 68*(2), 1472-1486.

144. Khattab, N. H., & Soliman, S. S. (2022, December). Optimal power allocation in NOMA-based diamond relaying networks. In *2022 5th International Conference on Communications, Signal Processing, and their Applications (ICCSPA)* (pp. 1-6). IEEE.

145. Huang, B. Y., Lee, Y., & Sou, S. I. (2020). Joint power allocation for NOMA-based diamond relay networks with and without cooperation. *IEEE Open Journal of the Communications Society, 1*, 428-443.

146. Lee, Y., Huang, B. Y., & Sou, S. I. (2020, December). An efficient algorithm for joint power allocation in NOMA-based diamond relay networks. In *2020 International Computer Symposium (ICS)* (pp. 288-293). IEEE.

147. Qian, S. (2023). Reliable and secure short-packet communications in untrusted diamond relay networks. *IEEE Access, 11*, 24686-24695.

148. Aldababsa, M., Göztepe, C., Kurt, G. K., & Kucur, O. (2020). Bit error rate for NOMA network. *IEEE Communications Letters, 24*(6), 1188-1191.

149. Kara, F., & Kaya, H. (2019). Error probability analysis of NOMA-based diamond relaying network. *IEEE Transactions on Vehicular Technology, 69*(2), 2280-2285.

150. Ferdi, K. A. R. A., & Hakan, K. A. Y. A. (2020, October). Improved error performance in NOMA-based diamond relaying. In *2020 IEEE Microwave Theory and Techniques in Wireless Communications (MTTW)* (Vol. 1, pp. 151-156). IEEE.

151. Khattab, N. H., Soliman, S. S., Darweesh, M. S., & El-Sherif, A. A. (2022, February). Relay selection in NOMA-based diamond relaying networks. In *2022 24th International Conference on Advanced Communication Technology (ICACT)* (pp. 13-19). IEEE.

152. Sun, L., & Du, Q. (2017). Physical layer security with its applications in 5G networks: A review. *China communications, 14*(12), 1-14.

153. Pakravan, S., Chouinard, J. Y., Li, X., Zeng, M., Hao, W., Pham, Q. V., & Dobre, O. A. (2023). Physical layer security for NOMA systems: Requirements, issues, and recommendations. *IEEE Internet of Things Journal*.

154. El Halawany, B. M., Ruby, R., Riihonen, T., & Wu, K. (2018, December). Performance of cooperative NOMA systems under passive eavesdropping. In *2018 IEEE global communications conference (GLOBECOM)* (pp. 1-6). IEEE.

155. Sharma, S., Roy, S. D., & Kundu, S. (2020, February). Secrecy at physical layer in NOMA with cooperative jamming. In *2020 National Conference on Communications (NCC)* (pp. 1-6). IEEE.

156. Lv, L., Jiang, H., Ding, Z., Yang, L., & Chen, J. (2019). Secrecy-enhancing design for cooperative downlink and uplink NOMA with an untrusted relay. *IEEE Transactions on Communications, 68*(3), 1698-1715.

157. Guo, C., Zhao, L., Feng, C., Ding, Z., & Wang, H. M. (2020). Secrecy performance of NOMA systems with energy harvesting and full-duplex relaying. *IEEE Transactions on Vehicular Technology, 69*(10), 12301-12305.

158. Lathiya, P., & Wang, J. (2021). Near-field communications (NFC) for wireless power transfer (WPT): An overview. *Wireless Power Transfer–Recent Development, Applications and New Perspectives*, 95-122.

159. Zhang, Z., Pang, H., Georgiadis, A., & Cecati, C. (2018). Wireless power transfer—An overview. *IEEE transactions on industrial electronics*, *66*(2), 1044-1058.

160. Bala, T., Bhatia, V., Kumawat, S., & Jaglan, V. (2018). A survey: issues and challenges in wireless sensor network. *Int. J. Eng. Technol, 7*(2), 53-55.

161. Hong, Y. W. P., Hsu, T. C., & Chennakesavula, P. (2016). Wireless power transfer for distributed estimation in wireless passive sensor networks. *IEEE Transactions on Signal Processing, 64*(20), 5382-5395.

162. Borgia, E. (2014). The Internet of Things vision: Key features, applications and open issues. *Computer Communications, 54*, 1-31.

163. Bhatti, N. A., Alizai, M. H., Syed, A. A., & Mottola, L. (2016). Energy harvesting and wireless transfer in sensor network applications: Concepts and experiences. *ACM Transactions on Sensor Networks (TOSN), 12*(3), 1-40.

164. Baranov, A., Spirjakin, D., Akbari, S., Somov, A., & Passerone, R. (2016). POCO:‘Perpetual’operation of CO wireless sensor node with hybrid power supply. *Sensors and Actuators A: Physical, 238*, 112-121.

165. Visser, H. J., & Vullers, R. J. (2013). RF energy harvesting and transport for wireless sensor network applications: *Principles and requirements. Proceedings of the IEEE, 101*(6), 1410-1423.

166. Kaur, A., & Hema, N. (2023, November). RF-Energy Harvester and Its Applications in IoT: A Review. In *2023 Second International Conference on Informatics (ICI)* (pp. 1-5). IEEE.

167. Ijemaru, G. K., Ang, K. L. M., & Seng, J. K. (2022). Wireless power transfer and energy harvesting in distributed sensor networks: Survey, opportunities, and challenges. *International journal of distributed sensor networks, 18*(3), 15501477211067740.

168. Kaswan, A., Jana, P. K., & Das, S. K. (2022). A survey on mobile charging techniques in wireless rechargeable sensor networks. *IEEE Communications Surveys & Tutorials, 24*(3), 1750-1779.

169. Zhang, H., Guo, Y. X., Zhong, Z., & Wu, W. (2019). Cooperative integration of RF energy harvesting and dedicated WPT for wireless sensor networks. *IEEE Microwave and Wireless Components Letters, 29*(4), 291-293.

170. Huang, J., Zhou, Y., Ning, Z., & Gharavi, H. (2019). Wireless power transfer and energy harvesting: Current status and future prospects. *IEEE wireless communications, 26*(4), 163-169.

171. Van Leemput, D., Sabovic, A., Hammoud, K., Famaey, J., Pollin, S., & De Poorter, E. (2023). Energy Harvesting for Wireless IoT Use Cases: a Generic Feasibility Model and Trade-off Study. *IEEE Internet of Things Journal.*

172. Niotaki, K., Carvalho, N. B., Georgiadis, A., Gu, X., Hemour, S., Wu, K., ... & Shinohara, N. (2023). RF Energy Harvesting and Wireless Power Transfer for Energy Autonomous Wireless Devices and RFIDs. *IEEE Journal of Microwaves, 3*(2), 763-782.

173. Tanash, R., AlQudah, M., & Al-Agtash, S. (2023). Enhancing energy efficiency of IEEE 802.15. 4-based industrial wireless sensor networks. *Journal of Industrial Information Integration, 33*, 100460.

174. Infrastructure, L. E. C., & Layer, M. L. P. (2015). Ieee standard for low-rate wireless networks. *IEEE Stand, 2015*, 1-708.

175. Rodrigues, L., Leao, E., Montez, C., Moraes, R., Portugal, P., & Vasques, F. (2018). An advanced battery model for WSN simulation in environments with temperature variations. *IEEE Sensors Journal*, *18*(19), 8179-8191.

176. Ahmad, I., Hee, L. M., Abdelrhman, A. M., Imam, S. A., & Leong, M. S. (2021). Scopes, challenges and approaches of energy harvesting for wireless sensor nodes in machine condition monitoring systems: A review. *Measurement*, *183*, 109856.

177. Yang, Z., Xu, W., Pan, Y., Pan, C., & Chen, M. (2017). Energy efficient resource allocation in machine-to-machine communications with multiple access and energy harvesting for IoT. *IEEE Internet of Things Journal, 5*(1), 229-245.

178. Boshkovska, E., Ng, D. W. K., Zlatanov, N., & Schober, R. (2015). Practical non-linear energy harvesting model and resource allocation for SWIPT systems. *IEEE Communications Letters, 19*(12), 2082-2085.

179. Xu, X., Özçelikkale, A., McKelvey, T., & Viberg, M. (2017, May). Simultaneous information and power transfer under a non-linear RF energy harvesting model. In *2017 IEEE International Conference on Communications Workshops (ICC Workshops)* (pp. 179-184). IEEE.

180. Alevizos, P. N., & Bletsas, A. (2018). Sensitive and nonlinear far-field RF energy harvesting in wireless communications. *IEEE Transactions on Wireless Communications, 17*(6), 3670-3685.

181. Sharma, H., Haque, A., & Jaffery, Z. A. (2019). Maximization of wireless sensor network lifetime using solar energy harvesting for smart agriculture monitoring. *Ad Hoc Networks, 94*, 101966.

182. Mallick, S., Habib, A. Z. S. B., Ahmed, A. S., & Alam, S. S. (2017, December). Performance appraisal of wireless energy harvesting in IoT. In *2017 3rd International Conference on Electrical Information and Communication Technology (EICT)* (pp. 1-6). IEEE.

183. Altinel, D., & Kurt, G. K. (2016). Energy harvesting from multiple RF sources in wireless fading channels. *IEEE Transactions on Vehicular Technology, 65*(11), 8854-8864.

184. Cansiz, M., & Altinel, D. (2023). Multiband RF energy harvesting for zero-energy devices. *Electrical Engineering, 105*(1), 91-100.

185. Gradshteyn, I. S., & Ryzhik, I. M. (2014). Table of integrals, series, and products. Academic press.

186. Edition, F., Papoulis, A., & Pillai, S. U. (2002). Probability, random variables, and stochastic processes. McGraw-Hill Europe: New York, NY, USA.

187. "Zolertia re-mote," https://github.com/Zolertia/Resources/wiki/RE-Mote, [Online; accessed 07-January-2019]

188. Yang, D., Mahmood, A., Hassan, S. A., & Gidlund, M. (2022). Guest editorial: Industrial IoT and sensor networks in 5G-and-beyond wireless communication. *IEEE Transactions on Industrial Informatics, 18*(6), 4118-4121.

189. Rahmani, H., Shetty, D., Wagih, M., Ghasempour, Y., Palazzi, V., Carvalho, N. B., ... & Grosinger, J. (2023). Next-generation IoT devices: Sustainable eco-friendly

manufacturing, energy harvesting, and wireless connectivity. *IEEE Journal of Microwaves, 3*(1), 237-255.

190. Sherazi, H. H. R., Grieco, L. A., Imran, M. A., & Boggia, G. (2020). Energy-efficient LoRaWAN for industry 4.0 applications. *IEEE Transactions on Industrial Informatics, 17*(2), 891-902.
191. Benbuk, A. A., Kouzayha, N., Costantine, J., & Dawy, Z. (2023). Charging and Wake-Up of IoT Devices using Harvested RF Energy with Near-Zero Power Consumption. *IEEE Internet of Things Magazine, 6*(1), 162-167.
192. Ji, B., Li, Y., Zhou, B., Li, C., Song, K., & Wen, H. (2019). Performance analysis of UAV relay assisted IoT communication network enhanced with energy harvesting. *IEEE Access, 7*, 38738-38747.
193. Singh, S., Mitra, D., & Baghel, R. K. (2021). Performance evaluation of relay assisted wireless powered network over fluctuating two ray fading channel with diversity reception. *Wireless Personal Communications*, 121(3), 1739–1755.
194. Nguyen, B. C., Le, X. H., Nguyen, V. D., & Dung, L. T. (2021). On the Capacity of Full-Duplex AF/DF Relay System with Energy Harvesting for Vehicle-to-Vehicle Communications. *Wireless Communications and Mobile Computing*, *2021*(1), 8865615.
195. Babaei, M., Aygölü, Ü., & Basar, E. (2018). BER analysis of dual-hop relaying with energy harvesting in nakagami-$ m $ fading channel. *IEEE Transactions on Wireless Communications*, *17*(7), 4352-4361.
196. Zou, Y., & Wang, G. (2015). Intercept behavior analysis of industrial wireless sensor networks in the presence of eavesdropping attack. *IEEE Transactions on Industrial Informatics*, *12*(2), 780-787.
197. Azevedo, J. A., Santos, F. E., Sousa, T. A., & Agrela, J. M. (2015). Impact of the antenna directivity on path loss for different propagation environments. *IET Microwaves, Antennas & Propagation*, *9*(13), 1392-1398.